

BIOMECHANICAL STRATEGIES FOR LOCOMOTION IN SOFT-BODIED ANIMALS

A dissertation

submitted by

Huai-Ti Lin

In partial fulfillment of the requirements
for the degree of

Doctor of Philosophy

in

Biology

TUFTS UNIVERSITY

May, 2011

© 2011, Huai-Ti Lin

Adviser

Dr. Barry A. Trimmer

Co-adviser

Dr. Luis Dorfmann

Abstract

Soft-bodied animals have relatively few mechanical constraints on movements. This freedom is expected to impose a great challenge to muscle force transmission and body coordination. I have used the caterpillar as a model system to explore the role of soft mechanics in the control of locomotion. Caterpillars are extremely successful herbivores that roam on complex branched structures. They have multiple discrete soft appendages (prolegs) that attach their bodies to the substrate and can be released on demand. This well-defined substrate interaction makes caterpillars ideal for studying force transmission in soft-bodied animals. In this study, a custom two dimensional force sensor array measures ground reaction forces from the caterpillar prolegs during crawling. The data show persistent inter-segmental tensions propagating forward along the caterpillar's body. By loading itself against the substrate, the caterpillar constrains its mechanics to preferentially stretch and achieve locomotion (a strategy I call "environmental skeleton"). While the substrate provides essential support for crawling caterpillars, inching caterpillars have to rely mostly on their hydrostatic skeletons. A field survey of caterpillar gait diversity reveals many different proleg configurations and their associated motor sequences. In caterpillars with partial proleg reduction, we found various intermediate gaits with characteristics of crawling and inching. The transition from crawling to inching seems to require two major evolutionary changes. The reduction of mid-body prolegs allows the body to loop away from the substrate, and strengthening the hydrostatic skeleton prompts the body to flex instead of compress. A model based on tissue properties of *Manduca* caterpillar suggests that smaller hydrostats are more stable, consistent with the observation that inching caterpillars tend to be smaller. This gait

transition was simulated in several soft-bodied robots. From a simple crawling gait, pacing the motor pattern and removing mid body attachment produce an inching gait comparable to inchworm locomotion. Further, my soft-bodied robots demonstrate how nonlinear loading and large deformation result in behaviors that are not sensitive to the variations in motor commands. Clever morphological designs therefore allow us to embed simple adaptive control in the soft structures (e.g. pre-stressing the body for a dynamic event). We expect to find similar control strategies in soft-bodied animals.

Acknowledgments

I would like to thank Dr. Barry Trimmer for his advice in caterpillar experiments, Dr. Luis Dorfmann for his guidance in solid mechanics, Dr. Gary Leisk for his assistance in instrumentation, and Dr. Daniel Janzen *et al* for providing field work support. Of course, my colleagues from the department of biology, Tufts Biomimetic Devices Laboratory, and Tufts Advance Technology Collaborative have been very supportive in every project I attempted. Finally, I need to acknowledge my family and friends who helped keep me sane over the years as I devoted myself to research.

My caterpillar studies were funded by The National Science Foundation (NSF) and my robotics work was funded by Defense Advanced Research Project Agency (DARPA).

Table of Content

Chapter 1: Caterpillar locomotion	1
1.1 An overview	1
1.2 Caterpillar morphology and proleg variations.....	2
1.2.1 The body wall.....	3
1.2.2 The muscles.....	3
1.2.3 Thoracic legs	4
1.2.4 Prolegs.....	5
1.3 Caterpillar gaits and behavioral adaptations.....	7
1.3.1 Crawling.....	7
1.3.2 Inching.....	8
1.3.3 Crawl-inch.....	8
1.3.4 Inch-crawl.....	9
1.3.5 A6-Inching	9
1.3.6 A6-Crawling.....	10
1.3.7 Locomotor redundancy.....	10
1.3.8 Special adaptations	11
1.4 Mechanics of caterpillar locomotion	12
1.4.1 Substrate interactions	13
1.4.2 Hydrostatic skeleton	14
1.5 Scope and hypotheses: biomechanics and control strategies.....	14
1.5.1 Force transmission in crawling caterpillars.....	15
1.5.2 Crawling vs. inching: constraints in the hydrostatic skeleton	15
1.5.3 From crawling to inching: mechanical based gait transition	16
1.5.4 Simplifying soft body control: mechanical coupling	16
1.6 Scientific contributions.....	17
<i>References</i> [Chapter 1]	17
<i>Graphics</i> [Chapter 1]	22
Chapter 2: Instrumentation, soft robots and field work	30
2.1 A mini force beam array for measuring caterpillar ground reaction forces.....	30
2.1.1 Design considerations.....	30
2.1.2 A hybrid Wheatstone bridge for bi-axial sensing	32
2.1.3 Materials and manufacturing of the force beam	36

2.1.4	Simple beam tests	37
2.1.5	FEA guided cantilever beam design	39
2.1.6	Calibration and performance	40
2.1.7	The 4 th generation MFBA	42
2.2	An uni-axial lever-arm system for miniature soft tissue mechanical tests	43
2.2.1	Mechanical tests of soft tissues	43
2.2.2	The lever-arm system control with video extensometry	44
2.3	For the soft robots.....	45
2.3.1	The kinematics tracking system	45
2.3.2	A miniature force plate design	47
2.3.3	Data acquisition and synchronization	48
2.4	Costa Rica field work	48
2.4.1	A general survey of caterpillar gaits.....	48
2.4.2	Area de Conservacion Guanacaste	49
2.4.3	Field activities	49
	<i>References</i> [Chapter 2]	50
	<i>Graphics</i> [Chapter 2]	51
	Chapter 3: Force transmission in caterpillar locomotion	67
3.1	Antagonist substrate reaction forces.....	67
3.2	The effect of substrate stiffness	68
3.3	Other effects of the substrate	68
	<i>Graphics</i> [3.1~3.3]	71
	<i>Publication-1:</i>	
	<i>The Substrate as a Skeleton: Ground Reaction Forces from a Soft-Bodied Legged Animal</i>	<i>72</i>
	<i>References</i> [Pub-1]	<i>91</i>
	<i>Graphics</i> [Pub-1]	<i>95</i>
	<i>Publication-2:</i>	
	<i>Caterpillars use the Substrate as their External Skeleton: A Behavior Confirmation</i>	<i>101</i>
	<i>References</i> [Pub-2]	<i>107</i>
	<i>Graphics</i> [Pub-2]	<i>110</i>
	Chapter 4: Tissue mechanics and hydrostatic skeleton.....	111
4.1	Scaling of constitutive models.....	111
4.2	From nonlinear materials to nonlinear structures	112

4.3	Underwater caterpillar crawl	113
4.4	Time-dependency and material adaptation	113
4.5	Flexion vs. compression	114
	<i>Referencs</i> [4.1~4.5]	116
	<i>Graphics</i> [4.1~4.5]	117
Publication-3 cover page		
	<i>Soft-Cuticle Biomechanics: A Constitutive Model of Anisotropy for Caterpillar Integument</i>	121
	<i>Publication-3 original</i>	122
Publication-4		
	<i>Ontogenetic scaling of caterpillar body properties and its biomechanical implications on the use of a hydrostatic skeleton</i>	133
	<i>References</i> [Pub-4]	152
	<i>Graphics</i> [Pub-4]	156
Chapter 5: From caterpillar locomotion to soft robots		168
5.1	Physical modeling of locomotion	169
5.2	Soft tensile actuator	171
5.3	Open-loop inching and nonlinear body loading	172
5.4	Hole traversal and nonlinear actuator properties	176
5.5	Climbing and retractable adhesion pads	180
5.6	Motor pattern pacing and gait transitions	182
5.7	One step closer to a biomimetic controller	184
	<i>References</i> [5.1~5.7]	187
	<i>Graphics</i> [5.1~5.7]	188
Publication-5		
	<i>GoQBot: a caterpillar-inspired soft-bodied rolling robot</i>	207
	<i>References</i> [Pub-5]	230
	<i>Graphics</i> [Pub-5]	233
Chapter 6: The principles of (loco)motion in soft-bodied animals		242
6.1	Hydrostatic skeleton vs. environmental skeleton	242
6.2	The evolution of caterpillar locomotor diversity	243
6.3	What does a caterpillar know and need to know during locomotion?	245
6.4	Morphological computation and the future of soft robotics	247
	<i>References</i> [6.1~6.4]	249

Chapter 1: Caterpillar Locomotion

1.1 An overview

The ability to make an articulated skeleton is a big evolutionary advance which improves force transmission and facilitates body posture control in animals. However, many animals function without any rigid support or joints. Soft bodied locomotion in a terrestrial setting (as opposed to aquatic) is particularly challenging since the animal must support its own weight and also interact with different materials in its environment. The entire body and physiology has to adapt to both large active deformation and imposed involuntary contortions. I am interested in the diverse control strategies soft-bodied animals use during locomotion. Caterpillars, the larval stage of Lepidoptera, are very useful as a model system for this inquiry (Fig.1-1A). As one of the most prevalent types of herbivore (in general) on the planet, the caterpillar specializes in moving through highly branched vegetation and transforming foliage into body mass. Most arthropods (with rigid body shells) ingest food stuff up to a few percent of their body weight each day (Reichle 1968) but caterpillars often consume more than their body weight each day (Jindra, Sehnal 1989) and multiply their body mass in days (Nijhout, Davidowitz & Roff 2006). As we marvel at their feeding capability, we must also appreciate caterpillars' locomotor abilities. Directing a sac of protein and sugar across many irregular defensive plant structures is really quite a feat. In this thesis, I will explore a few major biomechanical challenges a caterpillar faces in the context of soft-bodied locomotion.

In addition to traditional biomechanical measurements of animal locomotion, I incorporate a physical modeling approach to test some of the body control strategies in caterpillars. Biomimetics, bionics and bio-inspired engineering loosely define a discipline in which a biological morphology, function or working mechanism is translated to an artificial system. In biological research, this approach serves a

very important application. By replicating a biological system, one can quickly find out the constraints and challenges associated with operating such a system (Chirikjian, Burdick 1991, Daniel, Combes 2002, Ishida et al. 2001, McGeer 1990). The findings can then inform the biological research and help produce better hypotheses. This approach is particularly useful for systems with complicated physics and/or morphological constraints such as flying insects (Birch, Dickinson 2001, Poelma, Dickson & Dickinson 2006). The implementation of a robotic system in particular has gained increasing popularity over the decade. Some examples include simulating cockroach stride adaptation (Cham, Karpick & Cutkosky 2004), gecko climbing (Menon, Sitti 2006), snake undulation (Spranklin 2006), and more recently the inertial control of the reptile tails (Jusufi, Kawano & Libby 2010). For this research, we build soft-bodied robots as physical models for simulating caterpillar locomotion. By using the real physical devices, we bypass the technical hurdle of simulating soft body deformation accurately. Of course, one can take the working principles in biological systems and exploit them for real-world applications. More discussion of physical modeling and bio-inspired applications will be covered in chapter 5 and 6.

1.2 Caterpillar morphologies and proleg variations

Caterpillars have extremely diverse body morphologies and appendage arrangements (Scoble 1995). This section will review the four major load-bearing components in a caterpillar: external integument (resists body pressure), muscles layers (generate movements and create turgor), thoracic legs (aid body extension by shifting body weight), and abdominal prolegs (support body weight and anchor body segments). For experimental convenience, we use a common model system *Manduca sexta* for lab experiments. Therefore most quantitative animal data in this thesis will be based on *Manduca* caterpillars.

1.2.1 *The body wall*

Caterpillars have a very thin and flexible body wall (Fig.1-1B,C) consisting of un-tanned chitin and various collagen-like structural proteins (Hepburn 1976). These chitin micro fibrils form a tough matrix which is then coupled to a protein matrix via both covalent and non-valent bonds (Hackman, Goldberg 1978). Nanometer scale chitin crystallites are prevalent in soft cuticle of arthropods (Neville, Parry & Woodhead-Galloway 1976), and many surrounding proteins are highly elastic (Weis-Fogh 1960). Like most fiber-reinforced natural materials, soft cuticle of arthropods has laminations of chitin fibers in preferred orientations (Dennell 1976). In order to account for the continuous growth of body volume (integument stretching) the cuticle laminae further form microscopic pleats which can be expanded (Carter, Locke 1993). The resulting composite material exhibits nonlinear stress-stiffening mechanical properties and it is subject to chemical manipulation (Hepburn, Levy 1975) and hydration control (Wolfgang, Riddiford 1987). Therefore, soft-bodied arthropods such as the caterpillar can tune their integument properties via enzymes (chemically alter the structural components), hydration (physically change the H-bond affinity) and cuticle stress (mechanically stretch the chitin fibers). Details of caterpillar cuticle mechanics will be covered in chapter 4.

1.2.2 *The muscles*

Lining the caterpillar body wall are highly compliant muscles oriented mostly in the longitudinal direction (Fig.1-1B,C). These striated muscles (~70 muscles per segment) operate over an impressive strain range. When detached from the body wall, *Manduca* caterpillar muscles often contract to less than 50% of the original length. Similarly, stretching from the *in situ* resting length, these muscles can almost double in length without damage (Dorfmann, Trimmer & Woods 2007). Under the *in vitro* conditions, *Manduca* muscles can be stimulated to produce force from 50% to

150% strain with maximum force production right about resting length (108%) (Woods, Fusillo & Trimmer 2008). During crawling, abdominal muscles are expected to cycle through a strain range of 30%. For grooming or other reaching behaviors, muscles contraction can exceed this range. In general, caterpillar muscles exhibit pseudo-elastic behaviors in which loading and unloading curves do not overlap. Energy is dissipated in the process. During each loading event, the tensile stiffness of a single muscle increases continuously as the muscle lengthens (stress-stiffening). With tetanus stimulation, however, stretching has an opposite effect of reducing the stiffness (stress-softening) (Dorfmann, Trimmer & Woods 2007). In addition, under dynamic loading conditions, caterpillar muscles exhibit visco-elasticity. When subjected to higher cycling frequency, the muscles appear stiffer (Dorfmann, Woods & Trimmer 2008). In a stretch-and-hold experiment, the peak force in a *Manduca* muscles is proportional to the stretch velocity (Woods, Fusillo & Trimmer 2008). Interestingly, live *Manduca* muscles also show stress-adaptation. The tension developed from stretching always decays exponentially over time, and the time constant is inversely proportional to the stretch velocity. These nonlinear properties and time dependencies can determine the control mechanisms in caterpillar locomotion. For instance, the high damping from the pseudo-elastic property undermines that energy storage capability in caterpillar body. The stress-adaptation allows the caterpillar to undergo large body contortion without sustaining high muscle stress. Visco-elastic effects can compensate for sudden loading variations and produce smoother body control. Extended discussion on how material nonlinearities affect soft body control can be found in chapter 4 and 5.

1.2.3 Thoracic legs

Thoracic legs are the six articulated true legs that survive through metamorphosis (Fig.1-2A,B). They are responsible for locating the substrate and food (often the same thing) (Heinrich 1971). Because there are joint articulations on the exoskeleton, these legs can push as well as pull. They

also handle all the silk spinning tasks and perform life-line climbing behaviors (Brackenbury 1996). For the ambush predatory inchworms, thoracic legs are important for grabbing the prey (Montgomery 1982, Montgomery 1983). Some micro-Lepidoptera species such as *Coleophoridae* encase their entire abdomen in a silk reinforced shell. Since the thoracic legs are the sole appendages exposed to the environment, they have to carry out all the necessary tasks. This group of case-bearers includes a few species of Hawaiian carnivorous caterpillars that stalk snails with silk (Rubinoff, Haines 2005). Since this research focuses on the control strategies of large body deformation, the articulated thoracic legs are collectively treated as an anterior anchor point.

1.2.4 Prolegs

Prolegs are soft appendages only present in the caterpillar stage that develop from the ventral surface of abdominal segments A3-A6 and the last segment A10 (Fig.1-2C). These abdominal appendages are equipped with mini claw arrays around the soft plantar (Snodgrass 1965, Snodgrass 1993) and serve as discrete body anchors to the substrate. The number and arrangement of these claws vary across Lepidoptera species. *Manduca sexta*, for example, has a double array of interlacing crochets (claws) oriented in the ventral direction (Fig.1-2D). Only two major muscles control the deployment of these claws. The principle planta retractor muscle (PPRM) inserts directly at the planta where the double crochets array is located. The accessory planta retractor muscle (APRM) inserts at the lateral boundary of coxa (Fig.1-2C). Contraction of PPRM disengages the crochets from the substrate. Firing of APRM retracts the prolegs through the cuticular fold between the coxa and subcoxa (Mezoff et al. 2004). The coordination of these two muscles produces clean fail-safe proleg detachment from the substrate. The re-extension/attachment is driven by the inherent hydrostatic pressure. This passive gripping system allows the caterpillar to cling on to its food plant safely without spending any extra muscle energy.

Developmentally, abdominal appendages are controlled by the expression of homeotic genes (or Hox genes). More specifically, the proleg development is mediated by the gene complex *Distal-less* (*Dll*). Multiple Hox gene complexes regulate the transcription of *Dll*, and therefore produce the proleg distribution pattern (Warren et al. 1994). In Diptera and Lepidoptera, *Dll* is expressed in every abdominal segment. The Hox proteins from the Bithorax Complex (BX-C) repress *Dll* and determine the presence of prolegs in each segment. Larvae of *Hymenoptera* regulate the proleg development via a different mechanism (Suzuki, Palopoli 2001). Another regulator *E complex* also seems to repress *Dll*. A group of E mutants of silkworm *Bombyx mori* develop rudimentary supernumerary prolegs (Xiang et al. 2008). In addition, the Hox genes *abd-A* and *abd-B* are a proleg promoter and suppressor respectively (Tomita, Kikuchi 2009). Such an intricate developmental process is subject to perturbation. Indeed, *Manduca* caterpillars exposed to X-ray radiation develop abnormal proleg patterns (personal communication, M. Simon). With high sensitivity to mutation and direct functional consequences, caterpillar proleg distribution should be highly selected through evolution (Nagy, Grbic 1999).

The body plan with prolegs on abdominal segment A3-A6 and A10 is considered the most ancestral form in Lepidopteran larvae (Forbes 1910, Hinton 1955, Common 1975). Almost all groups of caterpillars with different proleg configurations can be shown to be derived from this default body plan. For example, within the family of *Geometridae* (true inchworms), the combined mitochondrial DNA and ribosomal RNA sequence analysis suggests that the lineage leading to the subfamily Geometrinae (loopers with only A6 and TP prolegs) branched out from the more primitive lineage leading to *Archiearinae* 45.9 million years ago (Yamamoto, Sota 2007). Being in the *Geometridae* family, *Archiearinae* caterpillars possess somewhat reduced yet full complement of larval prolegs. The other branching event from this lineage led to a sister group of *Geometrinae*, *Ennominae*. In

this subfamily of caterpillars, proleg reduction and inching locomotion is common but sometimes not to the extent as in *Geometrinae* (Abraham et al. 2001). Proleg reduction is indeed a progressive evolutionary adaptation which is expected to have some functional origin. This thesis will explore some main drivers of proleg evolution in the context of biomechanics.

1.3 Caterpillar gaits and behavioral adaptations

Caterpillar gaits and behavioral adaptation associated with locomotion vary dramatically. Nevertheless, due to the general body constraints, most gaits can be characterized as crawling, inching, or any combination of both. Here I attempt to review all the existing modes of locomotion as defined by the various prolegs arrangements. Examples are given and mapped onto a phylogenetic tree adapted from the *Tree of Life Web Project* [<http://tolweb.org>] (Fig.1-3A)

1.3.1 *Crawling*

Caterpillar locomotion is often depicted as an anterior-grade wave prorogating across the body. Such a wave is accompanied by very coordinated prolegs retraction to allow shifting of body mass. Starting from the terminal prolegs (or anal prolegs), the crochets are released from the substrate in sequence as the abdomen contracts. The terminal prolegs are replanted on the substrate often when A4 prolegs are about to be released. In the mean time, thoracic legs advance forward continuously. This overall crawling pattern is representative of many caterpillars with five pairs of abdominal prolegs such as caterpillars in the superfamily Bombycoidea, containing emperor moths (*Saturniidae*), silk moth (*Bombycidae*), and hawkmoths (*Sphingidae*) (Fig.1-3B). *Manduca sexta* (tomato hornworm) is a typical example of *Sphingidae* (Fig.1-5) and is used to illustrate the mechanics of crawling in this thesis.

1.3.2 *Inching*

Inching is another prominent mode of locomotion in caterpillars often with reduced prolegs. The family *Geometridea* (true inchworms; loopers) has lost the mid-abdominal prolegs through evolution. They initiate inching by releasing the terminal prolegs and A6 prolegs in a near synchronized manner (Fig.1-4). Then the whole body buckles upward to plant the two pairs of prolegs closely behind the thoracic legs before the thorax is disengaged from the substrate to reach forward. This reciprocal motion can be quite dynamic and nimble (cycle over 2Hz). Like any other caterpillar gaits, inching can be arrested in either stage: forward reaching or posterior replanting (although some transitional phases are not very stable). Each step can be treated as almost independent. Geometrids tend to be small in body size. *Sphacelodes* is one of the largest geometrid genera in the subfamily *Ennominae* and can develop to slightly over 3cm in length and 0.2g in weight (Fig.1-3C). The size limit was thought to be linked to the ecological parameters such as the substrate gap distances. The study of hydrostatic skeleton in my thesis suggests that there might be mechanical constraints as well.

1.3.3 *Crawl-inch*

Reduction in the number of prolegs is most commonly found in the mid abdominal segments (*i.e.* A3-A4). In particular, the family *Noctuidae* exhibit great variation in body size and proleg arrangement (Fig.1-4A). Many caterpillars in the subfamily *Hypeninae* and *Catacalinae* have lost functional A3 prolegs, and sometimes even A4 prolegs. This evolutionary process can be seen in *Azeta rhodogaster* (*Catacalinae*) which possesses reduced A3 prolegs. These residual abdominal appendages do not grip during locomotion and the caterpillars engage in a rapid crawl-inch gait (Fig.1-7A). This crawl-inch gait shift is exaggerated in the highly athletic subfamily *Catacalinae* genus *Anomis* (Fig.1-7B). In this group of caterpillars, rapid release of the remaining A5-A6 and

A10 prolegs is accompanied by almost dynamic buckling of the abdomen, producing the striking appearance of loopers. Inching is dominant in this case, but crawling sequences are still visible when the caterpillar slows down.

1.3.4 Inch-crawl

On the other hand, members of the subfamily *Gonodonta* incorporate proleg reduction into a different locomotor strategy (Fig.1-4A). This group of caterpillars retain functional A4 prolegs but have lost the A3 prolegs completely (Fig.1-8A,B). By default, the caterpillar flexes its body dorsally at abdominal section A2. Significant morphological modifications on the inter-segmental integument allow such 180 degrees flexion. To move forward, a *Gonodonta* caterpillar extends its thorax and therefore straightens its body (often using the thoracic legs). Subsequently the anterior-grade crawling is initiated from the A10 terminal prolegs and passes through the prolegs A6-A4 twice or thrice to recover the original flexed body posture. This inch-crawl gait is very robust and enables *Gonodonta* caterpillars to cover long distances on the large food plant (*Piper*) quickly.

1.3.5 A6-inching

Other caterpillars such as *Selenisa* in the family *Catacalinae*, incorporate proleg reduction from the posterior segments (Fig.1-4A). In the absence of A3-A4 prolegs, the A10 terminal prolegs are elongated extensively and serve as tactile appendages during normal locomotion (Fig.1-9A). With only two pairs of load bearing prolegs, *Selenisa* performs an **A6 initiated inching**. This group of caterpillars also possesses very slender thoracic legs which twitch during the substrate searching phase of an inch cycle. Similarly the tentacle-like terminal prolegs wave in the air wildly during the stance phase of the A5-A6 prolegs. Before each re-attachment event of the abdomen, the terminal prolegs will momentarily scissor the substrate in a clamping motion as if to guide the trajectory of

A5-A6 proleg attachment. Interestingly, proleg retraction reflex and gripping ability are both still present in the elongated terminal prolegs, signifying the existence of extremely long proleg retractor muscles and a functional crochet array (Fig.1-9B).

1.3.6 A6-crawling

Terminal proleg reduction is also found in the family *Notodontinae* (Fig.1-4A). Caterpillars in the subfamily *Cerurinae* have similar tentacle-like terminal prolegs as *Selenisa*. However, they retain all the rest of the prolegs (A3-A6) and employ an **A6 initiated crawling** (Fig.1-10A). These caterpillars habitually flex dorsally and choreograph various movements of the terminal prolegs. In this case, the terminal prolegs have a display function. Another subfamily *Didusiinae* consists of different species of *Crinodes*. These caterpillars also have elongated terminal prolegs and similar display posture (Fig.1-10B). Unlike in *Cerurina*, the terminal prolegs of *Crinodes* do participate in crawling, but spend considerable less time in the stance phase. In this case, the locomotor pattern does not have to be initiated from the terminal segments.

1.3.7 Locomotor redundancy

Like most biological systems, there is redundancy in caterpillar locomotion. For caterpillars that employ a crawling gait and use the entire proleg set, binding the thoracic legs does not inhibit locomotion (personal observation). Paralyzing posterior segments also cannot prevent the animal from crawling (personal communication, B. Trimmer). The anterior-grade body contraction wave simply resumes at the most posterior innervated segment. Many caterpillars also ignore missing grip at multiple prolegs during locomotion (personal observations). These redundancies offer room for evolutionary modifications and produce robust locomotion. This thesis focuses on analyzing the mechanics of caterpillar crawling, inching, and the transition/combination of the two. It is important,

however, to acknowledge other modes of locomotion in caterpillars. Therefore, the rest of this section will be devoted to reviewing special proleg adaptation and caterpillar locomotion.

1.3.8 Special adaptations

Caterpillars living in special environments tend to have very specific proleg reduction/modification. For example, large leaf rolling caterpillars of the skipper butterfly *Calpododes* develop flat prolegs that are suitable for attaching the abdomen on the flat leaf surface (Fig.1-3A). Protected by the leaf rolls, they have also lost pigmentation on the body wall and thus appear transparent (Fig.1-11A). On a much smaller scale, many leafminers commonly found in *solanaceae* plants are caterpillars with overall appendage reduction. They burrow inside the leaves using body undulation (Fig.1-11B). Many leafminer caterpillars can tolerate the low oxygen environment between leaf surfaces. For example, the larvae of *Tongeia hainani* feed on a very juicy tropical plant *Kalanchoe daigremontiana*. Their undulating locomotion resembles “swimming” in leaves.

The ability to tolerate anoxia allows some caterpillars to be semi-aquatic. In the family *Crambidae* (Fig.1-4B), *Cataclysta lemnata* (China-mark) feeds on a kind of free-floating aquatic plants *Lemna* and routinely follow the vegetation underwater. The water-lily leafcutter (*Synclita oblitalis*) constructs protective case using leaves and literally surfs on the water surface. Similarly, *Pyrausta penitalis* (lotus borer) has developed a lateral undulating sweeping motion specifically for water surface swimming (Welch 1919). These semi-aquatic caterpillars can often remain submerged for more than 1.5hr at a time. Completely aquatic caterpillars (e.g. some members in *Pyralidae*) survive by inverting the internal tracheal system outside and modify it into gill filaments (Berg 1950).

Caterpillars of subfamily *Spilomelinae* within the family *Crambidae* have adapted to the low vegetation environments (Fig.1-4B). They typically live in leaf rolls and feed on nettles. Beside the

extremely fast retreat behaviors in the leaf rolls, they also perform a wide variety of startle responses when dropped to the ground. Among them, a ballistic backward rolling reflex has been documented extensively in the caterpillars of *Pleuroptya ruralis* (mother-of-pearl moths) (Brackenbury 1997). We also observe similar behaviors in other genera of caterpillars in this family. Details of this escape behavior will be investigated with a soft robotic platform in chapter 5.

Finally, there is the slug caterpillar (*Limacodid*) in which the entire appendage array reduces into a flat “ventrum” (Fig.1-4C). By secreting the semi-fluid silk, the soft ventral surface creeps along flat substrate surfaces via a localized anterior-grade wave (Epstein 1996). The evolution of this flat ventrum is different from simple proleg reduction and can be traced in the *Limacodid* group. Caterpillar in the family *Zygaenidae* possess the A3-A6 prolegs with crochets under a greatly flattened body (Fig.1-12A). In the more derived families *Somabrachyidae*, *Megalopygidae* and *Aididae*, segment A2 and A7 also develop proleg structures with miniature crochets. Family *Dalceridae* and *Limacodidae* further develop sucker-like prolegs on the segment A1 and A8 (Fig.1-12B). The body profile becomes completely flat (Epstein 1995). Interestingly, the crochets are still present on the prolegs A2-A7, even though they are non-functional (Stehr, McFarland 1985).

1.4 Mechanics of caterpillar locomotion

Force transmission is the heart of animal locomotion. In general, biomechanists evaluate performance by looking at external forces (how animals interact with the environment) and analyze internal forces (how muscles generate forces and move the body structure) to look for control mechanisms. For articulated systems, reaction forces and joint torques can be accurately derived from kinematics (Bobbert et al. 2007, Forner-Cordero, Koopman & van der Helm 2006, Forner-Cordero, Koopman & van der Helm 2006, Audu, Kirsch & Triolo 2007). Simple locomotion models can be constructed using center of mass

mechanics (Blickhan 1989, Geyer, Seyfarth & Blickhan 2005, Ghigliazza, Holmes 2005, Kajita et al. 2003, Seyfarth et al. 2002, Taga 1995, Blickhan et al. 2007). Furthermore, inertial forces (forces due to accelerating masses) often dominate in dynamic locomotion performed by most legged animals. In fact, this is what force-plates studies have focused on for decades (Dutto et al. 2004, Fanchon et al. 2006, Kaya, Leonard & Herzog 2006, Move 1991, Nauwelaerts, Aerts 2006, Reinhardt, Weihmann & Blickhan 2009). Unfortunately, soft-bodied animal locomotion does not involve joint articulations and often lacks dynamics. It therefore deserves a completely different analytical approach. Caterpillars offer a good platform to study force transmission in soft-bodied animals as they possess well-defined discrete substrate contacts (appendages).

1.4.1 Substrate interactions

Substrate interactions can be very complicated for soft-bodied animals as their bodies are often softer than the substrates. Caterpillars develop prolegs as discrete body attachment devices together with the six true legs on the thorax (see *section 1.2*). In addition to the prolegs gripping mechanisms, caterpillars can use silk in a variety of contexts to provide mechanical anchors and supports. For instance, spinning a silk life-line has been a common practice in many species of small caterpillars and early stages of many large caterpillars (including *Manduca*). This safety cable catches the caterpillar in case it drops from the substrate. The animal can then climb back to the food plant using this thread (Brackenbury 1996). Many *noctuid* larvae perform this silk spinning behavior before they jump off the substrate to escape from predators (personal observations). For the purpose of studying gait transitions, this research focuses on force transmission via the prolegs.

Caterpillar crawling is characterized by static loading with very robust proleg attachments. When multiple legs are attached to the substrate, the animal and the substrate become a single mechanical system. The ground reaction force is, in a sense, another type of internal force in the “animal-

substrate” system. To measure these forces requires static measurement of every single footfall independently and simultaneously. A force beam array was specifically designed to measure the substrate reaction forces from a crawling *Manduca* caterpillar. Details of the instrumentation can be found in chapter 2, and the analysis of caterpillar ground reaction forces will be covered in chapter 3.

1.4.2 Hydrostatic skeleton

Most soft-bodied animals rely on some sort of pressurized structure to provide mechanical support, called a “hydrostatic skeleton”. In general, hydrostatic skeletons are created by inflating a cavity with fluid. By changing the mechanical properties of the shell and surface tension, such an inflated structure can morph and change in stiffness. Formal introduction of this concept can be dated back to the 1950’s largely from research on worms (cnidarians, annelids, and nematodes). Given that the internal fluid and soft tissues are incompressible, worms produce body extension through circumferential constriction (Wainwright 1988, Wainwright 1982). This process is facilitated by the helical reinforcing fibers in the body wall (Clark, Cowey 1958). The oblique fibers winding around the body allows very large overall longitudinal extension. This type of fiber reinforcement was also found in many other cylindrical biological structures including those of plants (Neville, Levy 1984). Beginning in the 80’s, more serious efforts went into modeling the locomotion and body control of soft-bodied animals with hydrostatic skeleton. A detailed review of some important models is provided in chapter 4.

1.5 Scope and hypotheses: biomechanics and control strategies

My research aims to explain the mechanism of locomotion in caterpillars and to discover general control strategies in soft structures. The entire work rests on four basic questions: 1) What is the mechanism of crawling in caterpillars? 2) Why some caterpillar inch and some crawl? 3) How did different caterpillar

gaits evolve? 4) Is there any way to simplify control in soft bodies? The following sections will introduce the questions and my original ideas on these topics.

1.5.1 Force transmission in crawling caterpillars

To move, animals need to transmit muscle forces to the environment. In articulated systems (animals with rigid jointed **internal** or **external skeletons**), muscles forces are effectively translated into joint torques and therefore mechanical interactions with the environment. Force transmission is therefore extremely difficult without skeletons. To solve this problem, soft-bodied animals pressurize their bodies to create more rigid hydrostatic skeleton on demand. Usually this involves using active musculature to squeeze a coelom with incompressible fluid (**coelomic hydrostat**). Sometimes the muscles can directly provide the resistance to compression as seen in **muscular hydrostats**. In this part of the study, I explore the extent to which soft-bodied animals exploit body attachments and use the substrate as their *ad-hoc* external skeleton. This **environmental skeleton** hypothesis predicts that the animals would achieve body deformation using ground reactions forces. The removal of the substrate reaction forces will lead to undesirable body postures and compromise the locomotion performances.

1.5.2 Crawling vs. inching: constraints in the hydrostatic skeleton

Many caterpillars can be shown to perform both crawling and inching gaits despite their default preference. Why, then, some prefer one mode of locomotion over the other? In the ecological context, inching is a behavioral adaptation which amplifies the substrate searching part of a caterpillar's locomotor repertoire. It allows caterpillars to bridge gaps between plant structures and cover large distances on a tree trunk. These environmental factors are expected to affect caterpillars' locomotor preference. In addition to these ecological factors, this thesis reveals some biomechanical

constraints on caterpillars' hydrostatic skeletons and suggests that the caterpillar proleg reduction might have a strong mechanical determinant in evolution.

1.5.3 From crawling to inching: mechanical-based gait transition

The use of an *environmental skeleton* is expected to be complementary to the use of a *hydrostatic skeleton*. Caterpillars with more proleg support can rely on the substrate rigidity to transmit forces and therefore require less support from the hydrostatic skeleton. This mechanical view suggests that the inching gait can be derived from the crawling gait in three steps. First of all, the wave of muscle activation becomes more synchronized as the caterpillar attempts to crawl faster. Then an increase in hydrostatic skeleton stiffness causes the body to loop away from the substrate instead of compressing upon axial loading. Finally, the absence of mid-abdominal proleg attachments allows the body to flex away from the substrate and to create the clearance characteristic of inching.

1.5.4 Simplifying soft body control: mechanical coupling

Soft-bodied locomotion is characterized by large body deformation and contortion caused by interactions with the environment. Soft-bodied animals and robots often can perform tasks normally despite various involuntary contortions. It follows that the passive behaviors of structure/materials must determine a significant portion of the body kinematics. One example of such an embedded behavior is the mechanical coupling of soft actuators in soft-bodied robotic devices. Such coupling phenomenon is common in soft-bodied animals as body forces tend to cause deformation over the entire body. The effect allows the soft-bodied animal or robot to distribute information about the biomechanical states instantaneously without neural processing. This could be an important mechanism for body control and an example of "*morphological computation*" (Hara, Pfeifer 2000,

Pfeifer, Iida & Bongard 2005). Essentially, some adaptive behaviors can be pre-programmed into the body morphologies and material properties.

1.6 Scientific contributions

This thesis advances the current knowledge of caterpillar locomotion and soft-bodied biomechanics in three major ways. **Firstly**, it explicitly shows how a crawling caterpillar transmits tension along the body and moves forward using the substrate as its external skeleton (Chapter 3). **Secondly**, the modeling of caterpillar hydrostatic skeleton and various behavioral experiments provide strong evidences to support the equivalency of crawling and inching gaits (Chapter 4). **Finally**, the implementation of caterpillar locomotion in soft robotic platforms reveals several simple control strategies for soft bodies including control pattern scaling and actuator coupling (Chapter 5).

References

- Abraham, D., Ryrholm, N., Wittzell, H., Holloway, J.D., Scoble, M.J. & Löfstedt, C. 2001, "Molecular phylogeny of the subfamilies in Geometridae (Geometroidea: Lepidoptera)", *Molecular phylogenetics and evolution*, vol. 20, no. 1, pp. 65-77.
- Audu, M.L., Kirsch, R.F. & Triolo, R.J. 2007, "Experimental verification of a computational technique for determining ground reactions in human bipedal stance", *Journal of Biomechanics*, vol. 40, no. 5, pp. 1115-1124.
- Berg, C.O. 1950, "Biology of Certain Aquatic Caterpillars (Pyrallidae: Nymphula spp.) Which Feed on Potamogeton", *Transactions of the American Microscopical Society*, vol. 69, no. 3, pp. 254-266.
- Birch, J.M. & Dickinson, M.H. 2001, "Spanwise flow and the attachment of the leading-edge vortex on insect wings", *Nature*, vol. 412, no. 6848, pp. 729-733.
- Blickhan, R., Seyfarth, A., Geyer, H., Grimmer, S., Wagner, H. & Günther, M. 2007, "Intelligence by mechanics", *Philosophical Transactions of the Royal Society A: Mathematical, Physical and Engineering Sciences*, vol. 365, no. 1850, pp. 199-220.
- Blickhan, R. 1989, "The spring-mass model for running and hopping", *Journal of Biomechanics*, vol. 22, no. 11-12, pp. 1217-1227.
- Bobbert, M., Gómez Álvarez, C., van Weeren, R., Roepstorff, L. & Weishaupt, M. 2007, "A new method to calculate peak vertical ground reaction forces on individual limbs from kinematics of trotting horses", *Comparative Biochemistry and Physiology, Part A*, vol. 146, no. 4S, pp. 110-110.
- Brackenbury, J. 1997, "Caterpillar kinematics", *Nature*, vol. 390, no. 6659, pp. 453.

- Brackenbury, J. 1996, "Novel locomotory mechanisms in caterpillars: life-line climbing in *Epinotia abbreviana* (Tortricidae) and *Yponomeuta padella* (Yponomeutidae)", *Physiological Entomology*, vol. 21, no. 1, pp. 7-14.
- Carter, D. & Locke, M. 1993, "Why caterpillars do not grow short and fat", *International Journal of Insect Morphology and Embryology*, vol. 22, no. 2-4, pp. 81-102.
- Cham, J.G., Karpick, J.K. & Cutkosky, M.R. 2004, "Stride period adaptation of a biomimetic running hexapod", *The International Journal of Robotics Research*, vol. 23, no. 2, pp. 141.
- Chirikjian, G.S. & Burdick, J.W. 1991, "Kinematics of hyper-redundant robot locomotion with applications to grasping", *1991 IEEE International Conference on Robotics and Automation, 1991. Proceedings.*, pp. 720.
- Clark, R.B. & Cowey, J.B. 1958, "Factors controlling the change of shape of certain nemertean and turbellarian worms", *Journal of Experimental Biology*, vol. 35, no. 4, pp. 731.
- Common, I.F.B. 1975, "Evolution and classification of the Lepidoptera", *Annual Review of Entomology*, vol. 20, no. 1, pp. 183-203.
- Daniel, T.L. & Combes, S.A. 2002, "Flexible Wings and Fins: Bending by Inertial or Fluid-Dynamic Forces? 1", *Integrative and Comparative Biology*, vol. 42, no. 5, pp. 1044-1049.
- Dennell, R. 1976, "The structure and lamination of some arthropod cuticles", *Zool.J.Linn.Soc-Lond*, vol. 58, pp. 159-164.
- Dorfmann, A.L., Trimmer, B.A. & Woods, W.A. 2007, "A constitutive model for muscle properties in a soft-bodied arthropod", *J.Roy.Soc.Interface*, vol. 4, pp. 257-269.
- Dorfmann, A.L., Woods, W.A. & Trimmer, B.A. 2008, "Muscle performance in a soft-bodied terrestrial crawler: constitutive modeling of strain-rate dependency", *J.Roy.Soc.Interface*, vol. 5, pp. 349-362.
- Dutto, D.J., Hoyt, D.F., Cogger, E.A. & Wickler, S.J. 2004, "Ground reaction forces in horses trotting up an incline and on the level over a range of speeds", *Journal of Experimental Biology*, vol. 207, no. 20, pp. 3507-3514.
- Epstein, M.E. 1996, *Revision and phylogeny of the limacodid-group families, with evolutionary studies on slug caterpillars (Lepidoptera: Zygaenoidea)*, Smithsonian Institution Press.
- Epstein, M.E. 1995, "Evolution of locomotion in slug caterpillars (Lepidoptera: Zygaenoidea: Limacodid group)", *Journal of Research on the Lepidoptera*, vol. 34, pp. 1-13.
- Fanchon, L., Valette, J.P., Sanaa, M. & Grandjean, D. 2006, "The measurement of ground reaction force in dogs trotting on a treadmill: an investigation of habituation", *Veterinary and comparative orthopaedics and traumatology : V.C.O.T.*, vol. 19, no. 2, pp. 81-86.
- Forbes, W. 1910, "A structural study of some caterpillars", *Annals of the Entomological Society of America*, vol. 3, no. 2, pp. 94-143.
- Forner-Cordero, A., Koopman, H. & van der Helm, F. 2006, "Inverse dynamics calculations during gait with restricted ground reaction force information from pressure insoles", *Gait Posture*, vol. 23, no. 2, pp. 189-199.
- Geyer, H., Seyfarth, A. & Blickhan, R. 2005, "Spring-mass running: simple approximate solution and application to gait stability", *Journal of theoretical biology*, vol. 232, no. 3, pp. 315-328.

- Ghigliazza, R.M. & Holmes, P. 2005, "Towards a neuromechanical model for insect locomotion: hybrid dynamical systems", *Regular and Chaotic Dynamics*, vol. 10, no. 2, pp. 193-225.
- Hackman, R.H. & Goldberg, M. 1978, "The non-covalent binding of two insect cuticular proteins by a chitin", *Insect Biochemistry*, vol. 8, no. 5, pp. 353-357.
- Hara, F. & Pfeifer, R. 2000, "On the relation among morphology, material and control in morpho-functional machines", *From animals to animats 6: proceedings of the Sixth International Conference on Simulation of Adaptive Behavior* The MIT Press, , pp. 33.
- Heinrich, B. 1971, "The effect of leaf geometry on the feeding behaviour of the caterpillar of *Manduca sexta* (Sphingidae)", *Animal Behaviour*, vol. 19, no. 1, pp. 119-124.
- Hepburn, H.R. 1976, *The Insect integument*, Elsevier Scientific Pub. Co., Amsterdam; New York.
- Hepburn, H.R. & Levy, P. 1975, "Mechanical properties of some larval cuticles", *J.Entomol.Soc.S.Afr.*, vol. 38, pp. 131-141.
- Hinton, H.E. 1955, "On the structure, function, and distribution of the prolegs of the Panorpoidea, with a criticism of the Berlese-Imms theory", *Transactions of the Royal Entomological Society of London*, vol. 106, no. 13, pp. 455-540.
- Ishida, H., Nakamoto, T., Moriizumi, T., Kikas, T. & Janata, J. 2001, "Plume-tracking robots: A new application of chemical sensors", *The Biological bulletin*, vol. 200, no. 2, pp. 222.
- Jindra, M. & Sehna, F. 1989, "Larval growth, food consumption, and utilization of dietary protein and energy in *Galleria mellonella*", *Journal of insect physiology*, vol. 35, no. 9, pp. 719-724.
- Jusufi, A., Kawano, D.T. & Libby, T. 2010, "Righting and turning in mid-air using appendage inertia: reptile tails, analytical models and bio-inspired robots", *Bioinspiration & Biomimetics*, vol. 5, pp. 045001.
- Kajita, S., Kanehiro, F., Kaneko, K., Fujiwara, K., Yokoi, K. & Hirukawa, H. 2003, "Biped walking pattern generation by a simple three-dimensional inverted pendulum model", *Advanced Robotics*, vol. 17, no. 2, pp. 131-147.
- Kaya, M., Leonard, T.R. & Herzog, W. 2006, "Control of ground reaction forces by hindlimb muscles during cat locomotion", *Journal of Biomechanics*, vol. 39, no. 15, pp. 2752-2766.
- McGeer, T. 1990, "Passive Dynamic Walking", *The International Journal of Robotics Research*, vol. 9, no. 2, pp. 62.
- Menon, C. & Sitti, M. 2006, "Biologically inspired adhesion based surface climbing robots", *Robotics and Automation, 2005. ICRA 2005. Proceedings of the 2005 IEEE International Conference on Ieee*, , pp. 2715.
- Mezoff, S., Papastathis, N., Takesian, A. & Trimmer, B.A. 2004, "The biomechanical and neural control of hydrostatic limb movements in *Manduca sexta*", *Journal of Experimental Biology*, vol. 207, no. 17, pp. 3043-3053.
- Montgomery, S.L. 1983, "Carnivorous caterpillars: the behavior, biogeography and conservation of *Eupithecia* (Lepidoptera: Geometridae) in the Hawaiian Islands", *GeoJournal*, vol. 7, no. 6, pp. 549-556.
- Montgomery, S.L. 1982, "Biogeography of the moth genus *Eupithecia* in Oceania and the evolution of ambush predation in Hawaiian caterpillars(Lepidoptera: Geometridae).", *Entomologia Generalis*, vol. 8, no. 1, pp. 27-34.
- Move, H.A. 1991, "Mechanics of a rapid running insect: two-, four-and six-legged locomotion", *Journal of Experimental Biology*, vol. 156, no. 1, pp. 215-231.

- Nagy, L.M. & Grbic, M. 1999, "Cell lineages in larval development and evolution of holometabolous insects", *The origin and evolution of larval forms*, , pp. 275.
- Nauwelaerts, S. & Aerts, P. 2006, "Take-off and landing forces in jumping frogs", *Journal of Experimental Biology*, vol. 209, no. 1, pp. 66-77.
- Neville, A.C. & Levy, S. 1984, "Helicoidal orientation of cellulose microfibrils in *Nitella opaca* internode cells: ultrastructure and computed theoretical effects of strain reorientation during wall growth", *Planta*, vol. 162, no. 4, pp. 370-384.
- Neville, A.C., Parry, D.A. & Woodhead-Galloway, J. 1976, "The chitin crystallite in arthropod cuticle", *Journal of cell science*, vol. 21, no. 1, pp. 73-82.
- Nijhout, H.F., Davidowitz, G. & Roff, D.A. 2006, "A quantitative analysis of the mechanism that controls body size in *Manduca sexta* ", *Journal of biology*, vol. 5, no. 5, pp. 16.
- Pfeifer, R., Iida, F. & Bongard, J. 2005, "New robotics: Design principles for intelligent systems", *Artificial Life*, vol. 11, no. 1-2, pp. 99-120.
- Poelma, C., Dickson, W.B. & Dickinson, M.H. 2006, "Time-resolved reconstruction of the full velocity field around a dynamically-scaled flapping wing", *Experiments in Fluids*, vol. 41, no. 2, pp. 213-225.
- Reichle, D. 1968, "Relation of body size to food intake, oxygen consumption, and trace element metabolism in forest floor arthropods", *Ecology*, vol. 49, no. 3, pp. 538-542.
- Reinhardt, L., Weihmann, T. & Blickhan, R. 2009, "Dynamics and kinematics of ant locomotion: do wood ants climb on level surfaces?", *Journal of Experimental Biology*, vol. 212, no. 15, pp. 2426.
- Rubinoff, D. & Haines, W.P. 2005, "Web-spinning caterpillar stalks snails", *Science*, vol. 309, no. 5734, pp. 575.
- Scoble, M.J. 1995, *The Lepidoptera: form, function and diversity*, Oxford University Press, USA.
- Seyfarth, A., Geyer, H., Günther, M. & Blickhan, R. 2002, "A movement criterion for running", *Journal of Biomechanics*, vol. 35, no. 5, pp. 649-655.
- Snodgrass, R.E. 1993, *Principles of insect morphology*, Cornell University Press.
- Snodgrass, R.E. 1965, *A textbook of arthropod anatomy*, Hafner New York.
- Spranklin, B.W. 2006, "Design, analysis, and fabrication of a snake-inspired robot with a rectilinear gait", .
- Stehr, F.W. & McFarland, N. 1985, "Crochets on Abdominal Segments 2 and 7 of Dalcerid Caterpillars: Missing Link or Anomaly", *Bulletin of the ESA*, vol. 31, no. 1, pp. 35-36.
- Suzuki, Y. & Palopoli, M.F. 2001, "Evolution of insect abdominal appendages: are prolegs homologous or convergent traits?", *Development genes and evolution*, vol. 211, no. 10, pp. 486-492.
- Taga, G. 1995, "A model of the neuro-musculo-skeletal system for human locomotion", *Biological cybernetics*, vol. 73, no. 2, pp. 97-111.
- Tomita, S. & Kikuchi, A. 2009, "Abd-B suppresses lepidopteran proleg development in posterior abdomen", *Developmental biology*, vol. 328, no. 2, pp. 403-409.

- Wainwright, S.A. 1988, *Axis and Circumference: The Cylindrical Shape of Plants and Animals*, Harvard University Press, Cambridge.
- Wainwright, S.A. 1982, *Mechanical Design in Organisms*, Princeton University Press.
- Warren, R.W., Nagy, L., Selegue, J., Gates, J. & Carroll, S. 1994, "Evolution of homeotic gene regulation and function in flies and butterflies", *Nature*, vol. 372, pp. 458-461.
- Weis-Fogh, T. 1960, "A rubber-like protein in insect cuticle", *J.exp.Biol.*, vol. 37, pp. 889-907.
- Welch, P.S. 1919, "The Aquatic Adaptations of *Pyrausta penitalis* Grt.(Lepidoptera)", *Annals of the Entomological Society of America*, vol. 12, no. 3, pp. 213-226.
- Wolfgang, W.J. & Riddiford, L.M. 1987, "Cuticular mechanics during larval development of the tobacco hornworm, *Manduca sexta* ", *The Journal of experimental biology*, vol. 128, pp. 19-33.
- Woods, W.A., Jr, Fusillo, S.J. & Trimmer, B.A. 2008, "Dynamic properties of a locomotory muscle of the tobacco hornworm *Manduca sexta* during strain cycling and simulated natural crawling", *The Journal of experimental biology*, vol. 211, no. Pt 6, pp. 873-882.
- Xiang, H., Li, M., Yang, F., Guo, Q., Zhan, S., Lin, H., Miao, X. & Huang, Y. 2008, "Fine mapping of Ekp-1, a locus associated with silkworm (*Bombyx mori*) proleg development", *Heredity*, vol. 100, no. 5, pp. 533-540.
- Yamamoto, S. & Sota, T. 2007, "Phylogeny of the Geometridae and the evolution of winter moths inferred from a simultaneous analysis of mitochondrial and nuclear genes", *Molecular phylogenetics and evolution*, vol. 44, no. 2, pp. 711-723.

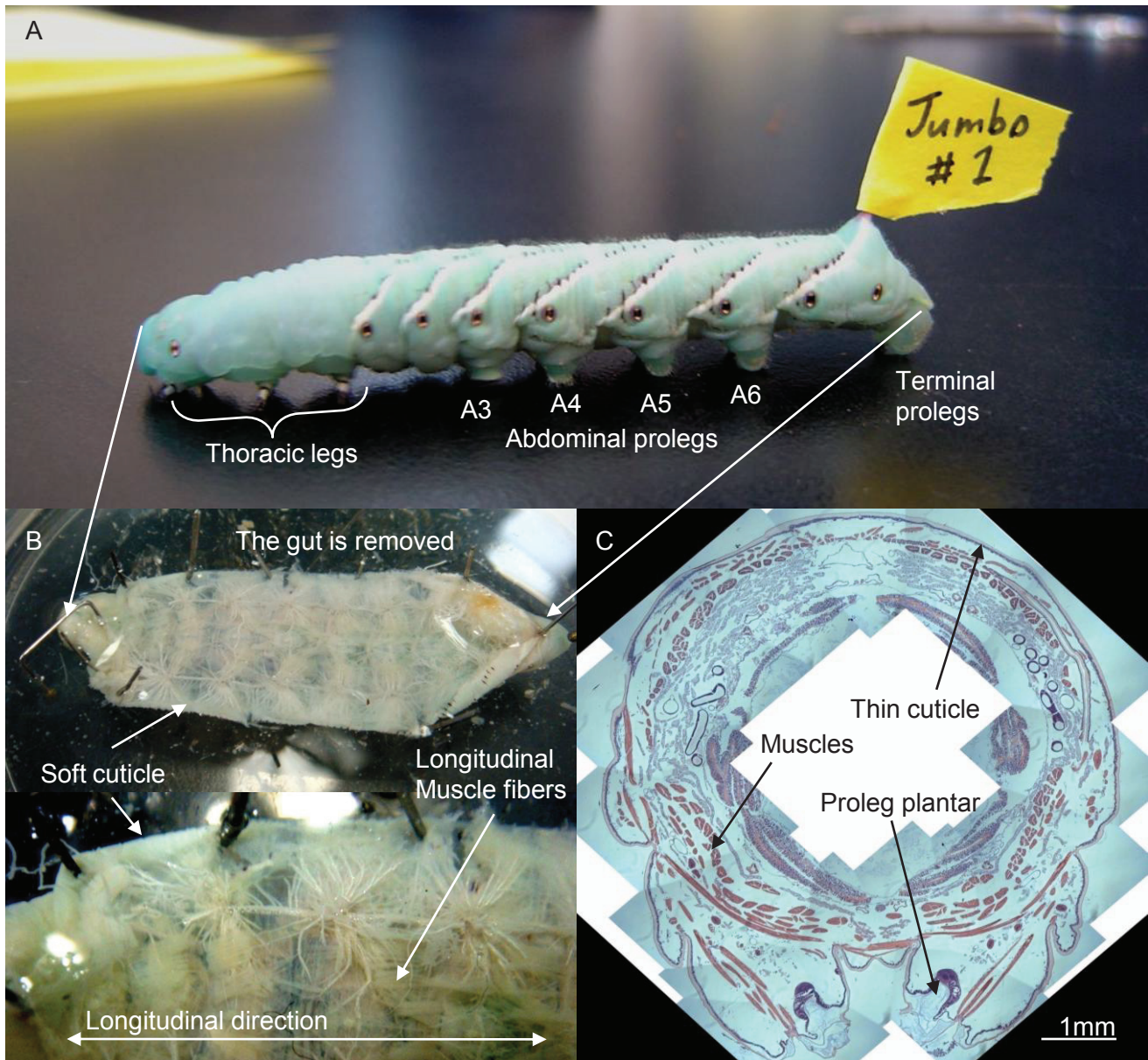


Fig.1-1 The caterpillar as a model system for soft-bodied locomotion. (A) *Manduca sexta* caterpillar. **(B)** The caterpillar is a single compartment cylinder with lots of air tubes (tracheal). The gut has been removed in this preparation. Semi-transparent muscle fibers are lining right beneath the thin and flexible cuticle. **(C)** A histology image of the cross section shows the proportion of different internal structures.

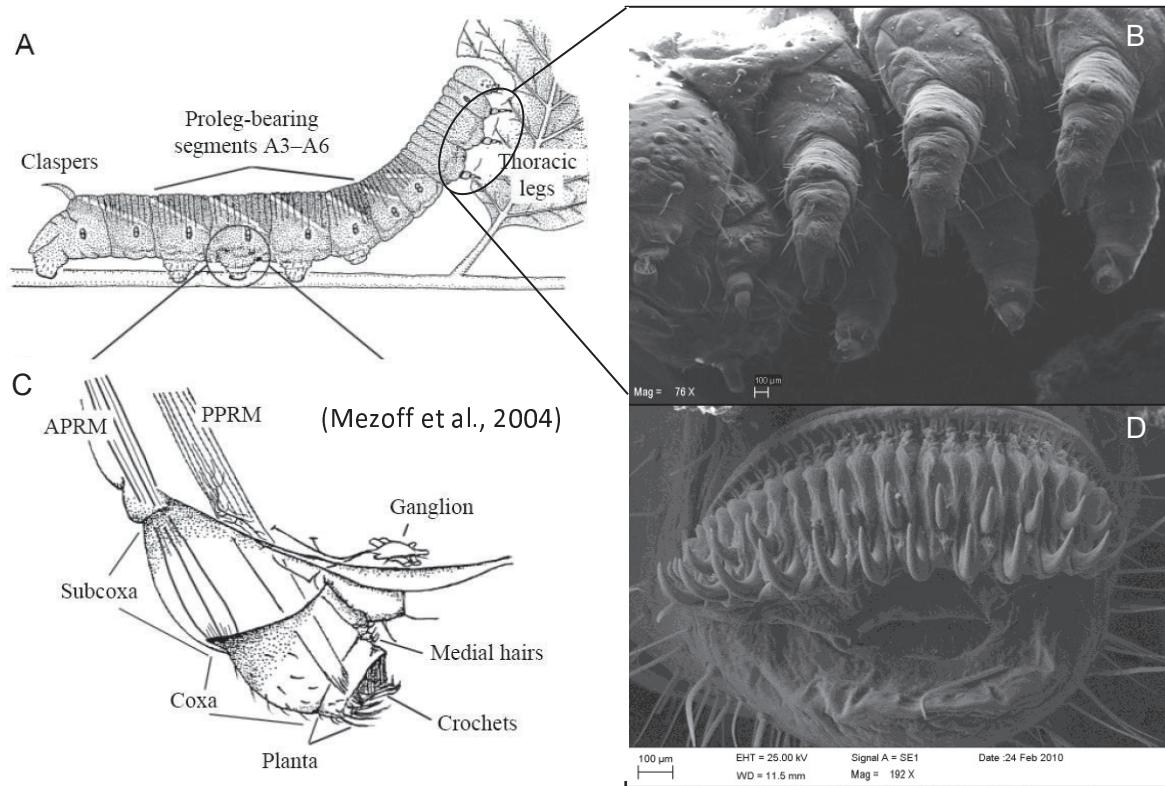


Fig.1-2 *Manduca* caterpillar external anatomy. (A)(B) Thoracic legs are articulated appendages in caterpillar. They are responsible for shifting body weight during locomotion and grabbing food stuff during feeding. **(C)** Proleg retraction mechanism **(D)** Crochets are micro claws on the plantar of caterpillar prolegs. They are responsible for secure substrate gripping.

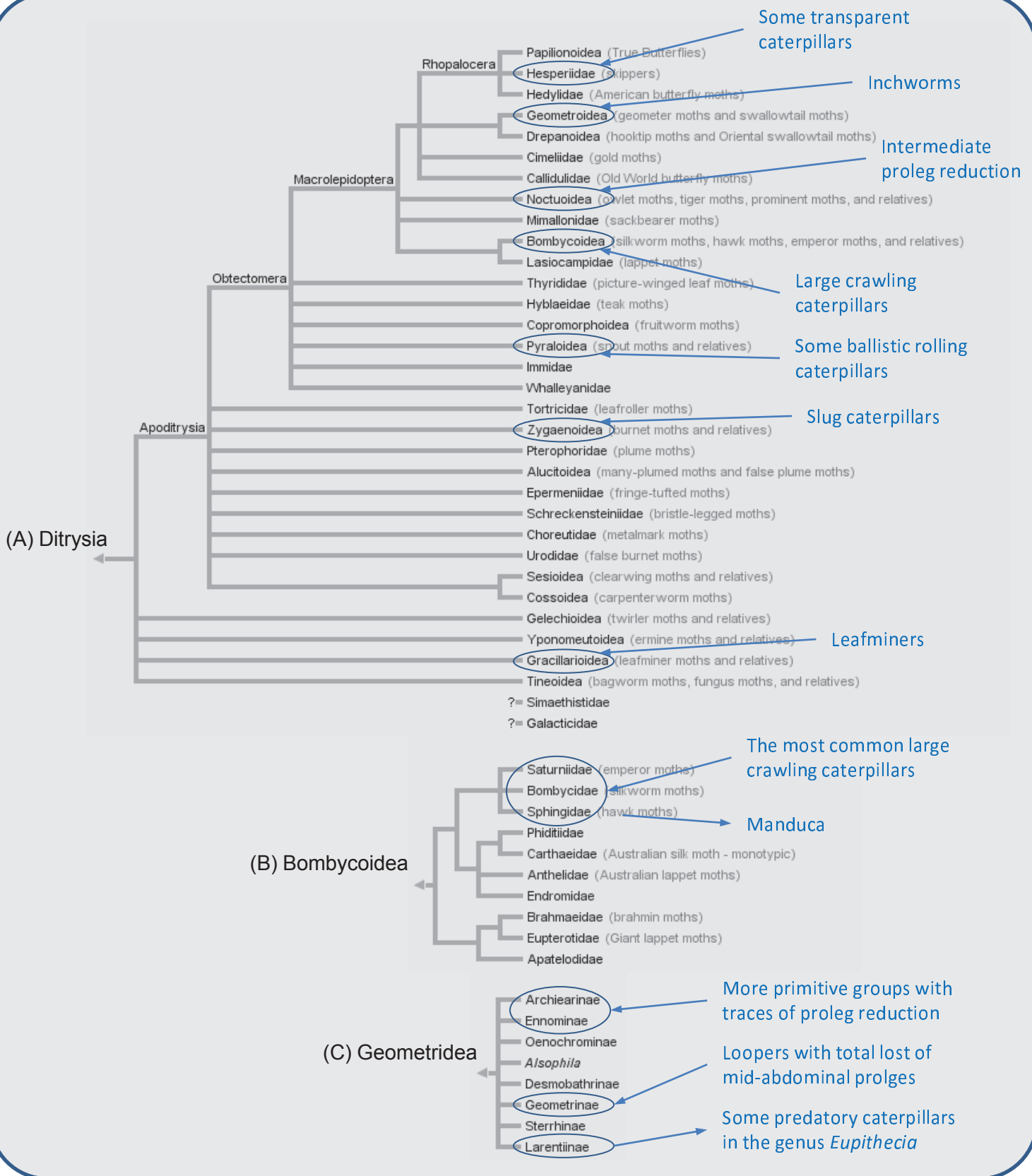


Fig.1-3 Current phylogenetic tree of the caterpillar examples. (A) *Ditrysia* is a superfamily that contains most butterflies and moths. All the caterpillars mentioned in this thesis can be mapped onto this phylogeny as annotated. (B) *Bombycoidea* contains some of the most common moths including silk moths and hawk moths. (C) Family *Geometridea* contains all the true inchworms which tend to be small and nimble. A few species are fast enough to catch small insects as predators.

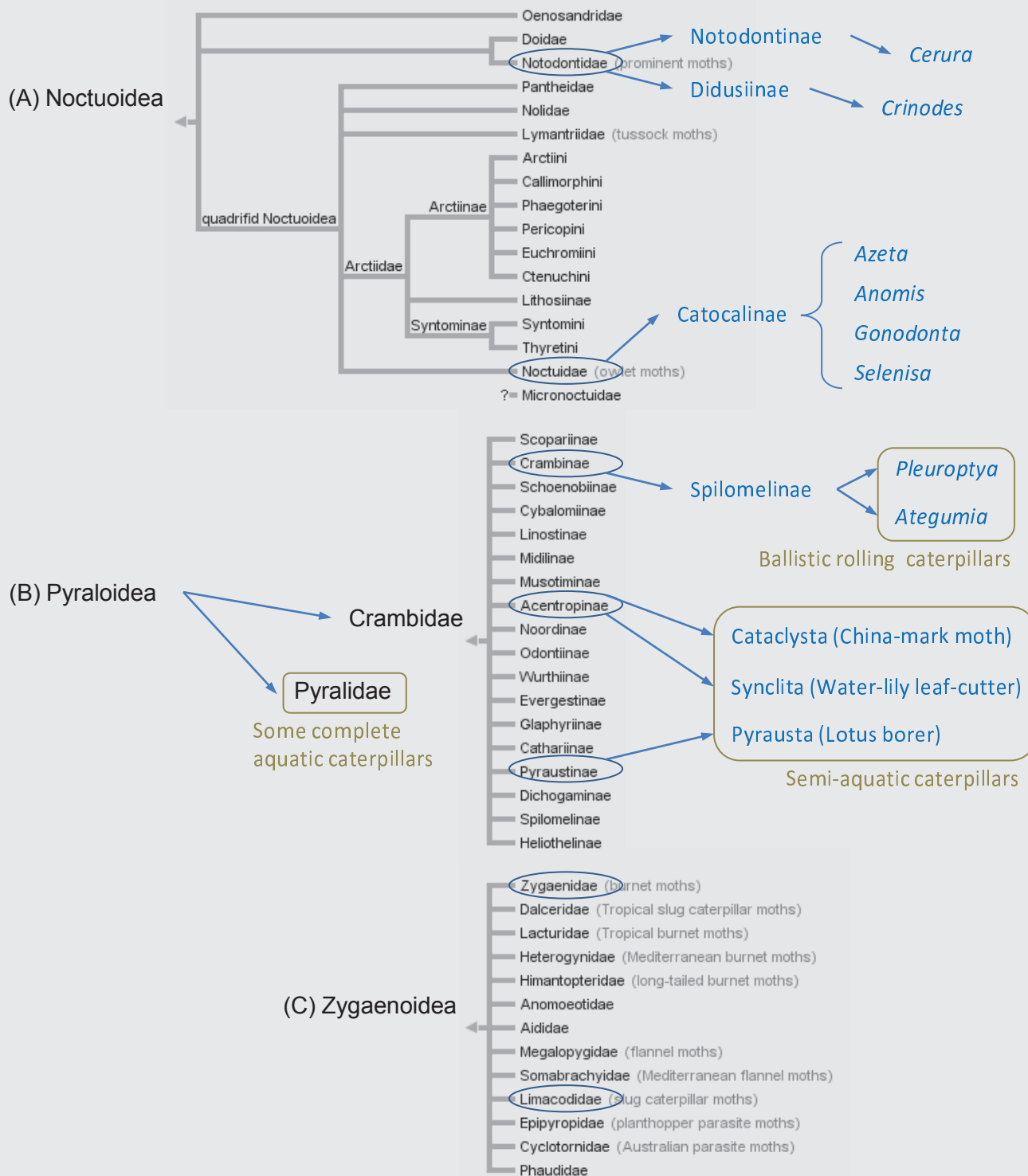


Fig.1-4 Phylogeny of some special caterpillars. (A) Superfamily *Noctuoidea* contains one of the most derived group of caterpillars with a wide variety of proleg arrangement. The larvae of prominent moths tend to have highly elaborated terminal proleg modification for warning display purposes. On the other hand, subfamily *Catocalinae* of *Noctuidae* contains caterpillars with various intermediate proleg reduction and crawl-inch gaits. **(B)** Superfamily *Pyraloidea* contains some small moths with probably the most diverse life history adaptations. Besides the leaf rollers that feed on low nettles (*Crambinae*), there are several semi-aquatic caterpillar groups. There are even some complete aquatic caterpillars in *Pyralidae*. **(C)** Superfamily *Zygaenoidea* represents a primitive lineage which led to slug caterpillars.

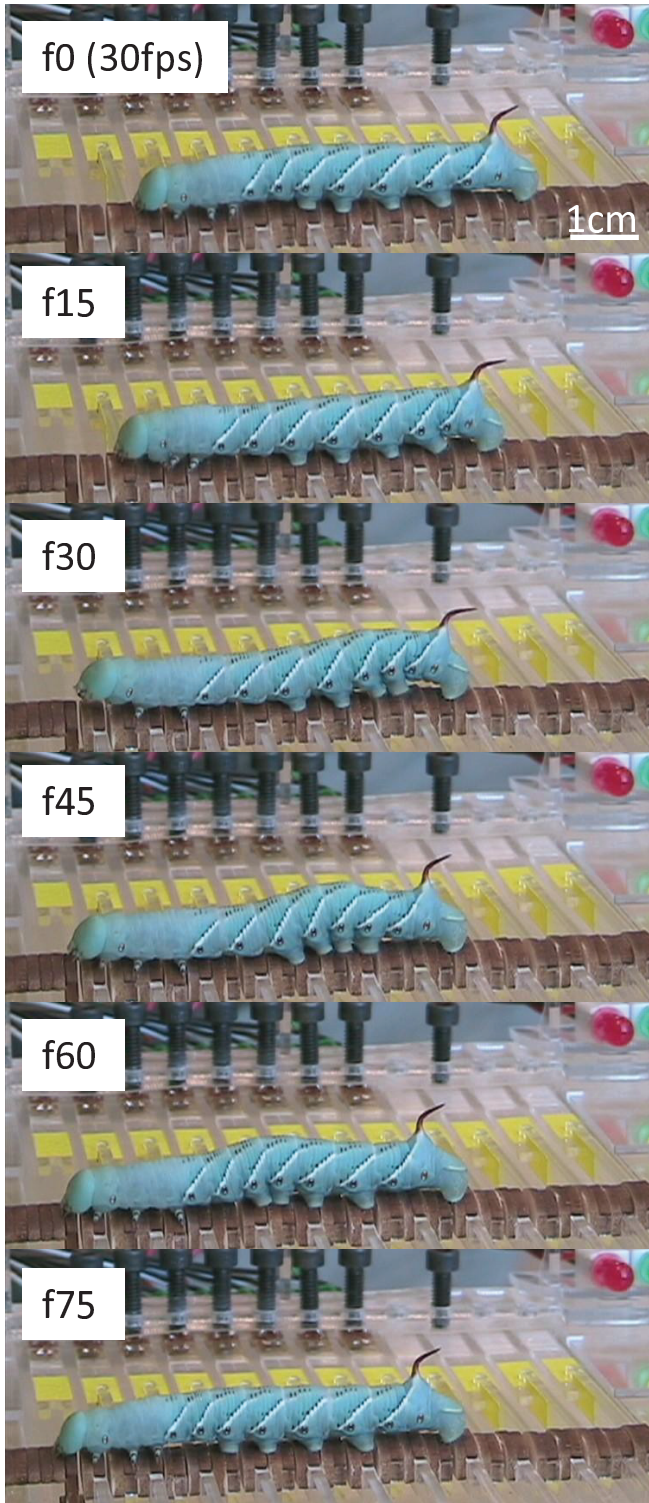


Fig.1-5 Crawling gait. *Manduca* is one of the largest sphingids. This caterpillar, however is only a second day 5th instar animal. It measures ~56mm long with ~6.3mm diameter and weighs 2.15g. (*Manduca* can reach body mass over 10g) The crawling speed and gait period averages to 2.8mm/s and 2.91s respectively.

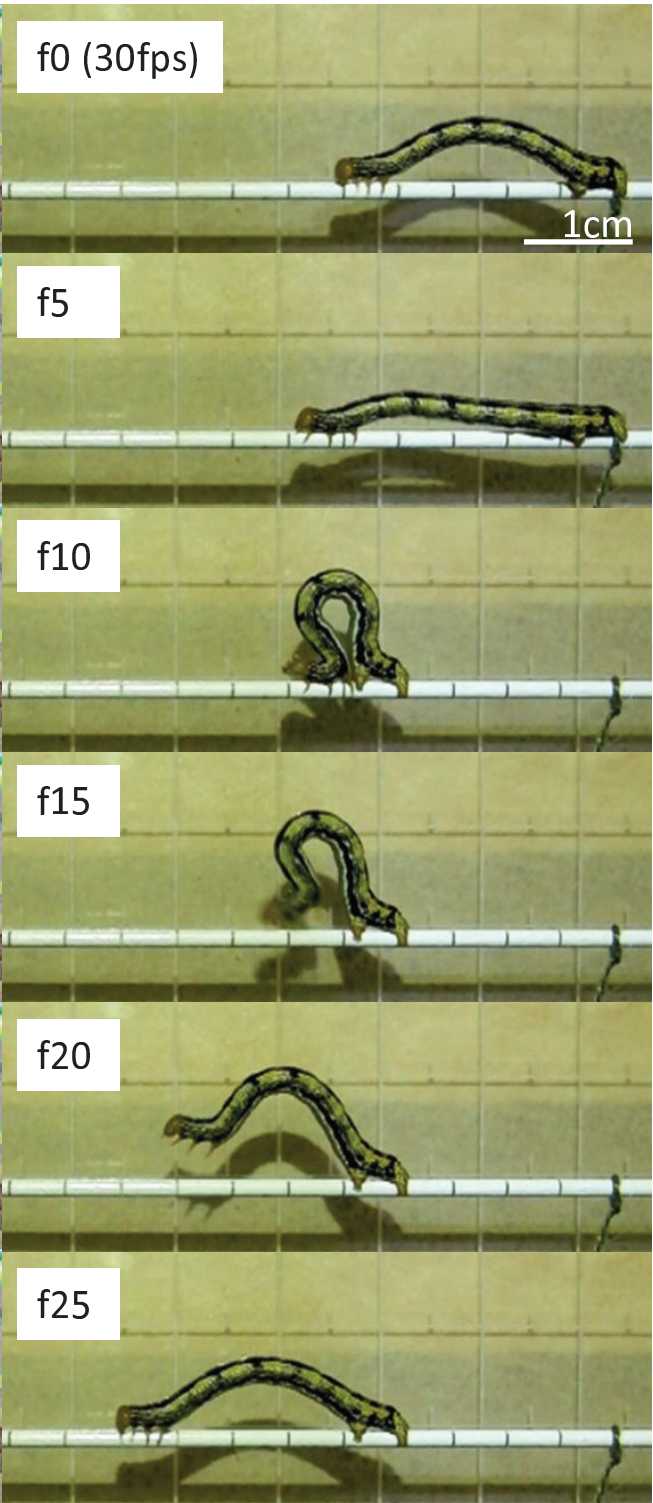


Fig.1-6 Inching gait. *Sphacelodes* is one of the largest geometrids. This particular animal is fully grown and almost ready for pupating. The body length measures 32mm. However, it only weighs about 0.2g due to the small diameter of ~2.4mm. The gait period is about 0.8s and with overall speed ~25mm/s.

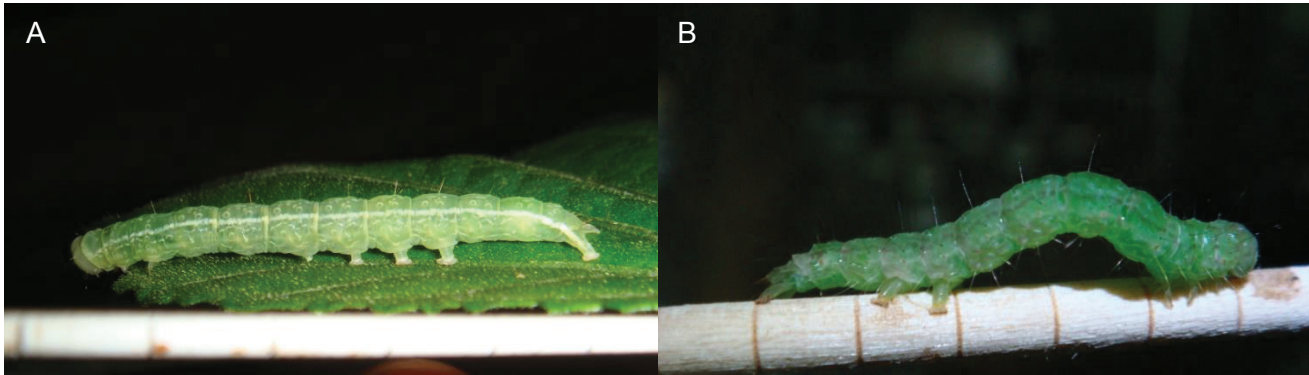


Fig.1-7 Crawl-inch (A) *Azeta* starts to show proleg reduction. The prolegs on the 3rd abdominal segment A3 do not actually touch the substrate during the crawl-inch gait. **(B)** *Anomis* further lost the A3-A4 prolegs completely through evolution. These caterpillar adapt a crawl-inch gait in which the body compression transforms into a dorsal buckling.

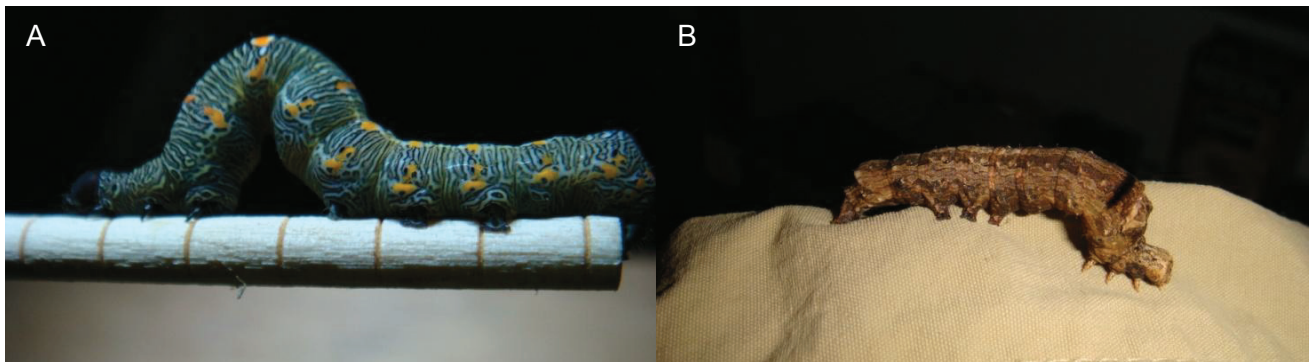


Fig.1-8 Inch-crawl. (A)(B) *Gonodonta* adapts a different gait for the lost of A3 prolegs. These large caterpillars keep the anterior abdomen constantly flexed. A inch-crawl cycle is marked by a initial body extension followed by two or three small crawls at the posterior segments.



Fig.1-9 A6-inching. (A) *Selenisa* has dramatically elongated terminal prolegs which serve as sensory appendages more than load bearing ones. (B) The elongated terminal prolegs still have some functional crochets as well as retraction reflex.

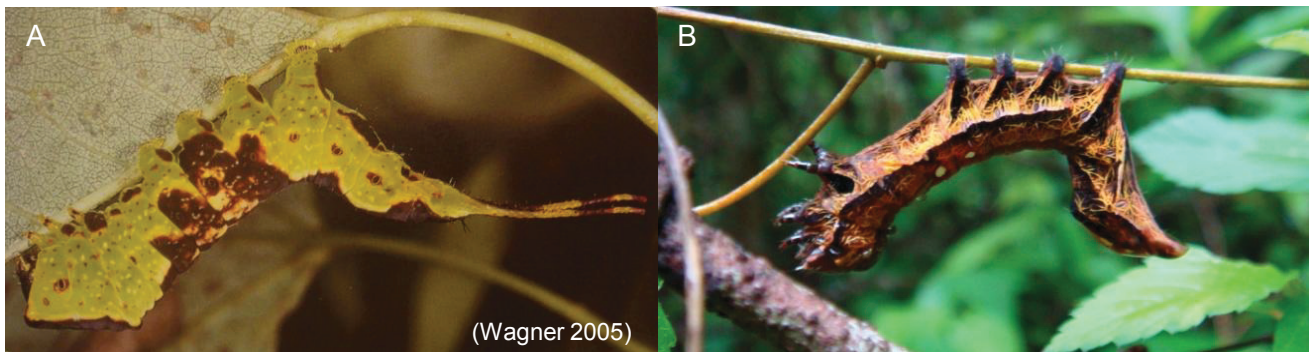


Fig.1-10 A6-crawling (A) *Cerurinae* lost the function of terminal prolegs but retained all the mid-abdominal prolegs. The crawling gait is initiated from the A6 prolegs. (B) *Crinodes* still use the terminal prolegs for locomotion but to a less extent.

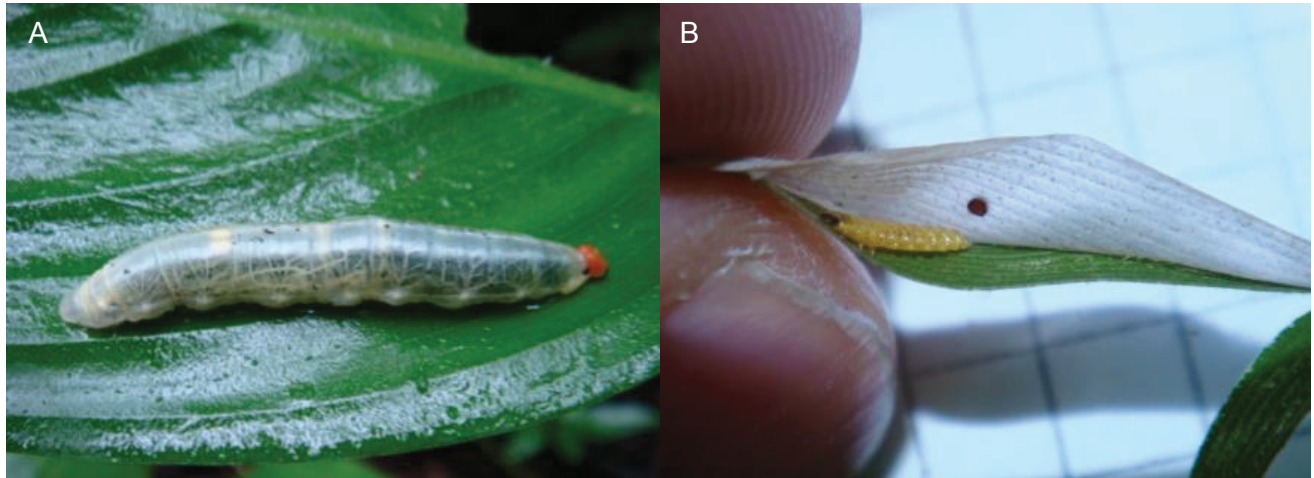


Fig.1-11 Special caterpillars (A) The skipper butterfly *Calpododes* caterpillars live in leaf rolls throughout their larval stage. Body pigments are therefore lost, leaving behind a transparent integument. (B) Leafminers make up one of the most primitive group of lepidoptera. Many caterpillars in the superfamily *Gracillarioidea* live and feed between the leaf boundaries. Locomotion is accomplished with short thoracic legs and many spiky structures on the abdomens. No real prolegs are present.

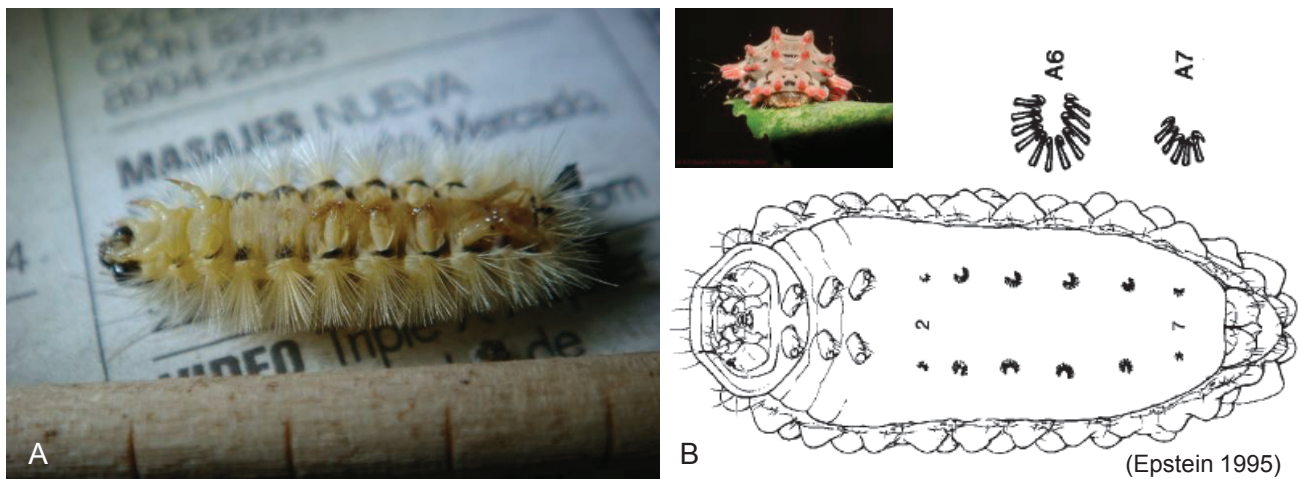


Fig.1-12 Slug caterpillars (A) *Zygaenidae* represents the basal group on the lineage to slug caterpillars. The full complement of prolegs are still present and functional but the body has been flattened significantly. (B) *Limacodidae* is a much more derived group within the superfamily *Zygaenoidea*. All the legs (including the thoracic legs) are reduced and the caterpillar move with a flat “ventrum” much like a slug. Tiny non-functional crochets are still present even at segment A2 and A7.

Chapter 2: Instrumentation, Soft Robotics and Field Work

This chapter introduces some of the major instrumentation processes as well as methodologies in this research. To begin, section 2.1 details the design process of a mini force beam array for measuring caterpillar substrate reaction forces. Instrumentation data are presented as appropriate, but the manufacturing techniques are excluded for simplicity. Section 2.2 covers the implementation of a real-time extensometry system for performing uni-axial material tests on millimeter scale soft tissue specimens. This is necessary for characterizing the mechanical properties of small bio-material samples such as the caterpillar soft cuticle. Section 2.3 reviews the overall data acquisition protocol for simultaneous ground forces and kinematics tracking of soft-bodied robots. This includes a custom force plate derived from the force beam array system presented in section 2.1. Finally, section 2.4 briefly describes the goals and activities of the field work component of this research.

2.1 A mini force beam array for measuring caterpillar ground reaction forces

2.1.1 Design considerations

As stressed previously, it is necessary to measure the reaction forces at all the contacts a caterpillar makes to the substrate during locomotion. This calls for a force sensor array that can resolve forces down to millinewton range in two directions: forward-backward (fore-aft) and the perpendicular (normal) (Fig.2-1). For a caterpillar crawling horizontally in a straight line, these two classes of reaction forces represent body axial loading and weight placement from each substrate contact. Custom force transducer systems for biomechanical analysis have developed rapidly in the recent decade. For animals with locomotor dynamics, robust force plate designs are readily available to handle the force range from millinewton to several newtons (Zumwalt, Hamrick & Schmitt 2006, Bartsch et al. 2007). For the sub-millinewton range, there are various microelectromechanical

(MEM) devices (Park, Goodman & Pruitt 2007, Reinhardt, Weihmann & Blickhan 2009). On the lowest range, there are optics based cantilever systems for the sub-micronewton measurements (Garcia-Webb et al. 2007). All these different designs and instrumentations have their advantages as well as constraints. An experimental biologist must carefully evaluate the animal system before adapting any particular design path. For caterpillar locomotion, there are four major design constraints for the force transducer array. First of all, the sensor array needs to be compact enough to accommodate for the relatively small stride-length (*Manduca* step $\sim 8.52\text{mm}$). In order to capture all prolegs contacts independently and simultaneously, the sensing substrate units have to also account for the inter-prolegs distances (2nd 5th instar *Manduca* A3-A4 distance $\sim 6\text{mm}$; A6-TP distance $\sim 15\text{mm}$). To maximize the chance of all the foot contacts landing on sensor units independently, an idea sensor pitch is between 3.5 and 4mm. Secondly, each sensing element needs to provide loading information on both directions: along the array direction and perpendicular to the array direction. Thirdly, the sensor sensitivity has to accommodate for a force range over at least two orders of magnitude and resolve single mN force. Finally, to cover the entire body length of a crawling caterpillar, around 12 sensor units are required. This large number of sensors imposes a cost issue on the overall instrumentation. While most other GRF studies can spend the entire budget on producing one sensor, our study must minimize the unit cost in order to produce sufficient number of sensors.

Luckily, caterpillar locomotion provides three important tolerances which alleviate the instrumentation challenge. First, the quasi-static motion with typical cycling frequency of $\sim 0.356\text{Hz}$ allows the sensor to have resonance frequency lower than 300Hz. Data can be also acquired at lower sampling rate (100Hz). Second, the lack of dynamics also eliminates the various measurement errors related to dynamic loading (viscoelasticity, impacts, random vibrations...etc).

Third, relative to the large body deformation, sensor deformation is quite negligible. For a 5th instar *Manduca* caterpillar, substrate deformation as large as 0.5mm is nothing significant. This allows considerably more displacement in the sensor array.

Considering the above requirements and special tolerances yields a multi-cantilever beam array design. This design consists of two parallel arrays of cantilever beams with beam tips interlacing (Fig.2-1). The result produces a linear path across many tightly aligned beam tips. Each beam has strain gages mounted at the base to measure the surface strain when the beam tip is loaded. A certain geometric design at the base amplifies this surface strain, on the cost of larger beam tip deflection. Due to the lack of dynamics, the force beams can be produced from inexpensive plastics. The viscoelastic effect is minimum under such loading conditions. The resulting beam is quite compliant and has a resonance frequency between 200Hz and 300Hz. Such a force beam is sufficient to monitor the contact reaction forces from a crawling caterpillar, and the cost per sensor is sufficiently low (force beams can be almost disposable).

The Mini Force Beam Array (MFBA) was a system built from scratch. The instrumentation includes mechanical designs of the cantilever beams, strain gage installation, force beam characterization, amplifier circuits design, custom PCB design, custom instrument interface design, software development, and a little bit of real-time image analysis. In the instrumentation process, I developed various new techniques in machining, gage bonding, circuit layout, and system coordination. However, for the scope of this thesis, this chapter will only focus on the force beam design and a novel strain gage arrangement for bi-axial sensing.

2.1.2 *A hybrid Wheatstone bridge for bi-axial sensing*

Piezo-resistive strain gages are widely used in force sensors for their simplicity and versatility. These gages are made out of piezo-resistive materials or special alloy which will change electric

resistance in response to mechanical deformation (Fig.2-6B). Most strain gages are designed to operate at the linear deformation condition with the change of resistance (ΔR) proportional to the strain ϵ :

$$\Delta R/R_{in} = G_f \epsilon \quad [1]$$

where R_{in} is the initial gage resistance and G_f is the proportional constant called the “gage factor”. Metal alloy foil strain gages work by elastic deformation and typically have a gage factor around 2. Semiconductor strain gages work by solid state transitions and therefore can have a gage factor over 20. However, they also cost one magnitude higher and are very fragile with respect to handling. As a result, semiconductor gages are usually used for well enclosed precision devices. Regardless of the gage styles, bonding strain gages on top of a solid structure establishes a direct correlation between the changes of gage resistances and the substrate material strain at the gauged locations. Calibrating this change of resistance to the corresponding load on the solid structure accurately translates forces into measurable electrical signals. This is the basis of most force transducers to date.

A “Wheatstone Bridge” is a circuit design commonly used to amplify the effect of small strain-induced resistance variations. In a half-bridge configuration, the matched piezo-resistive strain gages R_A and R_A' are each wired in series with a static resistor R_0 (Fig.2-2A). Under a constant excitation voltage V_{ex} , changing resistance in R_A or R_A' can affect V_A or V_B dramatically as it controls the current through each arm. Therefore, if the strain gages R_A and R_A' change identically in the opposite directions, a voltage difference $V_1 = V_A - V_B$ will be generated. Typically strain gages R_A and R_A' are bonded on the opposite sides of a cantilever beam (Fig.2-2B). When a point load F_y (red arrow) is applied on the beam tip from the top, the top surface experiences tension and the bottom surface experiences compression. This mechanical loading causes a measurable V_1

which simply reverses its sign upon loading in the opposite direction. Using this design, I manufactured force beams to perform normal force measurements with sensitivity $\sim 350\text{mV/V}$ at 0,1N rating (12 beams) (Fig.2-3).

To increase the sensitivity, a full Wheatstone bridge configuration employs four gages (R_A , R_A' , R_B , R_B') wired in a similar configuration (Fig.2-4A). In this configuration, the static resistors are replaced by another pair of piezo-resistors. Now, increasing R_A and R_B' will drop V_A and raise V_B respectively. Increasing the resistance in R_B and R_A' can produce the same effect. These two effects combined amplify the voltage differential V_1 dramatically. In a classic cantilever force transducer, piezo-resistor R_A and R_B' are bonded on the top of the beam while R_B and R_A' are bonded on the reverse side (Fig.2-4B). Matching identical piezo-resistors symmetrically on the exact opposite side of the beam results in a fairly linear V_1 in response to the beam tip loading F_y (within small deflection range). This style of force transduction is very common and can be found in a common laboratory precision transducer (Grass Products Group, West Warwick, RI). Performing force transduction on a second dimension normally involves implementing the exact strain gage design in the perpendicular orientation on the same cantilever beam. However, this also means doubling the cost and complexity of the force beam instrumentation. Since all the strain gages have to be installed manually, any increase of strain gage mounting also increases the risk of force beam manufacturing failure and human-induced inaccuracies. I took a completely different approach to incorporate force sensing in the second direction.

The alternative design involves extracting the resistance changes in all four piezo-resistors and produces two signals that represent loading in two directions. To start with, an additional pair of static resistors R_C and R_C' are inserted after the active piezo-resistors (Fig.2-5A). This new configuration provides two additional voltage nodes (V_C and V_C') in the circuit. The positions of R_A' , R_B and R_B'

are also swapped in the counter-clockwise direction (Fig.2-5B). This rearrangement allows us to position the four strain gages so that the active full Wheatstone bridge still operates to detect vertical beam tip loading as described previously. As the cantilever deflects downward upon vertical load \mathbf{F}_y , the resistances in gages R_A and R_B increase while the resistances in the matched gages R_A' and R_B' decrease. The V_1 signal essentially monitors the resistance difference between the gages R_i and their matched gages. Now, as we apply load on the horizontal direction \mathbf{F}_x (orange arrow), the gages R_A and R_A' are stretched while the gages R_B and R_B' receive additional compression. This leads to another voltage differential V_2 between V_C and V_C' . In effect, we can treat R_i and R_i' as an active unit in both arms as marked in blue rectangles. The measurement from V_2 is a half Wheatstone bridge setup (comparable to Fig.2-2A) with a functional full bridge setup inside (comparable to Fig.2-4A). Since the gages R_i and R_i' are matched across the cantilever beam, any resistance change due to vertical loading will cancel out when we treat them as one unit. In other words, vertical loading \mathbf{F}_y will not affect the operation of this external half bridge design (for measuring \mathbf{F}_x). However since R_C and R_C' are static resistors, they cannot compensate for the change of resistance across either R_i unit. As a result, horizontal loading will change the electric current across the two arms and affect the measurement of the embedded full bridge complex. This cross-talk issue can be solved by replacing R_C and R_C' by active gages mounted on the lateral sides of the cantilever, complicating the manufacturing in the process. A simpler approach is to characterize this one-way cross-talk and substrate it from any vertical load measurements with bi-axial loading conditions.

This hybrid Wheatstone bridge design can be described mathematically using simple beam theories with small deformation. Algebraic derivations show that V_2 is independent of \mathbf{F}_y , while V_1 consists of one term from \mathbf{F}_y and an additional offset from V_2 :

$$V_2 = S_x(V_{ex}) \times F_x = V_x \quad [2]$$

$$V_1 = [S_y(V_{ex}) \times F_y] + [V_x \times D] = V_y \quad [3]$$

where S_x and S_y are sensitivities of the cantilever beam to loading in either direction. D is a crosstalk constant that can be measured empirically. The derivation assumes that the cantilever beam is a homogeneous linear material undergoing small deformation due to beam tip loading. The internal strains caused by loading in the two directions are assumed independent and superimpose in the structure. R_A , R_A' , R_B and R_B' are identical strain gages with no width perfectly bonded to the substrate surface. In a special when R_C and R_C' are equal and twice the resistance of the active strain gage, D equals $\frac{1}{2}$ when F_y is zero. This condition served as a theoretical check for any such cantilever beam I manufactured. The actual force beam responses deviate from this prediction as any physical conditions deviate from above assumptions.

2.1.3 *Materials and manufacturing of the force beam*

Several plastic materials are great candidates for the cantilever beams, in order to obtain large strain from very small forces, More specifically, cast acrylic is a thermoplastic that is cheap and easy to machine using lasers (Fig.2-6A). In addition, acrylic is also stiffer ($\sim 3.2\text{GPa}$) than the polyimide ($\sim 2.5\text{GPa}$) backing of most strain gages. This is the softest material we can use since the strain gage deformation must not constrain the piezo-resistors from deforming with the substrate.

The choice of strain gage was first limited by the physical grid size. In order to produce sensor pitch less than 4mm (as reasoned in *Section 2.1.1*), we only have substrate area less than 3.5mm for gage bonding. Fortunately, the interlacing design allows us up to 7mm wide to work with. However, a full bridge configuration would requires squeezing two strain gages side by side into this 7mm wide substrate surface. The strain gage must have a grid width smaller than 3mm. A good semiconductor

strain gage can easily fit this specification (Fig.2-6B), but it would cost over \$30 per gage (four gages are required) and requires fairly demanding wiring procedures. For practical reasons such as cost and implementations, we resorted to traditional foil strain gages (Fig.2-6B). All piezo-resistors are sensitive to temperature fluctuation. It is important to choose strain gages with small thermal effects and to install matched gages as pairs. This is especially critical when the substrate is a plastic material (which is a bad heat sink). It also helps if the strain gages have very high electric resistance and operate with as little current as possible. Finally, the gages must accommodate large strain range as plastic substrates are quite soft. All these design requirements point to a small open-faced constantan foil gage with a thin, laminated, polyimide-film backing (Vishay Micro-measurements, NC, USA). This gage has a grid dimensions of $1.52 \times 2.54\text{mm}$ (L \times W) and 100ohm of nominal resistance.

All the force beam features are symmetric on both sides. Traditional laser cutting procedure does not allow dual side machining. By creating a clever self aligning mechanism, I was able to perform the same laser patterning on both sides of an acrylic substrate (Fig.2-6C). The patterns are aligned on top of each other within 0.1mm. In addition, I also developed various techniques for producing different laser machining results. Typical laser cutter only allows one to dice or etch a substrate in its default mode. Manual setting allows the user to set the laser beam power and focal point to achieve three dimensional features on a substrate. By defocusing the beam in different ways, one can further create various smooth fillets on a piece of thermal plastic (Fig.2-6D). The final version of the cantilever beam takes at least 5 steps in the laser machining process.

2.1.4 *Simple beam tests*

The hybrid gage arrangement was first tested on a large cantilever beam (Fig.2-7A). Four strain gages were installed at the base of this square beam as previously depicted (Fig.2-7B). Beam tip

loading was provided by a known weight via a tether through a pulley mechanism (Fig.2-7C). By changing the angle of the tether, one could direct any gravitational force on the beam tip from purely vertical to purely horizontal. Using the convention established in equation [2] and [3] we call V_1 as V_y and V_2 as V_x . For all the following cantilever beam tests, we use a standard DC excitation voltage of 3V and instrumentation signal amplification of gain 100. All the signals are referred as after amplification.

Uni-axial loading tests reveal linear response from both signals as expected (Fig.2-7D). When loaded vertically (\mathbf{F}_y) the force beam only produces a signal in V_y with a constant sensitivity $S_y(\mathbf{F}_y) = -18.6$ V/N and not in V_x (no cross-talk). On the other hand, pure horizontal load \mathbf{F}_x produces a large signal in V_x with sensitivity $S_x(\mathbf{F}_x) = -5.16$ V/N and a smaller cross-talk signal in V_y with sensitivity $S_y(\mathbf{F}_x) = -2.64$ V/N. Interestingly, this cross talk response is almost exactly half of the V_x signal ($2.64/5.16 = 0.512$) as predicted by the idealized model (*Section 2.1.2*). Under bi-axial loading conditions, the force beam produces the exact V_x signal as predicted from the sensitivity $S_x(\mathbf{F}_x)$ (red crosses) (Fig.2-7E). The same simple prediction with $S_y(\mathbf{F}_x)$, however, underestimates the magnitude of V_y signal (green crosses) for biaxial loading. This is because the horizontal loading generates an offset to the V_y signal as predicted in the second term of equation [3]. In any case, the offset due to V_x signal can be corrected by empirically measuring the cross-talk constant D alluded by equation [3]. Within the small deflection region this simple cross-talk correction allows independent load measurements from the two dimensions.

The large simple beam demonstrates that the hybrid gage arrangement can produce very linear signals with a constant cross-talk which can be corrected. The next step is to scale down the cantilever beam to the actual size that would be implemented in the force beam array (Fig.2-8A). This scaled simple beam was mounted on a custom force beam calibration apparatus which allows

the continuous load control of one dimension (to be illustrated in *Section 2.1.6*) (Fig.2-8B). In this case, we would apply a known horizontal force using a weight while controlling the vertical loading. Again the uni-axial loading tests produce the similar behaviors as the large simple beam (Fig.2-8C). Vertical loading again only produces signals in V_y with $S_y(\mathbf{F}_y) = -0.3086$ V/N, and nothing in V_x ($S_x(\mathbf{F}_y) = 0$). Horizontal loading induces a response in V_y half of the signal in V_x ($S_y(\mathbf{F}_x)/S_x(\mathbf{F}_x) = -0.02461/-0.04872 = 0.505$). The sensitivities are now one order of magnitude smaller than the large simple beam as a result of mechanical scaling.

To confirm that the cross-talk V_y receives is a pure V_x dependent offset, I perform uni-axial vertical loading tests on the beam at different fixed horizontal loads (Fig.2-8D). Indeed, regardless of the horizontal load, V_y responses to vertical loading with the same sensitivity around -0.3 V/N (black circles). Similarly, V_x does not respond to vertical loads regardless of what the horizontal load the force beam experiences (open circles). In summary, there are three constants that determine the behaviors of such a force beam: horizontal sensitivity due to horizontal loading $S_x(\mathbf{F}_x)$, vertical sensitivity due to vertical loading $S_y(\mathbf{F}_y)$, and the cross-talk constant D .

2.1.5 FEA guided cantilever beam design

Through the simple beam characterizations, the strain gage circuit is now well established (Fig.2-9A). However, is this cantilever configuration capable of measuring the ground reaction forces from a crawling caterpillar? The *Manduca* caterpillar has 5 pairs of prolegs plus six thoracic legs. The force range per leg contact can be estimated by dividing the body weight over 6 (treating the thoracic legs as one unit). This estimate gives a value of 2.45mN for a second day 5th instar *Manduca* caterpillar (~1.5g). With the standard excitation 3V, the scaled simple beam would generate 0.736mV for the vertical loading and only 0.119mV for the horizontal loading from 2.45mN. With higher excitation voltage 10V, the signals can be boosted up to 2.45mV and

0.398mV respectively. These signals are at the border or below the threshold of detection as the instrumental noise level is typically a few mV (all these values are after gain 100 amplification already). To improve the signal-to-noise ratio, one has to look into mechanical strain amplifications.

Gage bonding and small force beam manufacturing is very time consuming, it is not practical to screen through all the beam designs with physical samples. Since acrylic plastic is homogeneous and linearly elastic under small deformation, finite element modeling is an effective method to weed out many low-potential mechanical designs quickly. Computer aid drawings (CAD) of a force beam design can be produced in *SolidWorks* CAD software (SolidWorks, Concord, MA) (Fig.2-9B). Using *SolidWork Simulation* I generate simple bi-axial mechanical loading at the beam tip while fixing the base of the beam (Fig.2-9C). The strain levels could be read out directly from the simulations at the locations of strain gages. We could also examine the stress on the underside of the force beam (Fig.2-9D). Finally, the finite element simulations also give estimates of beam tip displacement (Fig.2-9E). Such displacement should not exceed the set tolerance of 0.5mm under expected loading condition. After screening through many designs using this procedure, I arrived at fewer than five designs which were then implemented into physical force beams (Fig.2-9F) for testing. These force beams all have three dimensional features symmetric on both sides (Fig.2-9G). The strain gage wirings were also designed into the force beams as press-fit grooves. A 6 pin male connector was then press-fit onto each force beam for quickly swapping force beams during calibration/testing process which will be cover in the next section.

2.1.6 Calibration and performance

The standard calibration apparatus was designed and machined out of hard plastic delrin. It has a calibration bay which holds up to five force beams at any given time. The force beams are connected to a simple excitation and signal amplification circuit via a 6 pin female connector (Fig.2-

10A-B). The force beam to be calibrated will take on a calibration substrate (Fig.2-10C) which has a thin nylon thread connected to a calibration weight through a pulley mechanism (Fig.2-10D). For vertical loading, there is a groove right beneath the beam tips which allows an ergometer (*Section 2.2*) to reach up with a small rare-earth magnet (Fig.2-10E). This magnet moves up and down according to the lever arm control and interacts with another magnet on the calibration substrate (Fig.2-10F). This no contact approach to vertical loading protects the precision sub-mN force sensor in the lever-arm motor (ergometer) and provides vertical loading.

This calibration apparatus allows cycling through a range of vertical loads while holding a given horizontal force. During a typical test, the design force beam produces an offset signal in both channels as soon as the fixed horizontal load is applied (Fig.2-11A). An arbitrary vertical force ramping is then applied via the lever-arm motor. As expected, only V_y has a response (Fig.2-11A). Plotting the V_y offset and the V_x signal against horizontal load F_x reveals the cross-talk constant which is close to unity in this particular example (Fig.2-11B). Checking the responses to F_y at different F_x confirms that the cross-talk is in fact just an offset (Fig.2-11C). With the exact same strain gage circuit, the mechanical design of this force beam has improved the cantilever sensitivities greatly compared to the scaled simple beam. The force beam now has -1.762 V/N in the vertical direction (>5 times higher than the -0.3086 V/N from the scaled simple beam), and -0.131V/N in the horizontal direction (more than double -0.04872 V/N also from the scaled simple beam). In the load cell specification standard, the force beam corresponds to $\sim 2\text{mV/V}$ (50mN rating) and $\sim 80\text{mV/V}$ (5mN rating) respectively.

Of course, as the force beam becomes more compliant, one has to check the resonance frequency. By suddenly releasing a vertical load, a stereotypic damped vibration signal can be obtained for analysis. The resonance frequency for this force beam is 273.44Hz (Fig.2-11D). Compared to the

intended data acquisition sampling rate of 100Hz, it is sufficiently high. Compared to the typical cyclic frequency of caterpillar locomotion ($<0.5\text{Hz}$), this is more than sufficient to capture any biological meaningful transient responses. Slightly different styles of force beams have been produced. Amount them only eight attained satisfactory performances. Their sensitivities and cross-talk constants vary quite a lot depending on the styles and human factors during manufacturing (Fig.2-11E). In general, the sensitivities are in both directions are correlated. Stiffer beams tend to be less sensitive in both directions. Curiously, some force beams have cross-talk constants less than one and still maintain high sensitivities. FB-X23, for example, is an experimental test beam which has a cross-talk constant slightly less than 0.5 with sufficiently high sensitivities. Since the force beam geometry design was mostly empirically based with a little help from FEA simulations, it is difficult to deliberately optimize the force beams. Via calibrations, however, these parametric irregularities can be compensated for accurate bi-axial force measurements

2.1.7 The 4th generation MFBA

The 4th generation MFBA system is mounted on a tripod which allows future experiments to adapt different orientations for the caterpillars to crawl (Fig.2-12A). The single DV camera simplifies the setup process. Although the custom *LabView* program has simple marker tracking capabilities, it is often easier to match footfalls in the data-synchronized videos during *post-hoc* analysis. Due to the lack of peripheral structures, caterpillars on the measurement track tend to crawl in a straight line over the force beam array (Fig.2-12B). The sensor spacing is optimized to accommodate the footfall pattern of 5th instar *Manduca* caterpillars. Installing UV markers is the easiest proleg tracking method which will come in handy when large volume data acquisition is needed (Fig.2-12C). All the electronics are installed in a custom enclosure with a LCD display of the current sensor

excitation level (Fig.2-12D). This is a generic analogy interface with basic signal amplifications which can be adapted for other similar laboratory applications in the future.

2.2 An uni-axial lever-arm system for miniature soft tissue mechanical tests

2.2.1 *Mechanical tests of soft tissues*

Soft materials in general are difficult subjects for mechanical tests. First of all, it is not easy to prepare soft materials into the standard specimen geometries. Soft materials tend to deform greatly during any cutting procedure. Molding is the best solution to produce consistent specimens whenever possible, but it is limited to mostly the castable synthetic materials. Secondly, it is difficult to distribute loads evenly in soft specimens. Traditional gripping devices tend to deform the material or introduce undesirable pre-stresses. To anchor a piece of soft material, alternative methods such as suturing are necessary. Thirdly, even with the best sutures the specimen anchors often produce nonlinear end-point effects. To track the specimen's deformation accurately, image based extensometry is necessary. This can be done with external markers or inherent features.

Soft tissues introduce a few more complications in the testing process. The mechanical properties of most soft tissues are highly dependent on the hydration states. To obtain accurate data, one must keep the specimen in a tight hydration control, in many cases within a liquid bath. While the testing specimens come from certain organisms, the dissection and tissue cutting process are much more complicated than preparing specimens from synthetic material. The size and geometry of the specimens are limited by the anatomy of the organism. Finally, biological specimens have very large variations. The procession of the mechanical tests data requires very considerate parameter extractions.

2.2.2 *The lever-arm system control with video extensometry*

Precision servo motor lever-arm systems are widely used in muscle physiology and various custom bio-material tests. I adapted the standard lever arm system (Muscle Lever Model 300C, Aurora Scientific Inc., Ontario, Canada) to a custom testing platform for mechanical testing (Fig.2-13A). A linear specimen of any kind can be fixed inside the saline dish with one loose end. The lever arm will then be lowered and connected to the loose end of the specimen via a steel pin linkage. Depending on the goal of the experiment, this lever arm can be programmed to execute any kind of movement from periodic cycling to arbitrary swings via a custom *LabView* program. The amplitude of the movements, however, comes from the real-time image analysis from the microscope camera (Basler Vision Tech., Ahrensburg, Germany) (Fig.2-13B). Under the scope, the specimen (a piece of caterpillar cuticle in this case) takes on two green florescent beads with only a small amount of lanolin gel or petroleum jelly for adhesion (Fig.2-14A). A steel pin with known length and diameter is placed in the same level as the specimen in the dish for image calibration. Using a custom UV LED cage (Fig.2-14B), the fluorescent markers appear brilliant through the imaging window on top of the UV cage (Fig.2-14C). This UV cage greatly improves the image quality by distributing the UV light evenly and blocking out unwanted UV back scatter that might saturate the CCD camera. The camera image is captured via an IEEE 1394 link and analyzed by the same custom *LabView* program that controls the level arm. The image analysis protocol in this program thresholds the image at a certain pre-defined intensity and converted the image into a binary format. This processed image then goes through a particle analysis function in *LabView*. The program then computes the distance between the centroids of the two particles (Fig.2-14D) using the calibration parameters obtained earlier. This process eliminates the margin effects in soft specimen mounting

and off-axis deformation (Fig.2-14E~F). The entire protocol is comparable to the extensometry in a standard uni-axial material tester (Instron, Norwood, MA).

It is important to note that real-time image analysis does take up a lot of computing bandwidth. Currently the lab PC can consistently handle up to ~10fps sampling rate. The lever arm, however, cannot be controlled directly with such a low sampling frequency. Instead, the results from the image analysis are used to modify the calibration factor of the lever arm movement. During each operation, the computer sends voltage signal to the level arm servo controller according to a predefined calibration factor. If the lever arm overshoots a target using the original calibration factor, the image analysis will dial down the calibration factor for future movements. Between the image analysis cycles, the lever arm simply assumes the same movement. This real-time image analysis feedback control was implemented for the caterpillar soft cuticle mechanical tests (Publication-3). It works very well for slow quasi-static mechanical tests. Attempting dynamic tests will run the risk of losing extensometry information and driving the lever arm out of control. More work is required to accommodate dynamic tests, which the lever arm can handle and most other material testers cannot. In the future implementation, we should also consider using inherent specimen features for deformation tracking, such as the black stripes in the caterpillar cuticle specimens (visible in Fig.2-13A,C,E).

2.3 For the soft robots

2.3.1 The kinematics tracking system

Kinematics tracking is a standard procedure for animal locomotion studies and robotics. There are many different 3D reconstruction techniques, and new video tracking methods are being developed rapidly. For example, a hull reconstruction motion tracking procedure has been developed recently

to capture fruit fly wing kinematics (Ristroph et al. 2009). The main stream systems, however, can be divided into two categories: video tracking and marker tracking. The former relies on multiple camera views of the subject to triangulate the positions of certain body features. The marker tracking method does the same thing except using pre-installed markers on the subject. Marker tracking involves more preparation work and is not always appropriate for the tracked subject. However, it simplifies the automation of 3D reconstruction by ignoring all the irrelevant visual information. Typically, marker tracking is achieved in the infrared (IR) spectrum with retro-reflective markers. The tracking IR cameras are fitted with high intensity IR LEDs which strobe with the image acquisition. Multiple such IR cameras are synchronized via some high speed link and real-time 3D reconstruction is possible. For our robot tracking application, we use a marker tracking system (VICON, Los Angeles, CA) (Fig.2-15A).

Systems like VICON have many built-in automation features that facilitate marker identifications. Unfortunately all these systems are built for tracking movement at scales in meters or centimeters. For sub-centimeter tracking in a volume of less than a 30cm cube, most default setups invariably fail. There are two inherent problems for marker tracking at this scale. First of all, the retro-reflective markers smaller than 1mm in diameter are very difficult to manufacture. They have to be custom made on a case by case basis. Because the retro-reflective performance correlates to the marker surface area, it is challenging to provide sufficient lighting for the markers. For the same surface area constraint, the luminous intensity is small in small markers.. Secondly, high intensity IR lighting in small volume unavoidable heats up the space and also creates unwanted back scatter. Even if the heating problem is solved, the back scatters are still difficult to eliminate with so many cameras facing across each others. To get around these problems, I switch the passive retro-reflective system to an active marker tracking method. More specifically, I remove all the IR light

sources and replace the retro-reflective markers with miniature IR LEDs. The LED of my choice SFH4050 (Opto Semiconductors, Regensburg, Germany) has small profile dimensions of 1.7mm×0.8mm×0.65mm (L×W×H) and a 160 degrees viewing angle (Fig.2-15B). Its emission peaks sharply at 850nm wavelength which is captured by the VICON IR cameras nicely (Fig.2-15C). Due to the intensity of the LED light source, focusing the IR cameras is less critical as these LEDs all appear like distant stars (point light sources) in the cameras. In order to obtain millimeter accuracy in high speed tracking, I also design a calibration apparatus with the same IR emitters (Fig.2-15D). A standard calibration wand and a dial calibration base allow dynamic calibration and define the global coordinate system. Selected soft robots are marked with the same miniature LEDs for kinematics tracking (Fig.2-15E). A simple free-joint model constructed in the VICON Nexus software facilitates markers to be tracked in 3D (Fig.2-15F).

2.3.2 *A miniature force plate design*

While the substrate reaction forces from caterpillars are captured by a force beam array (*Section 2.1*), the ground dynamics of soft robots requires a force plate that is compatible with the kinematics tracking system described in the previous section. I achieve this instrumentation task quickly by adapting the already characterized scaled simple force beam (Fig.2-16A). In fact, I directly instrument around the force beam calibration apparatus which contains all the necessary electronics and fixtures to operate any force beam (Fig.2-16B). A platform with a 30cm effective tract constructed with laser machined floor fitting allows the robot to transmit ground forces direct down to the force beam (Fig.2-16C). The kinematics 3D coordinate can be defined on top of this platform. The pre-amplified voltage signals are fed directly into the VICON system via the analogy inputs. This implementation allows the ground force data to be synchronized to the kinematics data automatically, resulting in a clean and integrated force plate system (Fig.2-16D).

2.3.3 *Data synchronization and triggering*

Besides the marker 3D coordinates and ground reaction forces in two directions, two more VICON analog channels were devoted to recording the current passing across the two major actuators in the soft robot. This was done by inserting a small precision resistor (tolerance $\pm 0.1\%$) in series with each of the robot actuator. By amplifying the voltage across these resistors, one can directly assess the current flow through the actuator circuits. For each experimental trial, the robot controller first sends a trigger to the VICON system to start recording of all the data (kinematics, dynamics, and actuator states). After a fixed offset time (typically 1s), the robot controller then sends the stimulation patterns to the robot. The recording is automatically terminated either after a fixed time period or earlier by an end trigger from the robot controller. This system was instrumented to capture the mechanics of the ballistic rolling behavior in GoQBot. See Publication-5 for details.

2.4 Costa Rica field work

2.4.1 *A general survey of caterpillar gaits*

As a complementary component to my studies of caterpillar locomotion and gait transitions, we did some field work in Costa Rica. The goal of this field work was to document every possible caterpillar gait there is with a focus on behavioral adaptation to different proleg configurations. The field work lasted for 16 working days excluding travel time from May 24th to June 10th 2010. Due to the time constraint, it was not possible to target a specific species for study. For this reason, the observations from this field work are not intended to draw definitive conclusions on any evolutionary path. Instead, the data are used throughout this thesis as behavioral evidences to support different findings and ideas about caterpillar locomotion.

Since we are only interested in the stereotypic locomotor patterns, sample size was not critical, but diversity was. Generally, we sought caterpillars with proleg arrangements different from the ancestral form (five pairs of functional abdominal prolegs) and characterized their gaits qualitatively. It was hypothesized that proleg reduction led to gradual synchronization of proleg detachment timing through evolution. Body buckling and inching gaits emerged naturally as the animal body scaled down.

2.4.2 *Area de Conservacion Guanacaste*

The field work was conducted at a large conservation area north of Liberia, Costa Rica. This conservation area consists of 18 sectors and covers the narrow neck of Central America from the Pacific to the Caribbean Sea. The 120,000 terrestrial hectares and 70,000 marine hectares include dry forests, wet forests, cloud forests, two volcanoes, and several pristine beaches (Fig.2-17A). The main research station and administration is located in sector Santa Rosa where we performed most of the caterpillar collection and observations. May is the beginning of the raining season for Santa Rosa, and this causes a dramatic vegetation bloom (Fig.2-17B). Most Lepidoptera species have to catch this opportunity to produce caterpillars. Our research logistics were handled by Mr. Roger Blanco Segura (director of the ACG research program). Caterpillar collection, rearing and identification were guided by Dr. Daniel Janzen (prof. at University of Pennsylvania whose research is based at ACG), Dr. Winnie Hallwachs, and their local research team.

2.4.3 *Field activities*

The actual field work consisted of caterpillar collection, filming the caterpillar locomotion, photographing special morphologies, and taking notes of some body dimensions. A high speed HD camera Casio F1 (Casio America, Inc., Dover, NJ) was used throughout to capture caterpillar behaviors (Fig.2-18A). A SONY Cybershot camera (SONY Inc., Tokyo, Japan) was used to take

super macro still images. Caterpillars were kept in large heavy duty plastic bags with their food plants. These bags were categorized and sorted on laundry lines in a semi-indoor facility (Fig.2-18B). Smaller caterpillars were kept in glass jars and lined on the work bench. Every working day after the collection, we would set up a filming arena and go through all the caterpillars (Fig.2-18C). Wild caterpillars were not as resistant to human handling so we typically released the animal as soon as we finished gait characterization. Sometimes the same animal would be filmed again at later stages if body scaling was of interest. The filming arena was a custom design with centimeter background grids and a calibrated horizontal beam for the caterpillar to crawl across (Fig.2-18D). A red LED light was use to mark the video frame whenever necessary.

References

- Bartsch, M.S., Federle, W., Robert, J. & Kenny, T.W. 2007, "A Multiaxis Force Sensor for the Study of Insect Biomechanics", *Journal of Microelectromechanical Systems*, vol. 16, no. 3, pp. 709.
- Garcia-Webb, M.G., Taberner, A.J., Hogan, N.C. & Hunter, I.W. 2007, "A modular instrument for exploring the mechanics of cardiac myocytes", *American Journal of Physiology- Heart and Circulatory Physiology*, vol. 293, no. 1, pp. H866.
- Park, S.J., Goodman, M.B. & Pruitt, B.L. 2007, "Analysis of nematode mechanics by piezoresistive displacement clamp", *Proceedings of the National Academy of Sciences*, vol. 104, no. 44, pp. 17376.
- Reinhardt, L., Weihmann, T. & Blickhan, R. 2009, "Dynamics and kinematics of ant locomotion: do wood ants climb on level surfaces?", *Journal of Experimental Biology*, vol. 212, no. 15, pp. 2426.
- Ristroph, L., Berman, G.J., Bergou, A.J., Wang, Z.J. & Cohen, I. 2009, "Automated hull reconstruction motion tracking (HRMT) applied to sideways maneuvers of free-flying insects", *J Exp Biol*, vol. 212, pp. 1324-1335.
- Zumwalt, A.C., Hamrick, M. & Schmitt, D. 2006, "Force plate for measuring the ground reaction forces in small animal locomotion", *Journal of Biomechanics*, vol. 39, no. 15, pp. 2877-2881.

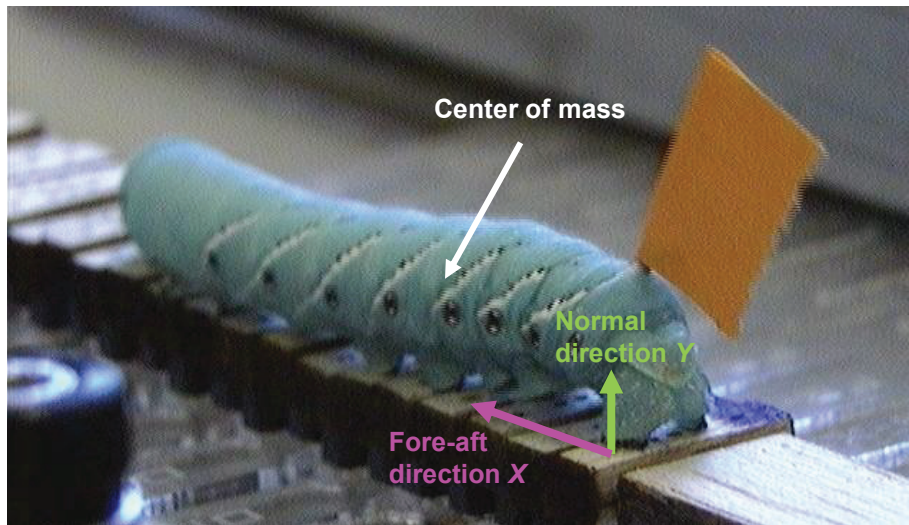


Fig.2-1 Measuring caterpillar ground reaction forces. In order to assess the inter-segmental forces during locomotion, caterpillar ground reaction forces have to be measured from all the leg contacts simultaneously. This requires a mini force beam array as shown.

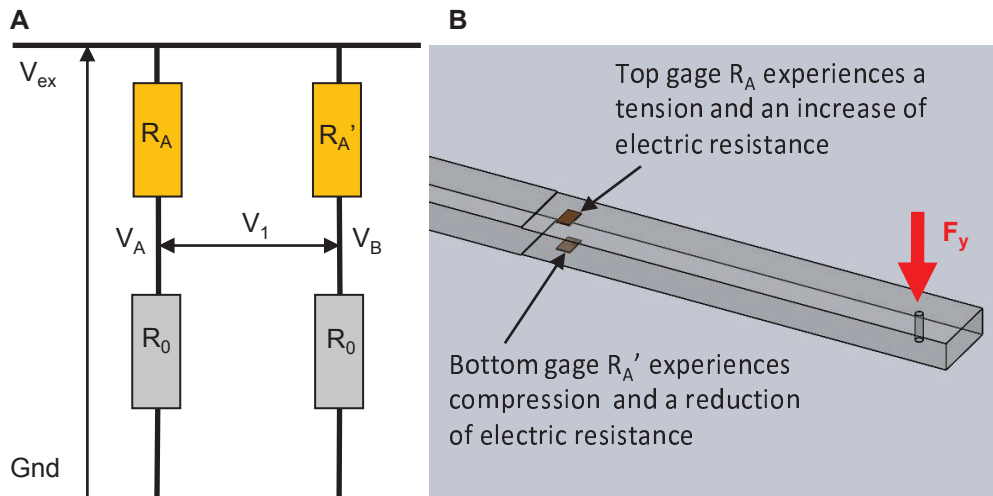


Fig.2-2 (A) This is one style of the half Wheatstone bridge circuits for detecting resistance changes in the two piezo-resistive strain gages. Given the constant excitation V_{ex} , the electric current through each bridge arm changes according to the resistance of the corresponding strain gage. **(B)** The simplest uni-axial force beam for sensing vertical loads F_y .

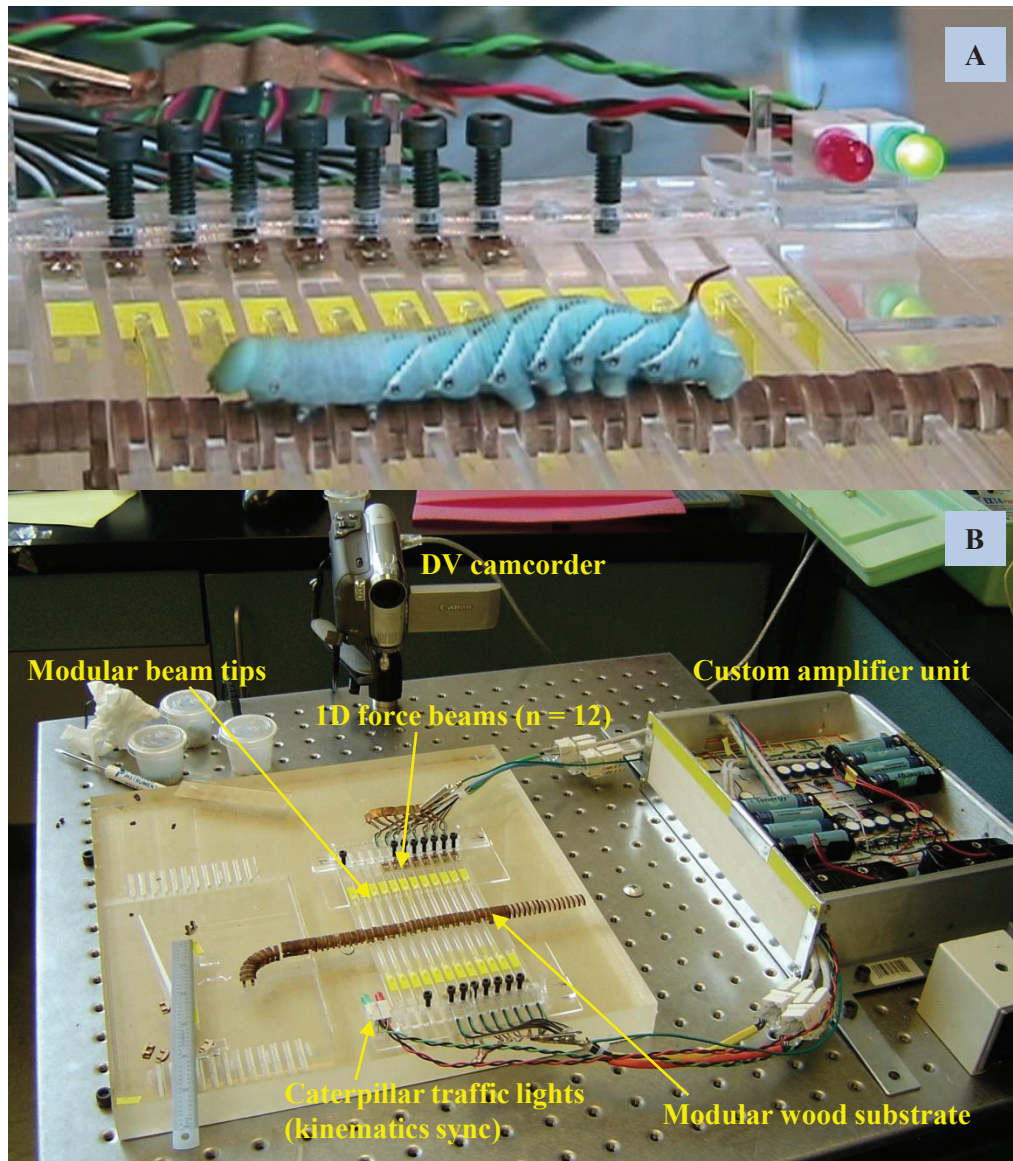


Fig.2-3 The 2nd generation Mini Force Beam Array (MFBA-II) for weight shift measurements. (A) A *Manduca* caterpillar was induced to crawl along the sensing substrate on the force beam array. Each independent laser-machined wooden substrate measures the vertical load at each footfall. (B) The entire system consists of the beam array and its control unit. A DV camera was used to capture the caterpillar behaviors for footfall matching.

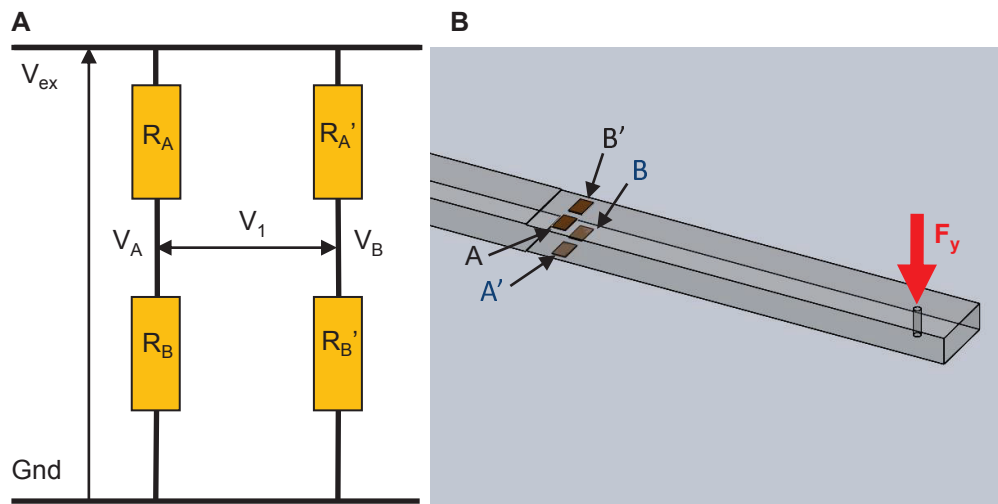


Fig.2-4 (A) The standard full Wheatstone bridge circuit maximizes the sensitivity of a cantilever force beam. The piezo-resistors R_A and R_B act in the same direction to produce a voltage difference between V_A and V_B . The same argument applies for the piezo-resistors $R_{A'}$ and R_B . **(B)** Matched gages (e.g. A and A') need to be installed at the same location on the opposite sides of the cantilever beam.

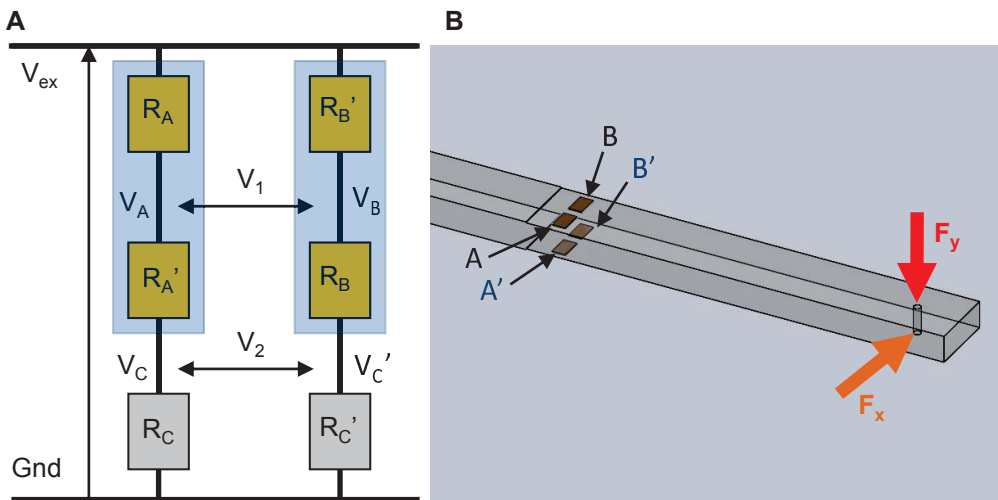


Fig.2-5 (A) A hybrid-bridge circuit was my own invention which employs only four gages for bi-axial sensing while maintaining the full bridge sensitivities. Signal V_1 reflects the resistance difference between primed and unprimed gages due to vertical loading F_y (red). Simultaneously, signal V_2 compares the resistance difference between A gages and B gages due to horizontal loading F_x (orange). Details about how to eliminate the inherent cross-talk can be found in *Chapter 2*. **(B)** Gage installation has been modified slightly to achieved bi-axial sensing.

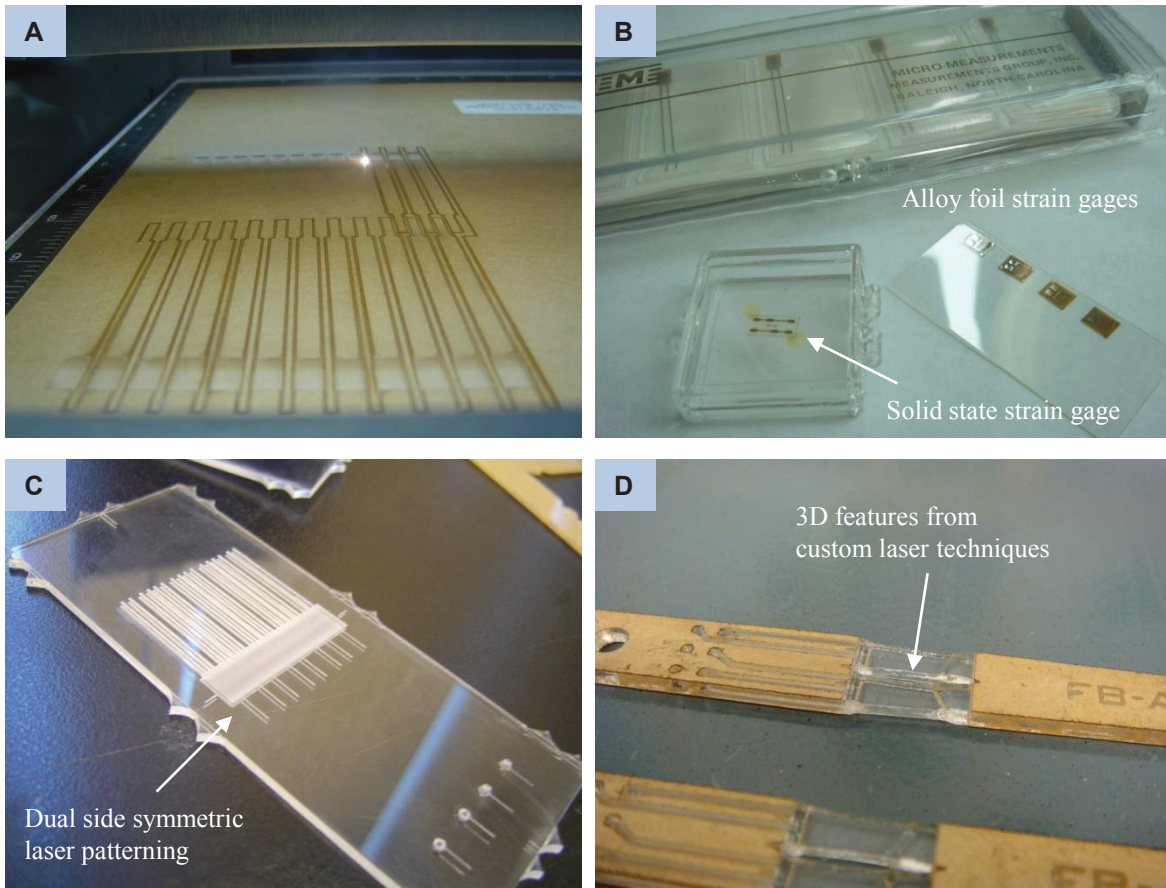


Fig.2-6 Manufacturing of force beams. (A) Laser cutting with custom settings allows accurate patterning and machining of thermoplastics. (B) Piezo-resistive strain gages are widely used for force measurement applications. (C) A alignment technique was developed to perform double side symmetric laser machining. (D) At least 5 laser procedures were required for each force beam in order to create the 3D features.

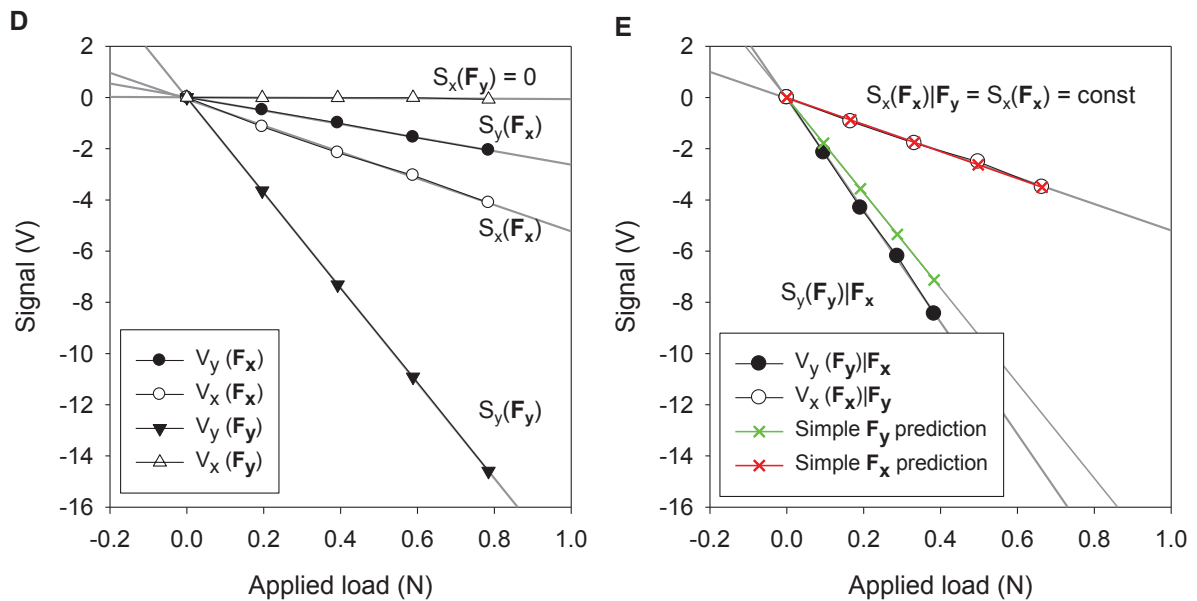
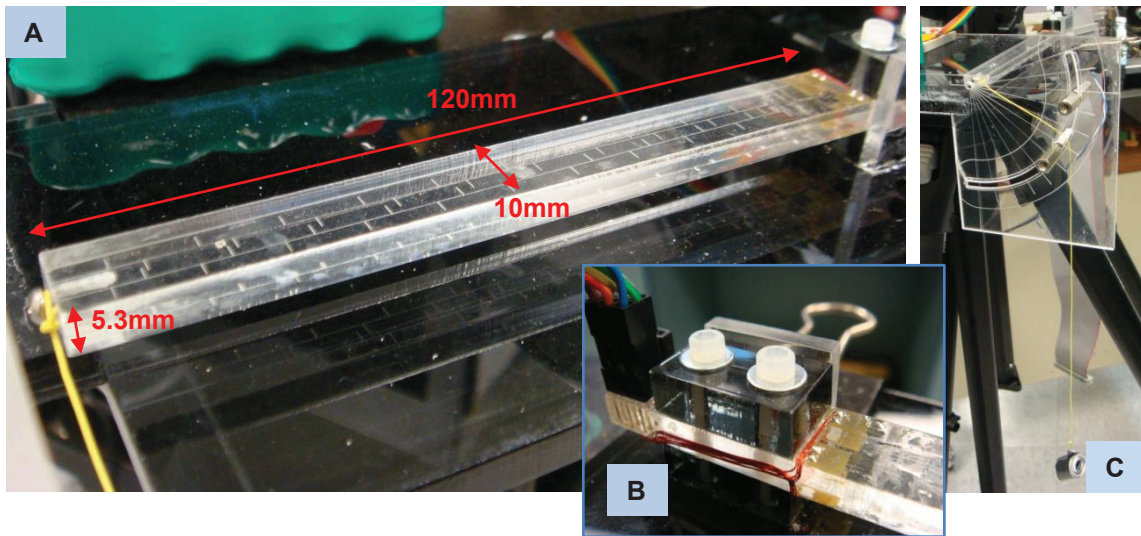


Fig.2-7 Large simple beam test (A) A large cantilever beam was produced to characterize the bi-axial sensing capability of the hybrid bridge circuit. **(B)** The strain gages were carefully bonded according to the design in Fig.2-5. **(C)** A custom apparatus allows us to generate a bi-axial load from a known weight. **(D)** Signals from the force beam show very linear responses due to uni-axial loading. In reference to Fig.2-5A, $V_y = V_1$ and $V_x = V_2$. **(E)** In the bi-axial loading condition, V_y signal is slightly higher than in the uni-axial condition. This discrepancy is due to a linear cross-talk from V_x which can be eliminated in the *post-hoc* analysis.

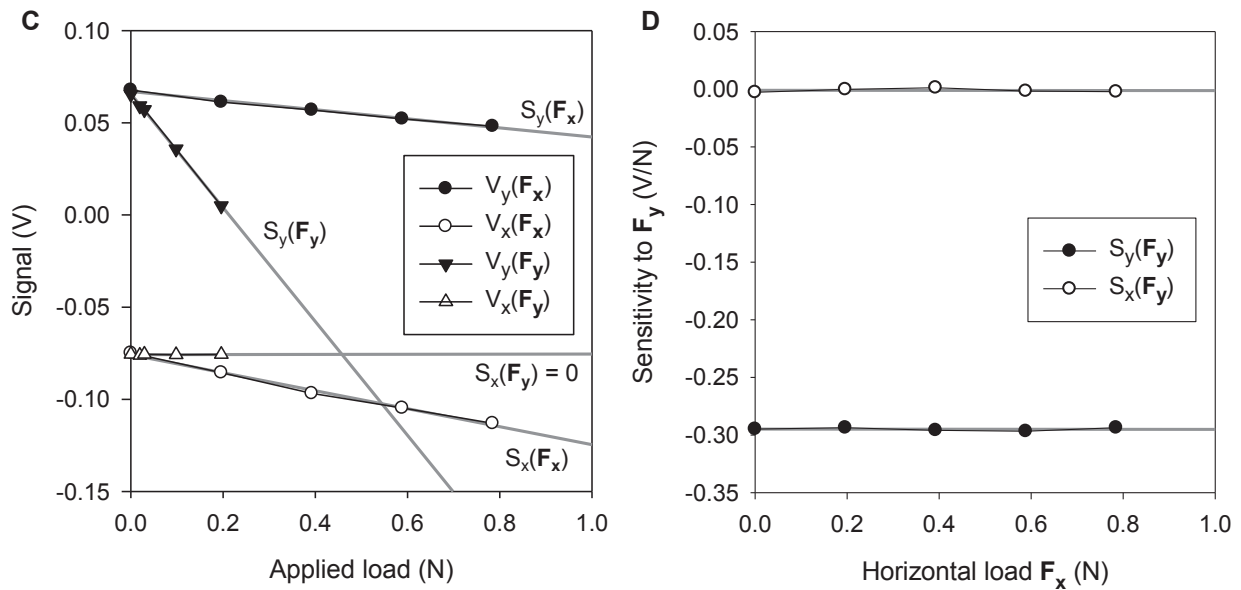
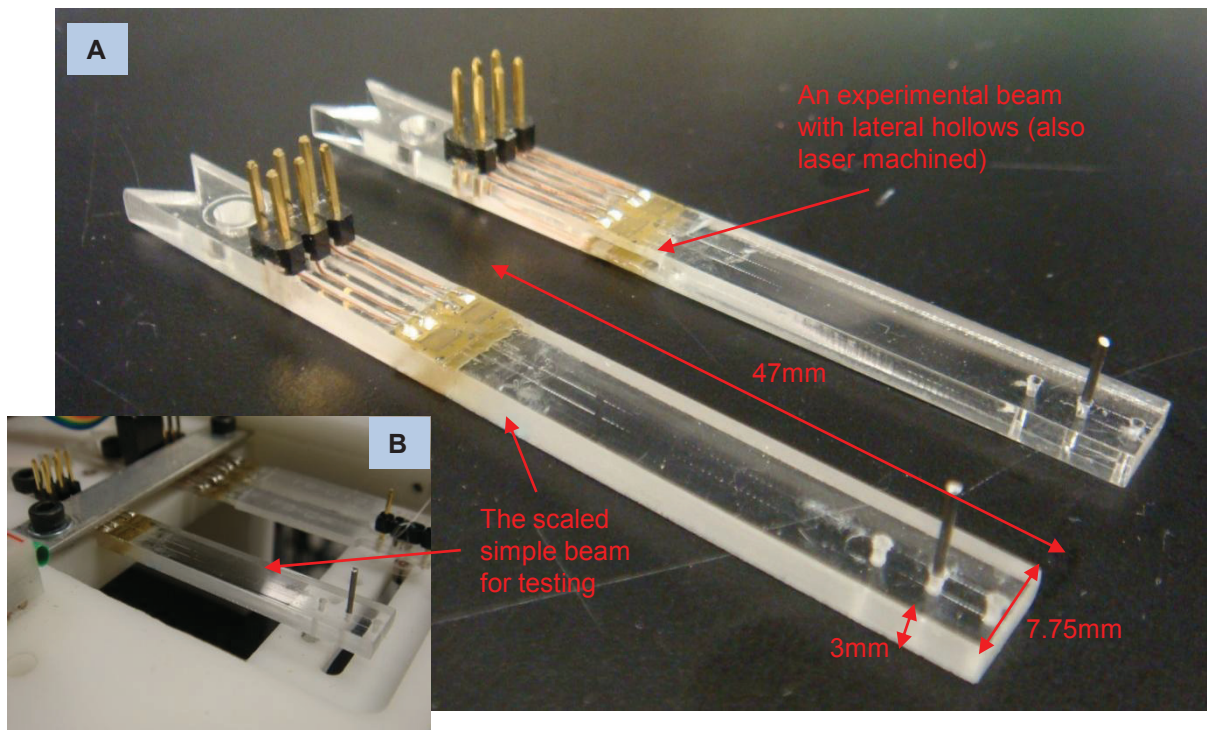


Fig.2-8 Scaled simple beam test. (A) The simple beam was scaled to the target size to simulate the beam sensor output. (B) The scaled simple beam was mounted on the custom calibration apparatus for testing. (C) Uni-axial tests confirm the one-way cross-talk as predicted. (C) The cross-talk is an offset which does not affect the beam sensitivities in either direction.

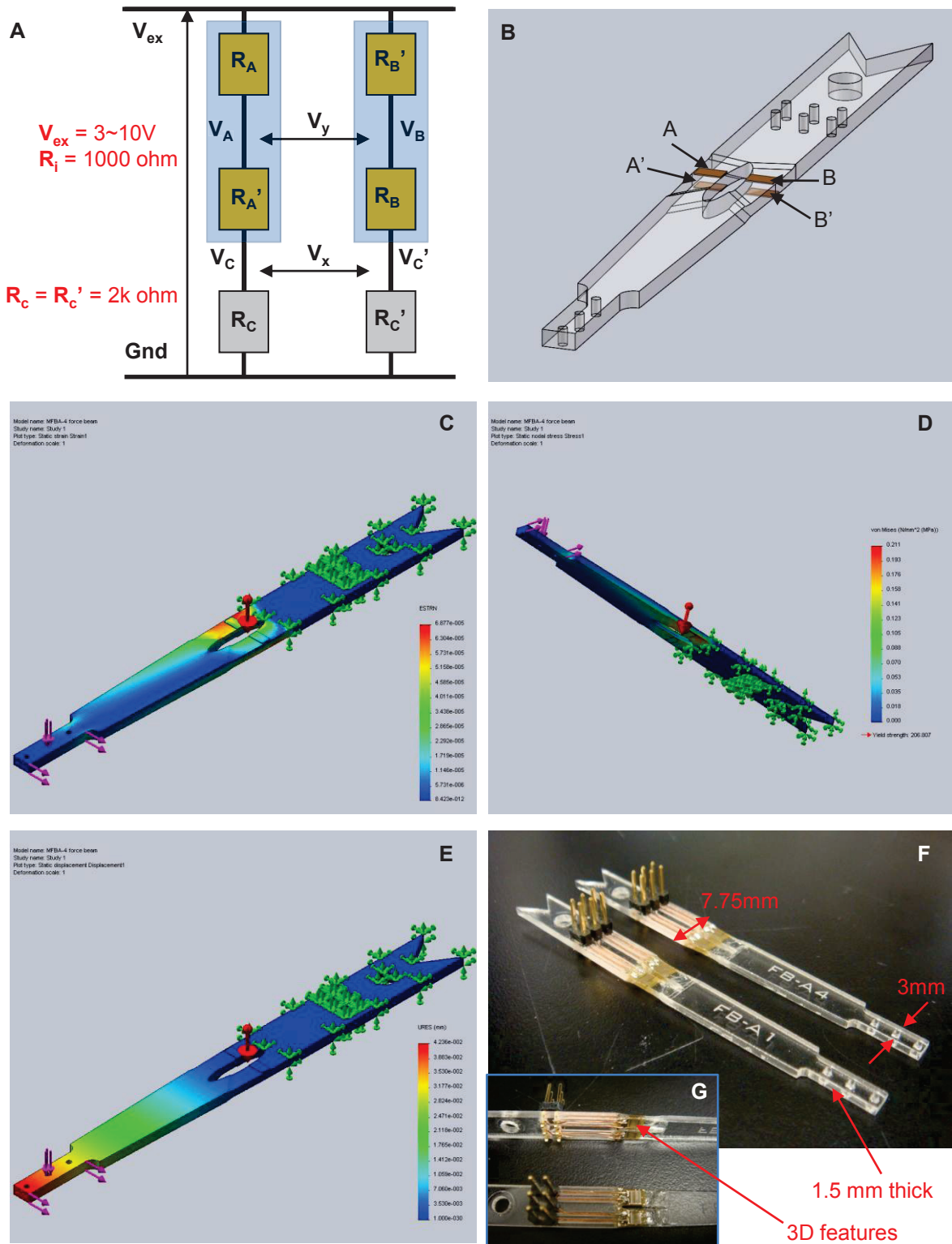


Fig.2-9 Mechanical design of the cantilever force beam. (A) The hybrid bridge circuit. (B) The CAD model of the force beam. (C) Strain plot when a bi-axial load is applied at the beam tip. (D) Stress plot of the underside under the same condition. (E) Displacement is very minimum (<0.4mm) under typical loads expected from the caterpillars. (F) Actual force beams are produced using highly elaborate laser protocols. (G) All the wiring groove are pre-designed into each force beam with a 6-pin connect pressed fitted on top.

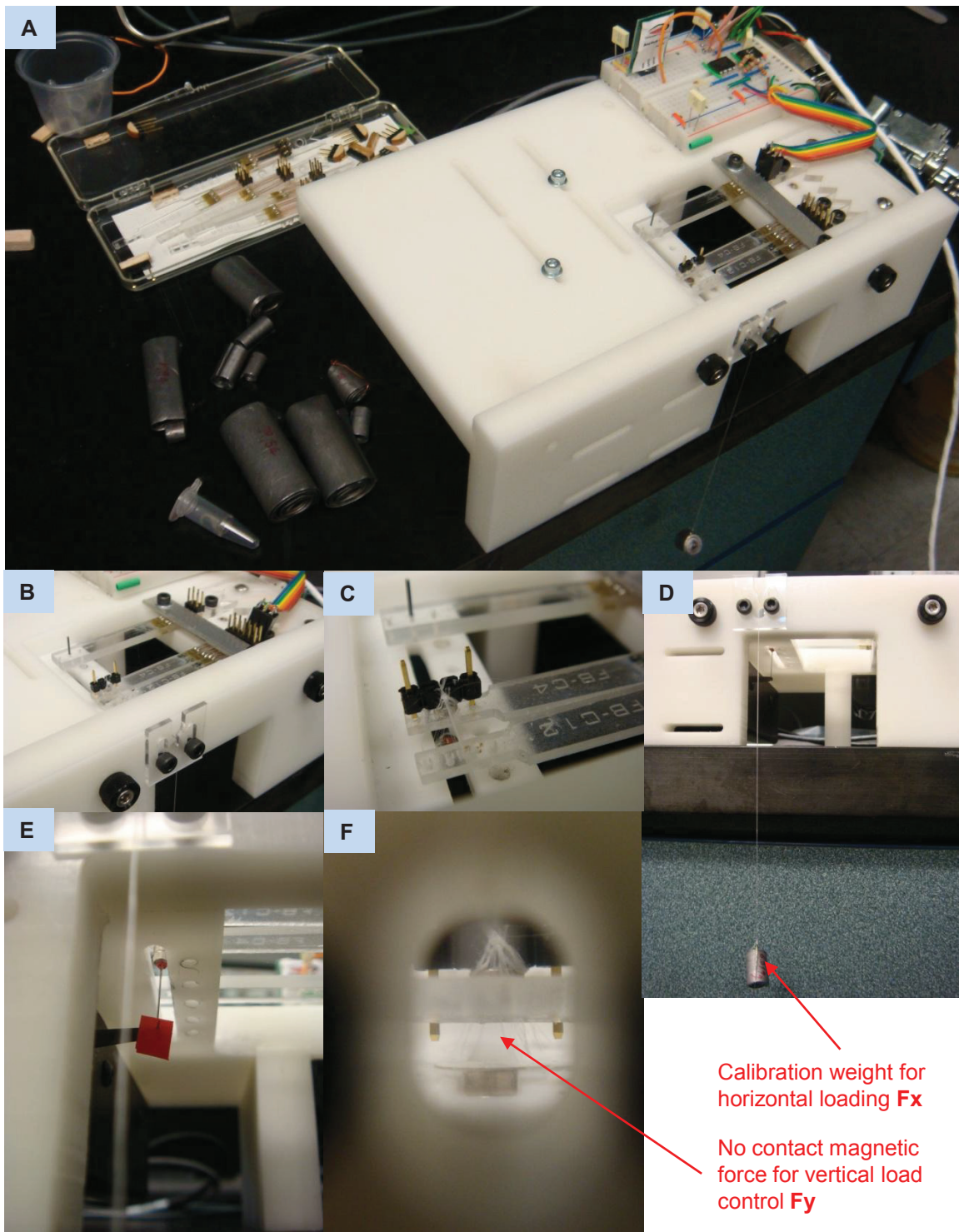


Fig.2-10 Two dimensional force beams calibration. (A)(B) The custom calibration apparatus can house up to 5 force beams at each given time. (C) A calibration substrate unit mounts securely on the force beam tip exactly like the real experimental substrates. (D) A know weight can be hang to provide the lateral load. (E) Vertical load was controlled by a level arm ergometer. (F) to protect the precision ergometer, the vertical force was mediated by a magnet setup as shown.

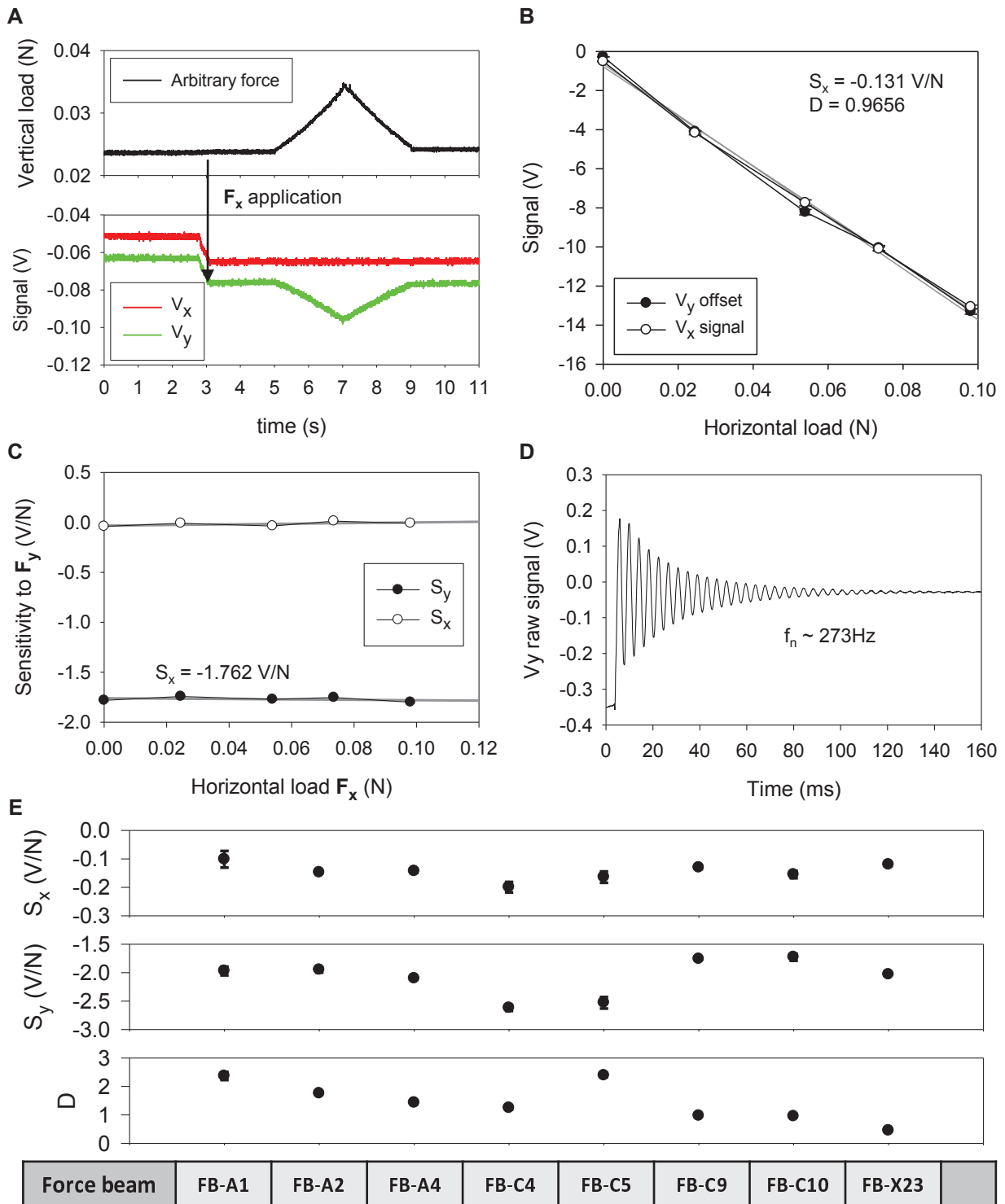


Fig.2-11 Force beam calibration data. (A) Example calibration signals. (B) The offset in V_y is directly proportional to the V_x signal by a constant D which we can determined experimentally for each individual beam. (C) The crosstalk is a pure offset which does not affect the sensitivities of the force beam in either direction. (D) Typical resonance frequency is between 200Hz and 300Hz. (E) The 3 empirically determined parameters for 8 two-dimensional force beams measured at standard 3VDC excitation.

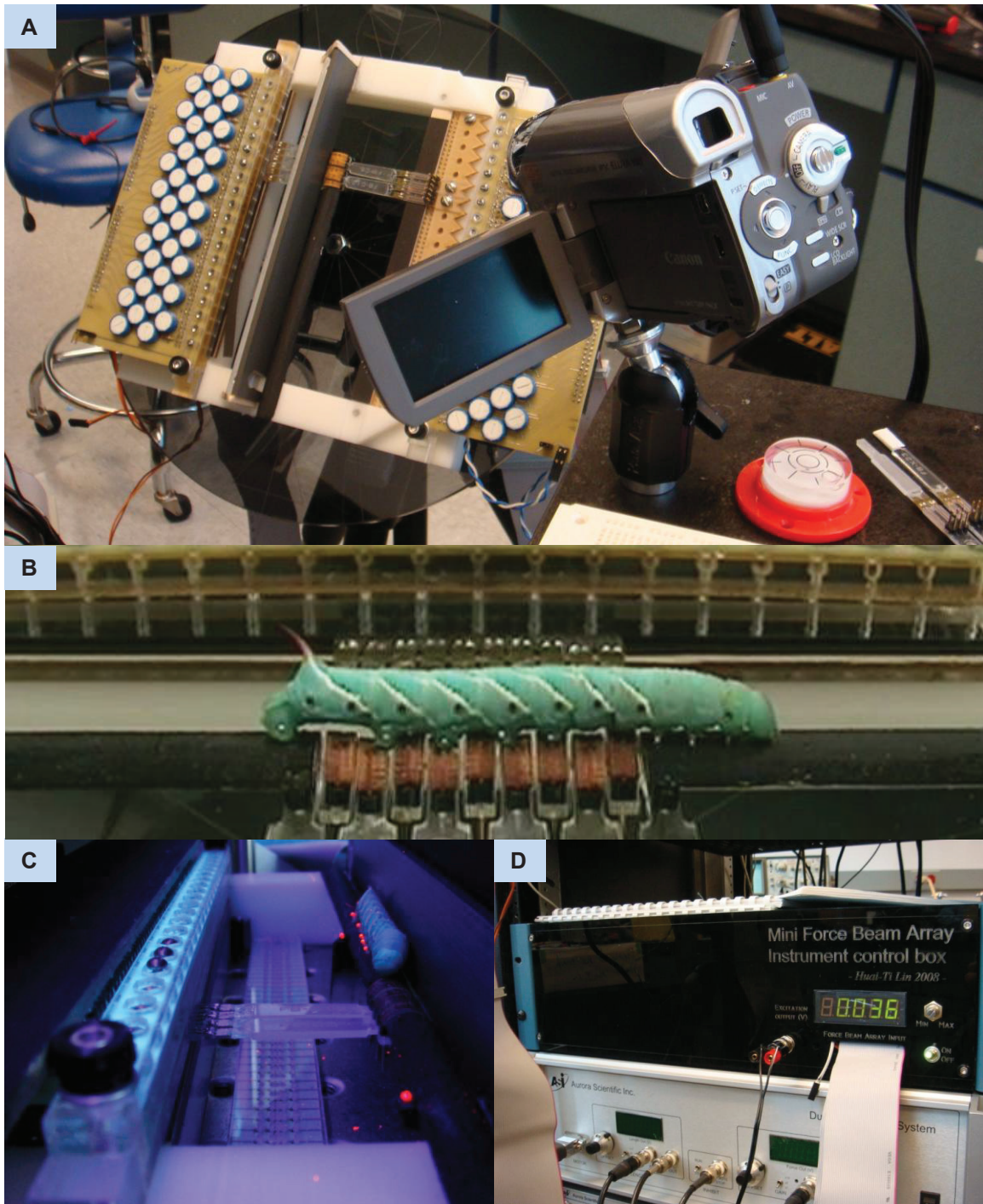


Fig.2-12 The 4th generation Mini Force Beam Array system. **(A)** The current MFBA has a custom mount which allows orientation studies on caterpillar ground reaction forces. Only one DV camera is required for footfall tracking. **(B)** The sensor spacing is optimized to accommodate the footfall pattern of 5th instar *Manduca* caterpillars. **(C)** With UV fluorescent marking, contact matching process can be better automated to facilitate large volume data acquisition. **(D)** All the custom electronics have been integrated into a custom enclosure with a user friendly interface. The input channels are wired with standard PCI ribbon cables, and the output is compatible with any standard National Instrument PCI data acquisition board.

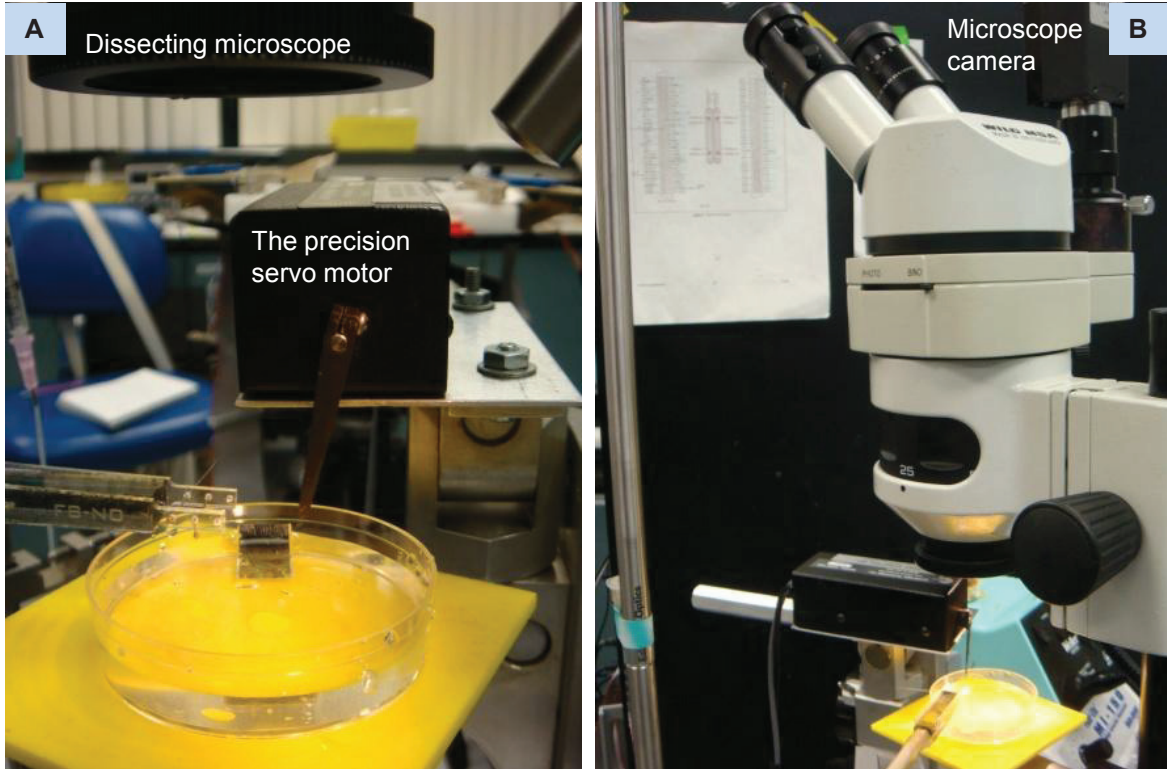


Fig.2-13 The lever-arm system. (A)(B) A standard ergometer system is coupled to a custom real-time image analysis protocol for uni-axial mechanical tests of soft tissues.

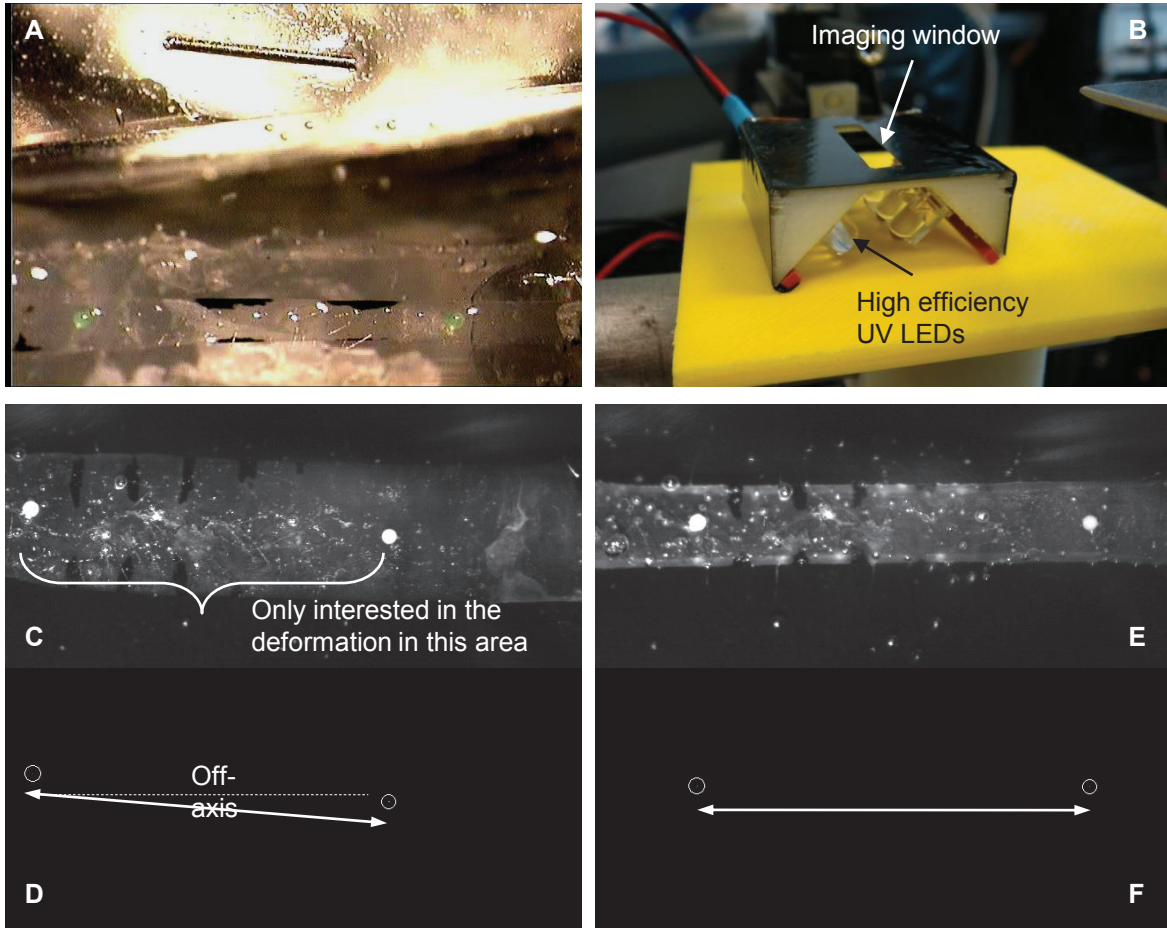


Fig.2-13 The video extensometry. (A) Marker tracking simplifies the image analysis protocol and allows real-time feedback for the lever arm system. A pin with known length and diameter was placed in the same level to the sample for calibration. (B) A custom UV lighting cage improve the scope imaging quality by blocking the back scatter from the saline dish. (C)(D) Extensometry is insensitive to undesirable specimen misalignment. (E)(F) UV fluorescent beads provide very accurate and reliable marking.

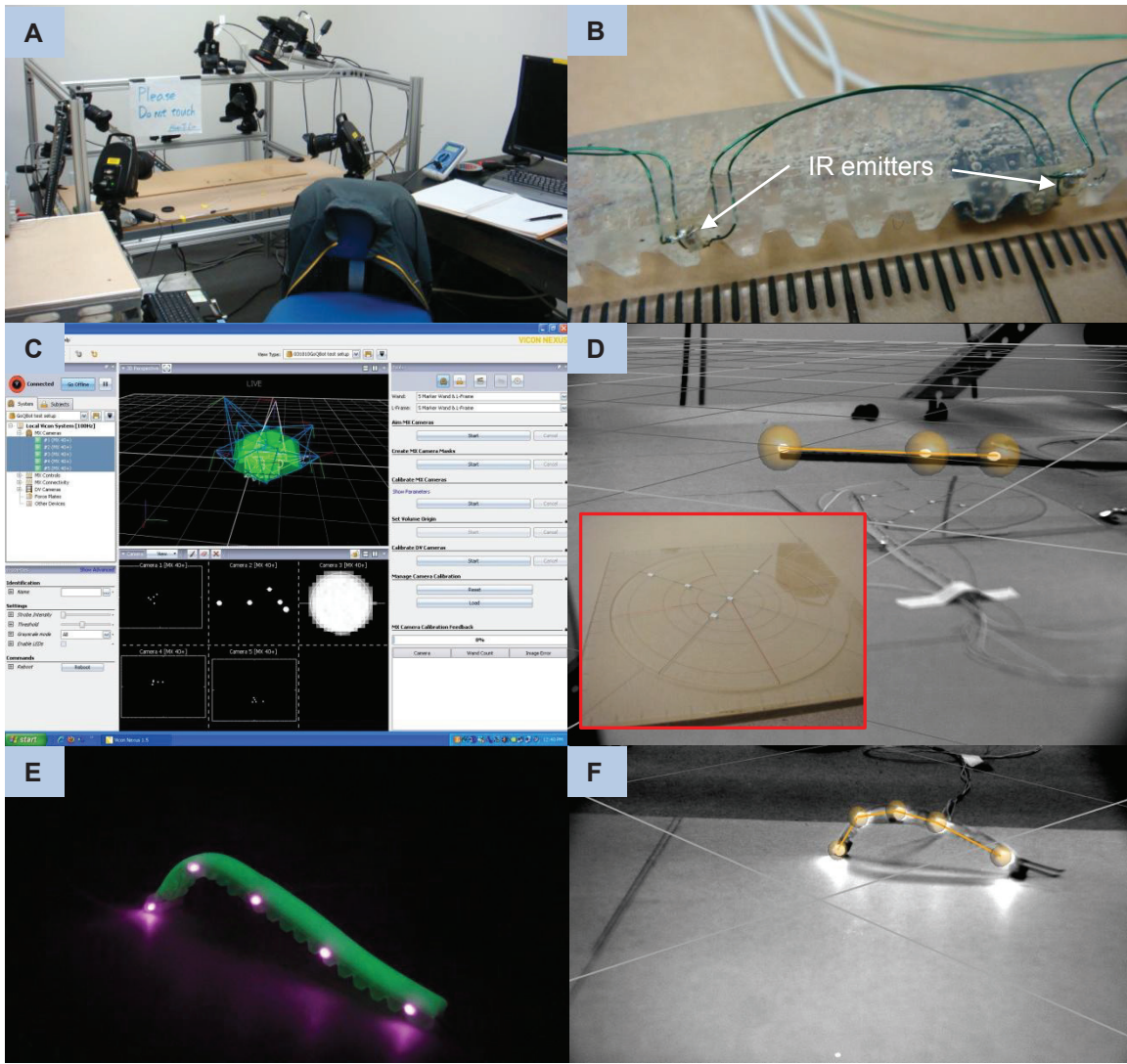


Fig.2-15 The customized VICON motion tracking system for soft robot kinematics analysis. (A) The VICON system consists of 5 infrared tracking cameras. Video cameras can be deployed simultaneously for visualization purposes. (B) Small IR emitters can serve as active markers in place of the retro-reflective beads. (C) The bright IR emitters appear as distant stars to the camera. Lens focusing becomes less critical. (D) A custom calibration wand and a static calibration plate help achieve sub-millimeter calibration accuracy. (E) The glory of GoQBot-V can only be captured in such a system. The robot performs a caterpillar-inspired ballistic rolling behavior and attains over 0.5m/s within 200ms. (F) A simple free joint model can serve as a tool for kinematics tracking.

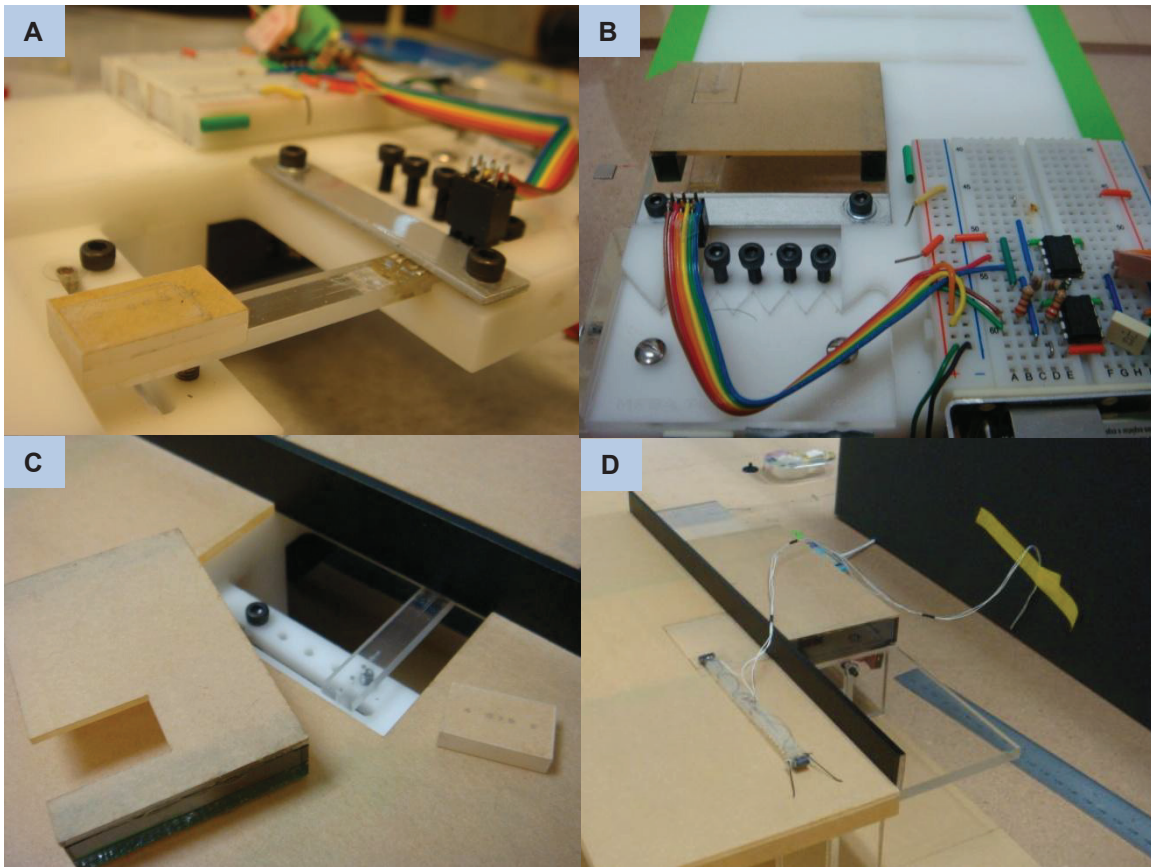


Fig.2-16 The force plate design. (A) To capture the GoQBot rolling dynamics, a force plate was instrumented around the previously characterized scaled simple beam as mounted on the calibration apparatus. (B) The calibration apparatus has all the necessary electronics to operate the force beam. (C)(D) A custom platform was fitted to make the force beam system compatible with the VICON tracking setup.

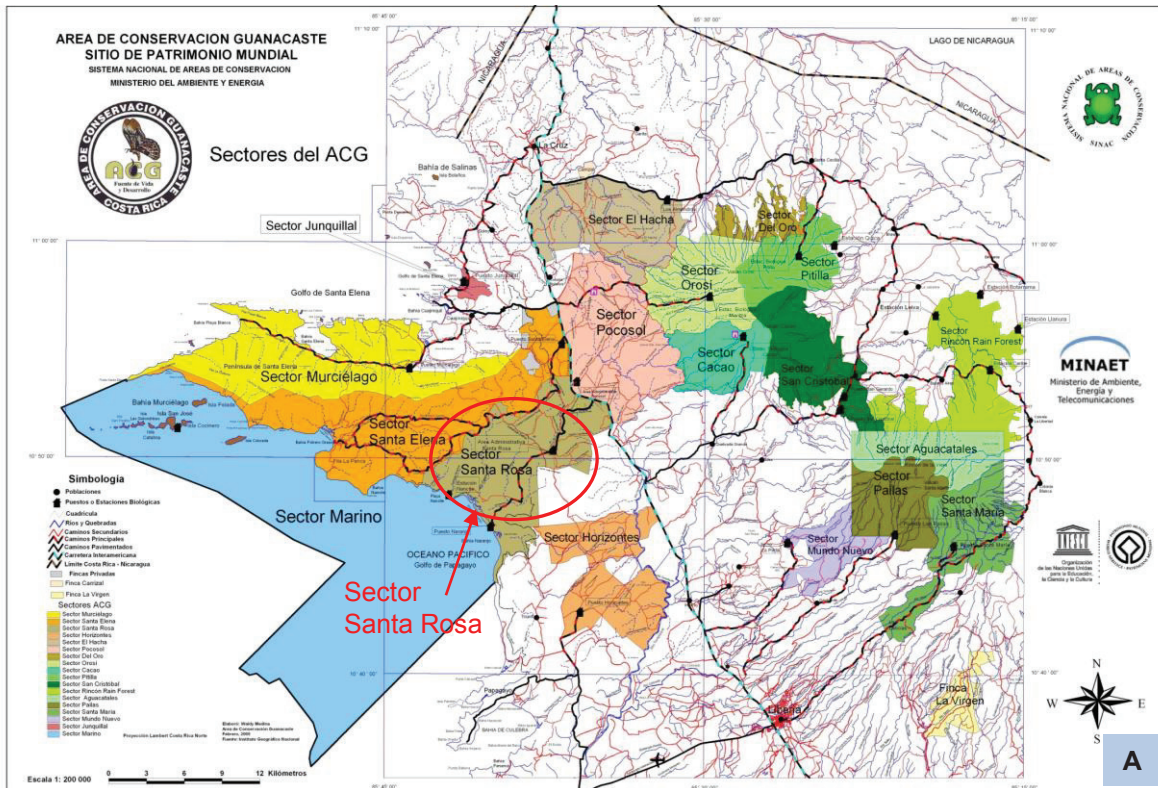


Fig.2-17 Costa Rica field work: *Area de Conservacion Guanacaste*. **(A)** The area map of the conservation shows 18 sectors. My field work was mostly done in the sector Santa Rosa. **(B)** The abundant rainfall during the raining season transforms the dry forest into a paradise for caterpillars.



Fig.2-18 Costa Rica field work: research activities. (A) High speed, high definition videography was the primary tool for characterizing caterpillar gaits. (B) Wild caterpillars were collected and temporarily kept in a semi-outdoor environment for observations. (C) Great effort was made to document the caterpillar locomotor patterns from all the caterpillars collected. (D) A filming arena was set up to facilitate the behavioral observations.

Chapter 3: Force transmission in caterpillar locomotion

Because caterpillars move relatively slowly and are subject to very large deformations external forces produced during locomotion cannot be derived from the kinematics. Furthermore, caterpillars usually have multiple contacts to the substrate making it difficult to estimate internally-acting forces. However, by making detailed measurements of substrate reaction forces at multiple contact points it is possible to derive the likely inter-segmental interactions and to monitor body tension. Here I will give an overview of some key aspects of this analysis.

3.1 Antagonist substrate reaction forces

A universal challenge for animals is to produce body or limb extension using contractile actuators (muscles). In systems with an articulated stiff skeleton, limb extension can be achieved by levering around the joint to straighten the appendage. During this process the skeleton resists compressive forces produced by the muscles and translates forces into a useful torque. To retract the same limb another muscle can pull on the opposite side of the joint to restore the flexed position. Although they use a different mechanical system, worms also employ antagonistic sets of muscles to extend and retract body parts. Because they lack a rigid body frame, worms rely on incompressible fluids and tissues to establish a hydrostatic skeleton. This fluid skeleton then resists the compressive forces from the muscles. Circumferential muscles constrict the body wall and cause extension because the body volume remains constant. The original body length (and shape) can be restored by relaxing these circumferential muscles and contracting longitudinal muscles. Curiously caterpillars do not have circumferential muscles suggesting that they do not rely on a simple antagonistic hydrostatic skeleton. How do caterpillars re-extend their bodies after each body contraction?

I propose that a soft-bodied animal can use the substrate as an external skeleton. Using this “environmental skeleton” strategy, a caterpillar can stretch its body by loading the body against the substrate. This mechanism is supported by measurements of the ground reaction forces exerted on prolegs during horizontal crawling (Publication-1). As soon as the terminal prolegs are planted on the substrate, the *Manduca* caterpillar stretches its body against these posterior prolegs across the unattached body segments. The contraction wave we observe is essentially a wave of body stretching propagating forward. Please refer to the discussion in Publication-1 for more details. In short, the caterpillar works its anterior muscles against the posterior muscles. The substrate will resist the compressive forces generated by the muscles just as a skeleton would.

3.2 The effect of substrate stiffness

If a normal crawling gait requires that the substrate resists muscles forces, then changes in substrate stiffness will affect locomotion performance. To confirm this, a behavioral experiment was carried out in which a *Manduca* caterpillar was suspended from its tail horn and head capsule (two relatively stiff components in the body). Different substrates could be placed under the caterpillar’s legs to test the substrate’s role in resisting compression and flexion (Publication-2.). Interestingly, *Manduca* caterpillars are capable of crawling on flexible substrates, but consistently fail to crawl normally on substrates that do not resist compression. Although caterpillars can stiffen their body through tonic muscle contraction (e.g., when cantilevering across gaps) they do not appear to use hydrostatic compensation when crawling on soft substrates. Extended discussions are provided in Publication-2.

3.3 Other effects of the substrate

What happens if a crawling caterpillar accidentally misses a step or loses grip? Typically caterpillars ignore occasional missing steps and perform the same motor pattern without compensation. Although

this could result in a few awkward crawl cycles the flexible body can accommodate small changes in body shape. As long as the animal does not fall these mechanical disruptions do not result in significant penalties. In fact, when the entire set of thoracic legs are bonded together *Manduca* caterpillars are still able to move on a flat surface. However, they move more slowly and are hesitant on a branch-like structure. When gripping is prevented altogether by placing *Manduca* caterpillars on a slippery flat surface they usually attempt to crawl using the same gait (Fig.3-1). Unable to grip the substrate, they have trouble moving forward and often tip sideways. Their movements resemble those produced on soft substrates. Sometime caterpillars refuse to crawl under these conditions. We exploit this behavior to guide the caterpillar onto the force beam array for ground reaction forces measurement. By presenting a designed track as the only graspable substrate within reach the caterpillars follow the designated path.

Several other observations are notable in the context of animal-substrate interactions. For example, if a branch supporting a crawling caterpillar is broken, the animal buckles at the flexion point (Fig.3-2A). One can bend the broken branch at this flexion point to any angle without resistance from the animal. A closer look reveals incredible body deformation. During 180 degree flexion the body folds almost in half and flattens at the flexion point to less than the normal body radius (Fig.3-2B). Eventually, the animal attempts to reorient with extreme body contortion. All these maneuvers have to rely on the substrate and very little on the hydrostatic skeleton. In fact, a proper hydrostatic skeleton would not allow free buckling and contortion in this manner.

Another simple experiment can be carried out to manipulate the body tension of a crawling caterpillar. If *Manduca* is allowed to crawl on an elastic material, the length (and tension) of the substrate can be altered at will (Fig.3-3A). When the substrate is stretched *Manduca* also elongates proportionally. A typical behavioral response is to initiate crawling. After the animal recovers its typical length, the substrate can be released to its relaxed length causing *Manduca* to compress proportionally (Fig.3-3B).

This transition typically elicits proleg repositioning and the initiation of another crawl cycle (Fig.3-3C). Caterpillars are indeed constantly sensing the body tension and it may even be an important trigger for locomotion



Fig.3-1 The *Manduca* caterpillar on a slippery substrate does not produced normal body deformation due to the lack of grips.

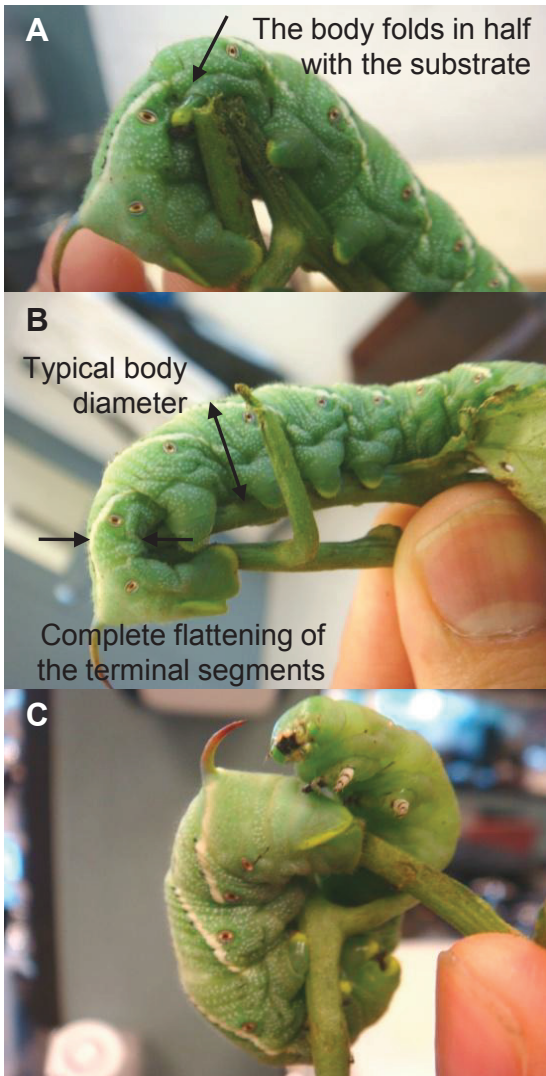


Fig.3-2 (A)(B) The caterpillar body can easily fold in half on a snapped branch with a relatively relaxed hydrostatic skeleton. **(C)** Extreme body maneuver can be performed when the hydrostatic skeleton is activated.

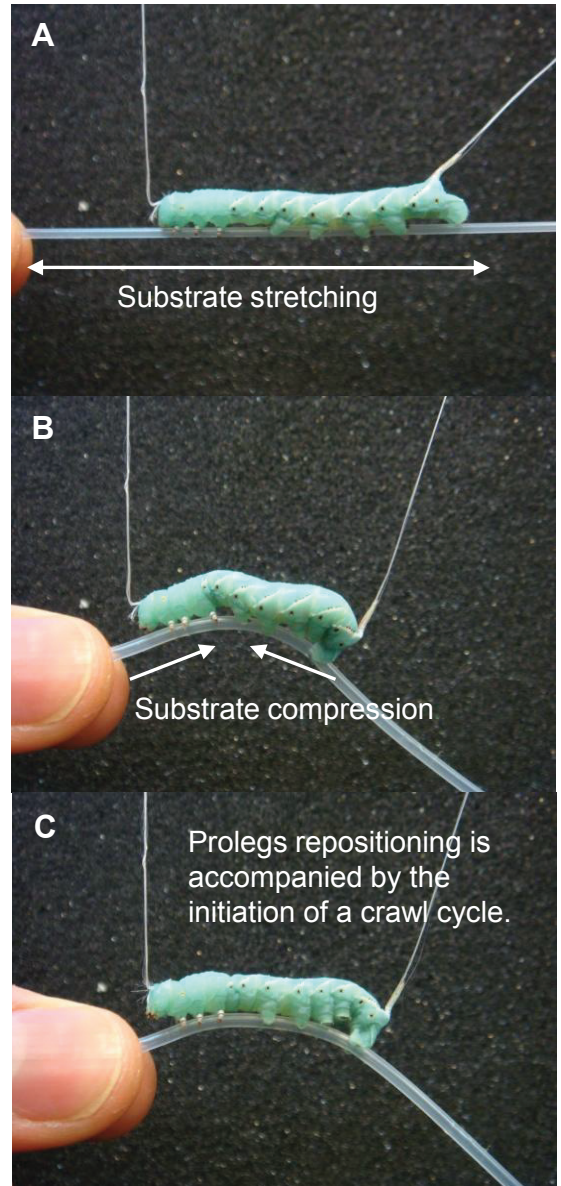


Fig.3-3 (A) Stretching the substrate can proportionally alter the body tension in a caterpillar. **(B)** Releasing the substrate tension compresses the caterpillar body proportionally. **(C)** Both manipulations trigger a proleg repositioning response accompanied by a crawl cycle.

Publication-1

Title: The substrate as a skeleton: ground reaction forces from a soft-bodied legged animal

Authors: Huai-Ti Lin and Barry Trimmer

Keywords: GRFs; legged locomotion; soft-bodied animal; *Manduca sexta*; caterpillar;

Summary

The measurement of forces generated during locomotion is essential for the development of accurate mechanical models of animal movements. However, animals that lack a stiff skeleton tend to dissipate locomotor forces in large tissue deformation and most have complex or poorly defined substrate contacts. Under these conditions, measuring propulsive and supportive forces is very difficult. One group that is an exception to this problem is lepidopteran larvae which, despite lacking a rigid skeleton, have well-developed limbs (the prolegs) that can be used for climbing in complex branched structures and on a variety of surfaces. Caterpillars therefore are excellent for examining the relationship between soft body deformation and substrate reaction forces during locomotion. In this study, we devised a method to measure the ground reaction forces (GRFs) at multiple contact points during crawling by the tobacco hornworm (*Manduca sexta*). Most abdominal prolegs bear similar body weight during their stance phase. Interestingly, forward reaction forces did not come from pushing off the substrate. Instead, most positive reaction forces came from anterior abdominal prolegs loaded in tension while posterior legs produced drag in most instances. The counteracting GRFs effectively stretch the animal axially during the second stage of a crawl cycle. These findings help to understand how a terrestrial soft-bodied animal can interact with its substrate to control deformation without hydraulic actuation. The results also provide insights into the behavioral and mechanistic constraints leading to the evolution of diverse proleg arrangements in different species of caterpillar.

Introduction

Locomotion by soft-bodied animals.

Articulated (stiff, jointed) and hydrostatic (soft wall, pressurized) skeletons (Chapman, 1958) are the two primary structural models used to characterize and explain the biomechanics of animal locomotion. In an articulated system, movements can be described precisely by the center of mass position and joint angles (Colobert et al., 2006; Holmes et al., 2006). Muscles work antagonistically around a joint to produce directionally constrained motions and structural levers allow the mechanical exchange of force and displacement.

A similar process occurs in many soft-bodied animals that exploit incompressible body-fluid to transmit forces and to actuate body parts (Kier, 1992; Niebur and Erdos, 1991; Quillin, 1998; Skierczynski et al., 1996; Wadepuhl and Beyn, 1989). For example, most annelids use circumferential muscles that operate antagonistically with longitudinal muscles to control extension and shortening (Kristan et al., 2005; Quillin, 1999). These animals produce different postures using a temporary stiff hydrostatic skeleton. Even animals such as the octopus, which does not have an open fluid-filled cavity, use the viscous, semi-fluid mechanical properties of connective tissues and muscles to transmit forces and control posture and movements (muscular hydrostats) (Kier and Stella, 2007).

Most current models of hydrostatic skeletons make the general assumption of volume conservation and use geometric approaches to predict movements (Skierczynski et al., 1996; Smolianinov and Mazurov, 1976; Wadepuhl and Beyn, 1989), sometimes employing tissue material properties in the simulations (Chiel et al., 1992; Herrel et al., 2002; Kier and Smith, 1985; Nishikawa et al., 1999). Although these modeling approaches can be used to estimate mechanical interactions the direct measurement of locomotor forces by soft-bodied animals remain scarce and highly constrained by

technical limitations (Keudel and Schrader, 1999; McKenzie and Dexter, 1988a; McKenzie and Dexter, 1988b; Quillin, 2000).

Caterpillars as a model system.

One group of animals that make an attractive model system for measuring such forces is the larval stage of the Lepidoptera (*i.e.*, caterpillars) because most interact with the environment via discrete contacts (prolegs). By measuring the substrate reaction forces of each proleg simultaneously, it should be possible to determine how body deformation translates into locomotor dynamics. Caterpillars are also interesting from biomechanical and neurobiological perspectives because they are pressurized soft cylinders capable of climbing in complex 3-dimensional environments. This is accomplished with only longitudinal muscles and a few short oblique muscles, making it puzzling how they manage to coordinate shortening and extension using a non-septate fluid and tissue-filled body cavity.

Caterpillars usually employ the abdominal prolegs for attachment to the substrate and produce anteriograde waves of movement, but there is considerable species diversity in the arrangement of these appendages and in their use during locomotion (Miller et al., 2006; Snodgrass, 1993). Four pairs of abdominal prolegs (on abdominal segments 3 through 6; A3~A6) and a pair of terminal (anal) prolegs (on abdominal segment 10; TP) are thought to be the ancestral/dominant form for lepidopteron (as labeled in Fig. 2) (Forbes, 1910; Hinton, 1955) but prolegs in different species can be lost from any segment (Wagner, 2005). For example, most caterpillars in the family *Notodontidae* have modified terminal prolegs for purposes other than locomotion and in the family *Noctuidae* both anterior and posterior prolegs are reduced. The subfamily *Hypeninae* have lost functional A3 prolegs while the terminal prolegs are elongated, and members of the subfamily *Catocalinae* have even lost the A4 prolegs. Species such as *Parallelia bistriaris* (maple looper) and *Caenurgina crassiuscula* (clover looper) do not have prolegs on segments A3 or A4 and they move with looping gaits. Members of the subfamily

Plusiinae (cabbage looper, soybean looper, celery looper) move by “inching” with prolegs on A5, A6, and the terminal segments. Of course, the inchworms (*Geometridae*) all perform inching locomotion with only the A6 and terminal prolegs. Some lepidopteran larvae do not need prolegs for locomotion and have reduced them into a continuous ventrum (slug caterpillars) (Epstein, 1996; Rubinoff and Haines, 2005) or transformed posterior legs into a hydraulic warning display (family *Notodontidae*). Case-bearer caterpillars only employ the six thoracic legs for locomotion. On top of this diversity, there is a large range of body size and cuticular adornments across lepidopteran species (Miller et al., 2006).

Manduca locomotion and mechanics.

The tobacco hornworm (*Manduca sexta*) is a well-studied model system in neurobiology, physiology, and ecology. Because their muscle anatomy is known so well, (Barth, 1937; Eaton, 1988; Kopec, 1919; Libby, 1959; Snodgrass, 1961; Snodgrass, 1993) and each muscle is generally innervated by a single motoneuron (Levine and Truman, 1985; Taylor and Truman, 1974; Weeks and Truman, 1984) these caterpillars show great promise for electromyographic studies of soft-bodied locomotion (Belanger and Trimmer, 2000; Dominick and Truman, 1986; Johnston and Levine, 1996a; Johnston and Levine, 1996b; Mezoff et al., 2004; Simon and Trimmer, 2009). *Manduca* is a relatively large insect (which helps force measurements) using 4 pairs of abdominal prolegs and a pair of terminal prolegs to generate most of its motion. A crawl typically consists of anteriograde waves of body muscle contractions with the prolegs releasing their grip (Belanger et al., 2000; Mezoff et al., 2004) to be carried forward for re-attachment. Several segments are in swing phase simultaneously and the wave of motion usually continues into the thorax and head as the next cycle begins from the terminal prolegs (Trimmer and Issberner, 2007). *Manduca* caterpillars weighing 2 g move at an average speed of 3.10 ± 0.24 mm/s during horizontal locomotion with low acceleration and hence very small center of mass dynamics (van Griethuijsen and Trimmer, 2009).

In preliminary experiments it was found that *Manduca* are able to crawl horizontally even when the thoracic legs are removed. Apart from the unsupported thorax sliding across the substrate and slower movements, these crawls appeared normal with appropriately sequenced steps in the abdomen. Another interesting finding is that the hemocoel pressure of restrained (Mezoff et al., 2004), and crawling *Manduca* (unpublished data) is not isobarometric nor do the fluid pressure changes correlate well with movements. This is supported by phase-contrast synchrotron X-ray videography showing that internal tissues such as the gut, hemolymph and trachea are in constant motion (Simon et al, in preparation), presumably generating, and responding to, pressure gradients. During crawling the gut movements in particular are quite large; this means we should be very careful interpreting static loads from inertial forces. In addition, the internal air cavity constitutes 3 ~ 10 % of body volume and air can be expelled during underwater locomotion suggesting that the internal volume is not necessarily constant (unpublished preliminary data).

These prior observations suggest that caterpillar locomotion is biomechanically distinct from the current models of soft-bodied terrestrial crawling. In this study, the central questions we would like to address are: 1) During crawling, how does a caterpillar extend its body without circumferential muscles? 2) Within a crawl cycle, how much weight shift occurs, and what are the roles of different prolegs? 3) Given that the body is not necessarily incompressible, how does *Manduca* transmit forces for posture support and propulsion?

A major finding is that caterpillars use the substrate to transmit forces from each contact point to other parts of the body. Instead of contact points propelling the center of mass forward, we propose that soft animals can employ an “*environmental skeleton*”. In this view, posture generated by stiff hydrostatic control has a smaller secondary role in locomotion.

Materials and methods

The measurement challenge

Reaction forces are usually measured with a force plate larger than the animal's total contact area (Goldman et al., 2006; Heglund, 1981; Zumwalt et al., 2006) but *Manduca* moves so slowly that it exerts very weak inertial forces (forces associated with acceleration). In other words, the overall acceleration of the caterpillar does not adequately reflect the size or direction of local ground reaction forces, some of which cancel out when measured collectively. Furthermore, because caterpillars' bodies deform massively between contacts it is not desirable to measure forces on one leg at a time as can be done for animals with stiffer skeletons (Blickhan et al., 2007; Dutto et al., 2004; Roberts and Belliveau, 2005). Instead, reaction forces from each proleg should be measured independently and simultaneously. Recent breakthrough in developing micro force sensor units has made insect locomotor dynamics much more accessible (Bartsch et al., 2007; Lemmerhirt et al., 2006; Reinhardt et al., 2009). However, these microelectromechanical fabricated or precision-machined sensors are very expensive and require specialized maintenance. For our application, we constructed a robust, low cost, sensory array to resolve forces from each contact point simultaneously. Our observations of *Manduca* with amputated thoracic legs suggested that the prolegs are sufficient for crawling. Therefore, the number and spacing of sensors was arranged to optimally capture data from the prolegs. Reaction forces from the thoracic legs can occasionally be resolved with this array (usually a single combined thoracic force, rarely as separate segments) and they are reported where available. The sensor array was paved over most of the caterpillar length so that the center of mass and weight redistribution could be tracked during locomotion.

The Manduca Force Beam Array

The device consisted of an array of cantilevered strain-gage based force beams each with four sensors arranged to detect both normal forces (*i.e.*, perpendicular to the crawl, aligned with gravity in horizontal crawling, nGRF) and axial forces (*i.e.*, fore-aft forces along the axis of a crawl, fGRF) (Fig. 1A). The beams were arranged with a pitch of 3.81 mm per sensor which is less than half the caterpillar average stride length (8.52 ± 0.22 mm) (van Griethuijsen and Trimmer, 2009). Preliminary data showed that each pair of prolegs takes up to 1/3 of the body weight (<7 mN for a 2 g fifth instar) and 3 times the body weight in the fore-aft direction (<60 mN). A custom built control system provided AC excitation, analog amplification and basic signal processing. A Basler 206A high speed camera (Basler, Ahrensburg, Germany) was used for real-time 2-D kinematics tracking and a Sony SSC S20 color camera (SONY, Tokyo, Japan) for detailed behavioral observation. Data collection was controlled by a custom program running in LabView 8.5 (National Instrument, Austin, TX, USA) (Fig. 1B). The program took images from the kinematics camera and identified markers on the animal, transformed the coordinates according to the location of the substrate and marked the touchdown of prolegs in a force data spreadsheet. The GRF data were displayed in real-time to help monitor experimental progress. The program saved 5 data files for every experiment. This included a reference recording for noise and offset analysis, the raw force data, kinematics raw data, processed force data with kinematics markings, and the synchronized behavioral video. Because this device is unique and suitable for use with a variety of species it will be described in more technical detail in a separate publication.

Animal subjects

Healthy second day 5th instar *Manduca sexta* caterpillars between 1.5~3 g were collected from our colony, corresponding to body length between 26.5 mm and 45.3 mm (based on a body dimension statistics for our colony, n=25). All animals were reared on an artificial diet and kept in a 17h:7h L:D

cycle at 27°C. The colony maintenance and rearing protocol can be referred to Bell *et al* (Bell and Joachim, 1976). Animal subjects were weighed, sexed, and labeled before being placed in a large transparent container (conditioning chamber) for 20 minutes of free roaming. Eight animals were used in this study.

GRF recording procedure

During the development of the sensor device data was collected from two sets of beam arrays. A 1D array consisting of twelve unidirectional force beams was used to collect weight shift information (Range = 45.72 mm, or ~100% resting length of a 5th instar *Manduca*). A second array consisting of five 2DoF force beams (Range = 19.05 mm, or ~40% resting length) was used for force correlation analysis. Prolegs were tracked using a bead (0.50 ± 0.05 mm diameter) coated with clear red UV fluorescent paint (Risk Reactor, Dallas, OR, USA) placed on each proleg on one side of the animal (Fig. 1B). The wet paint allowed the red fluorescent beads to adhere to the cuticle. A Black-Ray BL-15 UV lamp (UVP Inc., San Gabriel, CA, USA) was installed above the 2D array to excite the red fluorescent paint.

To encourage crawling, animals were lined up on a linear elevated wooden substrate (standby track) leading to the force beam array. Caterpillars were found to move forward when naturally probed by another conspecific. On the 1D beam array, data logging was started when the animal entered the buffer zone and stopped when either the animal stopped crawling or had covered the entire force beam array. For the shorter 2D array data logging did not begin until the thoracic legs triggered one of the active beams. After each trial, the animal was put back into the conditioning chamber for at least 3 minutes before it was returned to the standby track for another trial. All the data presented in this paper were from *Manduca* crawling horizontally in a straight-line, thus the normal GRFs (nGRFs) represent the body weight loading. A successful recording was one in which the caterpillar travelled *continuously* over the entire sensing zone. Since *Manduca* caterpillars tend to pause unpredictably, most animals

produced only one successful trial during the experimental session. To be consistent, we analyzed only one successful trial from each of the 8 experimental animals, resulting in 5 sets of nGRF data and 3 sets of 2D (nGRF and fGRF) data.

Data processing

Because the caterpillars moved slowly, force data were sampled at 100 Hz, kinematics image analysis at 10 Hz, and behavioral videos at 30 fps. In preliminary experiments (nGRF recorded at 1 kHz) it was found that stepping forces changed over about 0.5 s and that most high frequency signals were due to electromagnetic noise. Occasional drift due to thermal fluctuation was too slow to interfere with the force recordings. The raw data was filtered using a RC type low-pass filter at 2 Hz and then smoothed with a 2nd order polynomial over every 0.1 s. These curves were compared with the raw data to check consistency for every recording. Signal offsets were controlled under 6mV and subtracted out using the reference recording. Raw voltages were converted to forces using calibration curves made for each beam.

The resulting GRF data were normalized to the individual caterpillar bodyweight (BW). The normalized data were then checked with the behavioral videos for single steps that occasionally occurred across two adjacent force beams and these readings were summed. Crawls with several such overlapping steps were rated as unsuccessful and removed from the analysis.

Force attribution

Video tracking provided the first indication of proleg touchdown timing and location. Individual proleg GRFs were then extracted by identifying the points at which stance occurred and by using threshold detection (normal load crosses 1% animal's bodyweight). The 2D array captured at least one step per proleg in each trial. We therefore compiled at least one complete crawl cycle for each experimental animal for qualitative comparison. Although contact by a single pair of thoracic legs on the 2D force

beam was rare, some occurrences were identified from the videos. Examples of these 2D GRFs have been included for comparison with the prolegs GRFs.

Manduca Standard Kinematics Template

Using the extensive kinematics data collected from our research group (von Griethuijsen and Trimmer, 2009; Trimmer and Issberner, 2007), the 2D GRF data was scaled to the *Manduca* standard kinematics template representing the average step length and relative timing of proleg movements during a full crawl cycle (Fig. 2). The timing of the thoracic leg contacts are also noted on this template. A crawl cycle was defined as from the beginning of terminal prolegs swing phase to the beginning of A3 stance phase. We took the average stance phase time over a complete crawl time as the duty cycle of that particular proleg. By scaling all the corresponding GRF data to this template, we could analyze force interactions between different prolegs for different crawl cycles and animals. To match up thoracic legs in a crawl cycle, we analyzed the videos frame by frame to place the sample thoracic legs GRFs data into the appropriated time points of a crawl cycle (as indicated in Fig. 2).

Weight shift analysis

Manduca caterpillars do not change length more than 5% during normal locomotion so we could evaluate the overall weight shift by summing nGRFs from all contacts (including those from thoracic legs). This procedure produced an oscillating trace with each oscillation corresponding to one crawl cycle. Because inertial forces were so small these oscillations directly reflected the weight placements of the caterpillar. By measuring the loading change over each cycle, we could estimate how much mass was shifted forward and backward in one average step length (8.52 mm) per cycle period. Instead of tracking the center of mass, we assumed that only part of the body was accelerated forward in each crawl and that mechanical work associated with this weight shift could be evaluated.

Results

Prolegs normal loading

During a crawl a sequence of ground reaction forces was detected on each of the sensor beams. Frame-by frame analysis of the synchronized video allowed these forces to be attributed to different segmental appendages (Fig. 3A). Although the features of these forces varied in magnitude and duration each crawl, there were consistent differences in the nGRF profiles of each segment (Fig. 3B).

For the mid body segments (A4-A6) the ground impact and leg detachment were visible as two peaks in the nGRF data which overshoot the weight-bearing portion of the proleg stance phase. Behavioral observations suggested that these two peaks correspond to crochet protraction and retraction; both attachment and detachment involved momentary extension of the prolegs before the crochets grip or release. This may explain why there was no negative normal load in the recording of horizontal crawling. The initial loading and unloading rates were similar for each proleg in segments A3-A6 but differed for the terminal prolegs (TPs). After a more gradual loading phase, the TPs immediately started to unload as the animal shifted its weight forward. The vertical reaction forces due to crochets were less pronounced for the TPs, but the weight supporting section appeared highly variable just like the A3.

Weight shift

Overall weight shift can be observed from the net nGRF across all force beam channels. As the animal entered the sensor zone, forward and backward weight shifts appeared as nGRF fluctuation in each crawl cycle (Fig. 4A). When the animal was completely supported in the sensor zone the net nGRF was stable and equivalent to the weight of the animal (*e.g.*, for Fig. 4 the average nGRF = 16.94 mN, animal weight = 1.72 ± 0.01 g or 16.9 mN). The 1D array was accurate within 10 μ N for most recordings.

While complete tracking of the center of mass throughout a crawl required a force beam array longer than the current device (one body length plus two additional steps), it was possible to perform a preliminary assessment of the overall weight shift during each step. The peak-to-peak net nGRF changes were measured for about 10 steps in each of five animals, standardized to the crawl cycle and body weight, and combined to show the overall weight shift in a crawl (Fig. 4B). During the first 64.5% of a step, *Manduca* shifted 30% of its body weight forward and then sharply arrested the transfer. Then it moved 15% of body weight back again in the last 35.5% of the step.

A brief note on thoracic legs

Although the sensor array was optimized for proleg reaction forces it was occasionally possible to detect GRFs from the thoracic legs collectively (Fig. 3) or segmentally (Fig. 5). From this sparse data it was observed that: 1) In all the thoracic GRF fragments, fGRF is almost always positive. 2) The nGRF results suggest that each thoracic leg supports as much body weight as each proleg. 3) Force profiles for each thoracic leg overlap for much of the crawl cycle. Although the stiff articulated thoracic legs could withstand compressive forces they show no indication of decelerating fGRFs (Fig. 5A) which suggests that the posterior segments do not push the thorax while it is in stance. The timing of the thoracic maximum pull also coincides with periods of proleg “drag” and this is presumably responsible for body stretching (at least from T1~A3) during locomotion. There is some redundancy in the mechanism of body extension since abdomen extension (A3~A10) can be achieved using proleg interactions alone although it may be less effective. Further examination of this unexpected role for the thoracic legs will require modification to the sensor array

Prolegs fore-aft loading

The reaction forces in the direction of locomotion (fGRF) are similar in magnitude as the normal loads despite the lack of body dynamics (Fig. 5A). There are typically two negative impulses (decelerating forces) one at the start of stance and the other before the onset of swing, associated with proleg attachment and detachment. Terminal prolegs initiate each cycle with a decelerating impact and then rock briefly into a neutral state at about 20% of the stance phase. They then drag (negative fGRF) for most of the stance phase. A6 prolegs also decelerate during the terminal prolegs dragging phase, but they pivot into a positive pull as the terminal prolegs release from the substrate. Successive prolegs in segments A5-A3 share this force profile but the magnitude of the mid-stance fGRF is progressively less negative in more anterior segments and is generally positive (*i.e.*, a pulling force) in segments A4 & A3.

For analytical purposes, we divided a complete crawl into two stages and six phases (Fig. 5B):

Stage (1) --- Abdominal contraction

Phase A [TP takeoff ~ A6 takeoff]

In the beginning of a crawl cycle, anterior prolegs are detached and pulled forward. At the same time, the thoracic legs starts to walk the thorax forward, stretching the frontal abdomen in the process (preliminary GRF data for thoracic legs). This initiates the overall mass shift.

Phase B [A6 takeoff ~ A5 takeoff]

The release of A6 immediately leads to more drag on the A5, indicating that the body tension anterior to A5 is initially higher than that between A6 and A5. This is also when the caterpillar reaches the shortest body length.

Phase C [A5 takeoff ~ A4 takeoff]

With the detachment of A5, the nGRF in A4 declines and that in A3 increases. This demonstrates that *Manduca* can lift its abdomen with only the A3 proleg and thoracic legs attached. Thoracic legs begin a new crawl cycle during this phase.

Stage (2) --- Abdominal stretching

Phase D [TP touchdown ~ A3 takeoff]

A4 detachment releases the muscle strain energy between A3 and A4, but this contraction is soon anchored by the TP. This initiates the stretching stage where anterior muscles stretch the posterior muscles between two bridging anchors.

Phase E [A6 touchdown ~ A5 touchdown]

A6 attaches to the substrate to hold the stretch and propagates this antagonist stretching forward. By now the caterpillar has returned to the original length, using the thoracic legs to maintain it.

Body mass starts to rebound backward, probably through movements of internal organs and fluid.

Phase F [A5 touchdown ~ A3 touchdown]

The last phase of a crawl involves stretching the anterior abdomen back to its resting length using the thorax. Most abdominal muscles must do negative work in the process.

Discussion

Prolegs = attachments

From detailed observations (Snodgrass, 1961) and kinematic analyses (Belanger and Trimmer, 2000; Mezoff et al., 2004; Trimmer and Issberner, 2007; van Griethuijsen and Trimmer, 2009) it has been proposed that caterpillars such as *Manduca* do not use the prolegs as actuated propulsive limbs, but instead use them as support and to generate controllable grip. For the first time it has now been possible to measure the GRFs during *Manduca* crawling and to show that the prolegs are indeed anchors rather

than levers and that they are responsible for transmitting intersegmental forces. An analysis of the GRF profiles and segmental timing reveals several new and unexpected details.

Stiff legs push, soft legs pull

Most vertebrates exploit their stiff skeleton and joints to transfer muscle forces directly into limb displacements. They can apply large compressive forces to the skeleton and typically use their hind legs to push off and the front legs to decelerate (Biewener, 2003). In contrast, the prolegs are pouches of soft cuticle on the abdomen with no discrete articulation or structures for gaining a lever advantage. Moreover, because stress (and indirectly, stiffness) in the body wall is largely a function of hydrostatic pressure and curvature (Mezoff et al., 2004; Wainwright, 1988), it is impossible for the small radius prolegs to be stiffer than the body itself without additional chitin cross-linking or other structural changes. This means that prolegs are relatively soft and unsuitable for resisting large compressive loads. This is borne out by the fGRF results in which caterpillars mostly load their prolegs in tension and only momentarily experience compressive fGRF when TP and A6 “rock” the body mass over them. Caterpillars use the anterior prolegs to pull and the posterior prolegs to drag, effectively reversing the roles seen in most legged animals (Fanchon et al., 2006; Schmidt, 2005). Although the nGRFs during horizontal crawling are positive and therefore compress the prolegs (weight-bearing), these forces are only small fractions of body weight and can be easily supported by baseline body pressure.

The role of a stiff substrate

It is clear from the fGRFs that the substrate takes the compressive load during multi-legged stance phases. This was verified using a simple behavioral test. *Manduca* was suspended from the head capsule and the dorsal horn and curved substrates of different stiffness but similar curvature (caterpillars prefer rode-like substrates) were placed between the prolegs as the caterpillar tried to crawl. As expected,

relatively stiff substrates such as balsa wood were translocated backwards by the antero-grade segment movements. However, as the substrate became softer these movements were less effective. When presented with a soft wire or a silk braid that could only take tensile loads, *Manduca* was unable to extend and its locomotory movements failed to move the wire progressively (Fig. 6). The substrate is therefore an essential component of this mechanical system and *Manduca* is incapable of normal locomotion on surfaces that are softer and more compliant than its own body. Presumably, body stiffness is tunable within a narrow range through changes in muscle tone and internal pressure. This aspect of caterpillar locomotion could play an interesting ecological role since plant stiffness will affect the mobility of different caterpillar species. Unfortunately, we are not aware of any data correlating host plant foliage flexural stiffness to the mechanics of caterpillars feeding on them. We are therefore developing a numerical model of caterpillar mechanics based on tissue material properties (Lin et al., 2009), morphology and pressure. We intend to check this model against some ecological and morphological data in the near future.

Statics? Dynamics?

The weight shift estimation (Fig. 4) allows us to calculate the real locomotor acceleration and its associated forces for a fifth instar *Manduca* crawling with a single step length of 8.52 mm. According to the weight shift estimate, a 2.50 g caterpillar would move 0.3 of body weight (BW) in 0.654 of a crawl cycle. We can calculate the time for this forward weight shift from the average crawl period 2.778 s ($t = 2.778 \text{ s} \times 0.654 = 1.817 \text{ s}$). Assuming constant acceleration and that the mass moves with negligible friction, we can write:

$$|\mathbf{a}| = \frac{d}{t^2} = \frac{8.52(\text{mm})}{1.817^2(\text{s}^2)} = 2.58 \left(\frac{\text{mm}}{\text{s}^2} \right) \quad [1]$$

where \mathbf{a} is acceleration, d is step length, t is time; and

$$|\mathbf{F}| = m|\mathbf{a}| = 2.5(\text{g}) \times 0.3(\text{BW}) \times 2.58\left(\frac{\text{mm}}{\text{s}^2}\right) = 1.94(\mu\text{N}) \quad [2]$$

where \mathbf{F} is the accelerating force, and m is the body mass. This is a very small force (the single leg vertical force from a running *Blaberus* cockroach of similar weight peaks at 17 mN and the horizontal force is 5 mN (Full et al., 1995). With more funding and instrumentation, it is possible to expand the 2D force beam array to cover all the *Manduca* contact points simultaneously and directly demonstrate that the sum of the fGRFs is effectively zero.

Based on this force estimate, we can calculate the minimum energy expense associated with weight shift. Since the caterpillar prolegs have no leverage, we assume the breaking impulse provided by soft-tissues and the backward weight shift to be elastic rebound. The energy expenditure is therefore only in the forward mass acceleration:

$$E = |\mathbf{F}| \times d = 1.94(\mu\text{N}) \times 8.52(\text{mm}) \approx 16.5 \times \text{nJ} \quad [3]$$

and locomotor power P over a crawl period T :

$$P = \frac{E}{t} = \frac{16.5(\text{nJ})}{2.778(\text{s})} \approx 5.94 \times \text{nW} \quad [4]$$

This tiny energy expenditure per crawl can be converted to the cost of transport per kilogram of body mass: $E \div 2.5 \text{ g} = 6.6 \times 10^{-6} \text{ J/kg}$. It is indeed an insignificant fraction of either a gypsy moth caterpillar's average cost of transport (3.6 J/kg) (Casey, 1991) or that of a *Manduca* (22.5 J/kg, $n=5$; W. Woods Jr., personal communication). Caterpillar locomotion involves shortening and lengthening low resilience tissues (Lin et al., 2009) and viscous hemolymph, which all dissipate energy. In short, the energy required to move the body mass forward is minuscule due to the static nature of the locomotion. Most energy exchange is mediated by tissue stretching and recoil, further emphasizing the importance of pseudo- and visco-elastic properties of the tissues themselves.

Antagonist stretching and efficiency

Although *Manduca* is capable of extending its body using hydrostatic turgor (e.g., exploratory reaching/casting behavior), during horizontal crawling on a (relatively) stiff substrate *Manduca* instead uses the substrate to stretch out. In this process, the thorax walks forward but does not bring the heavy abdomen with it, thereby stretching the anterior segments. Abdominal segments shorten partly by releasing muscle strain energy between adjacent prolegs. To stretch the abdomen back out, the caterpillar anchors its two ends and pulls the posterior muscles with anterior muscles. Forces in the axial direction are responsible for extending the body and restoring muscle length. This is similar to the antagonist muscle stretching in vertebrates or stiff skeleton arthropods and it may convey several biomechanical advantages over a hydrostatic skeleton. First, by using the substrate as a skeleton, *Manduca* avoids the need to strongly pressurize its fluid filled body; the body need only be stiff enough to be self supporting. Second, by conforming to the substrate directly there is no need to maintain posture through local pressure control; the body does not need to be compartmentalized and the demands for neural-computation and proprioception can be minimized. Third, by avoiding hydrostatic control of locomotion, internal organ systems that interface with the exterior (e.g., gas exchange and digestion) can be decoupled from movements (in contrast with the hydrostatic limb extension system of many spiders that makes fast running and breathing incompatible (Parry and Brown, 1959; Prestwich, 1988)). These physiological advantages could also be evolutionary constraints that have contributed to the unique locomotion of caterpillars in general.

Implications on caterpillar prolegs diversity

From lepidopteron homeotic gene studies (Suzuki and Palopoli, 2001; Warren et al., 1994), comparative anatomy (Hinton, 1955), and X-ray induced mutation (M. Simon, personal communication), we know that caterpillars are capable of generating prolegs in any abdominal segments. It is therefore interesting

that some caterpillars share the same body plans while others differ so much. The new findings on caterpillar GRFs may provide insights into some of the biomechanical constraints favoring the evolution of different proleg configurations.

According to the GRF analysis in this study, prolegs anchor a caterpillar for body deformation. The posterior legs are responsible for holding the rear end while the anterior muscles stretch the abdominal muscles. During this process, the substrate takes on compressive loads and transmits the necessary forces across the body, analogous to a rigid bone in a skeletal system. This strategy is methodologically different from that of hydrostatic and articulated skeletons. Since the animal does not carry its own skeleton and simply adopts whatever it sits on, we call it an “environmental skeleton”. In a typical caterpillar body plan, the lack of prolegs in A7~A9 provides clearance for the terminal prolegs (TP) to swing forward and thus limits of the step size. *Manduca*’s center of mass is in A4, so the adjacent prolegs A3~A5 are critical for securing the body. Species that have a reduced number of prolegs may have an increased dependence on a hydrostatic skeleton. For example, we predict that caterpillars with looping gaits (and few proleg attachments) will have biomechanics dominated by a hydrostatic skeleton. In both *Manduca* casting behavior and inchworm looping locomotion, the A6 prolegs work closely with the terminal prolegs to produce leverage via the hydrostatic skeleton.

It is interesting to speculate on the evolutionary transition from ancestral crawling that relies so much on the substrate, to looping gaits. Because the cost of maintaining a hydrostatic skeleton is determined by the pressure required to inflate the body it is conceivable that as the caterpillars adapted to narrower environmental niches, their body size decreased and density increased. Under these conditions, the use of a hydrostatic skeleton may be more favorable than the environmental skeleton strategy. The findings reported here provide a new basis for exploring the relatively neglected role of locomotory mechanics in the evolutionary ecology of plant-insect interactions.

Acknowledgements

We would like to thank Caroline Blavet for collecting some nGRF data and Linnea van Griethuijsen for providing assistance in constructing the *Manduca* Standard Kinematics Template. The *Manduca* cost of transport data was provided by Dr. William Woods. This project was funded by NSF grant IOS 0718537 to B.A.T.

References

- Barth, R.** (1937). Muskulatur Und Bewegungsart Der Raupen. *Zool.Jb.Physiol* **62**, 507-566.
- Bartsch, M. S., Federle, W., Robert, J. and Kenny, T. W.** (2007). A Multiaxis Force Sensor for the Study of Insect Biomechanics. *J Microelectromech Syst* **16**, 709.
- Belanger, J. H., Bender, K. J. and Trimmer, B. A.** (2000). Context Dependency of a Limb Withdrawal Reflex in the Caterpillar *Manduca Sexta*. *Journal of Comparative Physiology A: Neuroethology, Sensory, Neural, and Behavioral Physiology* **186**, 1041-1048.
- Belanger, J. H. and Trimmer, B. A.** (2000). Combined Kinematic and Electromyographic Analyses of Proleg Function during Crawling by the Caterpillar *Manduca Sexta*. *Journal of Comparative Physiology A: Neuroethology, Sensory, Neural, and Behavioral Physiology* **186**, 1031-1039.
- Bell, R. A. and Joachim, F. G.** (1976). Techniques for Rearing Laboratory Colonies of Tobacco Hornworms and Pink Bollworms. *Ann. Entomol. Soc. Am.* **69**, 365-373.
- Biewener, A. A.** (2003). *Animal Locomotion*: Oxford University Press, USA.
- Blickhan, R., Seyfarth, A., Geyer, H., Grimmer, S., Wagner, H. and Günther, M.** (2007). Intelligence by Mechanics. *Philosophical Transactions of the Royal Society A: Mathematical, Physical and Engineering Sciences* **365**, 199-220.
- Casey, T. M.** (1991). Energetics of Caterpillar Locomotion: Biomechanical Constraints of a Hydraulic Skeleton. *Science* **252**, 112-114.
- Chapman, G.** (1958). The Hydrostatic Skeleton in the Invertebrates. *Biological Reviews* **33**, 338-371.
- Chiel, H. J., Crago, P., Mansour, J. M. and Hathi, K.** (1992). Biomechanics of a Muscular Hydrostat: A Model of Lapping by a Reptilian Tongue. *Biol. Cybern.* **67**, 403-415.
- Colobert, B., Crétaul, A., Allard, P. and Delamarche, P.** (2006). Force-Plate Based Computation of Ankle and Hip Strategies from Double-Inverted Pendulum Model. *Clin. Biomech.* **21**, 427-434.
- Dominick, O. S. and Truman, J. W.** (1986). The Physiology of Wandering Behaviour in *Manduca Sexta*. III. Organization of Wandering Behaviour in the Larval Nervous System. *J. Exp. Biol.* **121**, 115-132.

- Dutto, D. J., Hoyt, D. F., Cogger, E. A. and Wickler, S. J.** (2004). Ground Reaction Forces in Horses Trotting Up an Incline and on the Level Over a Range of Speeds. *J. Exp. Biol.* **207**, 3507-3514.
- Eaton, J. L.** (1988). *Lepidopteran Anatomy*: Wiley New York.
- Epstein, M. E.** (1996). *Revision and Phylogeny of the Limacodid-Group Families, with Evolutionary Studies on Slug Caterpillars (Lepidoptera: Zygaenoidea)*: Smithsonian Institution Press.
- Fanchon, L., Valette, J. P., Sanaa, M. and Grandjean, D.** (2006). The Measurement of Ground Reaction Force in Dogs Trotting on a Treadmill: An Investigation of Habituation. *Vet. Comp. Orthop. Traumatol.* **19**, 81-86.
- Forbes, W.** (1910). A Structural Study of some Caterpillars. *Ann. Entomol. Soc. Am.* **3**, 94-143.
- Full, R. J., Yamauchi, A. and Jindrich, D. L.** (1995). Maximum Single Leg Force Production: Cockroaches Righting and Running on Photoelastic Gelatin. *J. Exp. Biol.* **198**, 2441-2452.
- Goldman, D. I., Chen, T. S. and Dudek, D. M.** (2006). Dynamics of Rapid Vertical Climbing in Cockroaches Reveals a Template. *J. Exp. Biol.* **209**, 2990.
- Heglund, N. C.** (1981). Short Communication: A Simple Design for a Force-Plate to Measure Ground Reaction Forces. *J. Exp. Biol.* **93**, 333-338.
- Herrel, A., Meyers, J. J., Timmermans, J. P. and Nishikawa, K. C.** (2002). Supercontracting Muscle: Producing Tension Over Extreme Muscle Lengths. *J. Exp. Biol.* **205**, 2167-2173.
- Hinton, H. E.** (1955). On the Structure, Function, and Distribution of the Prolegs of the Panorpoidea, with a Criticism of the Berlese-Imms Theory. *Transactions of the Royal Entomological Society of London* **106**, 455-540.
- Holmes, P., Robert, J., Koditschek, D. E. and Guckenheimer, J.** (2006). The Dynamics of Legged Locomotion: Models, Analyses, and Challenges. *SIAM Reviews* **48**, 207-304.
- Johnston, R. M. and Levine, R. B.** (1996a). Crawling Motor Patterns Induced by Pilocarpine in Isolated Larval Nerve Cords of *Manduca sexta*. *J. Neurophysiol.* **76**, 3178-3195.
- Johnston, R. M. and Levine, R. B.** (1996b). Locomotory Behavior in the Hawkmoth *Manduca sexta*: Kinematic and Electromyographic Analyses of the Thoracic Legs in Larvae and Adults. *J. Exp. Biol.* **199**, 759-774.
- Keudel, M. and Schrader, S.** (1999). Axial and Radial Pressure Exerted by Earthworms of Different Ecological Groups. *Biol. Fertility Soils* **29**, 262-269.
- Kier, W. M.** (1992). Hydrostatic Skeletons and Muscular Hydrostats. *Biomechanics (Structures and Systems): A Practical Approach*, 205-231.
- Kier, W. M. and Smith, K. K.** (1985). Tongues, Tentacles and Trunks: The Biomechanics of Movement in Muscular-Hydrostats. *Zool. J. Linn. Soc.* **83**, 307-324.
- Kier, W. M. and Stella, M. P.** (2007). The Arrangement and Function of Octopus Arm Musculature and Connective Tissue. *J. Morphol.* **268**, 831-843.
- Kopec, S.** (1919). Lokalisationsversuche an Zentralen Nervensysteme Der Raupen Und Falter. *Zool. Jb. Physiol.* **36**, 453-502.

- Kristan, W. B., Calabrese, R. L. and Friesen, W. O.** (2005). Neuronal Control of Leech Behavior. *Prog. Neurobiol.* **76**, 279-327.
- Lemmerhirt, D. F., Staudacher, E. M. and Wise, K. D.** (2006). A Multitransducer Microsystem for Insect Monitoring and Control. *IEEE Transactions on Biomedical Engineering* **53**, 2084-2091.
- Levine, R. B. and Truman, J. W.** (1985). Dendritic Reorganization of Abdominal Motoneurons during Metamorphosis of the Moth, *Manduca sexta*. *Journal of Neuroscience* **5**, 2424-2431.
- Libby, J. L.** (1959). The Nervous System of Certain Abdominal Segments of the Cecropia Larva (Lepidoptera: Saturniidae). *Ann. Entomol. Soc. Am.* **52**, 469-480.
- Lin, H. T., Dorfmann, A. L. and Trimmer, B. A.** (2009). Soft-Cuticle Biomechanics: A Constitutive Model of Anisotropy for Caterpillar Integument. *J. Theor. Biol.* **256**, 447-457.
- McKenzie, B. M. and Dexter, A. R.** (1988a). Axial Pressures Generated by the Earthworm *Aporrectodea rosea*. *Biol. Fertility Soils* **5**, 323-327.
- McKenzie, B. M. and Dexter, A. R.** (1988b). Radial Pressures Generated by the Earthworm *Aporrectodea rosea*. *Biol. Fertility Soils* **5**, 328-332.
- Mezoff, S., Papastathis, N., Takesian, A. and Trimmer, B. A.** (2004). The Biomechanical and Neural Control of Hydrostatic Limb Movements in *Manduca sexta*. *J. Exp. Biol.* **207**, 3043-3053.
- Miller, J. C., Janzen, D. H. and Hallwachs, W.** (2006). *100 Caterpillars*: Belknap Press of Harvard University Press.
- Niebur, E. and Erdos, P.** (1991). Theory of the Locomotion of Nematodes: Dynamics of Undulatory Progression on a Surface. *Biophys. J.* **60**, 1132.
- Nishikawa, K. C., Kier, W. M. and Smith, K. K.** (1999). Morphology and Mechanics of Tongue Movement in the African Pig-Nosed Frog *Hemisus marmoratus*: A Muscular Hydrostatic Model. *J. Exp. Biol.* **202**, 771-780.
- Parry, D. A. and Brown, R. H. J.** (1959). The Hydraulic Mechanism of the Spider Leg. *J. Exp. Biol.* **36**, 423-433.
- Prestwich, K. N.** (1988). The Constraints on Maximal Activity in Spiders. *Journal of Comparative Physiology B: Biochemical, Systemic, and Environmental Physiology* **158**, 437-447.
- Quillin, K. J.** (1998). Ontogenetic Scaling of Hydrostatic Skeletons: Geometric, Static Stress and Dynamic Stress Scaling of the Earthworm *Lumbricus terrestris*. *J. Exp. Biol.* **201**, 1871-1883.
- Quillin, K. J.** (1999). Kinematic Scaling of Locomotion by Hydrostatic Animals: Ontogeny of Peristaltic Crawling by the Earthworm *Lumbricus terrestris*. *J. Exp. Biol.* **202**, 661-674.
- Quillin, K. J.** (2000). Ontogenetic Scaling of Burrowing Forces in the Earthworm *Lumbricus terrestris*. *J. Exp. Biol.* **203**, 2757-2770.
- Reinhardt, L., Weihmann, T. and Blickhan, R.** (2009). Dynamics and Kinematics of Ant Locomotion: Do Wood Ants Climb on Level Surfaces? *J. Exp. Biol.* **212**, 2426.
- Roberts, T. J. and Belliveau, R. A.** (2005). Sources of Mechanical Power for Uphill Running in Humans. *J. Exp. Biol.* **208**, 1963-1970.

- Rubinoff, D. and Haines, W. P.** (2005). Web-Spinning Caterpillar Stalks Snails. *Science* **309**, 575.
- Schmidt, M.** (2005). Quadrupedal Locomotion in Squirrel Monkeys (Cebidae: Saimiri Sciureus): A Cineradiographic Study of Limb Kinematics and Related Substrate Reaction Forces. *Primates* **128**, 359-370.
- Simon, M. A. and Trimmer, B. A.** (2009). Movement Encoding by a Stretch Receptor in the Soft-Bodied Caterpillar, *Manduca Sexta*. *J. Exp. Biol.* **212**, 1021.
- Skierczynski, B. A., Wilson, R. J. A., Kristan Jr, W. B. and Skalak, R.** (1996). A Model of the Hydrostatic Skeleton of the Leech. *J. Theor. Biol.* **181**, 329-342.
- Smolianinov, V. V. and Mazurov, M. E.** (1976). Kinematics of Crawling Locomotion. I. Ideal Elastic Model. *Biofizika* **21**, 1103-1108.
- Snodgrass, R. E.** (1961). The Caterpillar and the Butterfly. *Locomotor mechanisms of birds*, 1.
- Snodgrass, R. E.** (1993). *Principles of Insect Morphology*: Cornell University Press.
- Suzuki, Y. and Palopoli, M. F.** (2001). Evolution of Insect Abdominal Appendages: Are Prolegs Homologous Or Convergent Traits? *Dev. Genes Evol.* **211**, 486-492.
- Taylor, H. M. and Truman, J. W.** (1974). Metamorphosis of the Abdominal Ganglia of the Tobacco Hornworm, *Manduca Sexta*. *Journal of Comparative Physiology A: Neuroethology, Sensory, Neural, and Behavioral Physiology* **90**, 367-388.
- Trimmer, B. A. and Issberner, J.** (2007). Kinematics of Soft-Bodied, Legged Locomotion in *Manduca Sexta* Larvae. *Biol. Bull.* **212**, 130.
- van Griethuijsen, L. I. and Trimmer, B. A.** (2009). Kinematics of Horizontal and Vertical Caterpillar Crawling. *J. Exp. Biol.* **212**, 1455.
- Wadepuhl, M. and Beyn, W. J.** (1989). Computer Simulation of the Hydrostatic Skeleton. the Physical Equivalent, Mathematics and Application to Worm-Like Forms. *J. Theor. Biol.* **136**, 379-402.
- Wagner, D. L.** (2005). *Caterpillars of Eastern North America: A Guide to Identification and Natural History*: Princeton University Press, Princeton, NJ.
- Wainwright, S. A.** (1988). *Axis and Circumference: The Cylindrical Shape of Plants and Animals*. Cambridge: Harvard University Press.
- Warren, R. W., Nagy, L., Selegue, J., Gates, J. and Carroll, S.** (1994). Evolution of Homeotic Gene Regulation and Function in Flies and Butterflies.
- Weeks, J. C. and Truman, J. W.** (1984). Neural Organization of Peptide-Activated Ecdysis Behaviors during the Metamorphosis of *Manduca Sexta*. *Journal of Comparative Physiology A: Neuroethology, Sensory, Neural, and Behavioral Physiology* **155**, 407-422.
- Zumwalt, A. C., Hamrick, M. and Schmitt, D.** (2006). Force Plate for Measuring the Ground Reaction Forces in Small Animal Locomotion. *J. Biomech.* **39**, 2877-2881.

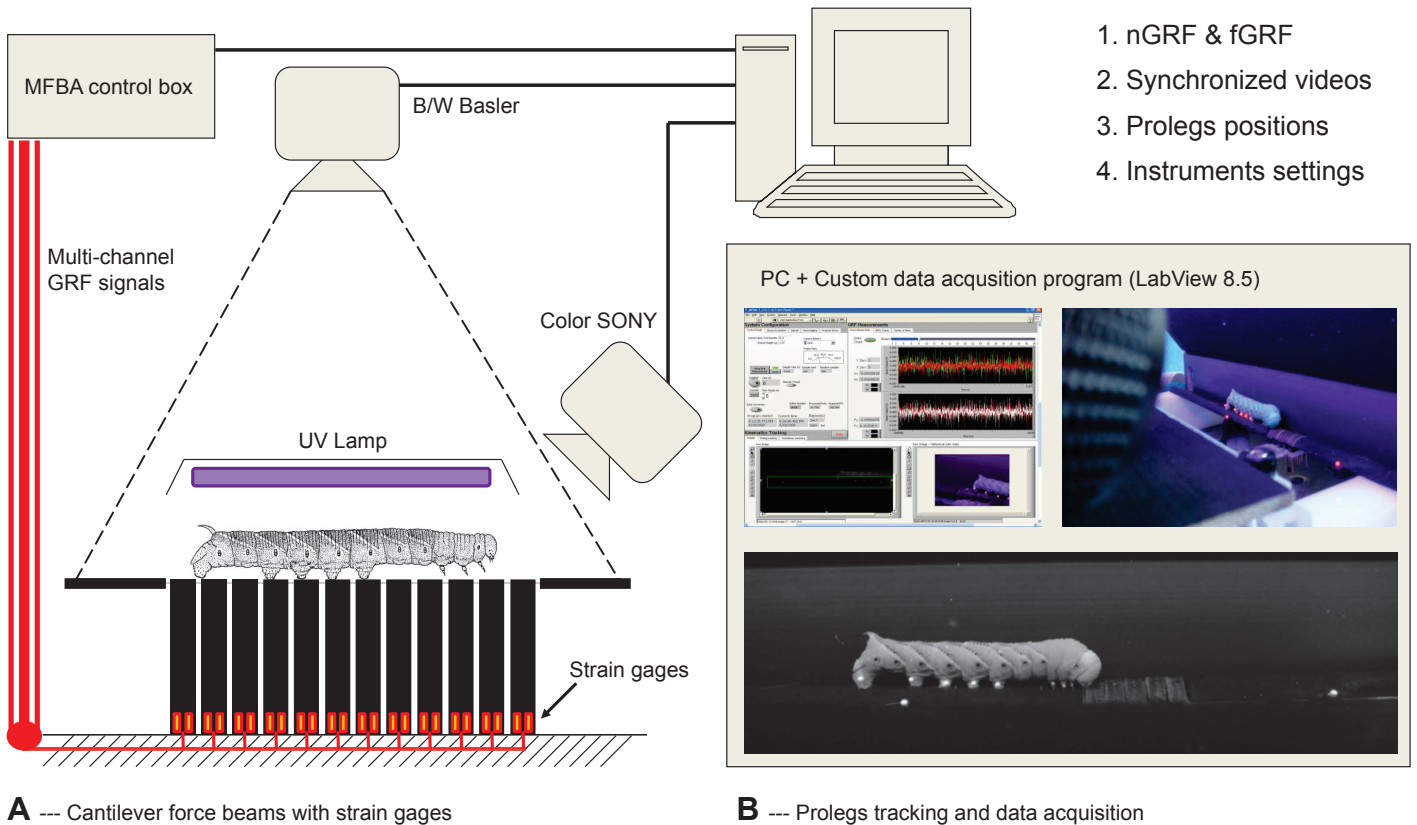


Fig 1: Manduca Force Beam Array (MFBA) setup. (A) Each force beam has strain gages bonded at its base to quantify deflection forces due to caterpillar steps. Force signals were passed through a control box for basic signal processing before going into the PC via a NI data acquisition card. (B) Caterpillars were marked with UV black paint coated beads for video tracking. The image from a monochrome video camera is used to track the proleg markers and to calibrate their position relative to two fixed dots on the substrate. An additional color CCD camera records a close-up view to determine which legs are in contact with each beam. A custom LabView program acquires both the visual and force data after some hardware signal processing. The software further processes the data to put out a set of data files.

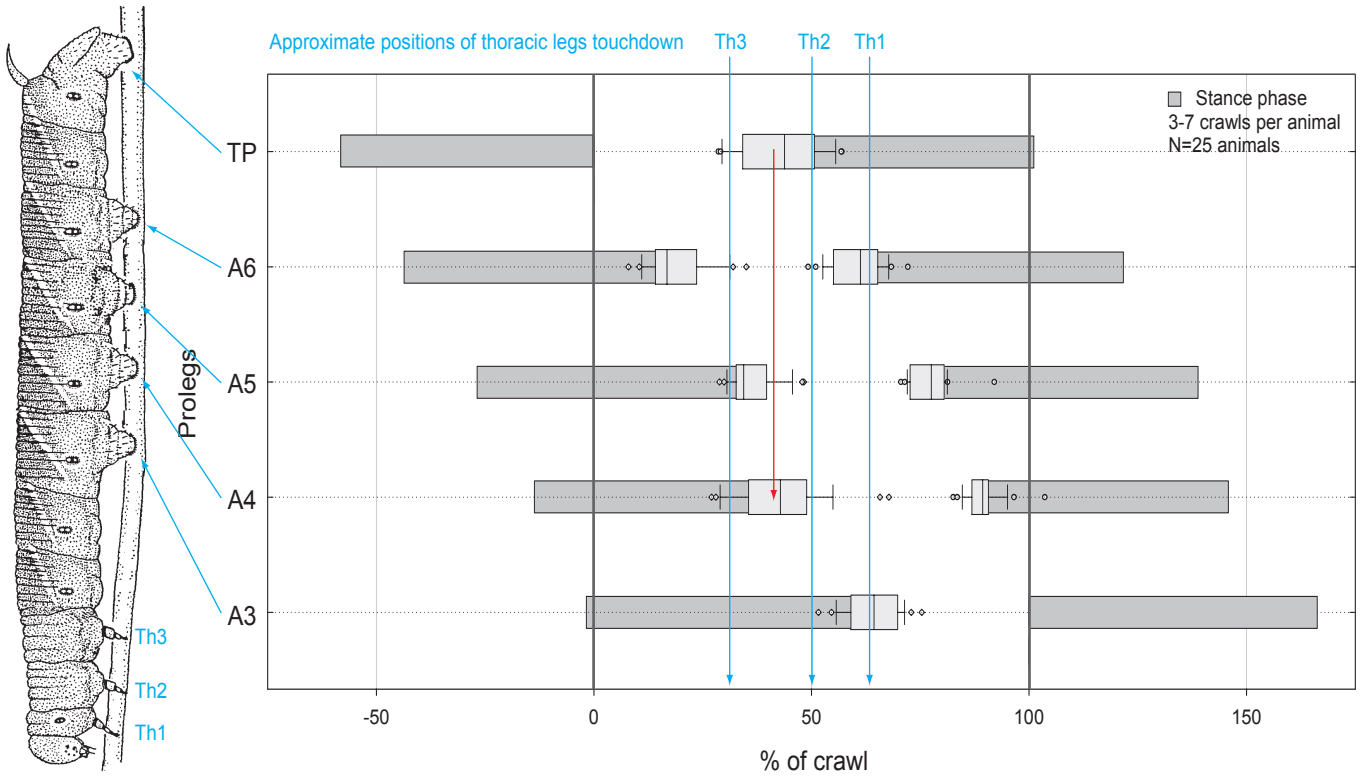


Fig 2: *Manduca* Standard Kinematics Template (SKT) and approximate thoracic legs touch down. The relative timing of the stance and swing phases of each proleg during a crawl. The stance phase is shown as a grey bar with box plots marking the mean and 95 % confidence intervals for the onset and end of stance (n= 25 caterpillars, adapted from data in (van Griethuijsen and Trimmer, 2009)}. A complete crawl cycle (100%) was defined as the start of TP swing phase to the end of A3 stance phase (dashed vertical lines), corresponding to the TP takeoff and A3 touchdown of the next cycle. Notice that the TP touchdown tends to coincide with the A5 and A4 take-off (red arrow). The thoracic legs were not tracked during previous kinematic studies, so the approximate touchdown timing is based on video observations.

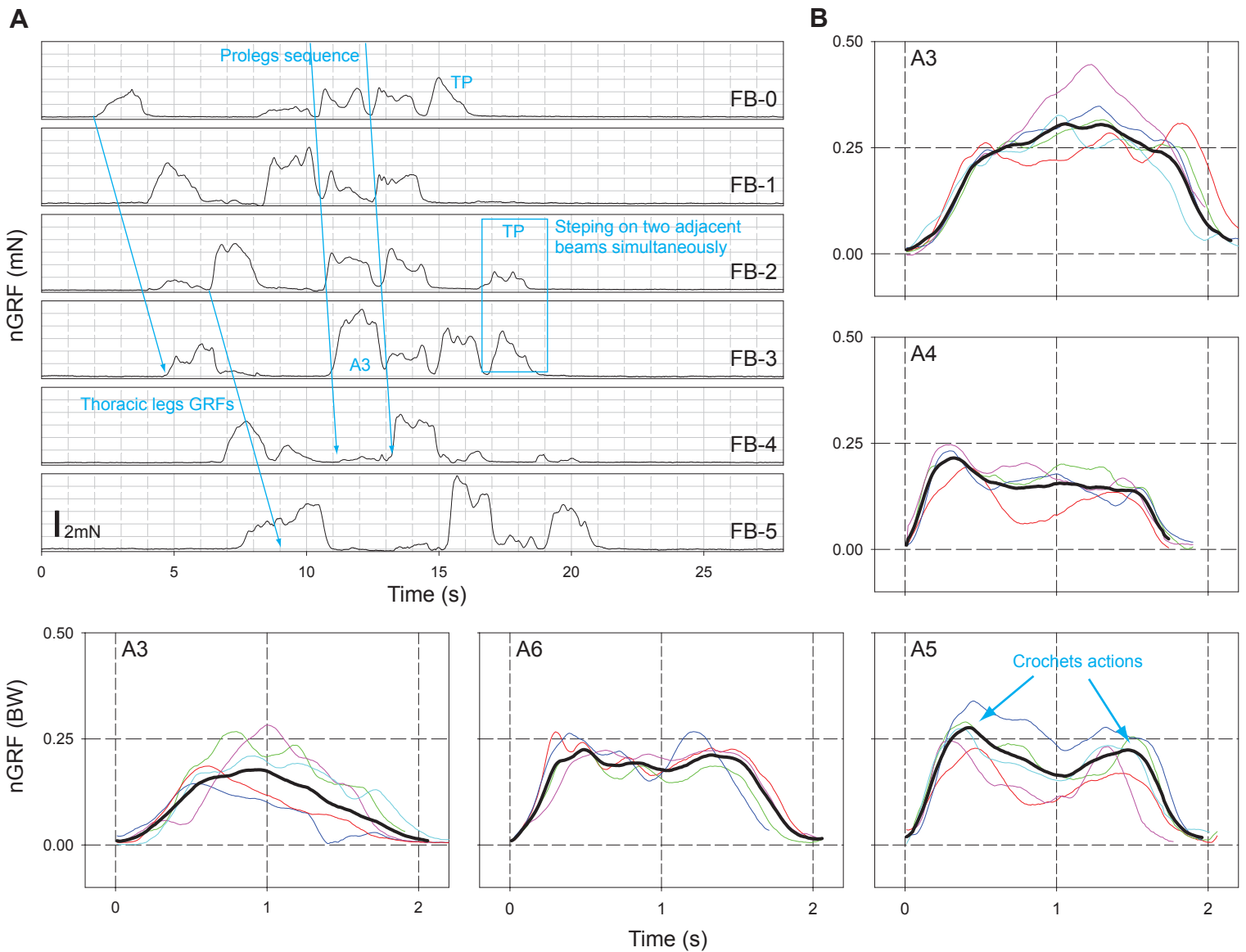


Fig 3: *Manduca* normal GRFs representative data set. (A) Examples of the forces recorded simultaneously on 6 adjacent force beams (FB-0~5) during a crawl. Forces are recorded as the animal initially steps onto FB-0 with its thoracic legs and then progressively moves across the beams until all of the proleg contact points are represented within the array. The final force profile in a sequence on each beam is that produced by the TP. In some instances (shown here on FB-2 and 3) the prolegs are in contact with two sensor beams simultaneously. Notice that each pair of prolegs generally loads up to 25% of total body weight and thoracic legs take similar if not more weight at the front. Indeed, *Manduca* needs 3~4 minimum leg contacts at any given moment. **(B)** The nGRF profiles from each proleg can be extracted and overlaid with one another on successive steps (thin colored lines). The mean profile for these steps is then calculated and plotted as a thick dark line. The force profiles for prolegs A4-6 are often quite similar with peaks at the start and end of stance corresponding to the deployment and detachment of the crochets (arrows). The force profiles of proleg A3 and TP were variable but usually distinguishable from the mid-body segments with a mid-stance peak and different rates of onset and liftoff forces. See text for details.

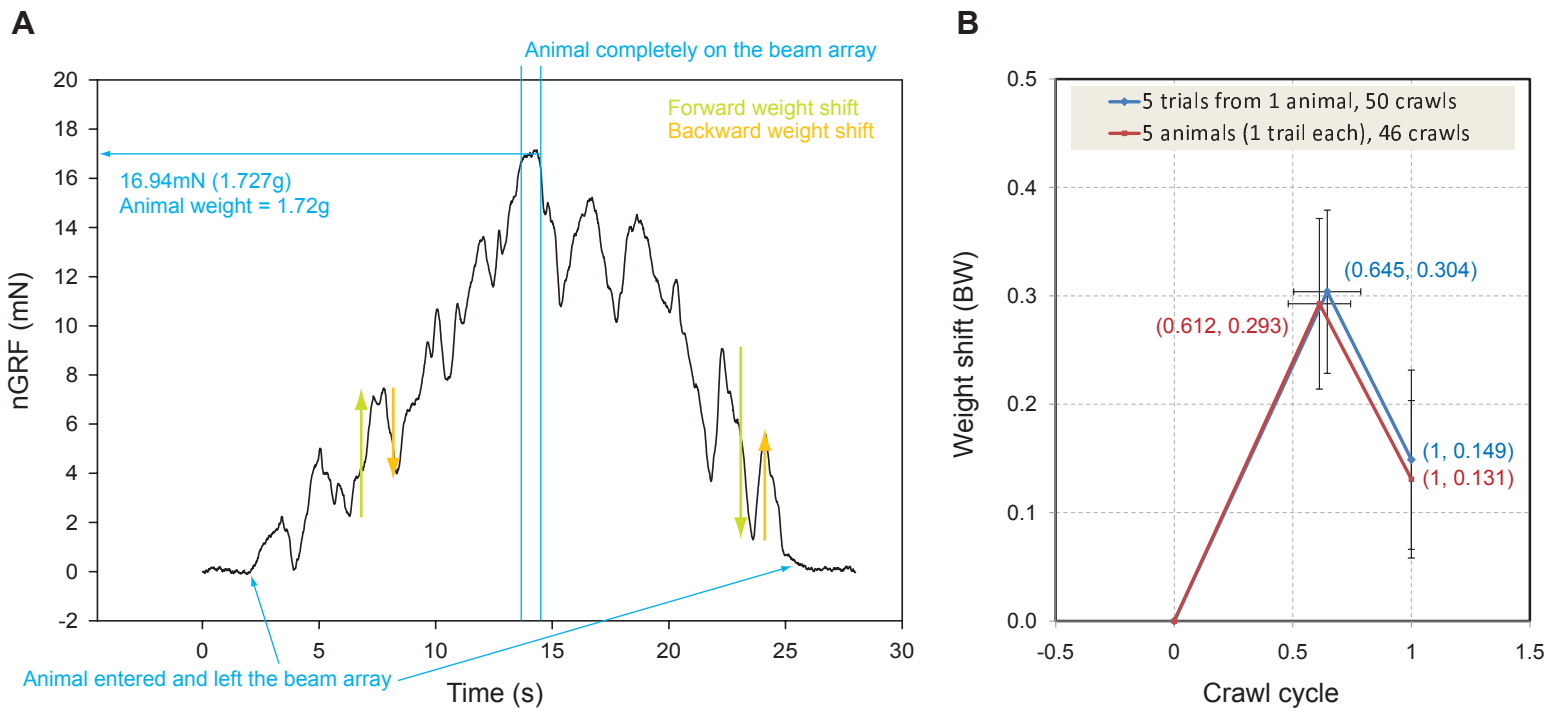


Fig 4: *Manduca* weight shift analysis. (A) A representative recording of the net nGRF oscillations caused by weight shifts as *Manduca* moves across the sensor array. For about one second, the animal stood completely on the beam array and the net nGRF corresponded to the animal body weight (horizontal line on the top left). Weight shifts were quantified by measuring the peak-to-peak forward and backward changes as marked in green and orange respectively. (B) These weight shifts (about 10 steps per trial) were measured in multiple trials from one animal (blue), and for one trial from each of five animals (red) and plotted as the mean proportion of body weight (BW) moving in each direction (\pm standard deviation, standard errors were negligibly small). *Manduca* shifts ~ 0.3 BW forward in the first ~ 0.65 of the crawl cycle before dropping ~ 0.15 BW back at the end of the crawl (as shown by the labeled coordinates). This results in a net weight transport of 0.15 BW per crawl, matching the observation of 6–7 crawls per body length of travel. This oscillating mass shift predicts higher transient accelerations than those estimated from the kinematics and can be used to estimate the baseline mechanical energy associated with crawling locomotion. The body length of *Manduca* changes within 5% during normal locomotion (see Fig. 5B). Extra weight shift may be contributed to large local deformation and internal mass redistribution.

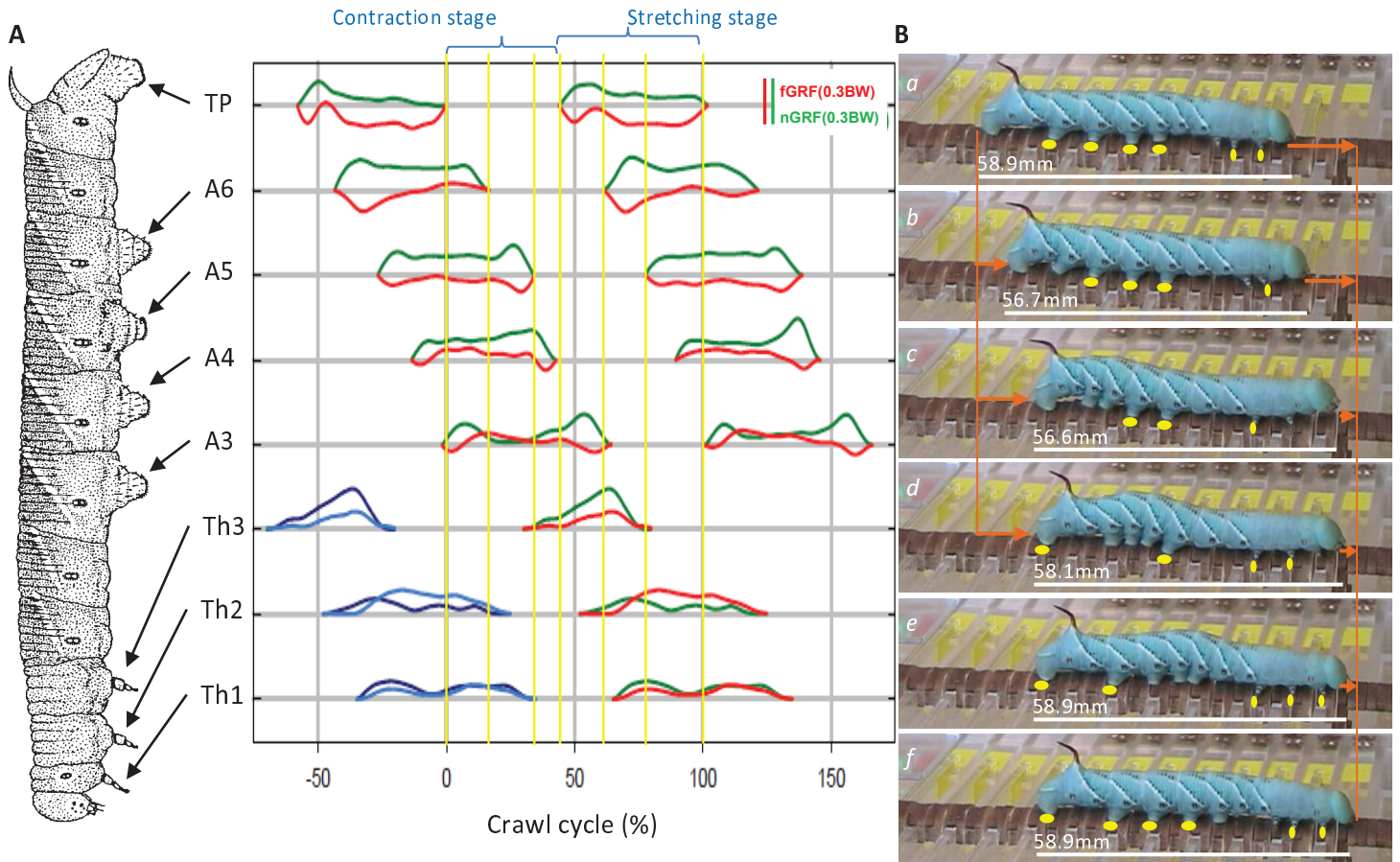


Fig 5: Representative data of *Manduca* normal and fore-aft GRFs. (A) Examples of simultaneous recording of nGRF (in green) and fGRF (in red) scaled to the *Manduca* standard kinematics template (Fig. 2) to illustrate the overall timing of each proleg during a crawl cycle. This experiment was not designed to collect thoracic legs GRFs and thoracic legs data were not tracked. However, for analytical purposes, one typical recording and its duplication (in blues) are manually inserted in this figure according to the behavioral videos. These data are representative of results from three experimental animals. All GRF traces are plotted as body weight (BW) as indicated by the reference bar on the upper right corner. Indeed, nGRFs can be characterized by pure weight placement. (B) Six phases are identified in a crawl cycle. In the first stage (phases a-c) there is a progressive loss of contact points as the prolegs are lifted and the posterior part of the body shortened. Body tension anterior to the anchoring legs may be important in lifting the abdomen as the thorax extends during this contraction stage. In the subsequent stretching stage (phase d-f) the abdomen is stretched out by anchoring the anterior part of the body. The white bar in each snapshot reflects the caterpillar's current body length. The orange arrows indicate forward displacements of the body. This sequence of movements can be used with the GRFs to predict muscle activation patterns and their associated work cycles (both negative and positive).

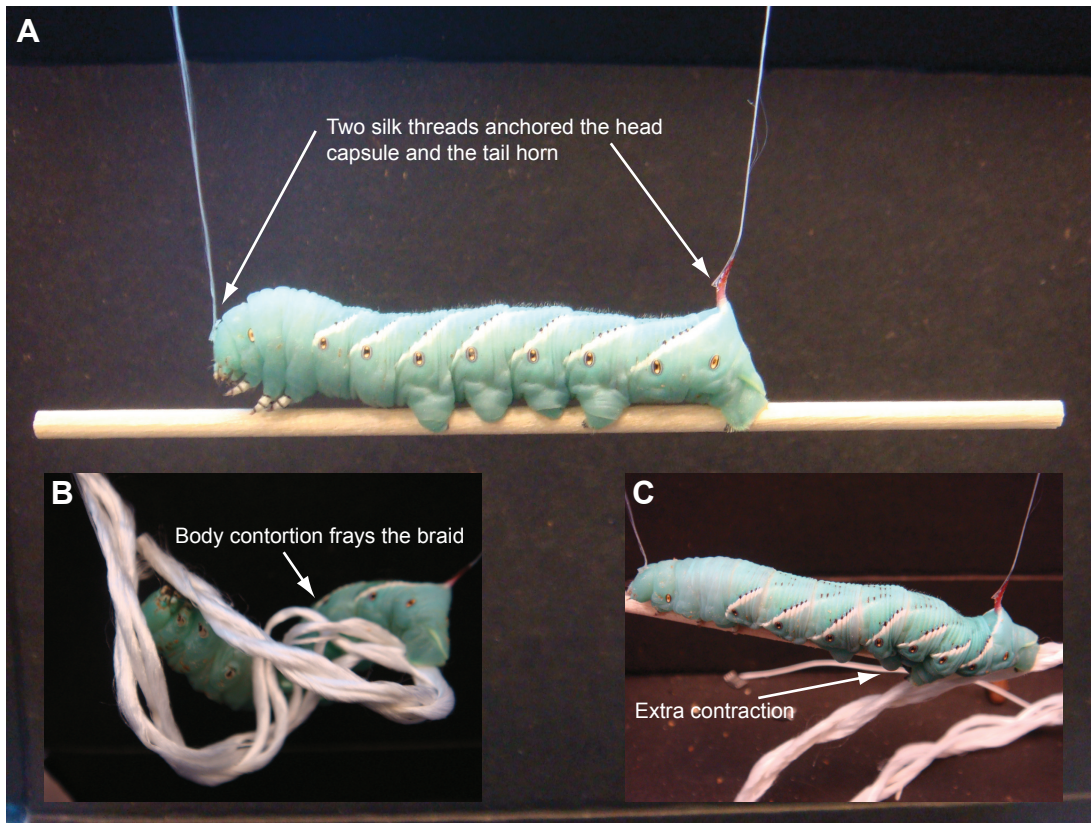


Fig 6: The importance of substrate stiffness can be shown in a behavioral experiment. (A) A 5th instar caterpillar was suspended from its head capsule and the dorsal horn but was otherwise free to move. It demonstrated normal crawling movements when a light piece of stiff balsa wood was placed between the prolegs. The wood steadily moved backwards as *Manduca* attempted to make forward progress. **(B)** When *Manduca* was presented with materials that deformed under compressive loads it was unable to extend its body or maintain a normal posture. For example, when a *Manduca* caterpillar tried to crawl on a silk braid (the same diameter as the balsa wood stick) the body became curved and it could not extend the anterior segments to make forward progress. Eventually, it started to fray the silk braid by pulling threads together. **(C)** When the entangled caterpillar was then allowed to move onto the balsa wood substrate it recovered normal crawling as the prolegs gradually reached the stiff substrate. Notice the extra body contraction at the interface between the silk braid and the balsa stick. The abdominal segments regained normal length only when their associated prolegs attached to the stiffer substrate.

Publication-2

Title: Caterpillars use the substrate as their external skeleton: a behavior confirmation

Authors: Huai-Ti Lin and Barry Trimmer

Addendum to:

Lin HT, Trimmer BA. The substrate as a skeleton: ground reaction forces from a soft-bodied legged animal. J Exp Biol 2010; 213:1133-42.

Keywords: Caterpillar locomotion; *Manduca sexta*; biomechanics; hydrostatic skeleton, environmental skeleton, crawling; inching

Abstract

Animals that lack rigid structures often employ pressurization to maintain body form and posture. Structural stability is then provided by incompressible fluids or tissues and the inflated morphology is called a hydrostatic skeleton. However, new ground reaction force data from the caterpillar, *Manduca sexta* suggests an alternate strategy for large soft animals moving in complex three dimensional structures. When crawling, *Manduca* can keep its body primarily in tension and transmit compressive deformation forces through the substrate. This effectively allows the caterpillar to minimize reliance on a hydrostatic skeleton and helps it conform to the environment. We call this alternative strategy an “*environmental skeleton*”.

Caterpillar locomotion

The primary role of lepidopteron larvae is to collect nutrients for future reproduction. Finding and maintaining access to resources by foraging requires locomotion. For most caterpillars there is no need to run away from predators (caterpillars are usually cryptic or toxic) so locomotion can be relatively slow, trading speed and agility for stability and a large carrying capacity. As with all animals it is presumably important to conserve energy whenever possible so caterpillars are expected to exploit efficient mechanical strategies

In addition to the six true legs present in adult insects, many larvae have extra limbs to support their large abdomen or to perform stage specific behaviors. In caterpillars these abdominal appendages are called “prolegs” and studies of gene expression patterns suggest that they can develop in any abdominal segment (Suzuki, Palopoli 2001, Warren et al. 1994) and different species have evolved different proleg configurations (Hall, Wake 1999) (Miller, Janzen & Hallwachs 2006) and a variety of gaits. (Brackenbury 1996, Brackenbury 1997, Brackenbury 1999) Most caterpillars initiate a body contraction from the posterior end and propagate the deformation forward: (Trimmer, Issberner 2007) (Trimmer, Issberner 2007)⁸ this anterior-grade wave resembles either crawling or inching depending on the configuration of the prolegs and the length of body that is lifted in each step (Fig 1).

Inching is probably one of the most primitive modes of locomotion due to its mechanical simplicity. In contrast to articulated legged systems where body masses are pivoted over the legs at the

footholds,(Holmes et al. 2006) an inching strategy benefits animals that cannot take compressive loads. Many legless animals can exploit this gait including leeches, snakes and earthworms. Even though they have legs, caterpillars use variations of inching to locomote because their stubby soft legs can neither transmit compressive load nor produce significant leverage. Large caterpillars such as *Manduca* employ a crawling gait that has more complex loading characteristics but there is still much that is reminiscent of inching. The progressive wave of movements can be regarded as segmental inching with the substrate used as a skeletal support (instead of the inherent hydrostatic skeleton). By supporting its body with an array of prolegs the caterpillar can afford to be much larger without sacrificing mobility or stability.

The role of prolegs in the context of locomotion

Lepidopteran prolegs can be specialized for many functions,(Scott et al. 2010) and their morphologies can vary dramatically (Snodgrass 1993). In locomotion, however, they are body anchors that lock sections of the abdomen to the substrate to counteract muscle contraction. In addition to providing dependable grip a key feature of the prolegs is that they must detach cleanly on demand. In *Manduca* the hooking strength of even a single plantar is sufficient to support the entire body weight so release must be completely reliable. This is borne out by the ground reaction forces measured from horizontal crawling caterpillars which were always positive (weight loading) and never negative (pulling upwards) in the normal direction indicating clean detachment from each step.(Lin, Trimmer 2010) As expected, most locomotor deformations are along the direction of travel (or the animal body axis). The vertical loading

on the prolegs during horizontal crawling resembles simple weight placement. The body center of mass does not vary over 10% the body length, and the overall body length never changes more than 5%. This implies that the animal rarely attempt to force any body curvature during its locomotion. The body simply takes on the curvature of the substrate. The major forces are directed along the animal body axis and probably generated by the large longitudinal muscles in the body.

Body tension and the crawling gait

A worm-like cylinder with only fluid inside tends to collapse under its own weight unless the internal pressure is sufficient to keep the body wall in tension. This sagging phenomenon becomes more significant as the structure scales up in size but it can be counteracted with additional support along the body. This seems to be the trend in caterpillars because larger species typically have more prolegs and small ones appear to have lost mid abdominal prolegs through evolution.(Wagner 2005) However, locomotion requires the release of prolegs from the substrate at least temporarily thus large caterpillars need to be able to maintain body posture during foothold exchange. Let us consider a scenario where a caterpillar is crawling on a branch upside down in the horizontal orientation, something very common in nature (Fig 2a). The caterpillar has two ways to control body sagging under gravity whenever the mid prolegs are disengaged. The first one involves increasing the body pressure to activate the hydrostatic skeleton. The body wall will be loaded against the incompressible body fluid, entering the classical hydrostatic support paradigm (Fig 2b). To counter the gravitational pull on any suspended segments, the

caterpillar might need to further tighten the dorsal muscles. An alternative method to prevent sagging is to simply load the body against the substrate, using the prolegs as anchors against the body contraction. This overall body tension will keep the body stable in much the same way as a laundry line can be pulled straight even under the load of the laundry (Fig 2c). The ground reaction force data suggest that large caterpillars such as *Manduca* prefer this tension strategy whenever they are attached to a substrate.

Of course it would be oversimplifying to suggest that the hydrostatic skeleton plays no role in caterpillar locomotion. During the first stage of a crawl cycle, *Manduca* must pick up the three most posterior body segments to advance the footholds. A certain amount of body rigidity is necessary, and the muscle contractions associated with lifting must help to pressurize the body. However, once the terminal prolegs are planted, the body immediately transits into a tension loaded condition in which mid body contractions are checked by the advancing thoracic legs and the locked terminal segments.

Thoracic legs and hydrostatic skeleton

Although we treat caterpillars as soft-bodied animals, they still have some rigid components. Beside the big head capsule which houses the massive mandibular muscles, they also have the six articulated true legs in the thorax. These legs can push and pull especially with claws at the metatarsal. This results in a continuous positive ground reaction force in the thorax. This is essentially how caterpillars can climb up their own silk threads (life-lines) when they drop from the trees (Brackenbury 1996). In some

caterpillars such as the case-bearing species only the thoracic legs are used for locomotion leaving the reduced prolegs to hold on to their protective shell.(Rubinoff, Haines 2005, Gaston, Reavey & Valladares 1991) To explore the functional contrast between thoracic legs and prolegs, we suspended *Manduca* from its head capsule and dorsal horn. When a stiff substrate was placed under the thoracic legs it was passed along to the abdominal prolegs and then backward as the caterpillar performed regular crawling kinematics. If this stiff wooden dowel was replaced with a flexible and curved silicon tube that could not be easily crumpled the crawling behavior was normal and the tube was “walked” backwards along the prolegs (Fig 3). This demonstrates that body posture is not an essential parameter in caterpillar crawling. In contrast, when *Manduca* was given a flexible and compressible substrate such as a silk braid the thoracic legs still progressed along the thread (as in silk climbing) but abdominal segments that rely on compressive loading in the substrate could not be stretched out sufficiently. As an interesting consequence, *Manduca* becomes stuck in the extension phase of the crawl cycle. In this phase, the posterior prolegs are brought forward and planted and the thoracic legs progress forward to stretch out the body. Since the silk braid does not offer any extension force between the thorax and the posterior abdomen, the animal simply kept spooling the substrate from the thoracic legs. This is distinct from a typical hydrostatic mechanism in which an animal straightens its body without the aid of any substrate. Because *Manduca* can perform “reaching” movements that involve stiff counter-levering of the anterior segments, this failure to crawl normally on a soft substrate might be a motor pattern constraint or a

behavioral preference. The overall body tension might be an important cue for the crawling gait, and such information could come from any stretch sensors since the same tension is felt across multiple segments in series.

Concluding remarks

The compliance of biological structures varies in a continuum, and depends on the relative scale. We can say tree branches are stiff because they maintain a configuration under their own weight. At other times, they are compliant under the aerodynamic loads of wind. A worm may not have any rigid structures to support itself. Yet when the body pressurizes to perform a task, the whole body becomes sufficiently stiff relative to the functional load. Caterpillars are soft because they give in to the “posture” of the substrate in most situations. This strategy not only ensures a good match between the caterpillar body curvature and that of the substrate but also create a robust animal-substrate system. With the prolegs as ultimate anchors, caterpillars can use any shape of substrate as their external skeleton. Staying sufficiently soft allows them to navigate complex environments and blend into the contours of their environment.

References

Brackenbury, J. 1999, "Fast locomotion in caterpillars", *Journal of insect physiology*, vol. 45, no. 6, pp. 525-533.

Brackenbury, J. 1997, "Caterpillar kinematics", *Nature*, vol. 390, no. 6659, pp. 453.

- Brackenbury, J. 1996, "Novel locomotory mechanisms in caterpillars: life-line climbing in *Epinotia abbreviana* (Tortricidae) and *Yponomeuta padella* (Yponomeutidae)", *Physiological Entomology*, vol. 21, no. 1, pp. 7-14.
- Gaston, K.J., Reavey, D. & Valladares, G.R. 1991, "Changes in feeding habit as caterpillars grow", *Ecological Entomology*, vol. 16, no. 3, pp. 339-344.
- Hall, B.K. & Wake, M.H. 1999, *The Origin and Evolution of Larval forms*, Academic Press, Boston.
- Holmes, P., Robert, J., Koditschek, D.E. & Guckenheimer, J. 2006, "The Dynamics of Legged Locomotion: Models, Analyses, and Challenges", *Society of Industrial and Applied Mathematics Reviews*, vol. 48, no. 2, pp. 207-304.
- Lin, H.T. & Trimmer, B.A. 2010, "The substrate as a skeleton: ground reaction forces from a soft-bodied legged animal", *Journal of Experimental Biology*, vol. 213, no. 7, pp. 1133.
- Miller, J.C., Janzen, D.H. & Hallwachs, W. 2006, *100 caterpillars*, Belknap Press of Harvard University Press.
- Rubinoff, D. & Haines, W.P. 2005, "Web-spinning caterpillar stalks snails", *Science*, vol. 309, no. 5734, pp. 575.
- Scott, J.L., Kawahara, A.Y., Skevington, J.H., Yen, S.H., Sami, A., Smith, M.L. & Yack, J.E. 2010, "The evolutionary origins of ritualized acoustic signals in caterpillars", *Nature Communications*, vol. 1, no. 1, pp. 1-9.
- Snodgrass, R.E. 1993, *Principles of insect morphology*, Cornell University Press.
- Suzuki, Y. & Palopoli, M.F. 2001, "Evolution of insect abdominal appendages: are prolegs homologous or convergent traits?", *Development genes and evolution*, vol. 211, no. 10, pp. 486-492.
- Trimmer, B.A. & Issberner, J. 2007, "Kinematics of Soft-bodied, Legged Locomotion in *Manduca sexta* Larvae", *Biol.Bull.*, vol. 212, pp. 130.
- Wagner, D.L. 2005, *Caterpillars of eastern North America: a guide to identification and natural history*, Princeton University Press, Princeton, NJ.
- Warren, R.W., Nagy, L., Selegue, J., Gates, J. & Carroll, S. 1994, "Evolution of homeotic gene regulation and function in flies and butterflies", *Nature*, vol. 372, pp. 458-461.

(a) Crawling



(b) Inching



Figure 1 Two dominant modes of locomotion in caterpillars: crawling (a) and inching (b).

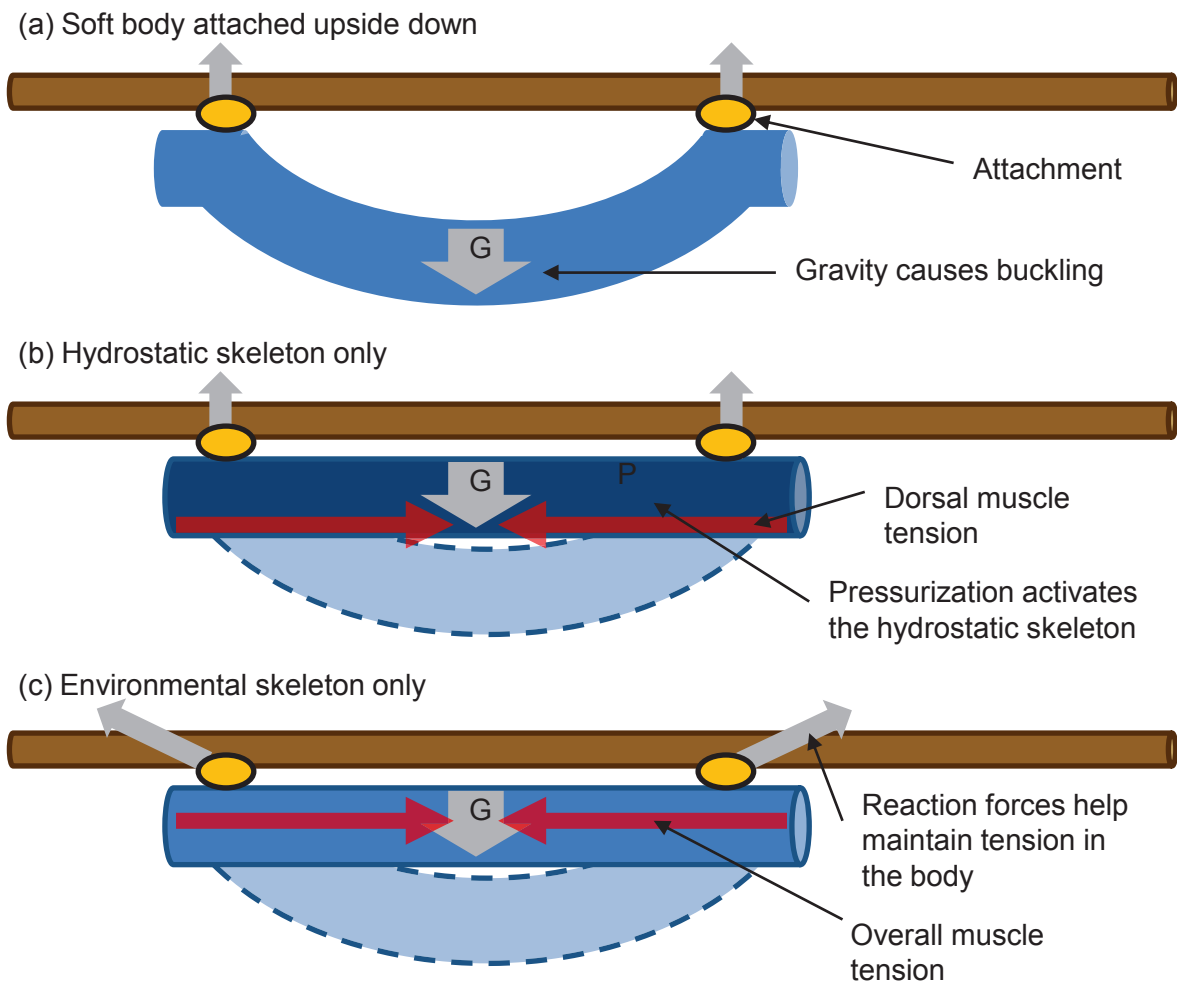
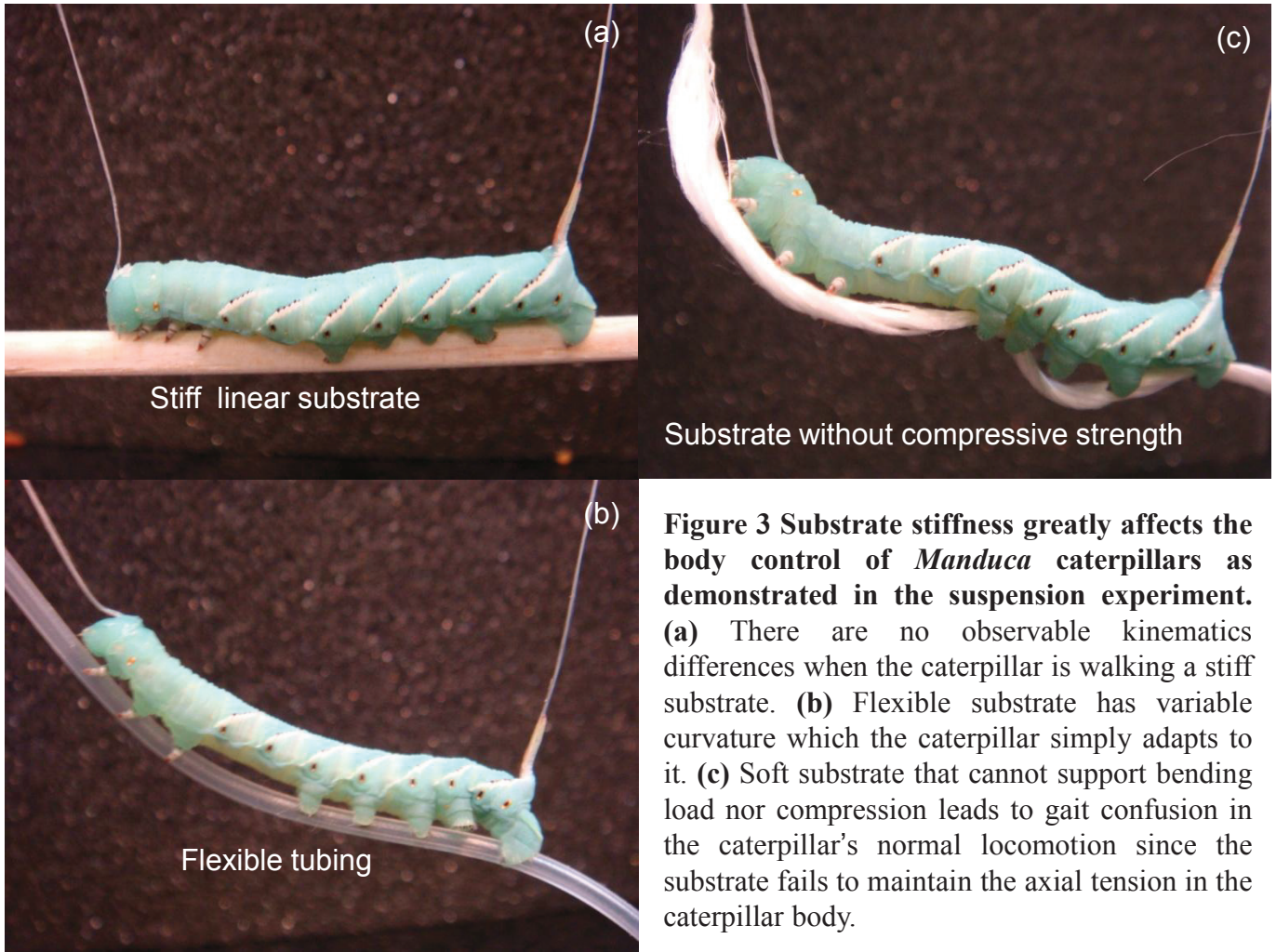


Figure 2 A simple scenario illustrates the difference between using hydrostatic skeleton and environmental skeleton for posture control. (a) A doubly supported soft beam will buckle dramatically under the influence of gravity. (b) Pressurization is one way to increase stiffness and therefore maintaining the linear configuration. The buckling side (dorsal) will experience greater stress according to the beam theory. (c) Alternatively, and overall increase of axial tension can straighten the body without pressurization. Yet the substrate needs to withstand substantial compressive load from the animal without buckling.



Chapter 4: Tissue mechanics and hydrostatic skeleton

The basis of all locomotion is a forceful interaction with the supporting substrate (Dickinson, Farley 2000). For a terrestrial soft bodied animal such as a caterpillar, tissue deformation and structural stability dictate the main substrate interactions. In this chapter, I present a method to describe tissue material properties using continuum mechanics. Specifically, the soft cuticle of *Manduca* caterpillars is modeled with constitutive equations in **Publication-3**. In order to retain all the equations, this publication is attached in its original format. Then I will explore how these nonlinear material properties translate into overall stiffness in a hydrostatic skeleton (**Publication-4**). Before these two publications, however, I would like to first comment on the approaches I took to study tissue mechanics and the caterpillar hydrostatic skeleton. Finally using two behavioral experiments, I will illustrate how the hydrostatic skeleton enables and limits caterpillar locomotion.

4.1 Scaling of constitutive models

Constitutive modeling provides a systematic formulation of material behaviors when loaded in different conditions. However, it is important to clarify two concepts in Publication-3. First of all, the fiber orientation mentioned in the modeling section is a virtual construct to capture the stress-stiffening effect. The actual chitin micro-fibrils in the caterpillar cuticle orient in a helical pattern around the body (Hepburn, Levy 1975) probably with the fiber angle biased to the circumferential direction. Since the hoop stress is higher in the circumferential direction for a long cylinder, the reinforcing fibers tend to align in this direction via stretching. In any case, the goal of phenomenological models is to capture the stress-strain relationship of a class of material with one single parsimonious formulation. In Publication-3, the difference between loading the *Manduca* cuticle in the circumferential and longitudinal directions

can be described by scaling one single parameter among the seven in the model. Much of the mathematics was directed towards achieving this goal.

Another point that needs to be addressed is the ability of a model to account for variations. Biological systems have inherent variations that are sometimes important and all the time present. Constitutive formulations typically use a representative data set which contains all the critical features. However, an experienced modeler would set up the model with adaptive power specific to the types of variation. For example, by changing the parameters J_m and λ_0 in the model presented in Publication-3, one can adjust the model to fit almost any loading-unloading behavior of *Manduca* soft cuticle loaded in any direction. How the model fits the data is a professional judgment based on the modelers' experience. Such a mathematical formulation of the material behavior serves as the basis for simulating any structure built from the given material.

4.2 From nonlinear materials to nonlinear structures

While micromechanical constitutive models have physical implications, phenomenological constitutive models by themselves are primarily just mathematical descriptions. However, using accurate phenomenological models of both the *Manduca* cuticle and muscle (Dorfmann, Trimmer & Woods 2007, Lin, Dorfmann & Trimmer 2009), it is possible to simulate the *Manduca* hydrostatic skeleton for the first time.

As an initial step, accurate biometric data has been incorporated into a simplified structural model to reveal how nonlinear material properties can strongly influence the mechanical performance of a hydrostat (Publication-4). For instance, stress-stiffening allows the caterpillar to change its body flexural stiffness by stressing the body wall. This active structural stiffening during muscle tetanus can be accomplished independent of scale. A detailed discussion of these effects can be found in Publication-4.

4.3 Underwater caterpillar crawl

As the operation of a hydrostatic skeleton is really an interplay between internal body pressure and body load, it is interesting to manipulate the effects of gravity and ambient pressure. One approach is to submerge the animal in water. In this behavioral experiment on the 5th instar *Manduca*, we effectively reverse the direction of body force and ambient pressure. When crawling underwater, caterpillars expel air from the spiracles in the body compression phase. This observation confirms that the body volume is not constant in caterpillars (Fig.4-1A). In fact, some caterpillars even exploit this active exhalation to produce alarm calls when startled (Bura et al. 2011).

The 5th instar *Manduca* caterpillar is buoyant in water at room temperature so the animal crawling underwater not only experiences zero gravity but also an upward body force. If the caterpillar typically uses body force to determine body orientation and heading, then water submergence should confuse the caterpillar. Indeed, many caterpillars tend to crawl downward underwater, reversing their normal tendency to climb up (Fig.4-1B).

4.4 Time-dependency and material adaptation

Both the *Manduca* cuticle model and the hydrostatic skeleton model consider only the static condition. However, time-dependent behaviors are quite important and should be incorporated into future modeling studies. Like many biomaterials, caterpillar soft cuticle also has visco-elastic properties. Higher strain-rates often lead to higher peak stress. More interestingly, the soft cuticle also exhibits stress adaptation. This is a very profound feature for an animal that has a rapidly fluctuating body volume and unpredictable body postures. In effect, the cuticle will undergo time-dependent deformation to release the surface tension as the animal increase its body volume. Conversely, the body wall is capable of re-establishing a baseline stress by shrinking, for example if the animal loses body volume.

Though the cuticle is the toughest material in a caterpillar it adapts to a few percent of deformation in a matter of seconds (Fig.4-2A). This is comparable to the gait period of normal crawling behaviors. Lining the inside of the cuticle are layers of muscle bundles that also adapt to stress over a similar time scale but experience a much larger strain range of 20%. (Fig.4-2B). Therefore, body force transmission is sensitive to the timing of body stretching. During a typical crawl cycle, muscles are stretched to develop tension. At the same time the body wall is partially adapting to the internal pressure fluctuation. These changes compromise the integrity of the hydrostatic skeleton and allow large deformations to occur. As soon as locomotion slows down or is arrested, the muscles adapt to the current body posture and release their accumulated stress automatically. The body wall can also settle to a stable stiffness which is more suitable for maintaining a hydrostatic skeleton for use in other behaviors. Most strikingly, the firing frequency of stretch receptor organs (SRO) associated with the abdominal muscles also exhibit stress adaptation (Fig.4-2C). Each SRO is a modified muscle that sends action potentials back to the central nervous system (CNS) upon stretching. It is possible that such neural adaptation has some mechanical components to it. Although SRO firing adaptation can occur over a time scale of a minute, it occurs most dramatically in the first few second after a length change. It is not known whether or how a caterpillar uses this sensory modality to modulate locomotion (Simon, Trimmer 2009). It is nevertheless striking to see parallel phenomena occurring at different levels in different components of a caterpillar.

4.5 Flexion vs. compression

The second hypothesis of my thesis (*Section 1.5.2*) proposes how caterpillars may change from a crawling gait to an inching gait through changes in body properties and attachments. One possibility is that the body flexion seen in inching locomotion is merely a consequence of removing the mid body substrate attachments. Publication-4 suggests that smaller caterpillars are more likely to make use of a hydrostatic skeleton and can withstand large flexion without unstable buckling. It is possible that body

flexion in inchworms is a result of loading a smaller hydrostatic skeleton longitudinally. The same loading condition leads to axial compression in a larger caterpillar and therefore anterior-grade contraction waves. To test this argument, I suppressed inching movements mechanically in two species of caterpillar: one in the family *Noctuidae* with proleg reduction and one true inchworm from the family *Geometridae*.

During typical locomotion an inchworm brings the posterior segment directly behind the thorax and loops the body away from the substrate (Fig.4-3A). If we place a heavy duty plastic film on top of an inchworm, the animal will be mechanically constrained from looping its body upward. The result is a characteristic crawling gait closely resembling that of other larger crawling caterpillars (Fig.4-3B). The gait period is slightly faster than typical crawling and more like that of inching. The abdominal segments undergo a series of anterior-grade contractions but there are no mid-abdominal prolegs to anchor these traveling deformations. Indeed, occasionally between crawl cycles, the inchworm body buckles into a lateral looping conformation (Fig.4-3C). Inching gait can be restored instantly by removing the plastic film or as the animal emerges from under the film (Fig.4-3D).

An even more dramatic demonstration of gait transition can be found in noctuid larva which only have vestigial A3-A4 prolegs and typically prefer to inch. During normal locomotion, this caterpillar pulls the posterior segments forward to meet the thorax dynamically at very high cyclic frequencies up to ~3Hz (Fig.4-4). The speed is comparable or even faster to inching by true inchworms (*Geometridae*). Despite the speed, this inching is still reminiscent of crawling because the terminal prolegs are detached before all the other abdominal prolegs. The A6 and A5 prolegs detach from the substrate within 30ms to each other. However, proleg reattachment sequencing is the same as a crawling gait with the terminal prolegs planted first. Unstable postures can be observed when the abdomen is slightly off center and the animal drags the posterior segment along the substrate, perhaps to help with stability. The thorax also does not

lift before the A4 prolegs are properly planted. Then, the body extension is a careful and deliberate movement which occupies more than 60% of the crawl cycle. This noctuid larva is twice the size of the inchworm described previously, and it seems to have much harder time holding its body using a hydrostatic skeleton alone.

This same noctuid is much more likely to crawl consistently under a plastic film (Fig.4-5). However, there is no major alteration of the gait cycling frequency or proleg attachment sequence. Very slight buckling can be seen at the anterior segments as soon as the A6-A5 prolegs are disengaged. Otherwise, the body deforms by compressing rather than bending, and such deformation travel forward just like typical crawling. A normal fast inching gait can be recovered as the animal emerges from under the plastic film. Perhaps the most striking finding of all is that this transition from crawling to inching can occur during a single gait cycle, instead of at the onset of the new step. In other words, the gait switch has a strong mechanical component. It is predicted that the mid-body attachment in this species would lead directly to a crawling gait if the A3-A4 prolegs were functional. From inching to crawling, a caterpillar can simply lock down its mid body segments and relax the hydrostatic skeleton to allow segmental compression.

References

- Bura, V.L., Rohwer, V.G., Martin, P.R. & Yack, J.E. 2011, "Whistling in caterpillars (*Amorpha juglandis*, Bombycoidea): sound-producing mechanism and function", *The Journal of experimental biology*, vol. 214, no. Pt 1, pp. 30-37.
- Dickinson, M.H. & Farley, C.T. 2000, "How Animals Move: An Integrative View", *Science*, vol. 288, no. 5463, pp. 100.
- Dorfmann, A.L., Trimmer, B.A. & Woods, W.A. 2007, "A constitutive model for muscle properties in a soft-bodied arthropod", *J.Roy.Soc.Interface*, vol. 4, pp. 257-269.
- Hepburn, H.R. & Levy, P. 1975, "Mechanical properties of some larval cuticles", *J.Entomol.Soc.S.Afr.*, vol. 38, pp. 131-141.
- Lin, H.T., Dorfmann, A.L. & Trimmer, B.A. 2009, "Soft-cuticle biomechanics: A constitutive model of anisotropy for caterpillar integument", *Journal of theoretical biology*, vol. 256, no. 3, pp. 447-457.
- Simon, M.A. & Trimmer, B.A. 2009, "Movement encoding by a stretch receptor in the soft-bodied caterpillar, *Manduca sexta*", *Journal of Experimental Biology*, vol. 212, no. 7, pp. 1021.

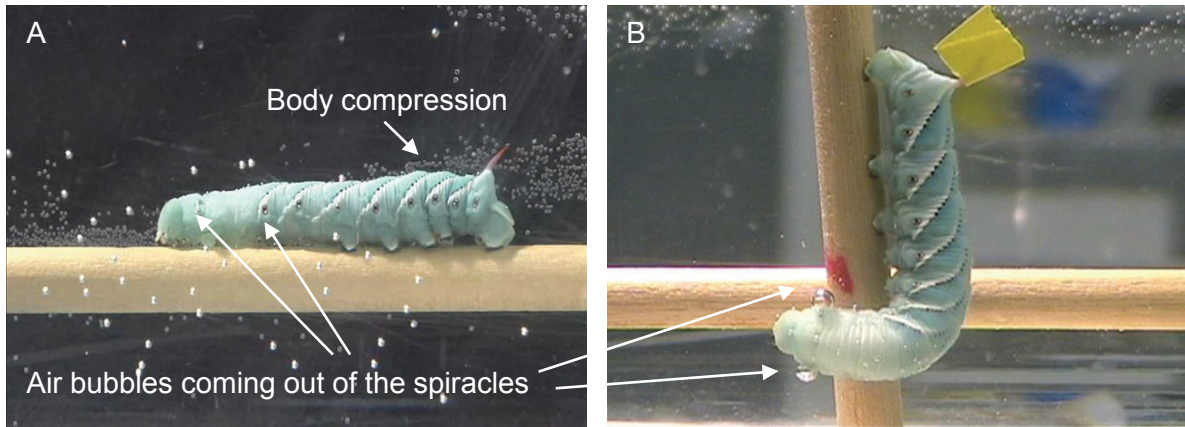


Fig.4-1 Underwater crawling. (A) Water submersion experiments dramatically increase the ambient pressure and reverse the direction of body load (5th instar caterpillars are buoyant in water). The resulting locomotion is surprisingly normal. (B) Air is apparently expelled during body compression through the spiracles. The body volume is clearly not constant and the hydrostatic skeleton is probably not constantly engaged.

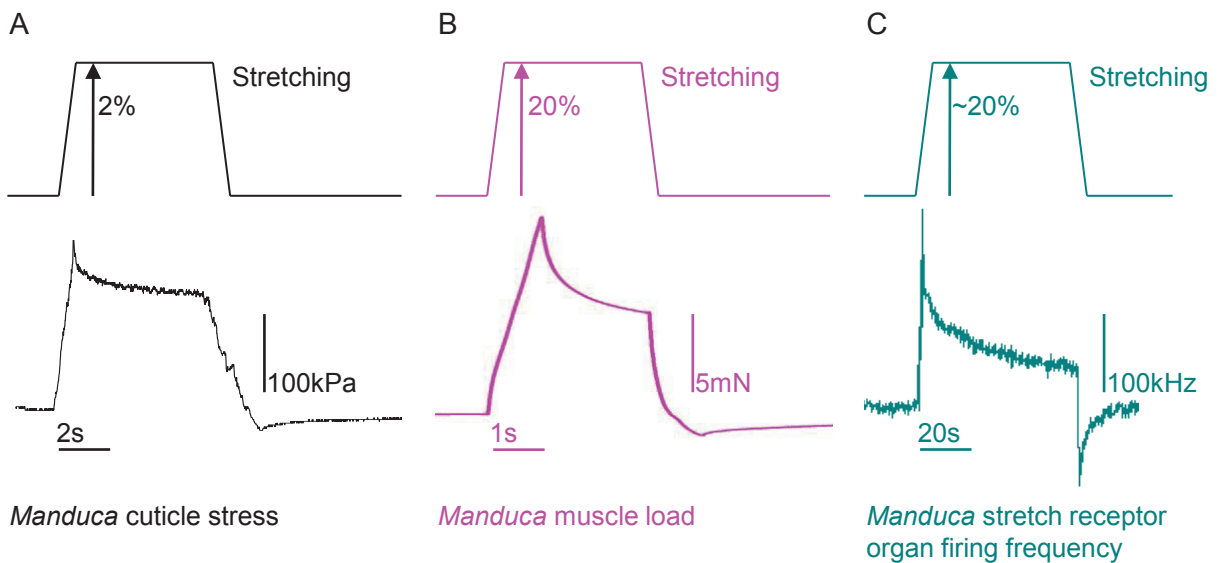


Fig.4-2 Stress adaptation in response to stretch-and hold. (A) The caterpillar cuticle stress quickly decays exponentially when held at a certain stretch. After the initial strain is restored, the cuticle gradually reestablishes internal stress. This particular sample was undergoing uni-axial test in a direction along the body axis of a *Manduca* caterpillar. (B) Along the same axis, the caterpillar longitudinal muscles also release load when held in position and recover forces when slackened. They are anatomically lining just beneath the cuticle, and are at least two orders of magnitude softer than the cuticle. (C) Still in the direction of the animal's body axis, stretch receptor organs are modified muscles tissues that send action potentials back to the central nervous system. They also exhibit stress adaptation in the form of their firing frequency.



Fig.4-3 Gait suppression in an inchworm. (A) Normally a true inchworm (family *Geometridae*) loops its body away from the substrate during locomotion. (B) Placing a plastic film can mechanically induce crawling gait by preventing the body from flexing upward. (C) Occasionally the body buckles sideways as the inchworm attempts to crawl faster. (D) The removal of the physical constraint immediately recovers the inching gait.

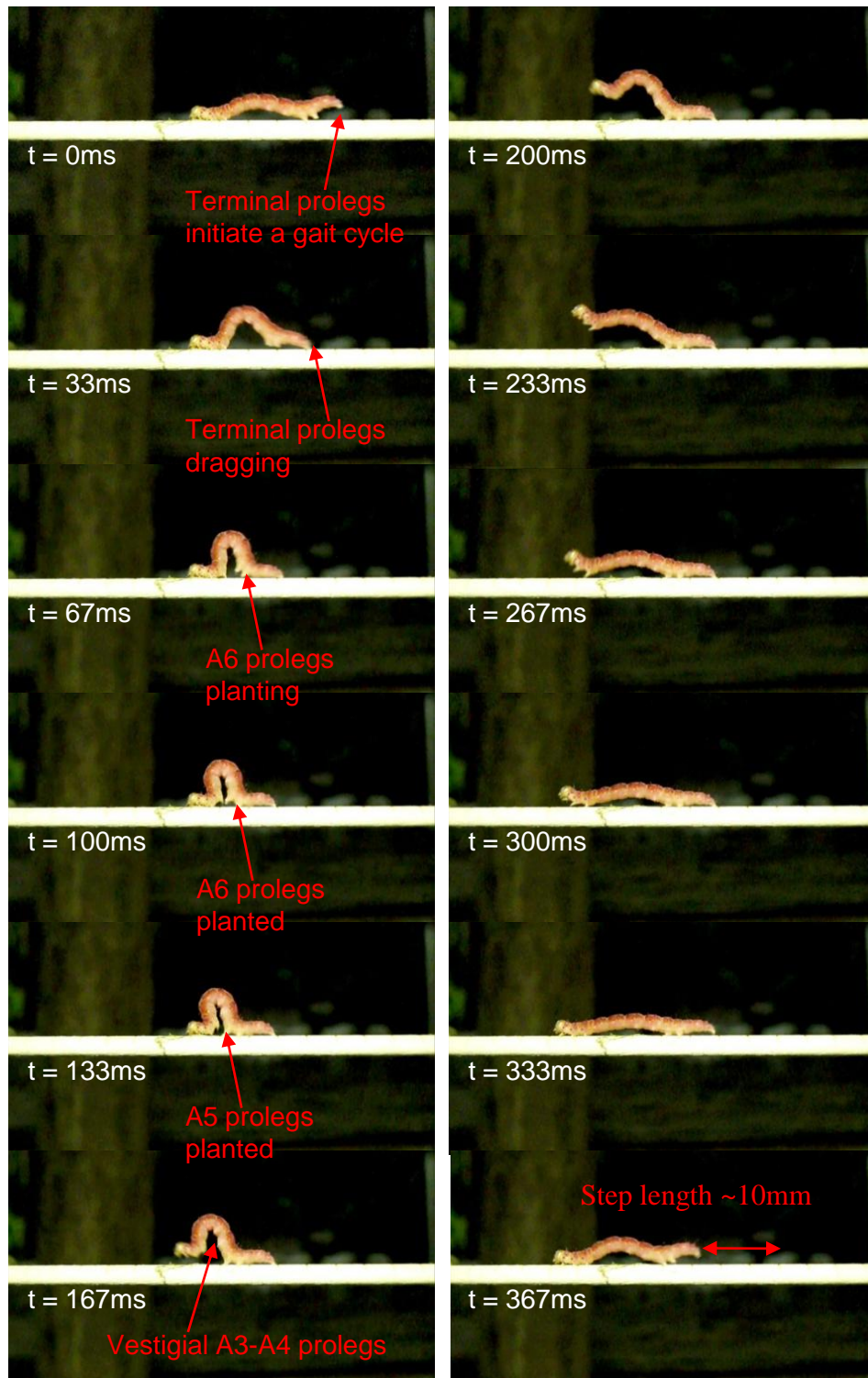


Fig.4-4 Natural fast inching. This *noctuid* caterpillar has vestigial A3 and A4 prolegs and prefers to inch. The inching gait, however, is very fast. The abdomen contraction was completed within 60ms.

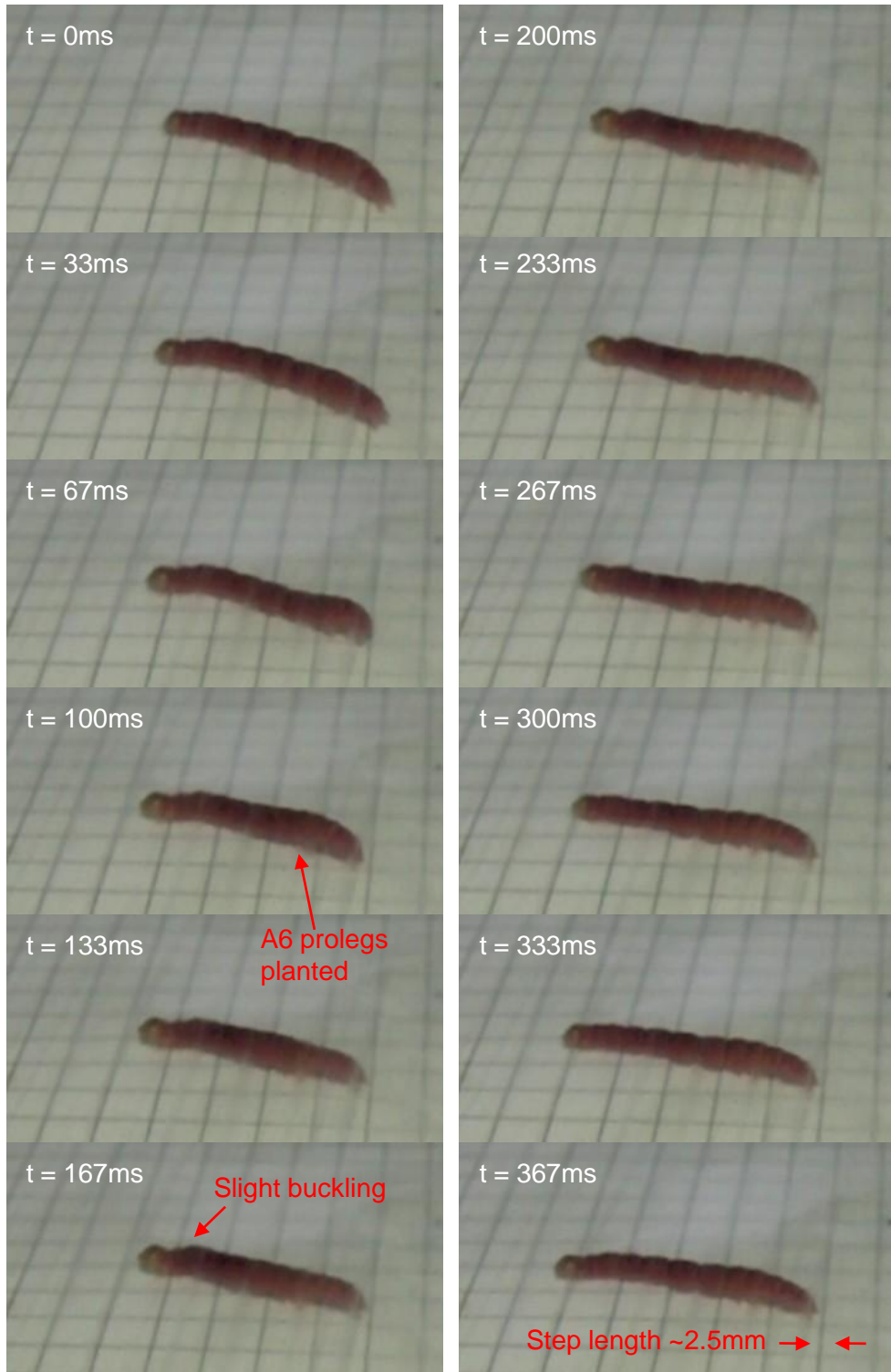


Fig.4-5 Mechanically induced crawling gait. The stereotypic crawling gait can be induced from the same *noctuid* caterpillar in **Fig.4-4**. Interestingly, the crawl cycle frequency and prolegs coordination are exactly identical to the original inching gait, except that the step length has been reduced to only a quarter or less.

Publication-3

Title: Soft-cuticle biomechanics: A constitutive model of anisotropy for caterpillar integument

Authors: Huai-Ti Lin, Luis Dorfmann and Barry Trimmer

Keywords: *Manduca sexta*; Soft cuticle; Finite deformations; Anisotropy; Constitutive modeling; Pseudo-elasticity; Biomechanics; Fiber reinforcement

Abstract

The mechanical properties of soft tissues are important for the control of motion in many invertebrates. Pressurized cylindrical animals such as worms have circumferential reinforcement of the body wall; however, no experimental characterization of comparable anisotropy has been reported for climbing larvae such as caterpillars. Using uniaxial, real-time fluorescence extensometry on millimeter scale cuticle specimens we have quantified differences in the mechanical properties of cuticle to circumferentially and longitudinally applied forces. Based on these results and the composite matrix–fiber structure of cuticle, a pseudo-elastic transversely isotropic constitutive material model was constructed with circumferential reinforcement realized as a Horgan–Saccomandi strain energy function. This model was then used numerically to describe the anisotropic material properties of *Manduca* cuticle. The constitutive material model will be used in a detailed finite-element analysis to improve our understanding of the mechanics of caterpillar crawling.



Soft-cuticle biomechanics: A constitutive model of anisotropy for caterpillar integument

Huai-Ti Lin^{a,c}, A. Luis Dorfmann^{b,c,*}, Barry A. Trimmer^{a,c}

^a Department of Biology, Tufts University, Medford, MA 02155, USA

^b Department of Civil and Environmental Engineering, Tufts University, Medford, MA 02155, USA

^c Tufts Biomimetic Devices Laboratory, 200 Boston Ave., Suite 2100, Medford, MA 02155, USA

ARTICLE INFO

Article history:

Received 23 July 2008

Received in revised form

5 October 2008

Accepted 9 October 2008

Available online 29 October 2008

Keywords:

Manduca sexta

Soft cuticle

Finite deformations

Anisotropy

Constitutive modeling

Pseudo-elasticity

Biomechanics

Fiber reinforcement

ABSTRACT

The mechanical properties of soft tissues are important for the control of motion in many invertebrates. Pressurized cylindrical animals such as worms have circumferential reinforcement of the body wall; however, no experimental characterization of comparable anisotropy has been reported for climbing larvae such as caterpillars. Using uniaxial, real-time fluorescence extensometry on millimeter scale cuticle specimens we have quantified differences in the mechanical properties of cuticle to circumferentially and longitudinally applied forces. Based on these results and the composite matrix–fiber structure of cuticle, a pseudo-elastic transversely isotropic constitutive material model was constructed with circumferential reinforcement realized as a Horgan–Saccomandi strain energy function. This model was then used numerically to describe the anisotropic material properties of *Manduca sexta* cuticle. The constitutive material model will be used in a detailed finite-element analysis to improve our understanding of the mechanics of caterpillar crawling.

© 2008 Elsevier Ltd. All rights reserved.

1. Introduction

Soft-bodied invertebrates such as caterpillars do not have a rigid skeleton and must use soft tissues and muscles to transmit forces during movements and to hold the body contents in place. If the body morphology is maintained by hydrostatic pressure then the body wall must be under constant stress (Niebur and Erdos, 1991). Under these circumstances the passive properties of the soft body wall could exert a major influence on the morphology and deformation of the animal.

Many soft-bodied animals can be described mechanically as constant volume hydrostats with a tendency to form spherical structures (Wainwright, 1988). However, in the periods between each molt, cylindrical caterpillars dramatically increase in size while their proportions (ratio of diameter to length) do not change significantly. Early work by Carter and Locke directly addressed this paradox. Using microscopic and histological techniques, they showed how during growth soft cuticle expands

more in the axial than the circumferential direction through the unfolding of microscopic pleats in the endocuticle (Carter and Locke, 1993). While stretching causes reinforcing fiber realignment in the circumferential direction, the axial pleats reduce this realignment along the animal's axis. The unfolding of pleats is essentially a structural compensation to maintain proportions during growth. However, aside from growth considerations caterpillars are still pressurized cylinders in which hoop stresses are twice the axial stresses and it is unknown how the material properties of the body wall are adapted to this difference.

Although internal muscles attached to the body wall have been previously modeled and shown to be nonlinearly pseudo-elastic (Dorfmann et al., 2007, 2008), no comparable work has been done on the integument. According to the limited data on *Manduca sexta* body pressure, the cuticle has to withstand a baseline pressure of several kPa (Mezoff et al., 2004). During locomotion and vigorous body swings (such as the strike reflex to noxious stimuli), local cuticle stretch may increase significantly via muscle action as well as pressure fluctuation. There are three aims in this project. First, we experimentally characterize the soft-cuticle properties in comparison to known tissue mechanics. Secondly, we formulate a phenomenological constitutive model to capture the mechanical response and finally, we explore the mechanics in the functional context of locomotion.

* Corresponding author at: Department of Civil and Environmental Engineering, Tufts University, Boston Avenue, Medford, MA 02155, USA. Tel.: +1617 627 6137.

E-mail addresses: Huai-Ti.Lin@tufts.edu (H.-T. Lin), Luis.Dorfmann@tufts.edu (A.L. Dorfmann), Barry.Trimmer@tufts.edu (B.A. Trimmer).

URLs: <http://ase.tufts.edu/msml/> (A.L. Dorfmann), <http://ase.tufts.edu/bdl/> (B.A. Trimmer).

Biological materials have stimulated a renewed interest in understanding the mechanical behavior of complex composites (Freier et al., 2005; Chen et al., 2006b; Vincent and Wegst, 2004). Insect cuticle is particularly attractive due to its light weight, adjustable strength, and bio-compatibility (Vincent, 2002). Insect integument consists of many components including stiff chitin microfibrils, elastomeric proteins such as resilin, lipids and heavy metals: their mechanical properties can change dramatically with small changes in composition such as the water content (Hepburn, 1972). In fact, insect cuticle stiffness can vary by eight orders of magnitude from 100 kPa to tens of GPa while appearing to have the same basic structure (Vincent and Wegst, 2004). More specifically, endocuticle seems to be responsible for most of the mechanics in soft cuticle. It often develops anisotropy, depending on the pre-stress during morphogenesis (Neville, 1967a).

Endocuticle is a continuously growing structure consisting of a silk-like protein matrix embedded with hydrophobic chitin nanofibrils (Wolfgang and Riddiford, 1986). Within this complex, layers of parallel fibers shift in orientation over successive lamina (Hepburn and Ball, 1973; Dennell, 1976; Hepburn, 1976), causing the well-known helicoidal appearance as described by Neville (1975) and Neville and Levy (1984). This cross fiber reinforcing strategy is biologically common (Locke, 1958) and has been intensely studied for its biomedical applications (Sanchez et al., 2005; Giraud-Guille, 1992; Belamie et al., 2006). In addition, cuticle chitin orientation changes by daily growth layers and has been documented in many insects (Neville, 1967b) and shown by scanning electron microscopy (Hughes, 1987).

The predominant molecular conformation of soft insect cuticle protein is antiparallel beta-pleated sheet (Iconomidou et al., 2001), and alpha chitin crystals are likely to bind to these proteins via H-bonds (Atkins, 1985). It has been proposed that protein hydrophobicity could take part in the control of cuticle hydration (Vincent, 2002). Further analysis on *Manduca* cuticular protein reveals the dynamic trafficking of proteins between endocuticular laminae and the hemolymph (Csikos et al., 1999). Like mammalian skeletons, caterpillar cuticle is more than just a passive structure; it is subject to constant chemical modulation by the body and acts as a protein storage and buffer, even though the chitin fibers do not change once laid down (Condoulis and Locke, 1966). Such dynamics can be demonstrated in the reversible 5-HT mediated plasticization of *Rhodnius* larvae cuticle (Reynolds, 1975).

Anatomically, *Manduca* only has a few oblique muscles and no circumferential muscles. The internal hemocoel is not physically compartmentalized so hydraulic pressure must be distributed over the entire body to minimize the energy. To accommodate about 10-fold change in volume within each intermolt period, the cuticle stretches with intussusceptions and unfolding. It has been shown that new 5th instars can be inflated to roughly twice their size, whereas the late 5th instar animals typically quadruple in volume (Wolfgang and Riddiford, 1981). This implies that *Manduca* caterpillars do not wrinkle less as they get bigger. In fact, their growth is close to linear scaling until the cessation of cuticle deposition. In 5th instar *Manduca*, cuticle thickness increases linearly with the body weight, but its stiffness declines due to growing hydration (Wolfgang and Riddiford, 1987). If the cuticle must maintain caterpillar's cylindrical morphology, anisotropy is expected to reinforce the circumferential direction as previously illustrated (Wainwright, 1982). While no such anisotropy has been reported, we hereby examine the mechanical properties of caterpillar cuticle in more detail using high resolution material testing equipment. For analytical purposes, we divide the endocuticle into three components: a homogeneous three-dimensional protein gel, an amorphous fibril two-dimensional reinforcement, and some fiber network with a preferred direction.

Following the tradition of nonlinear solid mechanics, we can characterize soft fiber-reinforced materials by deriving the constitutive relationship from an objective strain energy function (Holzapfel et al., 2000; Holzapfel, 2006). The proposed constitutive model accounts for large deformation, for the nonlinear pseudo-elastic material response and is suitable for implementation into a finite-element code. The long-term goal of this work is to use such material models in a detailed finite-element analysis of the caterpillar to improve our understanding on how the mechanical properties of soft tissues are exploited to control supply movements.

2. Experimental methods

Cuticle morphogenesis is rapid during the fifth instar so *Manduca* caterpillars were developmentally synchronized (Copenhaver and Truman, 1982) and used at 12 h post-ecdysis. Caterpillars were dissected, and two cuticle strips (5×1 mm) were harvested near the 3th abdominal segment (A3) dorsal midline from each animal. The circumferential strip was taken from the second annulus (there are eight annulus per segment) of A3, while the longitudinal strip was taken along the rest of the dorsal midline as shown in Fig. 1. Pilot tests showed that other abdominal segments are mechanically similar. The cuticle thickness (0.05 mm) was determined by identifying the endocuticle span in tissue cross section scanning electron micrograph. Great care was taken to avoid the inter-segmental folds for the longitudinal specimen and the inter-annulus crests for the circumferential specimen. Dissected cuticle strips were fragile, so the bonding margins were first treated with biological glue and then encapsulated by UV cured epoxy (Loctite, modified acrylamide) to produce specimen handles.

Uniaxial tests—The mechanical tests were performed in *Manduca* saline at room temperature (27 °C). One end of the specimen was fixed on an epoxy platform submerged in saline via the specimen handle. The other handle was attached to a Dual-Mode Lever System (Aurora Scientific Inc., Ontario, Canada) via a steel pin. The servo motor could be controlled by an analog voltage signal and the coupled load cell measured the instantaneous torque. Data were digitized at 100 Hz (NI PCI-2669 data acquisition board, National Instrument, Austin, TX). See the schematic in Fig. 2 for details.

Real-time extensometry—Green fluorescent microspheres (169 $\mu\text{m}/468$ nm peak excitation/508 nm, peak emission; Duke Scientific Co., Fremont, CA) were fixed about 2 mm apart along the stretching axis on the epicuticle side using lanolin. Four blue LEDs (465 nm; LEDtronics Inc., Torrance, CA) provided the optical excitation under a custom made shade. A black and white CCD camera Basler A602 (Basler Vision Tech., Ahrensburg, Germany) captured the specimen image via a compound dissection scope at $\times 12$ magnification as shown in Fig. 3. A custom LabView program (National Instrument, Austin, TX) acquired and analyzed the

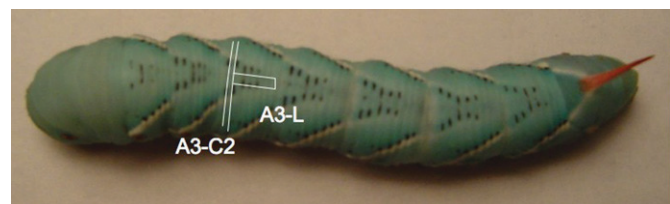


Fig. 1. Cuticle specimens were harvested from the dorsal abdominal segment three of a 12 h post-ecdysis *Manduca sexta* caterpillar. This figure shows the exact locations of the circumferential strip (A3-C2) and the longitudinal strip (A3-L) as labeled.

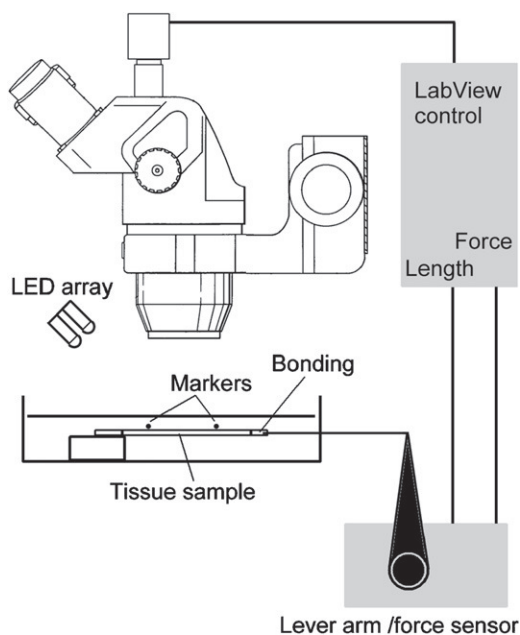


Fig. 2. The experimental setup consists of a camera equipped dissecting scope looking down into an LED lit *Manduca* saline dish where the cuticle specimen is being stretched by the servo lever arm. This uniaxial test, with real-time feedback from the image analysis, records the local deformation of the tissue and the associated tensile force.

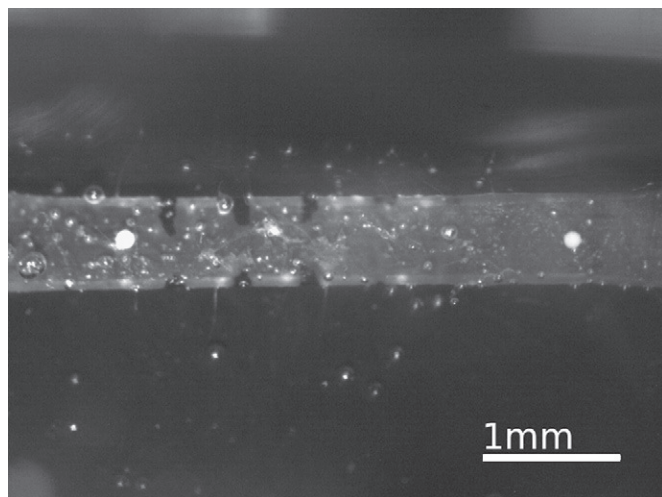


Fig. 3. Through the CCD camera on the microscope, we can resolve the fluorescent microspheres placed on the specimen. The LabView program fits the best circles around these two markers and performs real-time distance calculation.

images delivered by the IEEE1394 connection for real-time feedback control. In order to smooth out the major folds on the specimens, a pre-stretch was applied corresponding to an initial tensile load of 3.9 mN, equivalent to the baseline fluctuation of the load cell. The initial length between the fluorophores was averaged for 3 s and taken as the normalizing factor for all subsequent stretch calculation for the same specimen. The initial specimen dimensions were measured using ImageJ (NIH) and the microspheres as calibration references.

Cyclic loading—Each specimen was loaded at a quasi-static rate to a predefined maximum stretch of 1.06, which is slightly smaller than the stretch at failure. Unloading followed at the same quasi-static rate and terminated when the initial preload was reached. Six periodic loading–unloading cycles were repeated without intermission as indicated in Fig. 4.

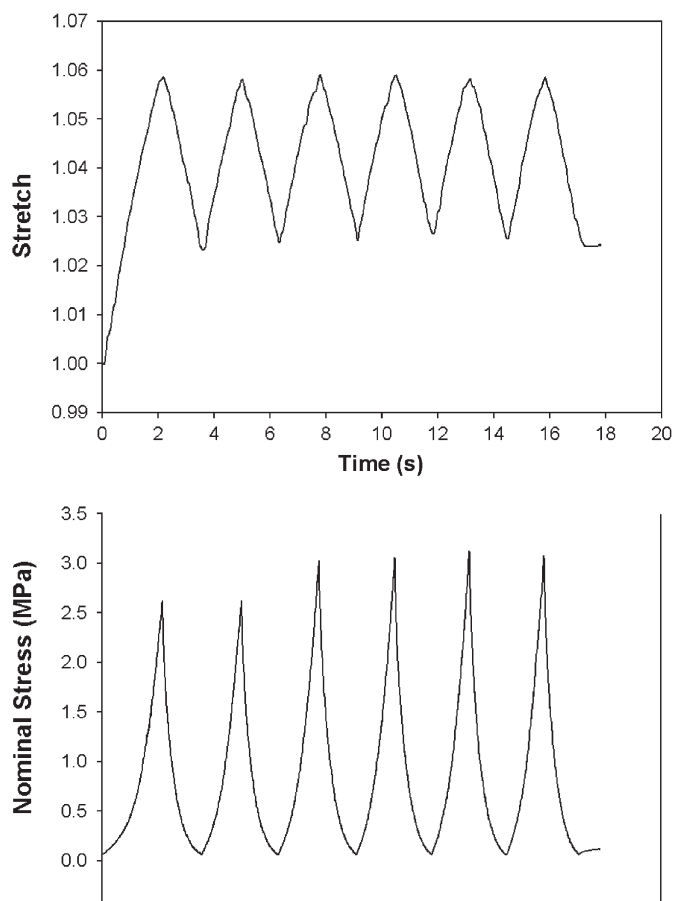


Fig. 4. A sample set of uniaxial data illustrates how the test was performed. Stretch and stress data were filtered by low-pass (2 Hz) Gaussian smoothing function. The specimen was stretched from unity stretch steadily to around 1.06 and cycled back until the initial preload was resumed. The initial offset of the nominal stress represents the preload. Nonlinearity is clear in the stress curves. Incidentally, the slight step-up of the later four peaks may be a stress-stiffening effect which is not quantified at this stage.

Numerical simulation—To simplify the formulation of the constitutive equation, it is convenient to treat the cuticle as an incompressible homogenized solid. The kinematic constraint of incompressibility is frequently adopted in the experimental and mathematical characterization of biological tissues, even if they contain a high percentage of intracellular and extracellular water. For example, arteries (Humphrey, 2002) and brain tissue (Franceschini et al., 2006) experience nearly isochoric deformations when subject to uniaxial loading conditions. In particular, the value of Poisson's ratio of brain parenchyma in drained uniaxial stress experiments has been found to be equal to 0.496 (Franceschini et al., 2006). This compares to Poisson's ratio of 0.5 corresponding to completely incompressible material behavior. Since the cuticle contains chitin fibers in a distribution of orientations, it is treated as a fiber-reinforced composite material. A transversely isotropic strain energy function is constructed to accurately describe the experimental data in both orientations. Numerical simulation and modeling were done in Matlab 2007a (MathWorks, Natick, MA). Without the complete ultra-structural analysis, we did not attempt to correlate model parameters to physiological mechanisms. They merely serve to capture qualitative features and scaling. This is consistent with the phenomenological approach, where model parameters are not correlated to information on the microstructure. Tests were carried out on 39 specimens from 18 animals, leading to technical refinements and three final successful complete tests. The test data shown in this

paper are from these three qualitatively similar sets of experimental results from three animals.

3. Experimental results

To assess the stress–strain response and associated anisotropy of the cuticle, periodic loading–unloading uniaxial extension tests were carried out at constant temperature of 27 °C. During each of the tests, the cuticle specimen was subjected to six cycles of pre-conditioning with constant strain rate up to pre-selected extension with stretch $\lambda = 1.06$. The pre-conditioning was performed in order to monitor the progression of stress softening and to determine the ultimate stress–deformation response for stretches up to $\lambda = 1.06$. The results are reported as Cauchy stress versus stretch λ and are shown in Fig. 5. The following observations are made:

- The mechanical response of the material in the longitudinal and circumferential directions is highly nonlinear. The increase in stress with stretch is exponential and similar to many other biological tissues (Fung, 1993).
- After the first loading–unloading cycle, the specimen does not return to the stress-free reference configuration. The accumulated residual strain may be time dependent, but this aspect has not yet been investigated in detail. The time dependent response is currently being evaluated.
- The stresses corresponding to the same stretch are larger for specimens loaded in the circumferential direction compared to specimens loaded in the longitudinal direction. This clearly indicates anisotropy in the material response.
- There are large differences in the stresses corresponding to the same stretch during loading and subsequent unloading. This is true for longitudinal and circumferential specimens. The area enclosed by the loading and unloading responses represents dissipation of energy.
- There is a reduction in the stress (stress softening) at a given stretch between the first and second loading. This reduction has only been observed for specimens loaded in the circumferential direction. This may indicate that stress softening is associated with the anisotropy of the material.

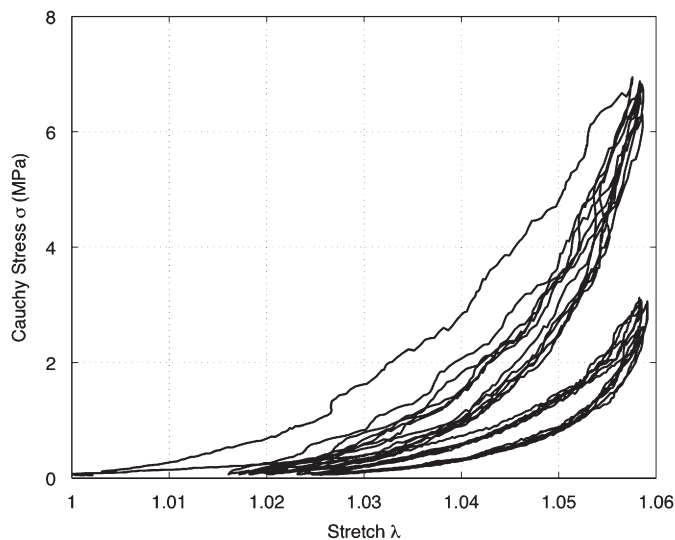


Fig. 5. The experimental response during cyclic loading of the cuticle harvested from *Manduca sexta* in the circumferential (upper trace) and axial directions (lower trace). The two specimens exhibit very similar nonlinear responses, and yet differ by roughly a factor of two in scale.

- After two pre-conditioning loading–unloading cycles the stress–stretch response of circumferential specimens is essentially repeatable and additional stress softening is not observed.

4. Constitutive modeling

Based on the experimental data shown in Section 3 the cuticle of the *Manduca* can be treated as a transversely isotropic nonlinear elastic material. The initial loading and subsequent unloading stress–stretch curves do not coincide indicating energy dissipation. Upon complete unloading, the material does not return to the initial state corresponding to the stress-free reference configuration, but exhibits a residual strain or permanent set. Therefore, the objective is to develop a constitutive model that accounts for the observed material response. We focus on the quasi-static context and do not allow material properties and deformation to depend on time.

In this section, we introduce the necessary notations to describe the kinematics, summarize appropriate strain and stress tensors along with their associated invariants. Constitutive laws for isotropic and transversely isotropic hyperelastic materials will be derived. The theory of nonlinear mechanics of continua can be found, for example, in the books by Ogden (1997) and Holzapfel (2000).

4.1. Kinematic

To describe a deformation, we denote the stress-free reference configuration of the subject by \mathcal{B}_r and identify a generic material point by its position vector \mathbf{X} relative to an arbitrary chosen origin. Application of mechanical forces deforms the body, so that the point \mathbf{X} occupies the new position $\mathbf{x} = \chi(\mathbf{X})$ in the deformed configuration \mathcal{B} . The vector field χ describes the deformation of the body and assigns to each point \mathbf{X} a unique position \mathbf{x} in \mathcal{B} and vice versa attributes a unique reference position \mathbf{X} in \mathcal{B}_r to each point \mathbf{x} . In other words, the deformation function χ is a one-to-one mapping with suitable regularity properties.

The deformation gradient tensor \mathbf{F} relative to \mathcal{B}_r is defined by

$$\mathbf{F} = \text{Grad } \mathbf{x}, \tag{1}$$

Grad being the gradient operator with respect to \mathbf{X} . The Cartesian components are $F_{i\alpha} = \partial x_i / \partial X_\alpha$, where x_i and X_α are the components of \mathbf{x} and \mathbf{X} , respectively, with $i, \alpha \in \{1, 2, 3\}$. Roman indices are associated with \mathcal{B} and Greek indices with \mathcal{B}_r . We also adopt the standard notation $J = \det \mathbf{F}$, with the convention $J > 0$.

The deformation gradient can be decomposed according to the unique polar decomposition

$$\mathbf{F} = \mathbf{R}\mathbf{U} = \mathbf{V}\mathbf{R}, \tag{2}$$

where \mathbf{R} is a proper orthogonal tensor and \mathbf{U} and \mathbf{V} are positive definite and symmetric, respectively, the right and left stretch tensors. These can be expressed in spectral form. For \mathbf{U} , for example, we have the spectral decomposition

$$\mathbf{U} = \sum_{i=1}^3 \lambda_i \mathbf{u}^{(i)} \otimes \mathbf{u}^{(i)}, \tag{3}$$

where the principal stretches $\lambda_i > 0$, $i \in \{1, 2, 3\}$, are the eigenvalues of \mathbf{U} , $\mathbf{u}^{(i)}$ are the (unit) eigenvectors of \mathbf{U} , and \otimes denotes the tensor product. For volume preserving (isochoric) deformation (good assumption for biomaterials), using Eqs. (2) and (3), we have

$$J = \det \mathbf{F} = \det \mathbf{U} = \det \mathbf{V} = \lambda_1 \lambda_2 \lambda_3 \equiv 1. \tag{4}$$

Using the polar decomposition (2), we define

$$\mathbf{C} = \mathbf{F}^T \mathbf{F} = \mathbf{U}^2, \quad \mathbf{B} = \mathbf{F} \mathbf{F}^T = \mathbf{V}^2, \quad (5)$$

which denote the right and left Cauchy–Green deformation tensors, respectively. According to the theory of invariants (Spencer, 1971), there exist three principal invariants for \mathbf{C} , equivalently \mathbf{B} , defined by

$$I_1 = \text{tr } \mathbf{C}, \quad I_2 = \frac{1}{2}[(\text{tr } \mathbf{C})^2 - \text{tr}(\mathbf{C}^2)], \quad I_3 = \det \mathbf{C} = J^2, \quad (6)$$

where tr is the trace of a second-order tensor. Alternatively, in terms of principal stretches, the invariants I_1, I_2, I_3 are expressed as

$$I_1 = \lambda_1^2 + \lambda_2^2 + \lambda_3^2, \quad I_2 = \lambda_1^2 \lambda_2^2 + \lambda_2^2 \lambda_3^2 + \lambda_3^2 \lambda_1^2, \quad I_3 = \lambda_1^2 \lambda_2^2 \lambda_3^2. \quad (7)$$

The *Manduca* cuticle has anisotropic material properties associated with chitin fibers embedded in the integument protein matrix which we assume to be isotropic relative to the chitin content. In a macroscopic sense, the cuticle has a preferred orientation in the circumferential direction and can therefore be regarded as transversely isotropic. Such anisotropy may be due to a biased fiber orientation as suggested in previous literatures (Seidel et al., 2008; Chen et al., 2006a; Hughes, 1987). Let the unit vector \mathbf{M} define the preferred direction in the reference configuration \mathcal{B}_r . Additional invariants, denoted I_4 and I_5 and associated with the direction \mathbf{M} , are given by

$$I_4 = \mathbf{M} \cdot \mathbf{C} \mathbf{M} = \mathbf{F} \mathbf{M} \cdot \mathbf{F} \mathbf{M} = \mathbf{m} \cdot \mathbf{m}, \quad (8)$$

$$I_5 = \mathbf{M} \cdot \mathbf{C}^2 \mathbf{M} = \mathbf{m} \cdot \mathbf{B} \mathbf{m}, \quad (9)$$

where we introduced the notation $\mathbf{m} = \mathbf{F} \mathbf{M}$ to define the mapping of \mathbf{M} under the deformation \mathbf{F} .

There is a simple geometric interpretation for the invariant I_4 . The square root of I_4 provides the stretch of the material in the direction \mathbf{M} . Unfortunately, there is no similar kinematical interpretation for I_5 .

4.2. Hyperelastic materials

The theory of hyperelasticity characterizes the elastic response of a body by a strain energy function W defined per unit volume in the reference configuration \mathcal{B}_r . For a homogeneous materials W depends only on the deformation gradient \mathbf{F} and we write $W = W(\mathbf{F})$. In this paper we restrict attention to incompressible materials, subject to constraint (4). Therefore, the nominal stress tensor \mathbf{S} and the symmetric Cauchy stress tensor $\boldsymbol{\sigma}$ are given, respectively, by

$$\mathbf{S} = \frac{\partial W}{\partial \mathbf{F}} - p \mathbf{F}^{-1}, \quad \boldsymbol{\sigma} = \mathbf{F} \frac{\partial W}{\partial \mathbf{F}} - p \mathbf{I}, \quad (10)$$

where p is an arbitrary hydrostatic pressure. Eq. (10) shows that for an incompressible material, the Cauchy stress $\boldsymbol{\sigma}$ and the nominal stress \mathbf{S} are related by $\boldsymbol{\sigma} = \mathbf{F} \mathbf{S}$.

Let the unit vector \mathbf{M} describe the preferred direction of a transversely isotropic material in the reference configuration \mathcal{B}_r . The material response is indifferent to an arbitrary rotation about the direction \mathbf{M} . Also the response is not altered by a change of direction from \mathbf{M} to $-\mathbf{M}$. Following the analysis of such materials given by Spencer (1971) and Ogden (2001), we define a transversely isotropic material as one for which the strain energy W is an isotropic function of the two tensors \mathbf{F} and $\mathbf{M} \otimes \mathbf{M}$. For an incompressible material $I_3 \equiv 1$ and the form of W is reduced to dependence on the four independent invariants I_1, I_2, I_4, I_5 . We write $W = W(I_1, I_2, I_4, I_5)$.

In order to obtain the explicit expressions of the nominal stress tensor \mathbf{S} and the associated Cauchy stress tensor $\boldsymbol{\sigma}$, the derivatives of the strain invariants with respect to \mathbf{F} are needed. Following

standard derivation rules, these are given by

$$\frac{\partial I_1}{\partial \mathbf{F}} = 2 \mathbf{F}^T, \quad \frac{\partial I_2}{\partial \mathbf{F}} = 2(I_1 \mathbf{F}^T - \mathbf{F}^T \mathbf{F} \mathbf{F}^T), \quad (11)$$

$$\frac{\partial I_4}{\partial \mathbf{F}} = 2 \mathbf{M} \otimes \mathbf{F} \mathbf{M}, \quad \frac{\partial I_5}{\partial \mathbf{F}} = 2(\mathbf{M} \otimes \mathbf{F} \mathbf{C} \mathbf{M} + \mathbf{C} \mathbf{M} \otimes \mathbf{F} \mathbf{M}). \quad (12)$$

A direct calculation of (10), using Eqs. (11) and (12) leads to

$$\mathbf{S} = 2(W_1 + I_1 W_2) \mathbf{F}^T - 2W_2 \mathbf{C} \mathbf{F}^T + 2W_4 \mathbf{M} \otimes \mathbf{F} \mathbf{M} + 2W_5(\mathbf{M} \otimes \mathbf{F} \mathbf{C} \mathbf{M} + \mathbf{C} \mathbf{M} \otimes \mathbf{F} \mathbf{M}) - p \mathbf{F}^{-1}, \quad (13)$$

$$\boldsymbol{\sigma} = 2(W_1 + I_1 W_2) \mathbf{B} - 2W_2 \mathbf{B}^2 + 2W_4 \mathbf{m} \otimes \mathbf{m} + 2W_5(\mathbf{m} \otimes \mathbf{B} \mathbf{m} + \mathbf{B} \mathbf{m} \otimes \mathbf{m}) - p \mathbf{I}, \quad (14)$$

where the abbreviations $W_i = \partial W / \partial I_i$, $i = 1, 2, 4, 5$ have been introduced. When the dependence on I_4 and I_5 in Eqs. (13) and (14) is omitted, the associated expressions for an isotropic material are obtained.

Traditionally, for transversely isotropic materials the strain energy is given by the sum of two contributions, one associated with the isotropic properties of the base matrix and the second with the anisotropy being generated by the embedded fibers. Therefore we can write

$$W = W_{\text{iso}}(I_1, I_2) + W_{\text{fib}}(I_4, I_5), \quad (15)$$

where the term W_{iso} represents the isotropic matrix material and W_{fib} accounts for the directional reinforcement (Qiu and Pence, 1997; Holzapfel et al., 2000; Merodio and Ogden, 2005; Horgan and Saccomandi, 2005; Ogden and Saccomandi, 2007; Dorfmann et al., 2007, 2008). Following the simplification in Holzapfel et al. (2000) and Holzapfel and Ogden (2008), we reduce the number of invariants and consider

$$W = W_{\text{iso}}(I_1) + W_{\text{fib}}(I_4), \quad (16)$$

which still provides sufficient flexibility to capture the anisotropic response of the *Manduca* cuticle.

4.3. Pseudo-elasticity

Pseudo-elasticity is defined as a material behavior in which loading and unloading do not coincide, even though the body may return to its original state (Fung, 1993). Therefore, loading and unloading can be described by a uniquely defined stress–strain law derived from proper strain energy functions (10). The constitutive framework of pseudo-elasticity has been developed by Ogden and Roxburgh (1999) to account for the Mullins effect in carbon-black reinforced elastomers. It modifies the elastic strain energy function $W(\mathbf{F})$ by incorporating an additional variable η

$$W = W(\mathbf{F}, \eta), \quad (17)$$

where the response of the material is then no longer elastic and $W(\mathbf{F}, \eta)$ is referred to as a *pseudo-energy* function. The inclusion of η allows the strain energy function to change during the deformation and hence capturing the observed stress–strain response. In this section we provide an overview of the theory of pseudo-elasticity. Appropriate specifications will be given in Section 5.

The additional variable η may be inactive or active; active η modifies the strain energy function and therefore introduces a change in the material properties. Based on the experimental data, it is convenient to use the beginning of unloading as the signal to activate η .

During loading the variable η is inactive and equal to unity. Therefore, we write

$$W_0(\mathbf{F}) = W(\mathbf{F}, 1) \quad (18)$$

for the resulting strain energy function. In (18) and in what follows the zero subscript is associated with the situation in which η is inactive. For an incompressible material the nominal stress associated with inactive η is denoted by \mathbf{S}_0 and given by

$$\mathbf{S}_0 = \frac{\partial W_0}{\partial \mathbf{F}}(\mathbf{F}) - p_0 \mathbf{F}^{-1}, \quad \det \mathbf{F} = 1. \quad (19)$$

If η is active we take it to depend on the deformation \mathbf{F} , i.e. $\eta = \hat{\eta}(\mathbf{F})$. The nominal stress, again for incompressible materials, is given by

$$\mathbf{S} = \frac{\partial W}{\partial \mathbf{F}}(\mathbf{F}, \eta) + \frac{\partial W}{\partial \eta}(\mathbf{F}, \eta) \frac{\partial \eta}{\partial \mathbf{F}}(\mathbf{F}) - p \mathbf{F}^{-1}, \quad \det \mathbf{F} = 1. \quad (20)$$

Following formulation from Ogden (2001) and Dorfmann and Ogden (2003, 2004), we take η to be given implicitly by the constraint

$$\frac{\partial W}{\partial \eta}(\mathbf{F}, \eta) = 0, \quad (21)$$

which uniquely defines η in terms of \mathbf{F} . We may write the solution to Eq. (21) formally as

$$\eta = \hat{\eta}(\mathbf{F}). \quad (22)$$

Then, the expression of the nominal stress (20) simplifies to

$$\mathbf{S} = \frac{\partial W}{\partial \mathbf{F}}(\mathbf{F}, \eta) - p \mathbf{F}^{-1}, \quad \det \mathbf{F} = 1, \quad (23)$$

whether or not η is active. When η is active the right-hand side is evaluated for η given by (22). It is convenient to introduce the notation w for the resulting (unique) strain energy function. Thus,

$$w(\mathbf{F}) \equiv W(\mathbf{F}, \hat{\eta}(\mathbf{F})), \quad (24)$$

and the nominal and Cauchy stress tensors for incompressible materials are given by the standard relations

$$\mathbf{S} = \frac{\partial w}{\partial \mathbf{F}}(\mathbf{F}) - p \mathbf{F}^{-1}, \quad \boldsymbol{\sigma} = \mathbf{F} \frac{\partial w}{\partial \mathbf{F}}(\mathbf{F}) - p \mathbf{I}. \quad (25)$$

Thus far we have not specified the form of the dependence of W on η , or, more particularly, the form of the function $\hat{\eta}(\mathbf{F})$ in (22). Following Ogden and Roxburgh (1999), Ogden (2001), and Dorfmann and Ogden (2003, 2004), we use the expression

$$W(\mathbf{F}, \eta) = \eta W_0(\mathbf{F}) + \phi(\eta), \quad (26)$$

where the function ϕ accounts for the energy dissipated during cyclic loading. It is therefore appropriate to refer to ϕ as a *dissipation function*. For consistency with (18), the function ϕ , for inactive η , must satisfy the condition $\phi(1) = 1$.

5. A model of *Manduca* cuticle

The theory of pseudo-elasticity is very general and allows for considerable flexibility. Pseudo-elasticity, for example, was used to account for stress softening in reinforced elastomers by Ogden and Roxburgh (1999), Ogden (2001), Dorfmann and Ogden (2003, 2004), and Horgan and Saccomandi (2005). In a different context, the pseudo-elastic framework was applied by Dorfmann et al. (2007, 2008) to represent the force–extension characteristics of *Manduca* muscles, both in the passive state and during tetanic stimulations.

In this section we modify the general theory of pseudo-elasticity to develop a constitutive model for the *inelastic* response of *Manduca* cuticle. The cuticle consists of a fibrous matrix material with an embedded network of elastic proteins responsible for the typical load–extension response of soft biomaterials. These are very flexible at low force levels followed by rapid increase in stiffness as the fibers engage and orient along the

loading direction. Similar to many other biological soft tissues, *Manduca* cuticle shows a distinct difference in the mechanical response of specimens loaded in the circumferential or axial directions, clearly indicating transverse isotropy. The proposed model will account for the nonlinear mechanical properties, including large strain, anisotropy, residual strain upon unloading and energy dissipation associated with hysteresis. We further assume incompressibility since changes in volume of biological tissues during loading are small (in general). The model is fitted to available data and the magnitude of the material parameters are determined.

For *Manduca* cuticle we propose the pseudo-energy function

$$W(I_1, I_4, \eta) = \eta W_0(I_1, I_4) + \phi(\eta), \quad (27)$$

which is Eq. (26) specialized to incompressible, transversely isotropic materials. Since it is very difficult to get enough experimental data to fully characterize the form of the strain energy function, we have reduced the number of invariants in (27) (i.e. we neglect the dependence of W on the invariants I_2 and I_5 as in Holzapfel and Ogden, 2008). The function ϕ , which depends only on η , accounts for the energy dissipation during a loading–unloading cycle and, for consistency with Eq. (18), must satisfy the condition $\phi(1) = 0$. Using Eq. (27) in (21) gives the important relation

$$\phi'(\eta) = -W_0(I_1, I_4), \quad (28)$$

where ϕ' is the derivative with respect to η . For a specific strain energy formulation W_0 , η can be determined implicitly in terms of the invariants I_1 and I_4 . Unloading, which may be initiated from any point on the loading path, is taken as a signal to activate η . We emphasize that $\phi(\eta)$ derived from Eq. (28) depends on the maximum values of I_1 and I_4 attained on the loading path, which are denoted by $I_{1\max}$ and $I_{4\max}$. Since $\eta = 1$ at any point on the loading path from which unloading is initiated, it follows from Eq. (28) that

$$\phi'(1) = -W_0(I_{1\max}, I_{4\max}) \equiv -W_{\max}, \quad (29)$$

wherein the notation W_{\max} is defined. This is the current maximum value of the energy achieved on the loading path. In accordance with the properties of W_0 , W_{\max} increases along a loading path. In view of (29), the function $\phi(\eta)$ depends on the point from which unloading begins through the energy expended on the loading path up to that point.

Unloading is associated with a monotonic decreasing function of η , with $\eta = 1$ at the start of unloading. If η is required to be positive then for the stress to vanish, the material must return to the reference configuration with $I_1 = 3$ and $I_4 = 1$. The minimum value of η is uniquely determined by Eq. (28) from

$$\phi'(\eta_{\min}) = -W_0(3, 1) = 0, \quad (30)$$

where we assumed that no elastic energy is stored in the reference configuration. The residual (nonrecoverable) energy is given by (27) and has the value

$$W(3, 1, \eta_{\min}) = \phi(\eta_{\min}). \quad (31)$$

This may be interpreted as a measure of the energy dissipated during the loading–unloading cycle. For uniaxial loading, (31) represents the area between the loading and the unloading curve (see Dorfmann et al., 2007, 2008).

In order to account for the residual strain, we assume that during unloading the value of η vanishes before the reference configuration is reached. The strain energy function W_0 does not vanish, but has the value denoted W_{res} . Use of Eqs. (21) and (27) together with $\eta = 0$ gives

$$\phi'(0) = -W_0(I_{1\text{res}}, I_{4\text{res}}) = -W_{\text{res}}, \quad (32)$$

where the value of the strain energy function W_{res} , associated with the residual strain invariants $I_{1,res}$ and $I_{4,res}$, has been defined. The function $\phi(0)$ represents the nonrecoverable part of the energy.

Biological soft tissues, in general, tend to stiffen rapidly as fibers are recruited and aligned along the loading direction. The rapid stiffening of the cuticle can best be described by an exponential formulation of a strain energy function. Following Demiray (1972) and Humphrey and Yin (1987), we propose the I_1 model for the isotropic matrix material given by

$$W_{iso} = \frac{\mu_{iso}}{2\alpha} \{ \exp[\alpha(I_1 - 3)] - 1 \}, \tag{33}$$

where μ_{iso} is shear modulus of the matrix material in the reference configuration and α is a positive parameter to be determined from experimental data.

Horgan and Saccomandi (2005) recently proposed a strain energy formulation that explicitly accounts for the rigidity of the fiber reinforcement. The Horgan–Saccomandi model includes the parameter n to account for the fact that with increasing applied load more and more fibers are recruited. Due to their wavy structure, these fibers engage in carrying load at different stretch ratios and ultimately align along the loading direction. It is therefore appropriate to use the Horgan–Saccomandi formulation to account for the chitin fibers in the *Manduca* cuticle as given by

$$W_{fib} = -\frac{\mu_{fib}}{n} J_m \ln \left(1 - \frac{(I_4 - 1)^n}{J_m} \right), \tag{34}$$

where μ_{fib} measures the degree of anisotropy and J_m is a dimensionless parameters to account for the degree of rigidity.

From Eq. (16), the total strain energy formulation of the *Manduca* cuticle during loading is then given by

$$W_0 = \frac{\mu_{iso}}{2\alpha} \{ \exp[\alpha(I_1 - 3)] - 1 \} - \frac{\mu_{fib}}{n} J_m \ln \left(1 - \frac{(I_4 - 1)^n}{J_m} \right). \tag{35}$$

Note that when $J_m \rightarrow \infty$, the strain energy (34) reduces to

$$W_{fib} = \frac{\mu_{fib}}{n} (I_4 - 1)^n, \tag{36}$$

which is often called the standard reinforcing model with a quadratic nonlinearity in I_4 ($n = 2$) (Qiu and Pence, 1997; Merodio and Ogden, 2005; Horgan and Saccomandi, 2005).

5.1. Loading

For loading the variable η is inactive and equal to unity. Using (19) with (27) and the reduced form of (13) gives the nominal stress during loading

$$\begin{aligned} \mathbf{S}_0 &= 2W_1 \mathbf{F}^T + 2W_4 \mathbf{M} \otimes \mathbf{F} \mathbf{M} - p_0 \mathbf{F}^{-1} \\ &= \mu_{iso} \exp[\alpha(I_1 - 3)] \mathbf{F}^T + 2\mu_{fib} \frac{J_m (I_4 - 1)^{n-1}}{J_m - (I_4 - 1)^n} \mathbf{M} \otimes \mathbf{F} \mathbf{M} - p_0 \mathbf{F}^{-1}. \end{aligned} \tag{37}$$

Similarly, from Eq. (14) we get the Cauchy stress tensor

$$\begin{aligned} \boldsymbol{\sigma}_0 &= 2W_1 \mathbf{B} + 2W_4 \mathbf{m} \otimes \mathbf{m} - p_0 \mathbf{I} \\ &= \mu_{iso} \exp[\alpha(I_1 - 3)] \mathbf{B} + 2\mu_{fib} \frac{J_m (I_4 - 1)^{n-1}}{J_m - (I_4 - 1)^n} \mathbf{m} \otimes \mathbf{m} - p_0 \mathbf{I}, \end{aligned} \tag{38}$$

where results from Eqs. (11)₁ and (12)₁ have been used.

5.2. Unloading

We take initiation of unloading as a signal to active the variable η . From (23), using (27), we have the nominal and Cauchy

stress tensors

$$\mathbf{S} = \eta \mathbf{S}_0, \quad \boldsymbol{\sigma} = \eta \boldsymbol{\sigma}_0, \tag{39}$$

with $\eta = 1$ at beginning of unloading, otherwise given by (21).

During unloading, when the body returns to the natural reference configuration associated with $I_1 = 3$ and $I_4 = 1$, we have the trivial solution $\mathbf{S} = \mathbf{0}$ (equivalently $\boldsymbol{\sigma} = \mathbf{0}$), i.e. there will be no residual strain. Alternatively, we require $\eta = 0$ in which case there will be a residual strain determined from Eq. (32).

In order to account for residual strain, we select ϕ to have the form

$$\phi(\eta) = -\frac{1}{4} \mu_{iso} \lambda_0^2 (\eta - 1)^2 - W_{max} (\eta - 1), \tag{40}$$

which satisfies $\phi(1) = 0$ and $\phi'(1) = -W_{max}$, as required. λ_0 is a material parameter that accounts for the amount of residual strain upon unloading. Substituting the derivative of Eq. (40) in (28) gives

$$\phi'(\eta) = -\frac{1}{2} \mu_{iso} \lambda_0^2 (\eta - 1) - W_{max} = -W_0(I_1, I_4), \tag{41}$$

and we obtain

$$\eta = 1 + \frac{2[W_0(I_1, I_4) - W_{max}]}{\mu_{iso} \lambda_0^2}, \tag{42}$$

which shows that at the beginning of unloading, where $W_{max} = W_0(I_{1,max}, I_{4,max})$, the variable $\eta = 1$.

6. Model results

In this section the constitutive equations are applied to basic deformation, known as pure homogeneous strain and given by

$$x_1 = \lambda_1 X_1, \quad x_2 = \lambda_2 X_2, \quad x_3 = \lambda_3 X_3. \tag{43}$$

The matrices of the Cartesian components of the deformation gradient tensor \mathbf{F} and the right Cauchy–Green tensor \mathbf{C} , denominated, respectively, by \mathbf{F} and \mathbf{C} , are

$$\mathbf{F} = \begin{pmatrix} \lambda_1 & 0 & 0 \\ 0 & \lambda_2 & 0 \\ 0 & 0 & \lambda_3 \end{pmatrix}, \quad \mathbf{C} = \begin{pmatrix} \lambda_1^2 & 0 & 0 \\ 0 & \lambda_2^2 & 0 \\ 0 & 0 & \lambda_3^2 \end{pmatrix}. \tag{44}$$

Consider a specimen of a *Manduca* cuticle in the \mathbf{e}_1 – \mathbf{e}_2 plane, where $\mathbf{e}_1, \mathbf{e}_2, \mathbf{e}_3$ are the unit vectors in a Cartesian coordinate system. With respect to these coordinate directions, the components of the single preferred direction \mathbf{M} are given by $(\cos \varphi, \sin \varphi, 0)$, where φ is a constant angle enclosed by the directions \mathbf{M} and \mathbf{e}_1 . Using the incompressibility condition $\lambda_1 \lambda_2 \lambda_3 = 1$, the invariants I_1 and I_4 are given by

$$I_1 = \lambda_1^2 + \lambda_2^2 + \lambda_1^{-2} \lambda_2^{-2}, \quad I_4 = \lambda_1^2 \cos^2 \varphi + \lambda_2^2 \sin^2 \varphi. \tag{45}$$

During loading, the Cauchy stress tensor (38) has components

$$\begin{aligned} \sigma_{011} &= 2W_1 \lambda_1^2 + 2W_4 \lambda_1^2 \cos^2 \varphi - p_0, \\ \sigma_{022} &= 2W_1 \lambda_2^2 + 2W_4 \lambda_2^2 \sin^2 \varphi - p_0, \\ \sigma_{033} &= 2W_1 \lambda_3^2 - p_0, \\ \sigma_{012} &= 2W_4 \lambda_1 \lambda_2 \sin \varphi \cos \varphi, \end{aligned} \tag{46}$$

and the remaining σ_{013} and σ_{023} vanish. The expressions of W_1 and W_4 are given in (38) and are not repeated here. Also note that the shear stress $\sigma_{012} \equiv 0$ if the preferred direction coincides with one of the coordinate axes, i.e. $\varphi = 0^\circ$ or 90° . In the following we assume that the fiber direction \mathbf{M} coincides with the direction specified by the unit vector \mathbf{e}_1 .

6.1. Loading–unloading in the fiber direction

For uniaxial loading and unloading in the fiber direction we have $\varphi = 0^\circ$, $\sigma_{022} = \sigma_{033} = 0$ and $\sigma_{012} = 0$. Conveniently we can denominate the independent principal stretch by λ using the incompressibility condition (4)

$$\lambda_1 = \lambda, \quad \lambda_2 = \lambda_3 = \lambda^{-1/2} \tag{47}$$

and from (46)₃ we get $p_0 = 2W_1\lambda_3^2 = 2W_1\lambda^{-1}$. The nontrivial stress component is then given by

$$\begin{aligned} \sigma_{011} &= 2W_1(\lambda^2 - \lambda^{-1}) + 2W_4\lambda^2 \\ &= \mu_{\text{iso}}(\lambda^2 - \lambda^{-1}) \exp[\alpha(I_1 - 3)] + 2\mu_{\text{fib}} \frac{J_m(I_4 - 1)^{n-1}}{J_m - (I_4 - 1)^n} \lambda^2, \end{aligned} \tag{48}$$

with $I_1 = \lambda^2 + 2\lambda^{-1}$ and $I_4 = \lambda^2$.

As explained earlier, unloading activates the variable η . Expression (39)₂, specialized to the uniaxial case, gives the nonzero stress component during unloading

$$\sigma_{11} = \eta\sigma_{011} \quad \text{with } \eta = 1 + \frac{2[W_0(I_1, I_4) - W_{\text{max}}]}{\mu_{\text{iso}}\lambda_0^2}, \tag{49}$$

where W_{max} is the value of the total strain energy $W_0(I_1, I_4)$ given by Eq. (35) at the moment unloading is initiated.

6.2. Loading–unloading in the transverse direction

For this loading–unloading condition we have $\sigma_{011} = \sigma_{033} = 0$ and $\sigma_{022} \neq 0$. Both, the deformation in the fiber direction λ_1 and the deformation normal to the cuticle specimen λ_3 are now a function of the applied deformation λ_2 . Using $\sigma_{011} = 0$ and Eq. (46)₁, we have for p_0 the expression

$$p_0 = 2(W_1 + W_4)\lambda_1^2. \tag{50}$$

From $\sigma_{033} = 0$ and Eq. (46)₃ gives

$$p_0 = 2W_1\lambda_3^2. \tag{51}$$

Using the incompressibility condition $\lambda_3 = \lambda_1^{-1}\lambda_2^{-1}$ gives the connection between λ_1 and λ_2

$$(W_1 + W_4)\lambda_1^4 = W_1\lambda_2^{-2}. \tag{52}$$

Similarly, using $\lambda_1 = \lambda_2^{-1}\lambda_3^{-1}$, the relation to express the dependence of λ_3 as a function of λ_2 is

$$(W_1 + W_4)\lambda_3^{-4} = W_1\lambda_2^2. \tag{53}$$

Eqs. (52) and (53) show that the connections between the applied transverse stretch and the deformations in the fiber direction as well as the changes in the thickness depend on the material properties. These equations therefore impose restrictions on the values of W_1 and W_4 . It is outside the scope of this paper to discuss the implication of these restrictions on the formulation of W . We refer to Qiu and Pence (1997) and Merodio and Ogden (2005) for a detailed discussion.

To eliminate the restriction imposed by (52) and (53), we assume buckling of fibers when subject to compression. This implies that for $\lambda_1 < 1$ the material response is not affected by the presence of the fibers. To express the independent principal stretch transverse to the fiber direction by λ , we write

$$\lambda_2 = \lambda, \quad \lambda_1 = \lambda_3 = \lambda^{-1/2} \tag{54}$$

and $p_0 = 2W_1\lambda^{-1}$. The component of the stress tensor transverse to the fiber direction during loading is then given by

$$\begin{aligned} \sigma_{022} &= 2W_1(\lambda^2 - \lambda^{-1}) \\ &= \mu_{\text{iso}}(\lambda^2 - \lambda^{-1}) \exp[\alpha(I_1 - 3)], \end{aligned} \tag{55}$$

which shows, as expected, how the material response is not affected by the fiber stiffness.

The beginning of unloading is again taken as the signal to activate the variable η . Similar to unloading in the fiber direction, the response is given by the expression

$$\sigma_{22} = \eta\sigma_{022}, \tag{56}$$

where the formulation of the variable η is again given by (42).

6.3. Numerical results

The primary loading in the fiber direction is fully determined by the elastic strain energy in Eq. (35) with material model parameters μ_{iso} , μ_{fib} , α , n and J_m . The values are summarized in Table 1. The solid line in Fig. 6 shows the numerical results of the Cauchy stress and compares them with the corresponding experimental data of the first loading up to $\lambda = 1.058$. At this point unloading is initiated and the variable η activated. The value of η , is given by (42) to account for the softening and residual deformation. There the additional material parameter λ_0 is defined. λ_0 determines the magnitude of the residual strain and its value is shown in Table 1. For completeness, Table 1 also includes the value of the angle φ enclosed by the preferred direction \mathbf{M} and the \mathbf{e}_1 direction of the Cartesian coordinate system.

Next, the material model is used to describe the response of the *Manduca* cuticle when loaded in the transverse direction, i.e. normal to the fiber orientation. The numerical results of the Cauchy stress for uniaxial loading up $\lambda = 1.059$ are shown in

Table 1
Summary of material model parameters for loading and unloading parallel and transverse to the fiber direction.

	μ_{iso}	μ_{fib}	α	n	J_m	λ_0	φ
Fiber direction	2	80	200	2.8	0.01	0.35	0
Transverse direction	2	80	200	2.8	0.01	0.178	0

The values of μ_{iso} , μ_{fib} are given in MPa, the angle φ in degrees.

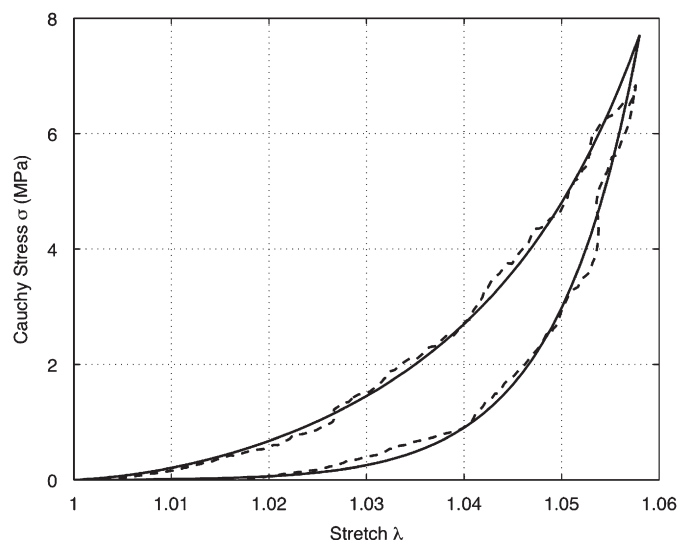


Fig. 6. The numerical (solid line) and experimental responses (dashed line) of the cuticle during loading and unloading in the fiber direction. A physiological stiffness can be estimated by finding the slope at the stretch 1.017, which corresponds to the stress in the cuticle necessary for holding body pressure on the kPa scale.

Fig. 7. Upon unloading, the algorithm developed in Sections 5.2 and 6.2 then determines the value of η and the corresponding Cauchy stress component. The values of the material parameters are again summarized in Table 1. The magnitude of the parameter λ_0 differs from the one used to simulate uniaxial loading–unloading in the fiber directions. The different value indicates a larger residual strain for uniaxial loading–unloading in the direction transverse to the fiber orientation.

Fig. 8 illustrates the anisotropy of the *Manduca* cuticle by comparing the uniaxial loading–unloading parallel and transverse to the fiber direction. The response of the transversely isotropic material is completely defined by the strain energy function (35), the corresponding stress components (38) and the formulation of η specified by (42). These results show that the constitutive equation is able to account for the transversely isotropic behavior of the cuticle. Also, the area between the loading and unloading curves represents the energy dissipation during each loading–unloading cycle. This can be calculated on the basis

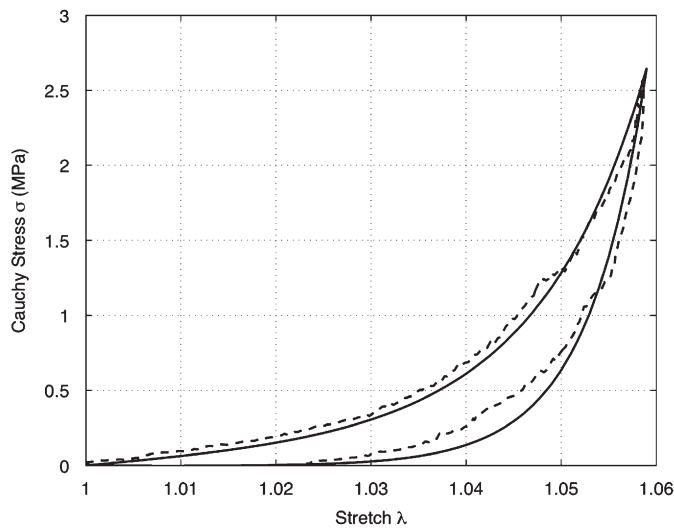


Fig. 7. The numerical (solid line) and experimental (dashed line) responses of the cuticle specimen during loading and unloading in the direction normal to the fiber orientation.

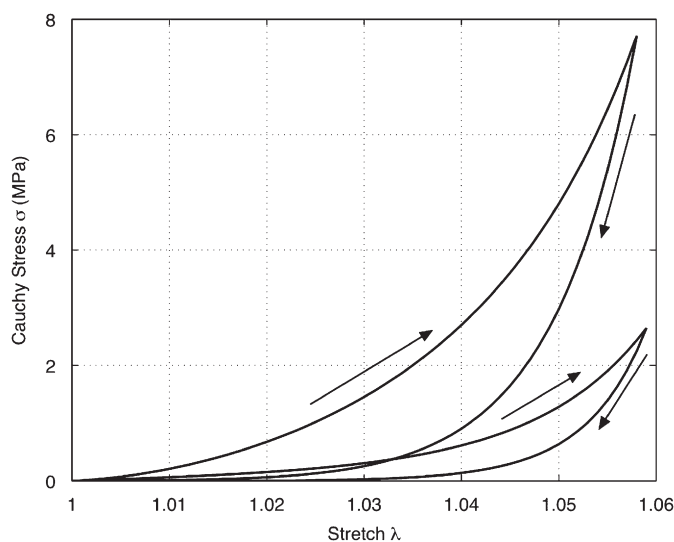


Fig. 8. Cauchy stress components for uniaxial loading–unloading parallel and normal to the fiber direction. The response is based on the strain energy formulation (35) and on η given by (42).

of Eq. (27), with φ given by (40), see Dorfmann and Ogden (2003) for details.

7. Discussion and concluding remarks

Cuticle anisotropy—The high circumferential stiffness of *Manduca* cuticle (relative to longitudinal) is similar to that seen in other pressurized hydrostatic animals (Trueman, 1975; Wainwright, 1988). This anisotropy is most probably due to the presence of apical pleats in the axial direction (Carter and Locke, 1993). Previous studies on *Manduca* dorsal cuticle reported much smaller stress values (Alexander et al., 1999) presumably because the reported specimen thickness (0.5 mm) was estimated using a caliper, leading to underestimation of tissue stiffness. Wolfgang reported cuticle modulus at tens of MPa (Wolfgang and Riddiford, 1987), which is much closer to the current study because tissue thickness was measured using a dry mass deduction method. In addition, both previous studies used specimens harvested as relatively large rectangular sheets (extending over several abdominal segments) and stretched at high force. This leads to nonhomogeneous deformation at the margins and poorly controlled strain estimation. Indeed, the servo motor readings from our own study also over-estimated deformation of the main body of the cuticle compared to that measured directly by video extensometry. The increased resolution of our microunaxial tests is necessary to detect the anisotropy in the material response, which has not been observed in previously reported measurements.

Using a long pressurized cylinder as an idealized representation of the body wall, the circumferential stress can be computed based on the internal pressure as

$$\sigma_c = \frac{rp}{t}, \tag{57}$$

where the body pressure $p = 5$ kPa, the radius $r = 0.5$ cm, and the wall thickness $t = 50 \mu\text{m}$. We can therefore estimate the physiological circumferential stress to be about 0.5 MPa. This stress corresponds to a circumferential stretch of 1.017 (by using the model curve). Therefore, this approximates the functional range of deformation of the *Manduca* cuticle with an associated tangential stiffness of 53.4 MPa.

Constitutive approach—The mechanical responses of the cuticle have largely been based on linear elastic theories, which impose various limitations (Hepburn and Levy, 1975; Joffe et al., 1975; Hepburn, 1976). With increased accuracy of experimental data, we can now exploit the nonlinear constitutive framework of fiber-reinforced soft materials. Here we adopt the Horgan–Saccomandi formulation to account for fiber reinforcements (associated with chitin fibers) in the circumferential direction, superimposed on the nonlinear base matrix. This model is based on the concept of inextensible reinforcing fibers (once fully straightened) and therefore captures the mechanical response of most fibrous tissues (Horgan and Saccomandi, 2005). These include the chitin-reinforced tissue such as caterpillar cuticle.

Modeling soft-bodied structures—Traditionally, soft-bodied biological structures have been modeled by requiring constant volume and uniform pressure. In a comprehensive attempt, Wadepuhl and Beyn constructed a virtual rectangular worm with both longitudinal and circumferential muscles (Wadepuhl and Beyn, 1989). While the results were insightful and generic, most soft body properties have been rendered to linear approximations. An elliptical virtual leech has also been assembled using empirical length–tension relationships that lumped muscles, connective tissues, and body wall together (Skierczynski et al., 1996). While this model includes nonlinearity by using polynomial-type curve

fitting of the geometry, the model parameters are mostly instrumental. Many other models explore the kinematics of peristaltic motion (Accoto et al., 2004; Quillin, 1999), bypassing the complicated internal dynamics all together. The applications listed above only apply to true hydrostatic skeleton with uniform body pressure and constant volume. This is perhaps not the case for a caterpillar body, which contains large amount of unconfined gas and non-Newtonian fluid. We stipulate that much of the locomotion is directly related to the nonlinearity of the mechanical responses of the body wall, muscles, and perhaps other body contents. Therefore, to improve our knowledge of the control mechanisms in soft-bodied animals, we need a better understanding of the mechanical interactions, whereby constitutive modeling and numerical simulations will support such a pursuit.

Acknowledgments

The authors gratefully acknowledge the support by the W.M. Keck Foundation Science and Engineering Program grant on Biomimetic Technologies for Soft-bodied Robots. This work was partially supported by Grant IOS-0718537 to BAT from the US National Science Foundation. We are grateful to Michael Simon for providing technical assistance in updating LabView software for data acquisition.

References

- Accoto, D., Castrataro, P., Dario, P., 2004. Biomechanical analysis of *Oligochaeta* crawling. *J. Theor. Biol.* 230, 49–55.
- Alexander, D.E., Ratzlaff, K.L., Roggero, R.J., Hsieh, J.S.Y., 1999. Inexpensive, semi-automated system for measuring mechanical properties of soft tissues. *J. Exp. Zool.* 284, 374–378.
- Atkins, E., 1985. Conformations in polysaccharides and complex carbohydrates. *J. Biosci.* 8, 375–387.
- Belamie, E., Mosser, G., Gobeaux, F., Giraud-Guille, M.M., 2006. Possible transient liquid crystal phase during the laying out of connective tissues: α -chitin and collagen as models. *J. Phys. Condens. Matter* 18, 115–129.
- Carter, D., Locke, M., 1993. Why caterpillars do not grow short and fat. *Int. J. Insect Morphol.* 22, 81–102.
- Chen, B., Peng, X., Cai, C., Fan, J., Wu, X., 2006a. Circumcolumnar microstructure of tumblebug cuticle and biomimetic application. *Mater. Sci. Eng. B Solid* 132, 159–163.
- Chen, B., Peng, X., Cai, C., Niu, H., Wu, X., 2006b. Helicoidal microstructure of *Scarabaei* cuticle and biomimetic research. *Mater. Sci. Eng. A Struct.* 423, 237–242.
- Condoulis, W.V., Locke, M., 1966. The deposition of endocuticle in an insect, *Calpodis ethlius* (stoll) (Lepidoptera, Hesperidae). *J. Insect Physiol.* 12, 311–323.
- Copenhaver, P.F., Truman, J.W., 1982. The role of eclosion hormone in the larval ecdyses of *Manduca sexta*. *J. Insect Physiol.* 28, 695–701.
- Csikos, G., Molnar, K., Borhegyi, N.H., Talian, G.C., Sass, M., 1999. Insect cuticle, an in vivo model of protein trafficking. *J. Cell Sci.* 112, 2113–2124.
- Demiray, H., 1972. Elasticity of soft biological tissues. *J. Biomech.* 5, 309–311.
- Dennell, R., 1976. The structure and lamination of some arthropod cuticles. *Zool. J. Linn. Soc. London* 58, 159–164.
- Dorfmann, A., Ogden, R.W., 2003. A pseudo-elastic model for loading, partial unloading and reloading of particle-reinforced rubber. *Int. J. Solids Struct.* 40, 2699–2714.
- Dorfmann, A., Ogden, R.W., 2004. A constitutive model for the Mullins effect with permanent set in particle-reinforced rubber. *Int. J. Solids Struct.* 41, 1855–1878.
- Dorfmann, A., Trimmer, B.A., Woods, W.A., 2007. A constitutive model for muscle properties in a soft-bodied arthropod. *J. R. Soc. Interface* 4, 257–269.
- Dorfmann, A.L., Woods, W.A., Trimmer, B.A., 2008. Muscle performance in a soft-bodied terrestrial crawler: constitutive modeling of strain-rate dependency. *J. R. Soc. Interface* 5, 349–362.
- Franceschini, G., Bigoni, D., Regitnig, P., Holzapfel, G.A., 2006. Brain tissue deforms similarly to filled elastomers and follows consolidation theory. *J. Mech. Phys. Solids* 54, 2592–2620.
- Freier, T., Montenegro, R., Koh, H.S., Shoichet, M.S., 2005. Chitin-based tubes for tissue engineering in the nervous system. *Biomaterials* 26, 4624–4632.
- Fung, Y., 1993. *Biomechanics: Mechanical Properties of Living Tissues*. Springer, New York.
- Giraud-Guille, M.M., 1992. Liquid crystallinity in condensed type I collagen solutions. A clue to the packing of collagen in extracellular matrices. *J. Mol. Biol.* 224, 861–873.
- Hepburn, H.R., 1972. Some mechanical properties of crossed fibrillar chitin. *J. Insect Physiol.* 18, 815–825.
- Hepburn, H.R., 1976. *The Insect Integument*. Elsevier Scientific Publishing Co., Amsterdam, New York.
- Hepburn, H.R., Ball, A., 1973. On the structure and mechanical properties of beetle shells. *J. Mater. Sci.* 8, 618–623.
- Hepburn, H.R., Levy, P., 1975. Mechanical properties of some larval cuticles. *J. Entomol. Soc. South Africa* 38, 131–141.
- Holzapfel, G., Ogden, R.W., 2008. On planar biaxial tests for anisotropic nonlinearly elastic solids: a continuum mechanical framework. *Math. Mech. Solids*, in press, doi:10.1177/1081286507084411.
- Holzapfel, G.A., 2000. *Nonlinear Solid Mechanics: A Continuum Approach for Engineering*. Wiley, Chichester.
- Holzapfel, G.A., 2006. Determination of material models for arterial walls from uniaxial extension tests and histological structure. *J. Theor. Biol.* 238, 290–302.
- Holzapfel, G.A., Gasser, T.C., Ogden, R.W., 2000. A new constitutive framework for arterial wall mechanics and a comparative study of material models. *J. Elasticity* 61, 1–48.
- Horgan, C.O., Saccomandi, G., 2005. A new constitutive theory for fiber-reinforced incompressible nonlinearly elastic solids. *J. Mech. Phys. Solid* 53, 1985–2015.
- Hughes, P.M., 1987. Insect cuticular growth layers seen under the scanning electron microscope: a new display method. *Tissue Cell* 19, 705–712.
- Humphrey, J.D., 2002. *Cardiovascular Solid Mechanics, Cells, Tissues, and Organs*. Springer, New York.
- Humphrey, J.D., Yin, F.C.P., 1987. A new constitutive formulation for characterizing the mechanical behavior of soft tissues. *Biophys. J.* 52, 563–570.
- Iconomidou, V.A., Chryssikos, G.D., Gionis, V., Willis, J.H., Hamodrakas, S.J., 2001. “Soft”-cuticle protein secondary structure as revealed by FT-Raman, ATR FT-IR and CD spectroscopy. *Insect Biochem. Molec.* 31, 877–885.
- Joffe, I., Hepburn, H.R., Andersen, S.O., 1975. On the mechanical properties of *Limulus* solid cuticle. *J. Comput. Physiol. B* 101, 147–160.
- Locke, M., 1958. The formation of tracheae and tracheoles in *Rhodnius prolixus*. *J. Cell Sci.* 3, 29–46.
- Merodio, J., Ogden, R.W., 2005. Mechanical response of fiber-reinforced incompressible non-linear elastic solids. *Int. J. Nonlinear Mech.* 40, 213–227.
- Mezoff, S., Papastathis, N., Takesian, A., Trimmer, B.A., 2004. The biomechanical and neural control of hydrostatic limb movements in *Manduca sexta*. *J. Exp. Biol.* 207, 3043–3053.
- Neville, A.C., 1967a. Chitin orientation in cuticle and its control. *Adv. Insect Physiol.* 4, 213–286.
- Neville, A.C., 1967b. Daily growth layers in animals and plants. *Biol. Rev.* 42, 421–439.
- Neville, A.C., 1975. *Biology of the Arthropod Cuticle*. Springer, New York.
- Neville, A.C., Levy, S., 1984. Helicoidal orientation of cellulose microfibrils in nitella opaca internode cells: ultrastructure and computed theoretical effects of strain reorientation during wall growth. *Planta* 162, 370–384.
- Niebur, E., Erdos, P., 1991. Theory of the locomotion of nematodes: dynamics of undulatory progression on a surface. *Biophys. J.* 60, 1132–1146.
- Ogden, R.W., 1997. *Non-linear Elastic Deformations*. Dover Publications, New York.
- Ogden, R.W., 2001. Elements of the theory of finite elasticity. In: Fu, Y.B., Ogden, R.W. (Eds.), *Nonlinear Elasticity: Theory and Applications*. Cambridge University Press, Cambridge, pp. 1–58.
- Ogden, R.W., Roxburgh, D.G., 1999. A pseudo-elastic model for the Mullins effect in filled rubber. *Proc. R. Soc. A Math. Phys.* 455, 2861–2877.
- Ogden, R.W., Saccomandi, G., 2007. Introducing mesoscopic information into constitutive equations for arterial walls. *Biomech. Modeling Mech.* 6, 333–344.
- Qiu, G.Y., Pence, T.J., 1997. Remarks on the behavior of simple directionally reinforced incompressible nonlinearly elastic solids. *J. Elasticity* 49, 1–30.
- Quillin, K.J., 1999. Kinematic scaling of locomotion by hydrostatic animals: ontogeny of peristaltic crawling by the earthworm *lumbricus terrestris*. *J. Exp. Biol.* 202, 661–674.
- Reynolds, S.E., 1975. The mechanical properties of the abdominal cuticle of *Rhodnius* larvae. *J. Exp. Biol.* 62, 69–80.
- Sanchez, C., Arribat, H., Guille, M.M.G., 2005. Biomimeticism and bioinspiration as tools for the design of innovative materials and systems. *Nat. Mater.* 4, 277–288.
- Seidel, R., Gourrier, A., Burghammer, M., Riekel, C., Jeronimidis, G., Paris, O., 2008. Mapping fibre orientation in complex-shaped biological systems with micrometre resolution by scanning X-ray microdiffraction. *Micron* 39, 198–205.
- Skierczynski, B.A., Wilson, R.J.A., Kristan, W.B., Skalak, R., 1996. A model of the hydrostatic skeleton of the leech. *J. Theor. Biol.* 181, 329–342.
- Spencer, A.J.M., 1971. Theory of invariants. In: Eringen, A.C. (Ed.), *Continuum Physics*, vol. 1. Academic Press, New York, pp. 239–353.
- Trueman, E.R., 1975. *The Locomotion of Soft-bodied Animals*. Edward Arnold, London.
- Vincent, J.F.V., 2002. Arthropod cuticle: a natural composite shell system. *Compos. Part A Appl. Sci.* 33, 1311–1315.
- Vincent, J.F.V., Wegst, U.G.K., 2004. Design and mechanical properties of insect cuticle. *Arthropod Struct. Dev.* 33, 187–199.
- Wadepuhl, M., Beyn, W.J., 1989. Computer simulation of the hydrostatic skeleton. The physical equivalent, mathematics and application to worm-like forms. *J. Theor. Biol.* 136, 379–402.
- Wainwright, S.A., 1982. *Mechanical Design in Organisms*. Princeton University Press, Princeton.

- Wainwright, S.A., 1988. *Axis and Circumference: The Cylindrical Shape of Plants and Animals*. Harvard University Press, Cambridge, MA.
- Wolfgang, W.J., Riddiford, L.M., 1981. Cuticular morphogenesis during continuous growth of the final instar larva of a moth. *Tissue Cell* 13, 757–772.
- Wolfgang, W.J., Riddiford, L.M., 1986. Larval cuticular morphogenesis in the tobacco hornworm, *Manduca sexta*, and its hormonal regulation. *Dev. Biol.* 113, 305–316.
- Wolfgang, W.J., Riddiford, L.M., 1987. Cuticular mechanics during larval development of the tobacco hornworm, *Manduca sexta*. *J. Exp. Biol.* 128, 19–33.

Publication-4

Title: Ontogenetic scaling of caterpillar body properties and its biomechanical implications on the use of a hydrostatic skeleton

Authors: Huai-Ti Lin, Daniel Slate, Chris Paetsch, Luis Dorfmann and Barry Trimmer

Keywords: *Manduca sexta* caterpillar; Hydrostatic skeleton; Biomechanics of scaling; Larval ontogeny; Finite element analysis; Crawling and inching

Abstract

Caterpillars can increase their body mass 10,000 fold in two weeks. It is therefore remarkable that caterpillars appear to maintain the same locomotion kinematics throughout their entire larval stage. This study examines how the body properties of a caterpillar might change to accommodate such dramatic changes in body load. Using *Manduca sexta* as a model system, we measured changes in body volume, tissue density, baseline body pressure, and the dimensions of load bearing tissues (the cuticle and muscles) over a body mass range from milligrams to several grams. All *Manduca* biometrics relevant to the hydrostatic skeleton scaled allometrically but close to the isometric predictions. Body density and pressure were almost constant. We next investigated the effects of scaling on the bending stiffness of the caterpillar hydrostatic skeleton. The anisotropic nonlinear mechanical response of *Manduca* muscles and soft cuticle has been previously quantified and modeled with constitutive equations. Using biometric data and these material laws, we constructed finite element models to simulate a hydrostatic skeleton under different conditions. Results show that increasing the internal pressure leads to a nonlinear increase in bending stiffness. Increasing the body size results in a decrease in bending stiffness. Muscle activation can double this stiffness in the physiological pressure range, but thickening the cuticle or increasing the muscle area reduces the structural stiffness. These nonlinear effects may dictate the effectiveness of a hydrostatic skeleton at different sizes. Given the dramatic size variation in Lepidoptera larvae these mechanical constraints are expected to influence locomotion strategies in different species.

1. Introduction

Biomechanical scaling of caterpillars

Typically, in terrestrial animals with rigid skeletons and constant bone density, the cross-sectional area of the skeleton scales significantly faster than a representative length as the body increases in size. This characteristic helps support the increasing body mass and resists the accompanying forces of locomotion, which scale roughly with body volume (Demetrius 2006, West, Brown & Enquist 1997, Prange, Anderson & Rahn 1979).

Mechanical scaling in soft-bodied animals is different because soft tissues undergo very large deformations and increased rigidity can only be achieved through pressurization. Rather than relying on increasing the amount of skeletal material, soft animals can employ hydrostatics to resist the increase in forces associated with locomotion. A true hydrostat, such as the earthworm, can scale isometrically over many orders of magnitude while maintaining similar static body stress (Quillin 1998, Quillin 1999). Leeches also move similarly at all body sizes (Jordan 1998). Numerous geometric models of hydrostats based on a constant body volume assumption capture the kinematics and dynamics of annelid locomotion (Skierczynski et al. 1996, Dobrolyubov, Douchy 2002). In locomotor modes with more complex substrate interaction, the body loading depends highly on the body size (Quillin 2000). During burrowing, for example, behavioral and morphological adaptations are necessary in order to operate at different scales (Che, Dorgan 2010). Studying the scaling of hydrostatic skeletons helps us understand how a soft-bodied animal copes with mechanical loads at different body sizes.

Soft animals do not all have the same body structure, and for some, the maintenance of a pressurized fluid cavity is limited by physiological and mechanical factors. Caterpillars, for example, deviate from the existing constant-volume worm models because they contain air. While worms breathe through their skin, caterpillars have a waxy external body surface to minimize water loss and an extensive internal system of gas-filled tubes (trachea) to facilitate gas exchange (Wasserthal 1996, Kramer, Wigglesworth 1950, Locke 1997). It has been shown behaviorally that gas inside the trachea can be compressed and expelled

from the spiracles during locomotion (personal observation, Lin *et al*). This air leak could compromise the efficiency of the hydrostatic skeleton. Instead of relying on a stiff hydrostatic structure, *Manduca* ground reaction forces suggest that crawling caterpillars can use the substrate for force transmission (an “environmental skeleton”) during normal locomotion (Lin, Trimmer 2010). In contrast, inchworms lift most of their body every stride and must be stiff enough to support elevated body positions. This difference suggests that the use of hydrostatic skeletons could be fundamentally different between animals that employ crawling as their primary form of locomotion and animals that employ an inching gait.

Adding to the complexity of caterpillar body mechanics, there is a developmental shift in the relative proportion of various tissues as the animals grow. First instar hatchlings sink in water but fifth instar *Manduca* caterpillars float, suggesting a change in body density. Unlike vertebrates, which tend to display isometric scaling of lung volume relative to body mass (West, Brown & Enquist 1997), many insects increase their mass-specific tracheation across instars to maintain sufficient oxygen intake (Lease, Wolf & Harrison 2006). Although fast growing caterpillars such as *Manduca sexta*, decrease their gas exchange capacity as they grow (Greenlee, Harrison 2005) a decrease in body density could be through a change in tissue composition, for example, the accumulation of fat tissues (Fernando-Warnakulasuriya, Tsuchida & Wells 1988, Tsuchida, Wells 1988).

In this study, we investigate the effects of different body properties (such as body size, tissue cross-sectional area, and the state of muscle activation) on the overall bending stiffness of the internal hydrostatic skeleton in caterpillars. Although *Manduca* can crawl using a tension-based strategy (Lin, Trimmer 2010) both first instar hatchlings (weighing 1~7 mg) and fifth instar caterpillars (>1 g) are able to cantilever their bodies with only three pairs of attached prolegs for support (Fig. 1A,B). Because complete anesthetization suppresses muscle activation and causes the animals to lose turgor (Fig. 1C) it is apparent that *Manduca* does not possess any structure that has significant bending stiffness. Instead, body stiffness relies on pressurization of the external soft body shell.

To characterize the hydrostatic skeleton in caterpillars, we measure the body length, diameter, volume, density, and baseline internal pressure of *Manduca*. Caterpillar body pressure is known to be highly variable (Mezoff et al. 2004) due to the internal flow of hemolymph and air cavities (personal observations) (Wasserthal 1981). We present a new measurement technique to define the baseline pressure in resting caterpillars. Finally, while previous studies document dramatic morphogenesis of load bearing tissues, such as the external cuticle, with respect to body mass (Wolfgang, Riddiford 1981, Wolfgang, Riddiford 1986), it is unclear how these tissues scale over the entire life cycle of the larvae. We determine the scaling of cuticle thickness and muscle cross-sectional area for *Manduca* caterpillars using histology imaging methods. These data allow us to numerically evaluate the loading characteristics of the hydrostatic skeleton in the physiological range and during growth.

Hydrostatic skeleton models in biology

The prevailing view of movement by animals without hard skeletons is that they must stiffen their body by pressurizing an internal body cavity such that forces can be transmitted to the substrate instead of being lost to tissue deformation (Vogel 2003, Wainwright 1988, Trueman 1975, Chapman 1958). For structures consisting of muscles, the muscles can act as both the structural support and the actuator (muscular hydrostats) (Kier 1992). Although an alternative locomotion strategy based on the controlled release of tension has recently been proposed (Lin, Trimmer 2010, Simon et al. 2010), it is limited to substrates that are stiffer than the animal. Directed movements on soft media and behaviors involving single point attachments must involve body stiffening, mostly through hydrostatics.

The modeling of biological hydrostatic structures (e.g. cnidarians, annelids, and nematodes) generally focuses on morphologies composed of soft tissues without any rigid skeleton (internal or external) supported by pressurized fluid. In particular, it has been shown that soft-bodied animals achieve extreme changes in overall length by using helical reinforcing fibers in the body wall (Clark, Cowey 1958), a property commonly found in cylindrical biological structures including those of plants (Wainwright 1988, Wainwright 1982). To move forward, animals can couple these dramatic extensions with the control of

friction or grip (Keller, Falkovitz 1983). This extension-grip-pull locomotion strategy can be found in many limbless animals, even snakes (Dobrolyubov 1986).

Hydrostatic mechanisms assume, in general, that the fluid content is incompressible and no significant change in body volume occurs, which for most organisms is a reasonable assumption (Wainwright 1988, Wainwright 1982, Wadepuhl, Beyn 1989, Kier, Smith 1985, Chiel et al. 1992). Finite element models for medical leeches have been created under these conditions (Wadepuhl, Beyn 1989, Muller, Nicholls & Stent 1981, Stern-Tomlinson et al. 1986, Sawyer 1986). These models incorporate animal geometry, elastic properties of the body wall, internal volume, and body pressure to reveal some principles of antagonism in worm-like structures as well as the pressure-volume interactions. As a step further, an empirically based leech model has been proposed with passive tissue properties, activation of muscle responses, and the transform from motor-neurons to muscles. It assumes elliptical cross-sections, constant volume, and simulates the vermiform elongation and pressure changes of a leech (Skierczynski et al. 1996). The motions of leeches have also been described using Lagrangian mechanics and a large system of differential-algebraic equations (Alscher, Beyn 1998) and by modeling a mass transfer wave that describes peristalsis (Dobrolyubov, Douchy 2002, Accoto, Castrataro & Dario 2004).

Although these models describe credible mechanisms for locomotion, they cannot be applied to hydrostatic skeletons that violate the constant body volume constraint. Caterpillars are yet to be described by any of the existing hydrostatic skeleton models for several reasons: 1) Extension in the longitudinal direction is accounted by numerous inter-segmental folds instead of body wall stretching (the classical helical fiber-reinforced cylinder model does not apply), 2) Body pressure is variable, especially during motion (reflecting fluid flow in the body, not static pressure), 3) The volume may not be constant since the tracheal air can escape (a constant volume assumption cannot be applied), 4) There is no segmental septum that compartmentalizes the animals (localized pressure control is not feasible), 5) Caterpillars are legged systems with discrete on-off attachments (frictional models based on mass transfer do not apply). Additionally, analysis techniques based on linear elastic theory are not applicable, as the mechanical

behavior of caterpillar's tissues is nonlinear and anisotropic. Under typical loading scenarios, these tissues undergo large deformations, and have complex boundary conditions. The approach we propose is more general and widely applicable to soft animals, because it facilitates structural analyses at different pressure states by relaxing the constant body volume requirement. We treat the hydrostatic skeleton as a shell structure in which the major tissue properties are described by anisotropic, nonlinear hyperelastic stress-deformation laws. For any applied body load, the body deformation is determined using large deformation theory and the material models developed in previous studies. This approach provides a more realistic approximation of a caterpillar's hydrostatic skeleton. For simplicity in this study, we evaluate only the static conditions.

2. Experimental methods

Experimental animals

Manduca sexta larvae were reared on artificial diet in an incubator at 27°C with a light:dark cycle of 17:7 hours (Bell, Joachim 1976). Third through fifth instars were selected for experimentation, ranging from 0.01 g to 3 g in mass. Twenty animals were used for biometry measurements, 39 animals for histology imaging, 27 for the body density measurement, 14 for determining the net tissue density, and 32 animals for the baseline pressure measurements.

Load bearing tissue quantification – tissue fixation and histology

Animals were euthanized by exposing them to ethyl acetate fumes for 30 min. They were then fixed using 10% formalin with phosphate buffered saline (PBS) and 10% dimethyl sulfoxide (DMSO) for 24~48 hrs until the external cuticle became rigid enough for slicing. The thoracic segments and terminal segments were removed on all animals to facilitate fixative perfusion. If possible, the gut content was also removed with the peritrophic membrane, leaving the interior hollow and allowing better penetration of the fixative. The 3rd abdominal segment (A3) was sectioned from each animal with all muscle attachments intact. The samples were then kept in the same formalin mixture and sent to *Tufts Cummings School of Veterinary*

Medicine Histology Lab for paraffin embedding and slicing. Cross-sectional slices (10 μm) were taken at the middle of segments A3 in all samples and stained with hematoxylin and eosin stain (H&E). Typically H&E stains cell nuclei blue and many proteins in the cytoplasm pink. The result allowed us to distinguish muscles from the cuticle and epithelium layers on the histology slides. Selected samples of the 5th abdominal (A5) segment were prepared in the same way, but we found no evident difference from the A3 samples' tissue thickness. All scaling measurements were therefore obtained from A3 samples.

Load bearing tissue quantification – imaging and image analysis

The histology cross-sections were imaged with a Zeiss Axiovert 40 CFL inverted microscope with standard dichromic mirrors (Fig. 2). Image collection was performed using QCapture Pro (QImaging, Surrey, BC). Color was autobalanced prior to collecting images and all images were collected at 5x magnification with a 2560x1920 acquisition resolution. It was found that the blue excitation light produced the most contrast between the muscles and the surrounding tissues. Because the sections were too large to view as a single image, multiple images were taken and stitched together using the “Photomerge” function in Adobe Photoshop (Adobe Systems, Inc., San Jose, CA). For the larger images, the resolution was halved during the image stitching process. All image analysis was done using ImageJ (NIH). First, a global calibration scale was applied by imaging a hemocytometer with lines of known distances. Next, the cuticle thickness was measured along the ventral body wall in between the prolegs (a location that can be easily identified in all slides). An average thickness was obtained from five measurements. All cuticle thickness measurements were done on sections of the 3rd abdominal segment (A3). Next, all easily discriminated non-muscle structures were manually removed from the image. The image was then converted to an 8-bit grayscale image and a grayscale histogram analysis was performed. Typically, two peaks were observed on the histogram, one representing the muscles while the other represented other structures and background noise. A threshold was set in between these two peaks and the image was then converted to a binary image containing only muscle. Using the “analyze particles” function, the area of each muscle was determined and summed to yield the total cross-sectional muscle

area. Before accepting the particle analysis, each image was checked manually and cross-referenced with the original image to ensure that the particles being counted represented all muscles and were specific to only muscles.

Body density measurements

The overall body density of third, fourth, and fifth instar *Manduca sexta* larva was determined by comparing the animal's body weight in the air and under water. First, an isometric force transducer (Grass Products Group, West Warwick, RI) was calibrated with objects of known mass. The caterpillars were then placed on a substrate (made of 2.4 mm diameter carbon fiber rod encapsulated by silicon tubing and sealant) suspended from the force transducer. The air weight of the caterpillar was measured by subtracting the transducer offset due to the substrate. The measured air weight was repeatable within 1% of the animal weight, determined from a Mettler laboratory scale (0.1 mg accuracy). The animal was slowly lowered into a beaker of de-ionized water in room temperature containing a few drops of surfactant to reduce surface effects upon submersion. The buoyant force of the caterpillar was calculated from the submerged total weight by subtracting the pre-determined effect of substrate immersion alone. Dividing the animal's body weight by its measured body volume gave the overall body density. Changes in water density due to surfactant and temperature were insignificant compared to the accuracy of the force transducer.

Tissue density measurements

Tissue density was determined by homogenizing third, fourth and fifth instar *Manduca sexta*. *Manduca* saline of 0.2 ml (for animals less than 0.5 g) or 0.5 ml (for larger animals) was added. This dilution resulted in 1:2 to 4:1 animal-saline ratio, with the smallest sample volume at least 0.3 ml. The remaining tissue fragments were further broken down using a sonifier (Branson Ultrasonics, Inc., Danbury, CT) for 15 sec at 20% power. This dicing and sonication process was repeated until a smooth tissue homogenate was produced. The samples were then centrifuged for two minutes to remove any remnant air vesicles in the tissue solution and allowed the final sonication step to produce a solution of uniform density. A fixed

volume (0.1 ml for animals less than 0.5 g and 0.2 ml for larger animals) of the homogenate was extracted with a 1 ml scale calibrated pipette and weighed to calculate the density. The measured density was then scaled up to account for the previous saline dilution. This sampling was performed twice per animal to obtain the average tissue density.

Body pressure measurements

In preliminary measurements of *Manduca* body pressure fluctuation, silicon catheters (ID~0.8 mm; OD~1 mm) were inserted into the tail horn of mildly-anesthetized caterpillars and connected to a small silicon piezoresistive pressure sensor (Honeywell, Freeport, IL). Such recordings revealed small, rhythmic pressure fluctuations that match the *Manduca* caterpillar heart rate (Smits 2000) and can be attributed to hemolymph flow produced by the dorsal vessel and abdominal contractions (Sláma 2003, Sláma 1984). As the animals resumed motion, the pressure changed inconsistently, rising or falling with the smallest movements and making this method inappropriate for establishing the static pressure range of a resting caterpillar.

Instead, an alternative method was used based on balancing fluid height in a capillary pipette. To minimize movements, the animals were uniformly air chilled to 10~15°C using a cold chamber. This temperature does not anesthetize the animals and is the minimum at which the muscles still respond to stimulation in the normal way (personal communication, W. Woods). Thin acupunctural needles (0.12 mm diameter; SEIRIN-America, Weymouth, MA) were used to introduce a weak point on the dorsal posterior cuticle surface to one side of the dorsal midline. A glass micropipette (tip ID~0.1 mm; tip OD~0.15 mm; tube OD=1 mm) was then wedged into the body at this weak point and hemolymph was drawn into the tube by capillary action aided by the internal body pressure. An adjustable water column was connected to the other end of the capillary tube to counterbalance the hemolymph pressure by forcing the hemolymph back into the animal. This water column also buffered transient pressure fluctuations and its height was recorded and converted to units of pressure. This method was calibrated using a silicone rubber “caterpillar mockup” with controllable internal pressure (a large water column reservoir, Fig. 3A).

During calibration the height of the water column directly mapped to the height of the water reservoir with a constant offset determined by the capillary effect of each glass pipette. A pressure transducer was used to detect any pressure fluctuation during each measurement. Typically, it took five seconds to reach equilibrium and readings were repeatable within 8% (54 calibration samples). Most animals were not responsive during the glass pipette insertion (Fig. 3B) and some survived to pupation.

Biometry measurement

Caterpillar bodies are fairly cylindrical (Fig. 2A). To determine scaling of the hydrostatic skeleton, we measured the body length and radius of caterpillars over a wide size range (Fig. 4). The body radius was defined as one half of the average height of the 1st, 3rd, and 7th abdominal segments viewed on the sagittal plane. Measurements were made from resting caterpillars photographed on a calibrated substrate using ImageJ (NIH).

Scaling data analysis

By convention, biological scaling data are modeled as a power function using the slope of a linear regression of each measured parameter plotted against body mass on a logarithmic plot. The slope obtained in this way represents the power by which the measured parameter scales with body mass. Referring to this important scaling constant, we use the word “scaling factor” and “scaling power” interchangeably throughout this paper. For any object that scales isometrically, the linear dimension would scale as a power of 1/3 and area 2/3 with respect to the volume. Assuming a constant density (very small variation in caterpillars), the isometric scaling power would be 0.33 for a linear dimension and 0.67 for an area. To evaluate the ontogenetic scaling of various biometrics in caterpillars, we compared the scaling factors from the experimental data against a reference value using Student’s t-statistics (Quillin 1998). All the isometric reference curves in this study were constructed by scaling the lowest values in the experimental data up with the isometric scaling factors.

3. Experimental results

Manduca body aspect ratio

Biometric data from our *Manduca* colony shows that the overall body length and radius scale allometrically but are not far off from isometric predictions (Fig. 4). Caterpillars generally grow from a slender body aspect ratio to a stouter one. Based on our data, the diameter-length aspect ratio scales from 0.118 to 0.137 (from a hatchling to a ~2 g fifth instar). Other species of caterpillar have much more dramatic allometric body scaling (personal observation).

Manduca cuticle ontogeny and muscle development

Both the average thickness of the endocuticle layers and overall muscle cross-sectional area scale allometrically, even though the data are very close to the isometric predictions (Fig. 5). The cuticle thickness scaling power is 0.43 which is significantly larger than the 0.33 isometric power ($t=2.52$, $p=0.008$, $df=37$). The muscle cross-sectional area increases in a step-wise manner at the beginning of each instar but roughly along the isometric reference (0.67). The typical ecdysis mass values were derived from an empirical *Manduca* growth model (Nijhout, Davidowitz & Roff 2006). Due to the technical difficulty of fixing all the internal structures, only 13 animal samples (out of 39 animals) allowed total muscle cross-section measurements on the 3rd abdominal segment.

Manduca body volume scaling

Manduca caterpillars become water buoyant after they molt into fifth instar. By comparing the air weight and submerged water weight of the same animal, the body volume can be estimated for a range of animals from third to fifth instar. The scaling coefficient of volume and mass on a logarithmic plot is 1.0184 ± 0.0046 ($R^2 = 0.9995$) with an almost negligible Y-intercept. This suggests that *Manduca* caterpillars become less dense than water when they exceed 1 g of body mass, crossing the point (0,0) on a log plot (Fig. 6A). This corresponds to the expected body mass (1.071 g) at the end of fourth instar (Nijhout, Davidowitz & Roff 2006). A one-sample, two-tail Student's t-test reveals that the 1.84% extra volume expansion is significantly different from the constant density unity scaling coefficient ($t=4.03285$;

$p < 0.001$; $df = 25$). *Manduca* caterpillars decrease in density as they get larger. While the accumulation of body fat could account for this change in body density (Tsuchida, Wells 1988), it could also result from changes in the tracheal system. Our data show decreasing trends with non-zero slopes in both the mean body density ($t = -4.0178$, $p = 0.0005$, $df = 25$) and the net tissue density ($t = -3.0925$, $p = 0.0093$, $df = 12$) (Fig. 6B). However, these two parameters also decrease with the same exponential power (slopes) ($t = 1.2132$, $p = 0.2327$, $df = 37$), suggesting that changes in body density are predominantly due to increasing body fat or other low-density tissue growth. Nevertheless, the air cavity volume (as a percent of the total body volume) increases significantly from 2.87% for a 0.05 g animal to 7.69% for a 2 g animal. This large volume of internal gas could influence dynamic loading of the hydrostatic skeleton.

Manduca baseline body pressure

Even under carefully controlled conditions, *Manduca* baseline pressure varied widely, with most measurements clustering between 1 kPa and 1.6 kPa (Fig. 7). Although body pressure tend to be lower in larger animals, there is no satisfactory linear regression to this trend ($r^2 < 0.2$). Evidently, caterpillars in different stages can function in a similar pressure range. The mechanical consequences of this large operation pressure range were evaluated using a nonlinear finite element model.

4. Modeling approach for a hydrostatic skeleton

Unlike engineered structures, it is difficult to subject living animals to standard mechanical tests. As an alternative approach, mathematical and numerical models can be used to investigate and predict the structural responses of animals. There has been a great deal of effort in developing analytical solutions for inflatable structures, going beyond elementary beam bending theory (Le Van, Wielgosz 2005, Thomas, Jiang & Wielgosz 2006). To remove constraints and simplifications associated with analytical solutions, we develop an empirically-based numerical approach to explore the mechanical responses of the hydrostatic skeleton in caterpillars. The ontogenetic scaling data presented in this paper provide realistic values to implement a numerical simulation.

Caterpillars' hydrostatic skeleton

Caterpillars have a very complex, multi-scale structure with body weight and other applied loads jointly supported by the cuticle and muscles. Experimental results show that the mechanical response of the cuticle in the longitudinal and circumferential directions is highly nonlinear, with stresses increasing exponentially with stretch (Lin, Dorfmann & Trimmer 2009). For a given stretch, stresses are larger for cuticle specimens loaded in the circumferential direction compared to the specimens loaded in the longitudinal direction, indicating anisotropy in the material response (Fig. 8A). In particular, higher stiffness in the circumferential direction is necessary to support hoop stress generated by pressurization. Muscles are primarily oriented in the longitudinal direction and can be activated to increase body pressurization. A detailed description of the mechanical response of the ventral interior lateral muscle of the 3rd abdominal segment, both with and without stimulation, has been provided in recent publications (Lin, Dorfmann & Trimmer 2009, Dorfmann, Woods & Trimmer 2008, Dorfmann, Trimmer & Woods 2007).

Data show that muscles have deformation-dependent properties, exhibit loading-unloading hysteresis and are capable of increasing stiffness during stimulation. The effect of the stimulus depends nonlinearly on the amount of deformation (Fig. 8B). All other tissues of *Manduca* are highly compliant relative to the cuticle or muscles. While these tissues do not carry a significant load, they are necessary to maintain internal pressure and to prevent the cuticle from collapsing. Also, leg structures are protrusions that do not affect the overall stiffness of the hydrostatic skeleton.

Finite element model

To model the hydrostatic skeleton of a caterpillar, we consider an inflatable, horizontal, cylindrical tube with a circular cross-sectional area. The shell of this tube is endowed with two families of perfectly aligned, homogenous, superimposed fibers. Fibers in the circumferential direction account for the anisotropic behavior of the cuticle (Fig 8A); fibers along the longitudinal direction account for the behavior of major body muscles. The muscles can be switched between passive (tonic) and active (tetanus) states (Fig. 8B). In the proposed model the total length is denoted by L , the radius by R , the cuticle layer

thickness by t_1 and the equivalent muscle layer thickness by t_2 (Fig. 9). We assume that the total cross-sectional muscle area can be smeared uniformly around the perimeter of the model. Therefore, the muscle layer thickness t_2 is given by the equality $2\pi R t_2 = \text{total cross-sectional muscle area}$. Two shell layers having thicknesses t_1 and t_2 are superimposed and share the same nodal points, in accordance with the parallel modeling approach (Nelson, Dorfmann 1995). Finally, the left end of the finite element model is restraint to eliminate any rigid body motion, while the right end is capped.

The constitutive equations used to describe the nonlinear mechanical response of the cuticle in the longitudinal and in the circumferential directions are based on an exponential stress-stiffening formulation (Fig. 8A) (Lin, Dorfmann & Trimmer 2009, Dorfmann, Woods & Trimmer 2008, Dorfmann, Trimmer & Woods 2007). The force-extension characteristics of *Manduca* muscles under constant-rate loading and unloading can be simulated using a pseudo-elastic reinforcing model both in a passive state and during titanic stimulation (Fig. 8B) (Lin, Dorfmann & Trimmer 2009, Dorfmann, Woods & Trimmer 2008, Dorfmann, Trimmer & Woods 2007). In addition to strain-dependent stress softening, the responses of *Manduca* muscle depend on the rate of loading and unloading (Lin, Dorfmann & Trimmer 2009, Dorfmann, Woods & Trimmer 2008, Dorfmann, Trimmer & Woods 2007). For the purposes of this work, we focus on the time independent formulation thereby neglecting rate and viscous effects. To examine the effects of scaling on caterpillar hydrostatic skeletons, we consider the sizes of a fifth instar and a hatchling *Manduca*. Table 1 summarizes the values of the geometric parameters used for both size scales. In addition, we consider muscle fibers to be either in an active (tetanus) or passive (tonic) state. With the two possible size scales and the two muscle conditions, we consider four models in total.

Each of the four models was analyzed following a two-step process. During the initial step, a pressure was applied to the inner surface of the cylindrical tube and to the cap at the free end. This pressure increased monotonically to a predefined target value. During pressurization, the model was subject to longitudinal extension and radial inflation. The correlation between change in radius R and change in length L , at a given pressure, was nonlinear and depended on the magnitude of the geometric parameters,

the cuticle stiffness, the passive properties of the muscles and on the force developed during activation. The resulting stable deformed configuration was cylindrical with a circular cross-section and the longitudinal axis pointed in the horizontal direction. In the second step of the analysis, a body force was added with the vertical component gradually increasing from zero, with the applied pressure held constant. We monitored the vertical deflection of the free end until the configuration became unstable following a compression buckling mode, localized at the fixed end. The model detailed here was implemented in the nonlinear finite element package Abaqus (SIMULIA, Providence, RI). The above two-step procedure decoupled the body pressurization from muscle activation, and therefore allowed us to simulate the hydrostatic skeleton at any target states.

Results of the four models are reported as normalized body force versus normalized tip deflection. The body force is normalized by the selected body weights (2 g and 0.05 g) and the tip deflection by the initial body length L . The geometric dimensions of the undeformed configuration are derived from the experimental fits presented earlier. The total cross-sectional area of the muscles is assumed isometric (0.67 power scaling) (Table 1). The initial slope of the normalized body force as a function of the normalized tip deflection is used to define the specific bending stiffness (a dimensionless parameter in this case).

5. Modeling results

At any given internal pressure, the model tip deflection increases linearly with applied body force up to a critical point (examples given in Fig. 10). The specific bending stiffness of the large scale model is much lower compared to that of the small scale model. This is a combined result of the increasing bending moment and the scaling of overall structural parameters (Table 1). In addition, previous studies on inflatable beams (with linear-elastic membrane) showed that pressurization delayed the buckling deflection but had little effect on the initial flexural stiffness (Veldman, Bergsma & Beukers 2005, NASA 1965, Fichter 1966). In contrast, results from our finite element simulation show how an increasing

pressure directly stiffens the structure (increase in initial slope). This is due to the nonlinear, stress-stiffening properties in the tissues and the large deformation kinematics considered in the analysis.

The bending stiffness increase nonlinearly with increasing internal pressure (Fig. 11) across the two model sizes, and the two muscle states: passive (tonic) and active (tetanus). The resulting trends clearly show that the increase in stiffness due to pressurization is much higher for the smaller model (by at least an order of magnitude as shown in the semi-log plot in Fig. 11). Also, the increase in stiffness is more pronounced at low values of internal pressure, becoming less significant at high pressures.

The effect of cuticle thickness on model stiffness was very revealing. Specifically, we considered the small scale model with muscle in the passive (tonic) state and with an internal pressure of 1 kPa (typical body pressure in *Manduca*). We doubled the cuticle thickness t_l from the original value of 0.007 mm to 0.014 mm. Contrary to intuition, the model appeared softer during loading, and became unstable at a smaller applied body force. This is a direct consequence of the nonlinear constitutive model used for the cuticle. The exponential increase of stress with applied stretch is equivalent to an increase in stiffness with increasing load in the cuticle (Fig. 8). For a given internal pressure, the increase in cuticle thickness reduces the hoop and longitudinal stresses and therefore the material stiffness. A similar argument applies, but to a lesser extent, when the total cross-sectional area of the muscles is increased (Fig. 11).

6. Conclusions and discussions

Our findings have several implications for the use of a hydrostatic skeleton as body support. First of all, bending stiffness in a pressurized cylinder with a hyperelastic shell is determined by three major factors: internal pressure, shell wall thickness and material properties. Baseline internal pressure dictates the amount of pre-stress in the shell wall before applying a load. Shell wall thickness determines the distribution of this stress. The nonlinear material properties relate the stress in the shell wall to the resulting strain. These three parameters therefore have a major impact on the initial conditions and structural stiffness of an inflated cylinder. Of course, whether this stiffness is sufficient to allow the body

to be functional when cantilevered depends on the body loading condition, which comes from the overall body dimensions and body weight.

There are two major mechanisms to control the body stiffness in caterpillars. Body pressurization stretches the body shell in the longitudinal and circumferential directions. Due to the stress-stiffening property of the tissues, the overall body bending stiffness increases in response to pressurization. However, such increasing trend in stiffness eventually plateaus as the stress-stiffening effect diminishes in the tissues at high stress states. Further stiffening can be achieved by muscle activation, which not only increases body shell stiffness, but also resists body elongation. The animals are most likely to employ both mechanisms simultaneously. Although this study explored these two mechanisms independently, the results reveal the range of capable states a caterpillar can achieve. The next step will be to examine how muscle activation determines body volume and pressure.

Curiously, increasing muscle cross-sectional area or thickening cuticle thickness will not result in higher structural bending stiffness for a given internal pressure. For a pressurized cylindrical shell, an increase in the wall thickness decreases the stress for the same applied forces (i.e. internal pressure). To stress the added material to the same state, the hydrostatic skeleton has to operate at a higher baseline pressure, which may not be ideal for the animal. This may be why caterpillars such as *Manduca* maintain almost isometric scaling for the muscle and cuticle thickness.

Alternatively, the animal can solve the body support problem by simply limiting its size. Since the body load scales with body volume, and the body dimensions scale almost linearly, overall size reduction alleviates the body load dramatically. For an inflatable cylinder with a constant internal pressure, the hoop stress is proportional to the body radius and disproportional to the body wall thickness. In *Manudca* caterpillars, slight allometric scaling in the body wall implies higher hoop stress in small hydrostatic skeletons. This puts stress-stiffening material into a higher initial stress. Consequently, small hydrostatic skeletons are actually operating at higher stress for the same pressure. Of course, changing the body length-diameter aspect ratio could affect the overall structural stiffness and the loading condition.

Therefore, another simple solution to improve body support is to change the aspect ratio with increasing body size as seen in most caterpillars. This is in fact quite dramatic in some caterpillar species where the hatchling has a diameter-length ratio of ~ 0.1 and triples to ~ 0.3 as the last instar (unpublished data, Lin *et al*). In fact, some small inchworms can also maneuver and remain stable even with diameter-length ratio of ~ 0.05 .

The above analyses may allow us to address an important dichotomy in caterpillar locomotion: why do some inch and others crawl? Inching involves well-controlled casting behavior to find a target substrate and precise placement of the posterior legs to meet the anterior ones. This mode of locomotion requires an effective hydrostatic skeleton and body coordination as predicted in computer simulations (Ghanbari et al. 2008). On the other hand, crawling can be identified by the propagation of an antero-gradual body contraction wave (Snodgrass 1993). This mode of locomotion does not necessarily rely on a hydrostatic skeleton. Ground reaction force analysis of *Manduca* locomotion shows that a crawling caterpillar can use the substrate as an “environmental skeleton” to transmit compressive forces while keeping most of the body in tension (Lin and Trimmer, 2010). Why do different species of caterpillars adapt inching and/or crawling while sharing the same general body anatomy? The answer could be simply a matter of size. There might be a mechanical limitation to maneuvering primarily with hydrostatic skeleton when the caterpillar is big.

Hydrostatic body support for large caterpillars requires muscle activation and significant pressurization. To avoid constant high pressure in the body and to minimize muscle work, large caterpillars keep their body aligned with the substrate most of the time supported by closely spaced prolegs. Small caterpillars on the other hand can easily achieve self-supporting body stiffness even with muscle at the tonic state. The hydrostatic skeleton can operate at the normal physiological pressure and the body responds to muscle control dynamically. Under these conditions, smaller caterpillars do not need many leg supports and inching becomes an appealing locomotion strategy, especially when they are very small compared to the branched plant structures. This argument may apply to all small caterpillars, as well as hatchlings of

large caterpillars. Why then doesn't the *Manduca* change from inching to crawling as it grows? Perhaps such a switch is difficult for the control of prolegs since it involves a major modification of the gripping pattern. It is interesting to note, however, that *Manduca* caterpillars in the first two instars have noticeably smaller mid-abdominal prolegs (more like inchworms). It is very likely that hatchlings spend more time picking up their bodies in search of new food substrates. An extensive behavioral survey should be able to confirm this speculation.

To summarize, we have determined the biometric scaling of *Manduca* caterpillars over two orders of magnitude body mass during development. The body density and baseline pressure drop only slightly. Combining these new scaling data with two previously published constitutive models of caterpillar muscles and cuticle, we used a nonlinear finite element model of an inflatable cylinder to represent the hydrostatic skeleton of a caterpillar. This model shows that increasing body pressure has a direct impact on the overall bending stiffness up to the physiological pressure range. Starting from the minimum physiological pressure, any increase of body pressure does not give rise to significant increase in structural bending stiffness. However, muscle activation can double this stiffness regardless of the body size. The model also demonstrates that near isometric scaling can decrease the overall bending stiffness dramatically. Although the initial parameters were based on *Manduca*, this modeling approach can be applied to different body forms and sizes. It can be used to examine mechanical constraints on other caterpillars of different sizes or species. More specifically, the decrease of inherent stiffness due to up-scaling may impose a great biomechanical cost to large caterpillars and therefore lead to behavior preference to crawling. In contrast, inching is much more commonly found in caterpillars with small bodies.

References

- Accoto, D., Castrataro, P. & Dario, P. 2004, "Biomechanical analysis of Oligochaeta crawling", *Journal of theoretical biology*, vol. 230, no. 1, pp. 49-55.
- Alscher, C. & Beyn, W.J. 1998, "Simulating the motion of the leech: A biomechanical application of DAEs", *Numerical Algorithms*, vol. 19, no. 1, pp. 1-12.
- Bell, R.A. & Joachim, F.G. 1976, "Techniques for rearing laboratory colonies of tobacco hornworms and pink bollworms", *Annals of the Entomological Society of America*, vol. 69, no. 2, pp. 365-373.
- Chapman, G. 1958, "The hydrostatic skeleton in the invertebrates", *Biological Reviews*, vol. 33, no. 3, pp. 338-371.
- Che, J. & Dorgan, K.M. 2010, "It's tough to be small: dependence of burrowing kinematics on body size", *Journal of Experimental Biology*, vol. 213, no. 8, pp. 1241.
- Chiel, H.J., Crago, P., Mansour, J.M. & Hathi, K. 1992, "Biomechanics of a muscular hydrostat: a model of lapping by a reptilian tongue", *Biological cybernetics*, vol. 67, no. 5, pp. 403-415.
- Clark, R.B. & Cowey, J.B. 1958, "Factors controlling the change of shape of certain nemertean and turbellarian worms", *Journal of Experimental Biology*, vol. 35, no. 4, pp. 731.
- Demetrius, L. 2006, "The origin of allometric scaling laws in biology", *Journal of theoretical biology*, vol. 243, no. 4, pp. 455-467.
- Dobrolyubov, A.I. 1986, "The mechanism of locomotion of some terrestrial animals by travelling waves of deformation", *Journal of theoretical biology*, vol. 119, no. 4, pp. 457-466.
- Dobrolyubov, A.I. & Douchy, G. 2002, "Peristaltic Transport as the Travelling Deformation Waves", *Journal of theoretical biology*, vol. 219, no. 1, pp. 55-61.
- Dorfmann, A.L., Trimmer, B.A. & Woods, W.A. 2007, "A constitutive model for muscle properties in a soft-bodied arthropod", *J.Roy.Soc.Interface*, vol. 4, pp. 257-269.
- Dorfmann, A.L., Woods, W.A. & Trimmer, B.A. 2008, "Muscle performance in a soft-bodied terrestrial crawler: constitutive modeling of strain-rate dependency", *J.Roy.Soc.Interface*, vol. 5, pp. 349-362.
- Fernando-Warnakulasuriya, G.J.P., Tsuchida, K. & Wells, M.A. 1988, "Effect of dietary lipid content on lipid transport and storage during larval development of *Manduca sexta*", *Insect Biochemistry*, vol. 18, no. 2, pp. 211-214.
- Fichter, W.B. 1966, "A theory for inflated thin-wall cylindrical beams", *NASA Technical Note D-3466, National Aeronautics and Space Administration, Washington, DC*, .
- Ghanbari, A., Rostami, A., Noorani, S.M. & Fakhrabadi, M.M. 2008, "Modeling and Simulation of Inchworm Mode Locomotion", *Proceedings of the First International Conference on Intelligent Robotics and Applications: Part I* Springer, , pp. 617.
- Greenlee, K.J. & Harrison, J.F. 2005, "Respiratory changes throughout ontogeny in the tobacco hornworm caterpillar, *Manduca sexta*", *Journal of Experimental Biology*, vol. 208, no. 7, pp. 1385-1392.

- Jordan, C.E. 1998, "Scale effects in the kinematics and dynamics of swimming leeches", *Canadian journal of zoology*, vol. 76, no. 10, pp. 1869-1877.
- Keller, J.B. & Falkovitz, M.S. 1983, "Crawling of worms", *Journal of theoretical biology*, vol. 104, no. 3, pp. 417-442.
- Kier, W.M. 1992, "Hydrostatic skeletons and muscular hydrostats", *Biomechanics (Structures and Systems): A Practical Approach*, , pp. 205–231.
- Kier, W.M. & Smith, K.K. 1985, "Tongues, tentacles and trunks: the biomechanics of movement in muscular-hydrostats", *Zoological Journal of the Linnean Society*, vol. 83, no. 4, pp. 307-324.
- Kramer, S. & Wigglesworth, V.B. 1950, "The outer layers of the cuticle in the cockroach *Periplaneta americana* and the function of the oenocytes", *Journal of cell science*, vol. 3, no. 13, pp. 63.
- Le Van, A. & Wielgosz, C. 2005, "Bending and buckling of inflatable beams: Some new theoretical results", *Thin-Walled Structures*, vol. 43, no. 8, pp. 1166-1187.
- Lease, H.M., Wolf, B.O. & Harrison, J.F. 2006, "Intraspecific variation in tracheal volume in the American locust, *Schistocerca americana*, measured by a new inert gas method", *Journal of Experimental Biology*, vol. 209, no. 17, pp. 3476.
- Lin, H.T., Dorfmann, A.L. & Trimmer, B.A. 2009, "Soft-cuticle biomechanics: A constitutive model of anisotropy for caterpillar integument", *Journal of theoretical biology*, vol. 256, no. 3, pp. 447-457.
- Lin, H.T. & Trimmer, B.A. 2010, "The substrate as a skeleton: ground reaction forces from a soft-bodied legged animal", *Journal of Experimental Biology*, vol. 213, no. 7, pp. 1133.
- Locke, M. 1997, "Caterpillars have evolved lungs for hemocyte gas exchange", *Journal of insect physiology*, vol. 44, no. 1, pp. 1-20.
- Mezoff, S., Papastathis, N., Takesian, A. & Trimmer, B.A. 2004, "The biomechanical and neural control of hydrostatic limb movements in *Manduca sexta*", *Journal of Experimental Biology*, vol. 207, no. 17, pp. 3043-3053.
- Muller, K.J., Nicholls, J.G. & Stent, G.S. 1981, *Neurobiology of the Leech*, Cold Spring Harbor Laboratory Pr.
- NASA 1965, "Bucklin of Thin-Walled Circular Cylinders", *NASA space vehicle design criteria*, , no. SP-8007.
- Nelson, R.B. & Dorfmann, A. 1995, "Parallel elastoplastic models of inelastic material behavior", *Journal of Engineering Mechanics*, vol. 121, pp. 1089.
- Nijhout, H.F., Davidowitz, G. & Roff, D.A. 2006, "A quantitative analysis of the mechanism that controls body size in *Manduca sexta* ", *Journal of biology*, vol. 5, no. 5, pp. 16.
- Prange, H.D., Anderson, J.F. & Rahn, H. 1979, "Scaling of skeletal mass to body mass in birds and mammals", *The American Naturalist*, vol. 113, no. 1, pp. 103-122.
- Quillin, K.J. 2000, "Ontogenetic scaling of burrowing forces in the earthworm *Lumbricus terrestris*", *Journal of Experimental Biology*, vol. 203, no. 18, pp. 2757-2770.

- Quillin, K.J. 1999, "Kinematic scaling of locomotion by hydrostatic animals: ontogeny of peristaltic crawling by the earthworm *lumbricus terrestris*", *Journal of Experimental Biology*, vol. 202, no. 6, pp. 661-674.
- Quillin, K.J. 1998, "Ontogenetic scaling of hydrostatic skeletons: geometric, static stress and dynamic stress scaling of the earthworm *lumbricus terrestris*", *Journal of Experimental Biology*, vol. 201, no. 12, pp. 1871-1883.
- Sawyer, R.T. 1986, *Leech biology and behaviour*, Clarendon Press Oxford.
- Simon, M.A., Fusillo, S.J., Colman, K. & Trimmer, B.A. 2010, "Motor patterns associated with crawling in a soft-bodied arthropod", *Journal of Experimental Biology*, vol. 213, no. 13, pp. 2303.
- Skierczynski, B.A., Wilson, R.J.A., Kristan Jr, W.B. & Skalak, R. 1996, "A Model of the Hydrostatic Skeleton of the Leech", *Journal of theoretical biology*, vol. 181, no. 4, pp. 329-342.
- Sláma, K. 2003, "Mechanical aspects of heartbeat reversal in pupae of *Manduca sexta*", *Journal of insect physiology*, vol. 49, no. 7, pp. 645-657.
- Sláma, K. 1984, "Recording of haemolymph pressure pulsations from the insect body surface", *Journal of Comparative Physiology B: Biochemical, Systemic, and Environmental Physiology*, vol. 154, no. 6, pp. 635-643.
- Smits, A.W. 2000, "Developmental changes in in vivo cardiac performance in the moth *Manduca sexta*", *Journal of Experimental Biology*, vol. 203, no. 2, pp. 369-378.
- Snodgrass, R.E. 1993, *Principles of insect morphology*, Cornell University Press.
- Stern-Tomlinson, W., Nusbaum, M.P., Perez, L.E. & Kristan, W.B. 1986, "A kinematic study of crawling behavior in the leech, *Hirudo medicinalis*", *Journal of Comparative Physiology A: Neuroethology, Sensory, Neural, and Behavioral Physiology*, vol. 158, no. 4, pp. 593-603.
- Thomas, J.C., Jiang, Z. & Wielgosz, C. 2006, "Continuous and finite element methods for the vibrations of inflatable beams", *International Journal of Space Structures*, vol. 21, no. 4, pp. 197-222.
- Trueman, E.R. 1975, *The Locomotion of soft-bodied animals*, Edward Arnold: London.
- Tsuchida, K. & Wells, M.A. 1988, "Digestion, absorption, transport and storage of fat during the last larval stadium of *Manduca sexta*. Changes in the role of lipophorin in the delivery of dietary lipid to the fat body", *Insect Biochem*, vol. 18, pp. 263-268.
- Veldman, S.L., Bergsma, O.K. & Beukers, A. 2005, "Bending of anisotropic inflated cylindrical beams", *Thin-Walled Structures*, vol. 43, no. 3, pp. 461-475.
- Vogel, S. 2003, *Comparative biomechanics*, Princeton University Press Princeton, NJ.
- Wadepuhl, M. & Beyn, W.J. 1989, "Computer simulation of the hydrostatic skeleton. The physical equivalent, mathematics and application to worm-like forms.", *J.Theor.Biol.*, vol. 136, pp. 379-402.
- Wainwright, S.A. 1988, *Axis and Circumference: The Cylindrical Shape of Plants and Animals*, Harvard University Press, Cambridge.
- Wainwright, S.A. 1982, *Mechanical Design in Organisms*, Princeton University Press.

- Wasserthal, L.T. 1996, "Interaction of circulation and tracheal ventilation in holometabolous insects", *Adv.Insect Physiol*, vol. 26, pp. 297-351.
- Wasserthal, L.T. 1981, "Oscillating haemolymph 'circulation' and discontinuous tracheal ventilation in the giant silk moth *Attacus atlas* L.", *Journal of Comparative Physiology B: Biochemical, Systemic, and Environmental Physiology*, vol. 145, no. 1, pp. 1-15.
- West, G.B., Brown, J.H. & Enquist, B.J. 1997, "A general model for the origin of allometric scaling laws in biology", *Science*, vol. 276, no. 5309, pp. 122.
- Wolfgang, W.J. & Riddiford, L.M. 1981, "Cuticular morphogenesis during continuous growth of the final instar larva of a moth.", *Tissue Cell*, vol. 13, pp. 757-772.
- Wolfgang, W.J. & Riddiford, L.M. 1986, "Larval cuticular morphogenesis in the tobacco hornworm, *Manduca sexta* and its hormonal regulation.", *Dev.Biol.*, vol. 113, pp. 305-316.

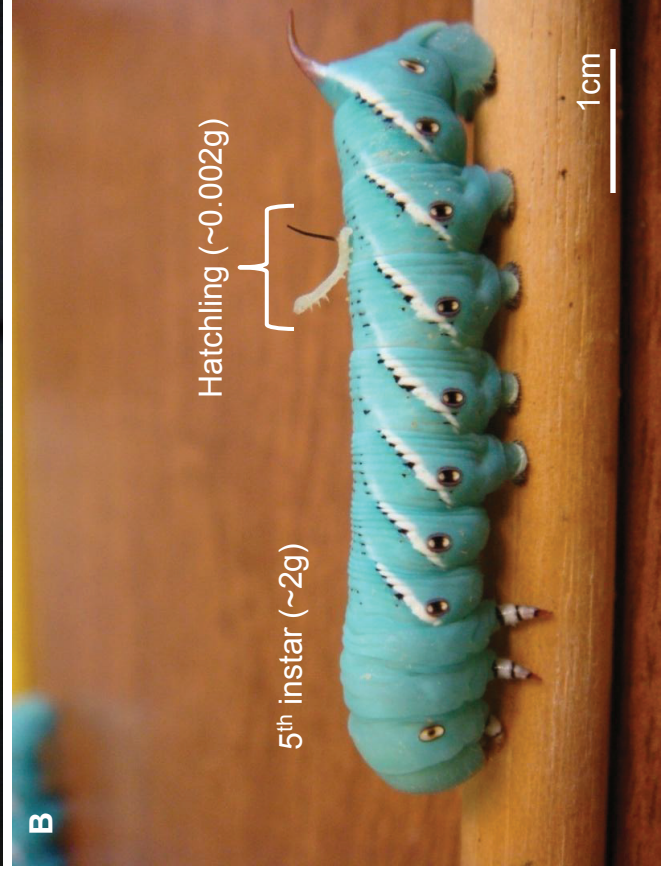
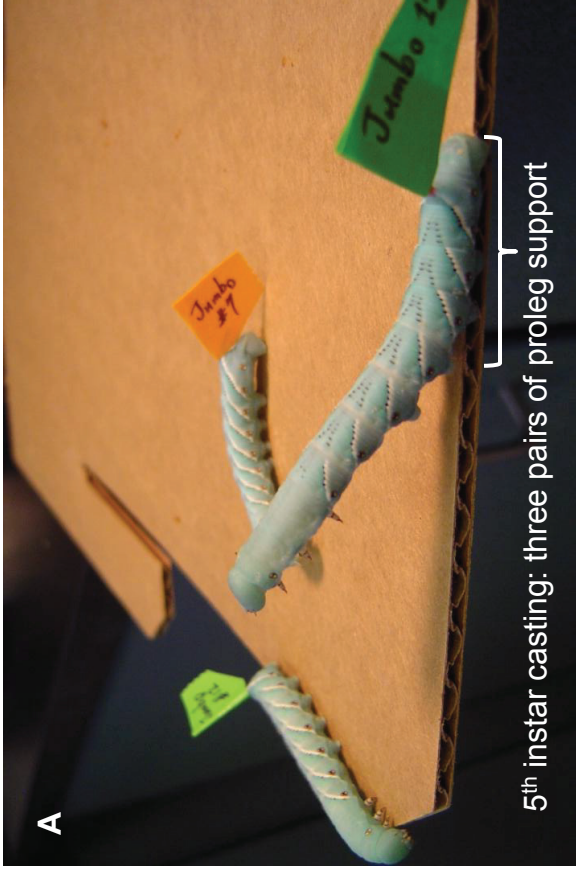


Figure 1. (A) *Manduca* caterpillars can develop sufficient hydrostatic pressure to cantilever their bodies. (B) During casting behavior, hatchlings three orders of magnitude smaller (by volume) than the fifth instar animals also cantilever their body. (C) Complete anesthetization suppresses muscle tone and causes the caterpillar to lose turgor.

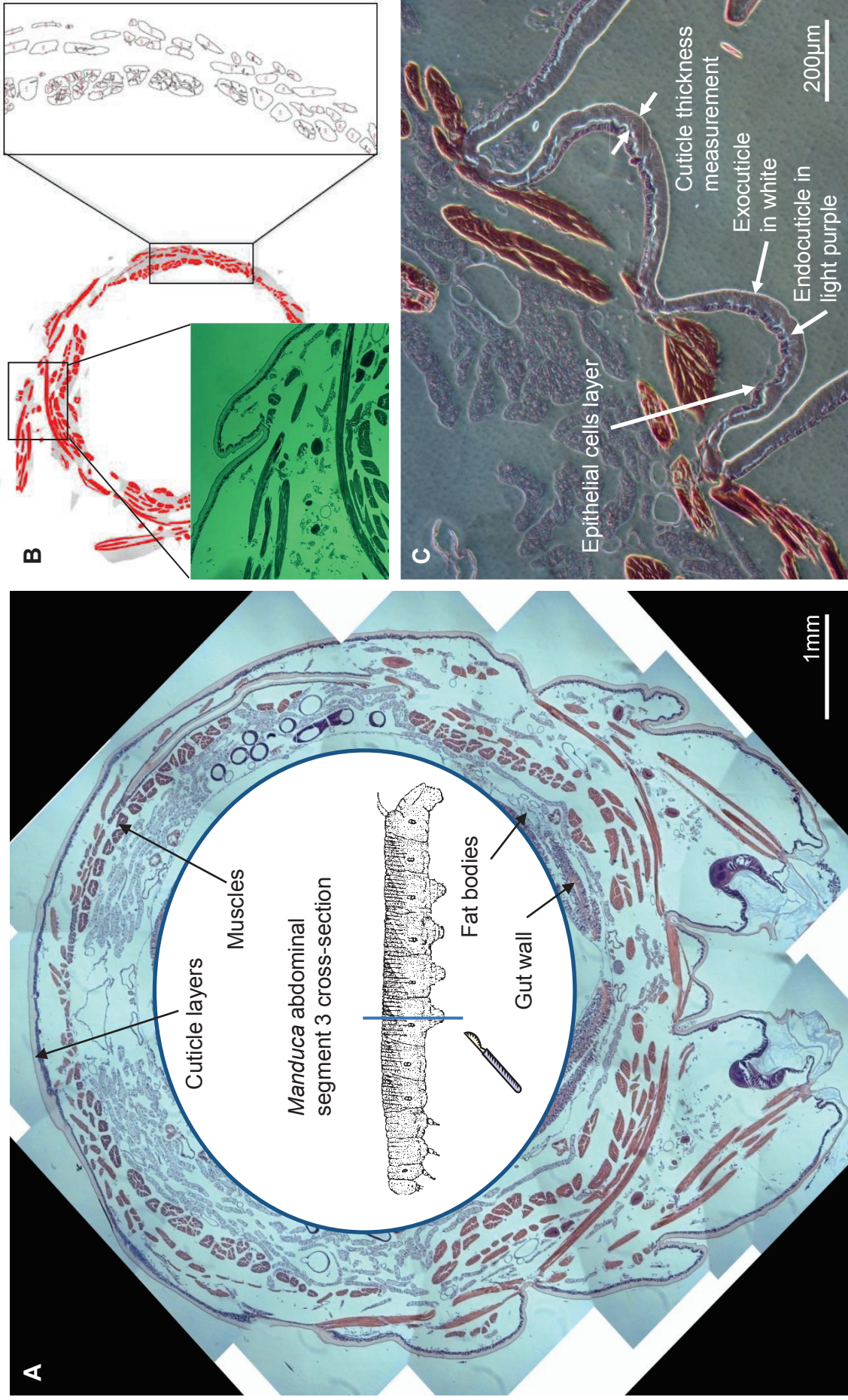


Figure 2. Histology of *Manduca sexta* caterpillar. (A) Adjacent histology images of the abdominal segment 3 were stitched together from multiple microscopic images. The example cross-section came from a 5th instar animal. H&E stained most of the soft tissues inside the body. (B) Blue light excitation (observed in green) emphasized muscle fibers so that they could be identified by image analysis. (C) The endocuticle and exocuticle layers are easily distinguished from the soft flaky epithelial cell layer which was excluded from the cuticle thickness measurements. The gut wall is orders of magnitude softer than the muscle fibers in the longitudinal direction and cuticle in the circumferential direction. It is therefore omitted in the measurements of mechanical components.

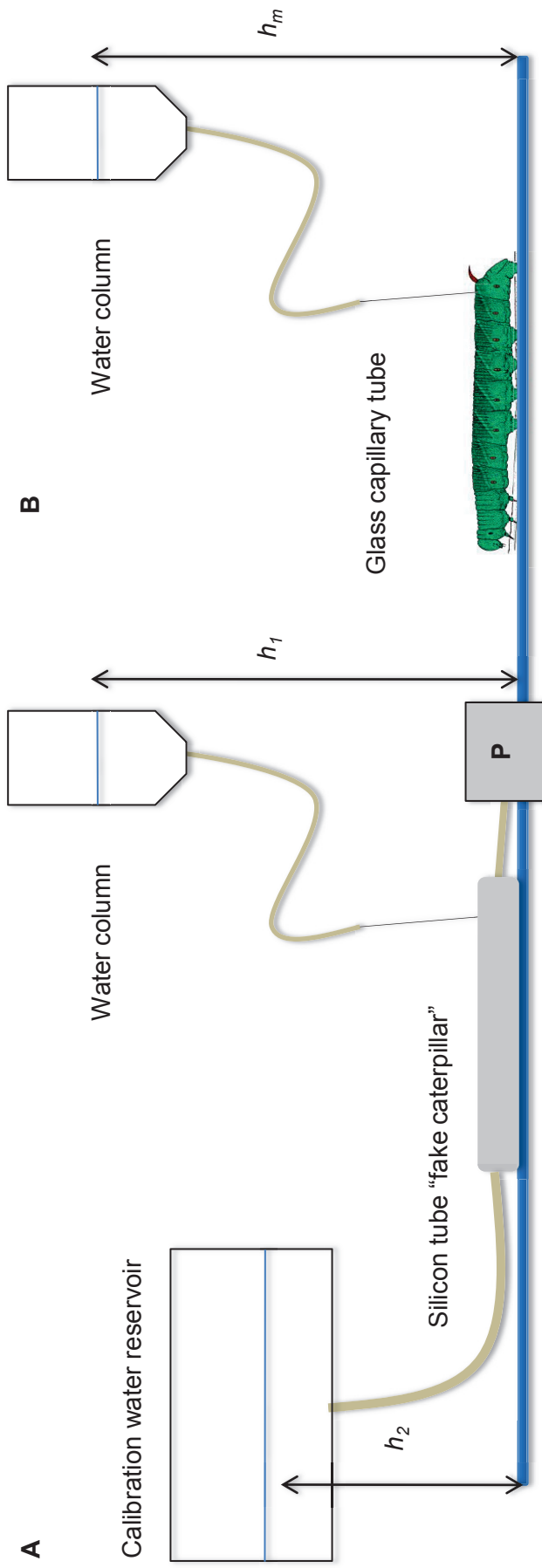


Figure 3. Baseline body pressure measurement. (A) To calibrate pressure measurements using the capillary system, a “fake caterpillar” was constructed from silicon tube similar in diameter to the animal. The internal pressure was controlled and buffered by a large water reservoir. The linearity of the change of pressure was independently monitored by the pressure transducer, P, on the other end. A glass capillary micropipette was inserted into the fake caterpillar to assess the internal pressure. The level of the water column h_1 was mapped to the calibration water reservoir h_2 in the calibration process. (B) The pipette was then inserted into a live *Manduca* to obtain a baseline resting pressure using height of the water column h_m .

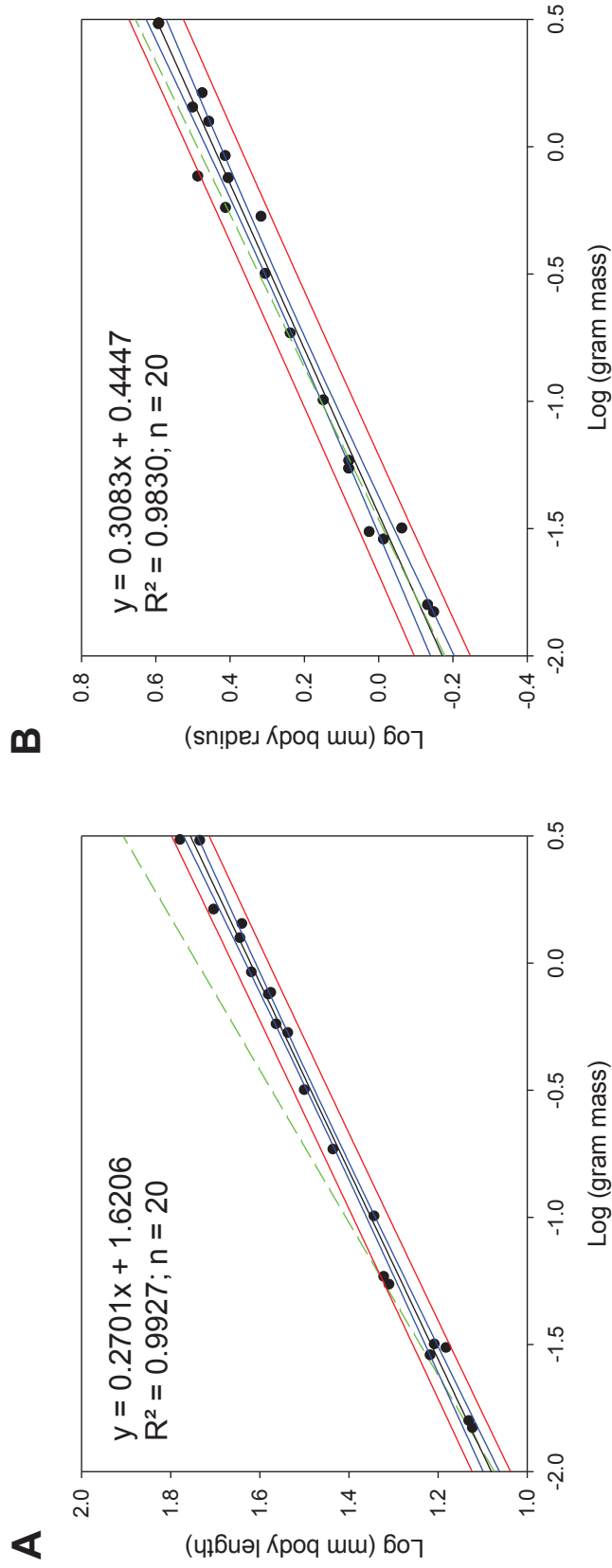
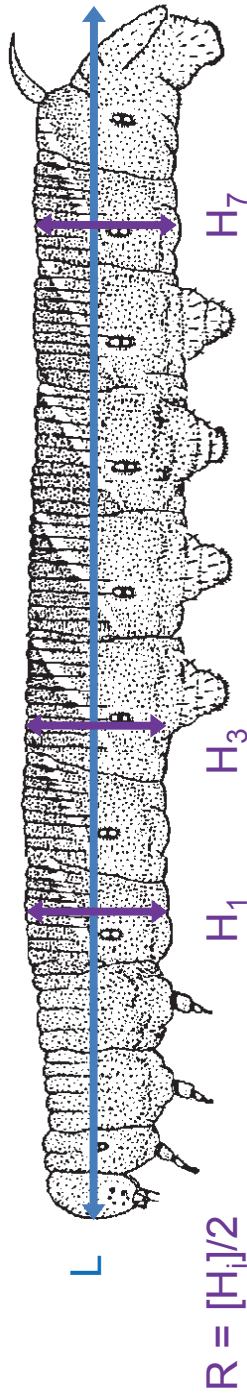


Figure 4. Ontogenetic scaling of *Manduca* body proportion. The body length is measured between the head capsule and anus, while the body radius is defined to be one half of the average height measured at segments 1, 3 and 7 in the calibrated images. Both quantities increase as a power function of body mass (**A, B**). Both linear regressions significantly deviate from the isometric slope of 0.33 (green dash) as demonstrated by the two-tail t-tests for body length ($p < 0.001$) and radius ($p = 0.0346$). The 95% confidence band and 95% predicted band are plotted in red and blue respectively.

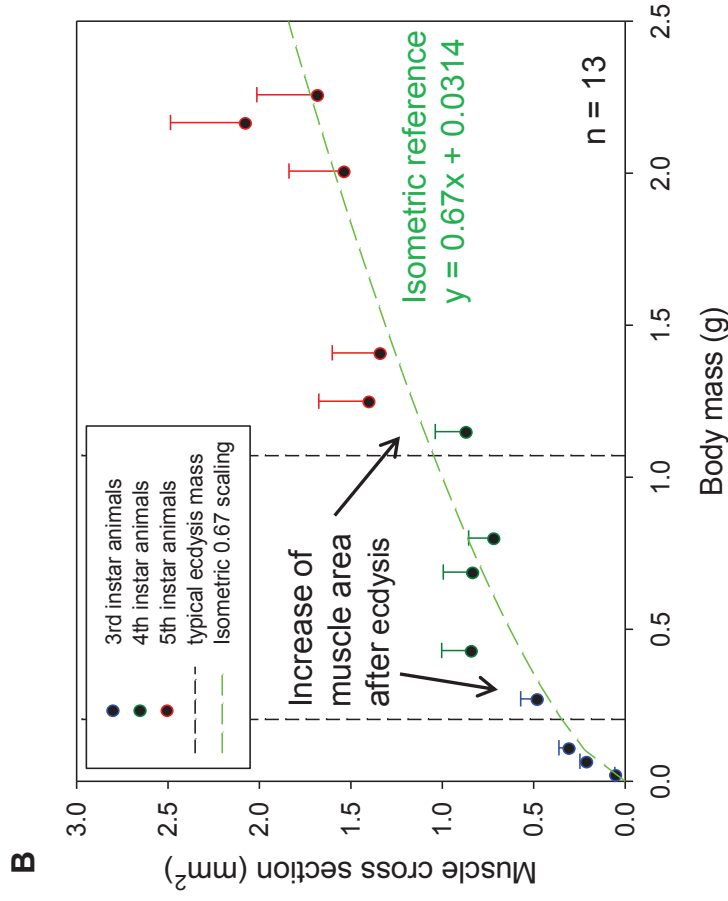
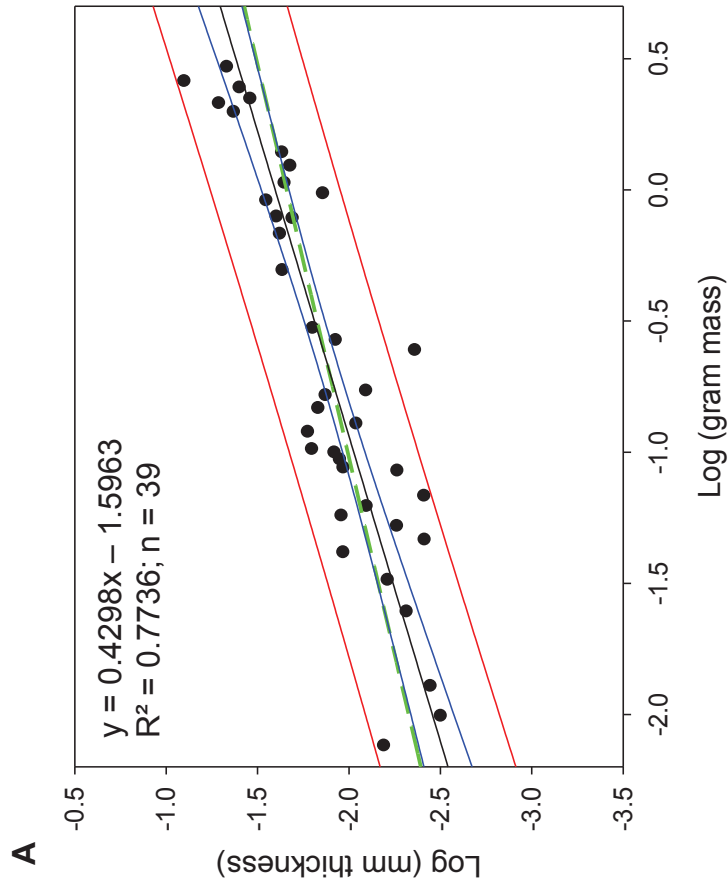


Figure 5. Onogenetic scaling of *Manduca* cuticle and muscle. Load bearing tissues thicken in developing *Manduca* caterpillar as measured by histology imaging. **(A)** Cuticle thickness increases with a power 0.4298 with respect to body mass, which is significantly greater than the isometric scaling of 0.33 for a linear dimension ($p < 0.05$, test power = 0.8153). However given the variation the isometric reference line (green dash curve) is still well contained in the 95% predicted interval (in red). The 95% confidence band is plotted in blue. **(B)** Muscle cross sectional area increases step wise at ecdysis so curve fitting cannot be applied. However, the data closely follow the isometric scaling power (0.67 green isometric reference curve).

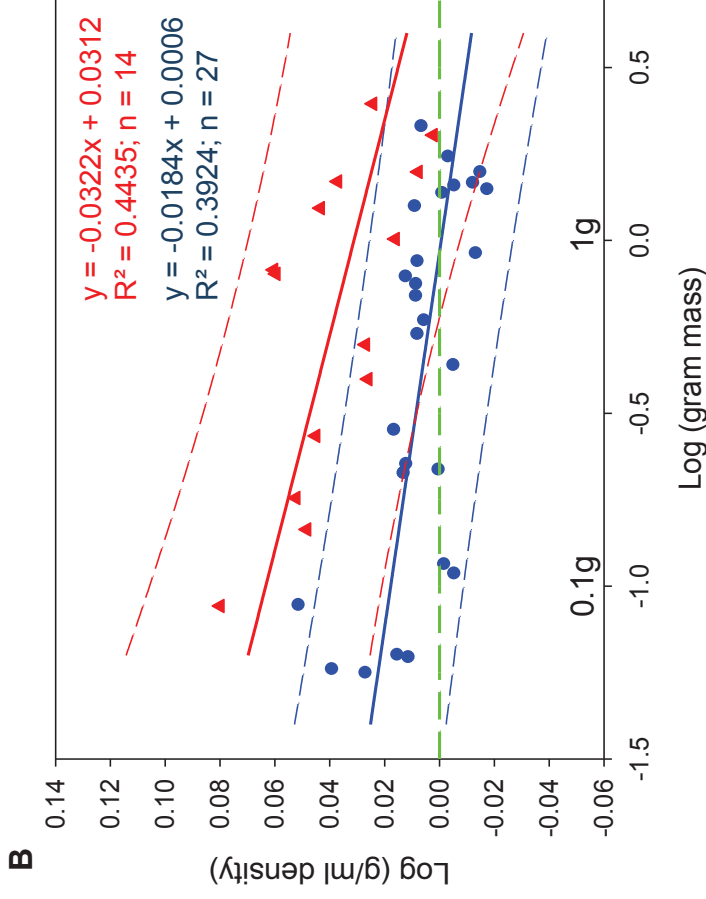
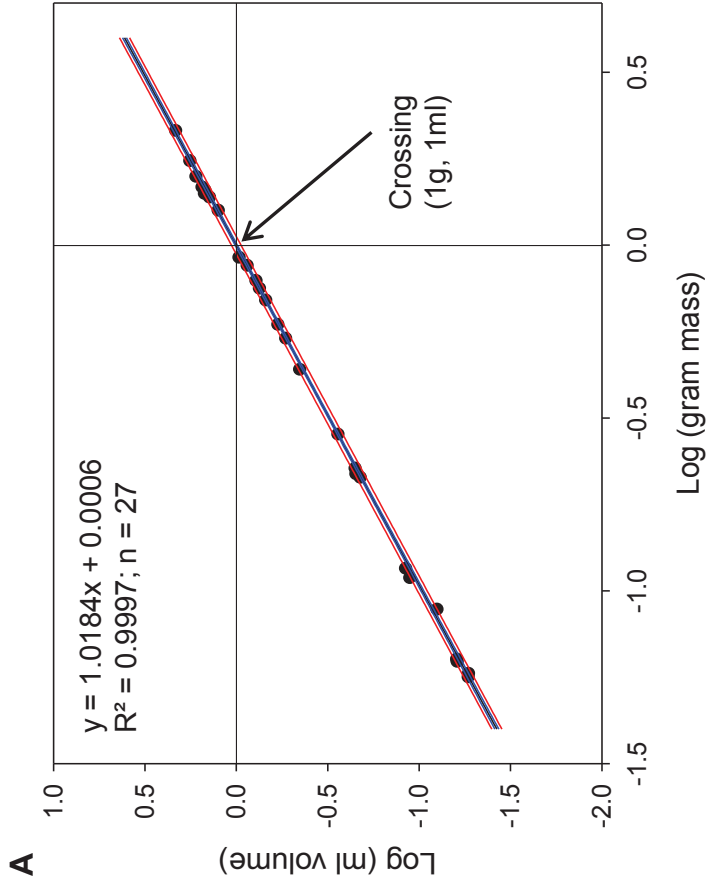


Figure 6. Ontogenetic scaling of *Manduca* overall body density and net tissue density. (A) Plotted on a logarithmic scale, a regression line of body volume as a function of body mass passes through the null intercept (0,0), indicating that animals heavier than 1 g were less dense than water. The slope is significantly different from unity ($p < 0.001$). (B) The body density (in blue) and the tissue density (in red) both decline in developing caterpillars and the slopes are both significantly different from zero (body density: $p < 0.01$, tissue density: $p < 0.001$) but not significantly different from each other ($p = 0.1158$). The red and blue dash lines represent the 95% predicted bands which overlap greatly. Despite the large variation, the decrease of overall body density is quite evident.

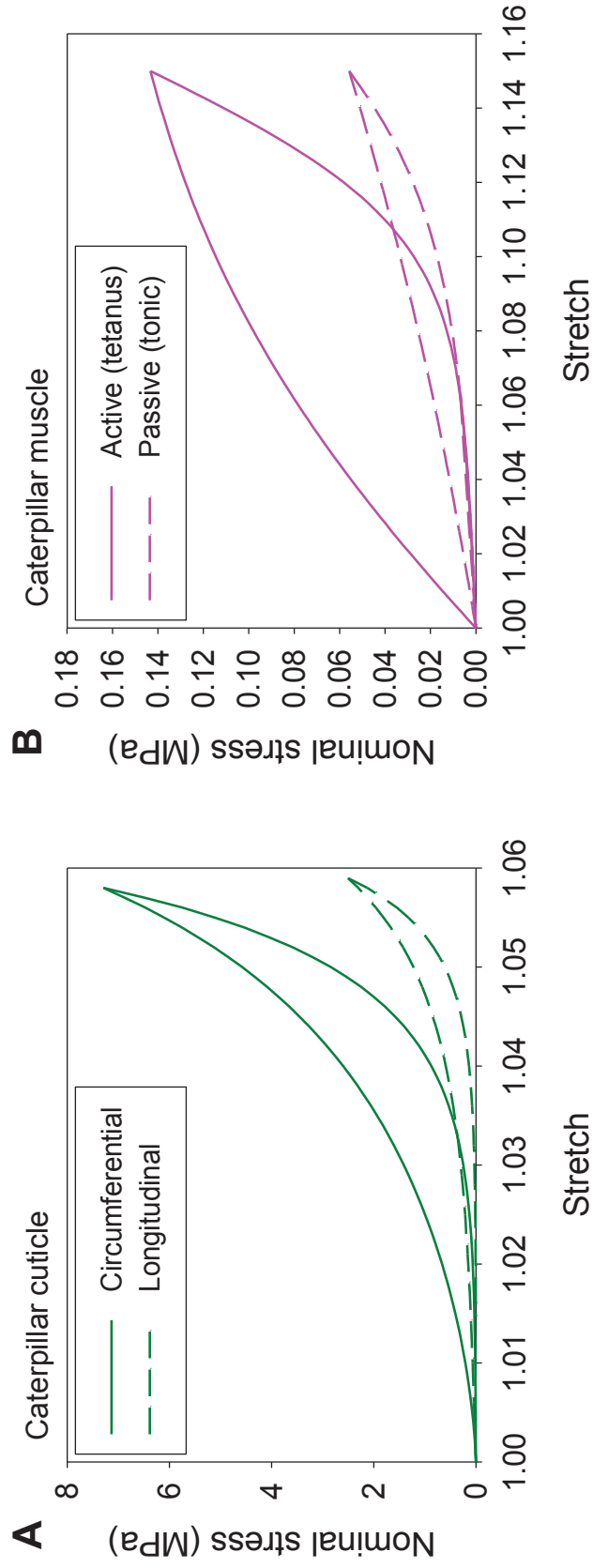


Figure 8. Material properties of caterpillar muscles and cuticle. (A) The soft cuticle of *Manduca sexta* has a variable stiffness which increases with higher stress. The solid curve represents the cuticle loaded in the circumferential direction while the dotted curve shows the loading behavior in the longitudinal direction. Note that the cuticle is stiffer in the circumferential direction presumably accounting for the lack of circumferential muscles. (B) *Manduca* muscles also exhibit pseudo-elastic behaviors in both the active (tetanus) state (solid curve) and passive (tonic) state (dotted curve). These highly nonlinear behaviors cannot be approximated by any analytical models based on linear elastic theories.

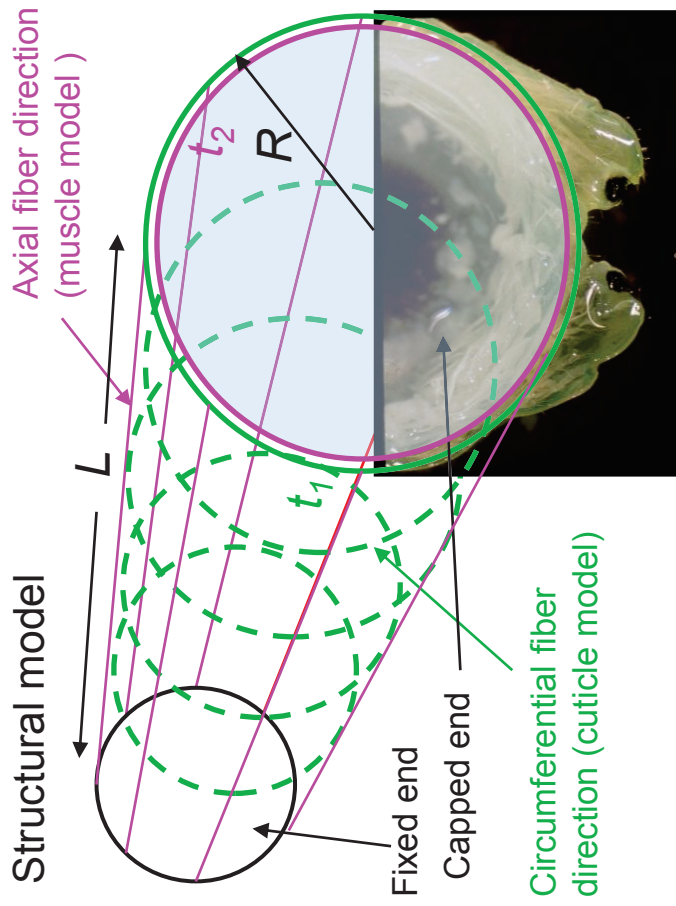


Figure 9. Structural model of the hydrostatic skeleton in caterpillars. The hydrostatic skeleton in the caterpillar is realized as an inflatable cylindrical tube with transverse isotropy due to the fiber reinforcement. The body length L , radius R , body wall thickness t_1 , and equivalent muscle layer thickness t_2 were derived from the animal biometric data fits at body mass of 2 g and 0.05 g respectively (see Table 1). The body wall contains two sets of fiber reinforcement, the first in the circumferential direction characterized by the cuticle mechanics (cuticle thickness) and a second set characterized by the muscle mechanics. The muscle's stress-dependent stiffness simulates the behavior of either *Manduca* muscles in tetanus or tonic condition

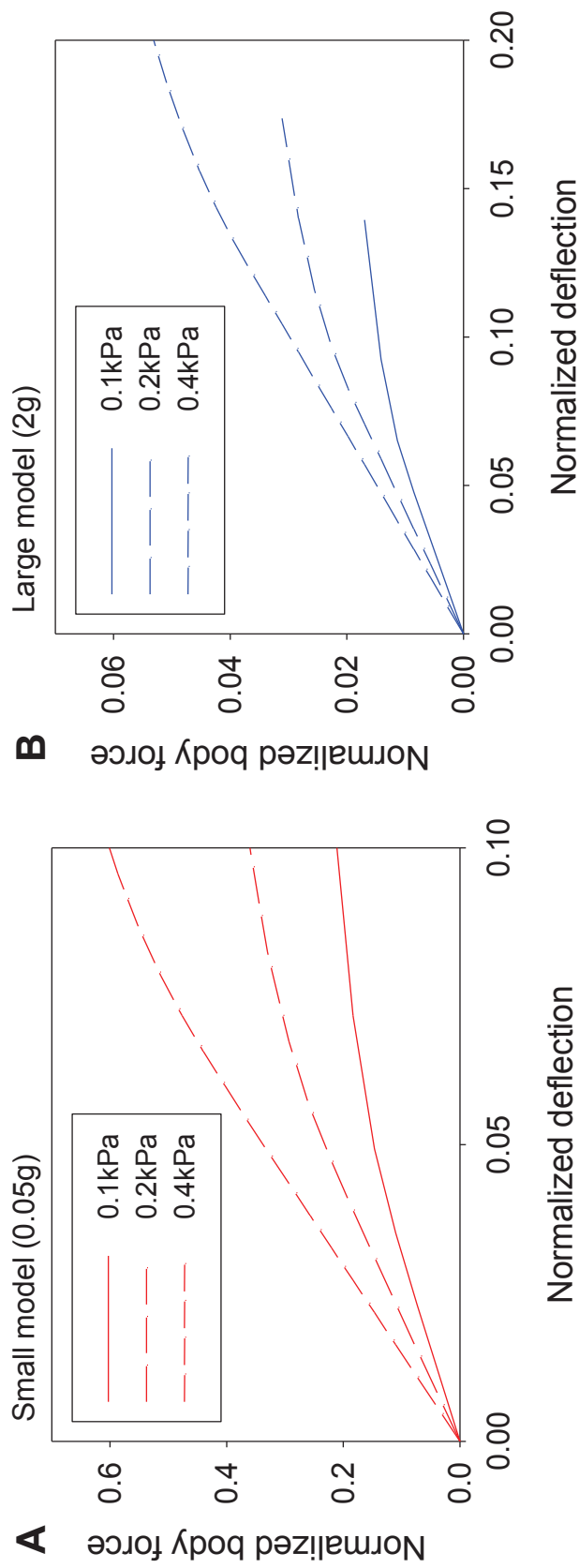


Figure 10. Results for finite element model of the hydrostatic skeleton in caterpillars. (A) Flexural tests can be performed on the finite element model at any constant pressure. Examples curves from pressure 0.1, 0.2, 0.4 kPa are shown for the small model. Body force was evenly distributed to all the finite elements and normalized to the body weight derived from the model sizes listed in Table 1. Model tip deflection was normalized to the initial model body length L as given also in Table 1. **(B)** The corresponding curves from the large model are shown. It is evident that the small model has much higher bending stiffness given the same internal pressure.

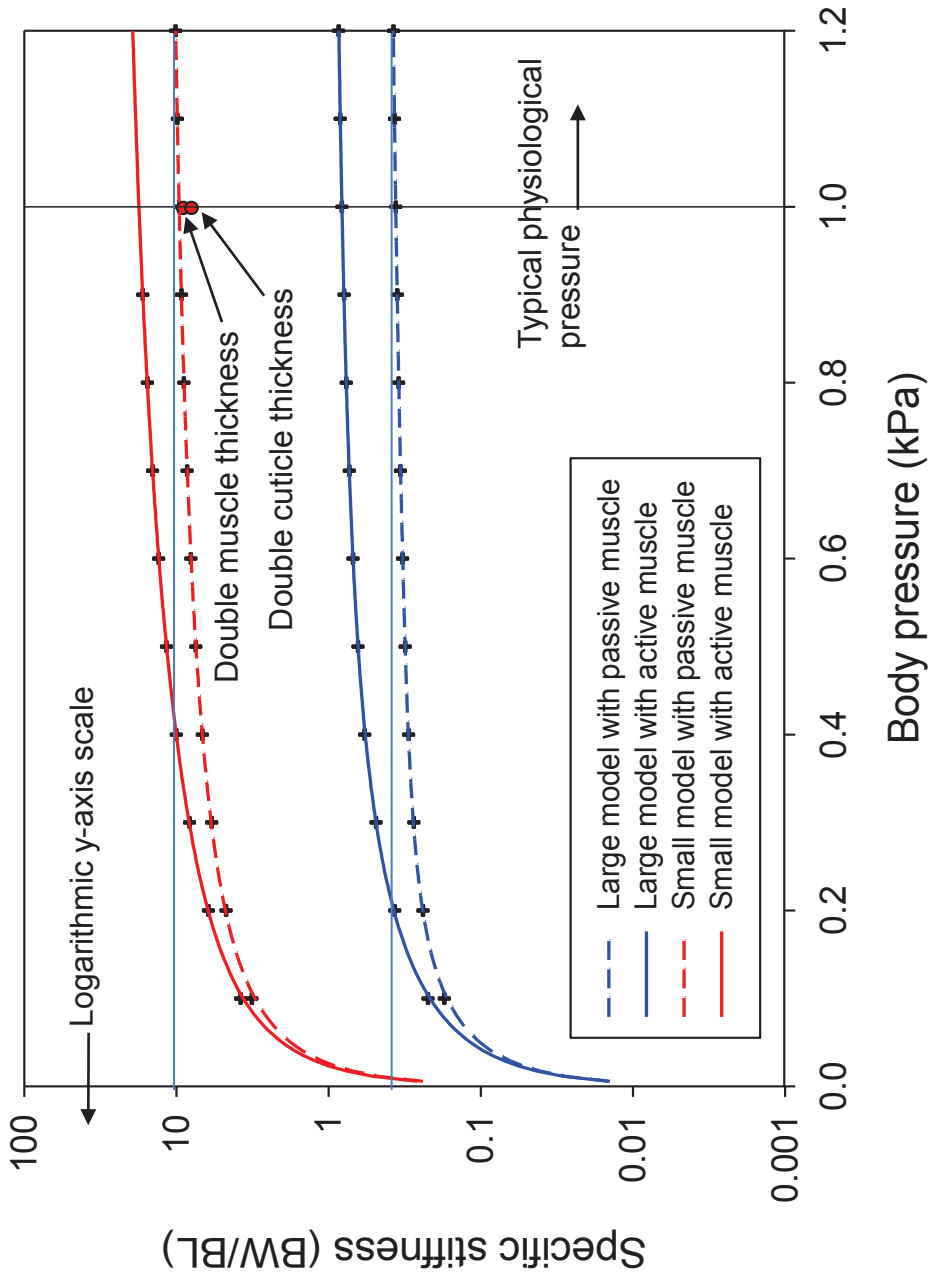


Figure 11. Normalized body stiffness comparison. The hydrostatic skeleton model was tested at two sizes and two states (data plotted in semi-log scale). A simple spline fit was applied to illustrate the trends. The active state simulates when the muscles are receiving tetanic stimulation, while the passive state represents resting muscles with proper muscle tone. The overall structural stiffness was much greater in small models (red) than in large models (blue) by more than one order of magnitude. Interestingly, as the models enter the typical physiological pressure range, the stiffness plateaus in all cases. Muscle activation roughly doubles the structural stiffness in this range.

Table 1. Modeling parameters derived from the experimental scaling data fits for two body sizes.

	Small (0.05g)	Large (2g)	Scaling factor
L	18.6 mm	50.3 mm	0.27
R	1.10 mm	3.45 mm	0.31
t_1	0.007 mm	0.034 mm	0.43
A	0.144 mm ²	1.71 mm ²	~0.67
t_2	0.021 mm	0.079 mm	Derived from A

Chapter 5: From caterpillar locomotion to soft robots

Force measurements, material tests, and behavioral experiments are powerful tools to tease out different components necessary for soft-bodied locomotion. The animal studies presented in the previous two chapters clarify how caterpillars can use body deformation to locomote but it is still unclear how different caterpillar gaits emerge. Can open-loop control really produce stable locomotion? How does controllable gripping establish climbing gaits? What gait modifications are required for burrowing? Is there a simple parameter that determines gait transition? All these questions are difficult to answer with animal experiments as we cannot isolate individual variables or directly control caterpillar gaits. Model simulations, on the other hand, can help us tackle these questions effectively.

This chapter begins with *Section 5.1* by introducing the concept of physical modeling and the process of reducing a physical system into simple components. *Section 5.2* justifies why we use the extremely inefficient shape memory alloy (SMA) coils as the actuators for the soft robots. *Section 5.3* documents early attempts in producing simple inching gaits. The results suggest that a great portion of soft body behaviors might come from the non-linear loading. I then demonstrate how to produce nonlinear loading conditions with linearly elastic materials. Moving from nonlinear body loading to nonlinear actuator properties, I describe how SMA actuations produce complex behaviors in soft robots in *Section 5.4*. The example robots maneuver through a narrow ground hole and a mouse hole under manual operation. These tasks require adaptive control from a human operator since the SMA actuator responses are somewhat context dependent. An extensive SMA actuation characterization follows to illustrate how different conditions affect the actuator output. *Section 5.5* addresses challenges in climbing with two soft robots. It details my solutions with gait modification and implementation of retractable adhesion pads. After reviewing the mechanical behaviors of soft bodies, soft actuators and soft adhesion morphologies, I would like to investigate the control of motor patterns in soft robots. *Section 5.6*

presents the idea of motor pattern scaling and gait transition with one tethered robot. Finally, **Section 5.7** illustrates the need of an adaptive nonlinear controller for non-linear actuators working against nonlinear loads. A miniature articulated robotic arm was implemented for testing different control patterns. In addition to these general studies of soft-bodied control, I provide one specific example of embedded adaptive behavior in the high-speed ballistic rolling robot “GoQBot” (**Publication-5**).

5.1 Physical modeling of locomotion

Mathematical models of animal locomotion have been very effective in illustrating many control strategies in articulated systems. Unfortunately, modeling soft-bodied animals in the same way is not as straightforward. It is difficult to capture soft body deformations accurately and a complete description usually requires extensive mechanical characterization of the tissues. Detailed structural models are often too complicated to be useful. An alternative approach is to create a physical model that simulates the key aspects of the animal behavior of interest. By simulating animal locomotion in the physical world, we can learn about the physical limitations of different designs and obtain very realistic mechanical behaviors. For example, a biomimetic robot can be used to explore how different control patterns might affect locomotion.

The very first question one should consider before designing a biomimetic device is what to copy and what not to copy from the biological system. Obviously, duplicating everything from an organism is neither practical nor useful. The soft-bodied robot, in the context of caterpillar locomotion, is a physical model that captures the general mechanisms of locomotion and serves as a platform for testing hypotheses about gait transitions. For the current application, the physical reduction process needs to retain the following three components of caterpillar locomotion (Fig.5-1A). First of all, it must create displacement by deforming a soft body along the direction of locomotion. This requirement incorporates

the nonlinear properties of large deformation into the mechanics. Because deformable materials are typically used in engineered devices simply as dampers relatively little is known about the detailed behaviors of synthetic soft materials. To simplify the implementation, we need a homogeneous material that can be characterized easily and a mode of deformation which can be controlled easily. Castable silicone rubber is a linearly elastic homogeneous synthetic material suitable for our application. With different formula of mixture, one can produce materials with different stiffness and visco-elasticity. Bending is a very stable mode of deformation that is characterized by nonlinear loading. Therefore all my robots are designed to flex as the primary functional deformation.

Secondly, the robot must create motions using only soft tensile actuators. This constraint is a major challenge for mimicking any muscle-actuated animal. For soft-bodied animals, the challenge is even more severe because the body also does not have self-supporting flexural stiffness. Shape memory alloy (SMA) coils are tensile actuators analogous to animal muscles in several aspects. SMA coils are extremely flexible and can be integrated into a soft-body easily. They can be made to contract forcibly by applying an electric current to cause resistive heating. The current can be pulsatile to mimic neural activation of muscle or it can be made to generate persistent force resembling muscle tetany. In addition, SMA coils can be stretched and preconditioned during installation to simulate various passive properties of live muscles. Finally, while the substrate can be an external skeleton for the caterpillar, the soft robot must be capable of gripping the substrate on demand. Instead of engineering a micro-hook array, I explored the inherent adhesion properties of silicone rubber and created localized anchors using sticky pads or unidirectional gripping structures. By limiting the robotic locomotion on a flat surface, I further reduced the responsibility of these anchor structures to shear forces/friction.

In summary, the physical reduction process models the caterpillar as a soft body with multiple controllable substrate anchors (Fig.5-1B). The tensile actuator SMA coils produce internal forces across

the body and deform the body via flexion. Substrate anchors are provided by three retractable adhesion pads: anterior, mid-body, and posterior. They functionally represent the thoracic legs, mid-abdominal prolegs, and the terminal prolegs respectively. Retractable adhesion pads allow such body deformation to produce ground displacement for locomotion (Fig.5-1C). The removal of the mid-body adhesion pad allows simulation of caterpillar proleg reduction and the emergence of inching gaits (Fig.5-1D).

5.2 Soft tensile actuator

Before discussing further about the implementation of soft robots, it is important to review why SMA coils can be treated like animal muscles in the first place. Despite its poor efficiency, the shape memory alloy coil actuator has **five major characteristics** that closely mimic muscles. **First** and foremost, SMA coils are tensile actuators that only develop tensile forces. They do not have any flexural stiffness and cannot produce extension. To recover from a recent contraction, it must be cooled down and stretched back out by another force (Kim et al. 2009). **Secondly**, shape memory alloy deforms via a material state transition, vaguely comparable to muscle active-passive state transition. While the myosin molecules can be in the randomly association state or the cross-bridge bonded state (Warshaw et al. 1998), SMA crystals are either in the martensite or austenite phase. A population of two-state systems can naturally produce nonlinear graded responses to stimuli. **Thirdly**, the phase transition in SMA actuators is triggered by a diffusive physical parameter: heat (Shaw, Kyriakides 1995). Similarly, animal muscle cross-bridge formation is triggered by calcium ions which also have to diffuse locally to spread the signal. This diffusion dependent activation introduces another source of nonlinearity. **Fourthly**, SMA actuators are typically activated by resistive heating. The control input can be pulse-modulated just like the spike trains from descending motor neurons (Ayers, Davis & Rudolph 2002, Szücs et al. 2000). Packing more electric pulses (spikes) temporally accumulates heat in the SMA actuator and therefore produces muscle-like tetanic contraction. **Finally**, both myosin cross-bridges formation and SMA phase

transition acts on the primary material structure. There are many secondary structures that account for the various passive muscle properties important to the biomechanics. Forces generated by myosin activities have to stretch all the structural proteins across the sarcomeres and over the entire muscle fiber before reaching any skeletal components. Similarly SMA activation only changes the geometry of the alloy wire. The overall actuator output emerges from the torsion of the coil helix and the passive stiffness of the coil. These secondary structures modify the overall SMA force production and contribute to the already complex nonlinear actuator behaviors.

5.3 Open-loop inching and nonlinear body loading

The behavioral and kinematics studies suggested that moment-to-moment feedback might not be necessary for basic locomotion in caterpillars. Therefore, the first goal of my soft robot simulation was to test if different inching gaits can be produced using an open loop command system. The robotic devices then can be used to characterize the kinematic variations from open-loop control and how these variations affect the performances of locomotion. InchBot-II was a test device for simple gait development (Fig.5-2A). It has a 20cm long silicone rubber foam body shaped like a half cylinder. Both the front and back ends have a unidirectional gripping flap that only allows forward sliding. Two shape memory alloy (SMA) coils are installed on the ventral side and one on the dorsal side. Together, these three tensile actuators can create a variety of body undulations.

To simulate the open-loop control, I implemented a simple analog central pattern generator (CPG) consisting of two oscillators. The master oscillator sets the gait cycle period ($\sim 2s$) and drives the anterior body flexion for a fixed amount of time. During this time, a capacitor is being charged up slowly. As this capacitor reaches a threshold, the second oscillator fires and drives the posterior body contraction. Such coupling can be tuned to produce a large variation of behaviors. I empirically determined an

optimal gait for flat ground locomotion that can be best depicted as anterior inching (Fig.5-3A). In this gait, the robot pulls its body forward by flexing the anterior segment. The posterior part of the body is lifted in the process which reduces the dragging friction. Posterior gripping flap is then lowered to stop the body from sliding backward as the anterior segment re-extends. Such body coordination works surprisingly well with no feedback despite the large kinematic variations.

The oscillator coupling was set with a threshold trigger in the shallow part of the capacitive charging curve. The result was a timing variation of 5~10% in the oscillator coupling. In most robotic systems, such a variation would be detrimental for the robot performance. However, we found no observable difference in overall locomotion performance (distance traveled over fixed number of cycles) when the CPG motor pattern was implemented using a computer generated series of pulses (minimum timing variation). This insensitivity to command variation might be due to the large intrinsic mechanical variability of soft structures: the motor pattern variability then becomes only a small component of the overall mechanics. This fuzzy CPG was implemented inside an updated robot InchBot-III to allow untethered locomotion (Fig.5-2B). This robot moves at a typical speed of 5mm/s on the flat level surface, and can handle slight slope variation of 10 degrees. Even on a level homogeneous surface, the step length of InchBot-III varies from 4.7mm to 12.2mm, similar to the variations in the computer controlled condition. There is also no apparent correlation between consecutive steps. Apparently, the source of kinematics variability is probably in the nonlinear behaviors of the soft body deformation and the robot-substrate surface interactions.

Linearly elastic homogeneous materials, such as silicone rubber, can still produce nonlinear loading behaviors. They can result from different loading conditions, material lamination, internal pre-stress, and chemical slacking. These treatments will be introduced in details in turns as I demonstrate how to produce nonlinear behaviors with 5 different material samples. These samples are prepared to exhibit:

load-softening, load-stiffening, visco-elasticity, preload effects and history effects. To simplify the problem, we focus on two uni-axial loading behaviors in the silicone rubber samples: stretching and buckling. The experiment consists of a computer-controlled lever arm ergometer which stretches or compresses the specimen (see *Chapter 2 section 2.2*) (Fig.5-4A). The lever arm also measures the force in the direction of loading with positive load represents tension and negative load represents compression. All specimens are cast to be 40mm in length and 7mm in width. They are named after their color for convenience (Fig.5-4B~F). The specimen thicknesses vary depending on the treatment (reported later as mentioned in sequence). The stretching/buckling protocols were designed to achieve 1~4mm displacements (2.5~10% specimen length) with different rates (Fig.5-5A).

The first two specimens, *Green* and *Red* are made out of two different kinds of silicone rubber, VTV800 (MTT Tech Inc. Knoxville, TX), and Dragonskin 20 (Smooth-On, Easton, PA) respectively. They have been thoroughly prepared into the standard specimen dimensions with 1.5 ± 0.04 mm thickness (Fig.5-4B, C). The quasi-static stretching protocol (2.5% strain per second) reveals very linear responses from both specimens with the green producing 379.4 N/m (modulus ~ 1.445 MPa) and the red producing 140.0 N/m (modulus ~ 0.533 MPa) (Fig.5-5B). The buckling protocol however, reveals highly nonlinear loading curves with hysteresis. The simple buckling mode was set up with a slight preload to ensure smooth initial buckling (Fig.5-5B). For the green specimen, removal of this biasing preload leads to a stiff initial compression (dark green curve). This is followed by a sudden release of load as the specimen yields to the normal buckling mode. Increasing the preload would pre-condition the specimen to buckle in the typical mode (dark blue curve as “preset buckling”). Large bending in the buckling configuration is a load-softening condition. The tension between the two ends is largest during the initial part of the loading. As the structure bends, the loading moment increases and the tension required to hold the two ends together decreases.

By bonding the identical replicates of specimen green and red on top of each other, we have the third specimen called *Green-Red*. Since the bonding was done by curing the two specimens together, specimen *Green-Red* is considered a composite (Fig.5-4C). The stretching protocol shows that this composite is still a linear material. It is softer than the green specimen and stiffer than the red specimen alone with 327.7N/m slope (modulus ~ 0.6242 MPa) (Fig.5-5C). Buckling is again highly nonlinear, and preload significantly changes the loading responses. Most interestingly, buckling in the opposite direction (bending toward the stiffer green side) produces a completely different level of response at the same preload (green curves in the negative displacement side). Hence this composite exhibit different flexural stiffnesses depending on which side it bends. More complex behaviors can be produced by restraining the rotations of one end of the specimens. In this case, the preload only affects the loading and unloading paths while the specimen converges to the same flexion state (Fig.5-5D).

The fourth specimen is a laminated composite consisting of a red specimen bonded to a 120% pre-strained black silicone rubber sheet (Fig.5-4E). In this configuration, the specimen buckles naturally due to the residual stress in the black rubber. In the stretching protocol this *Red-Black* specimen produces load-stiffening behaviors closely correlated to the amount of preload (Fig.5-6A). In essence, any stretching force has to unbuckle the specimen before it can engage in the linear material stretching. The unbuckling process dials in the material stiffness gradually as the structure aligns itself to the loading direction. At high load, the composite is again linear just like the *Green-Red* composite. Reducing the preload means starting the loading at a more buckled configuration, and therefore engages more load-stiffening effects. This behavior and all the nonlinear behaviors presented so far are highly reproducible but not rate dependent. Doubling or quadrupling the loading speed does not change the loading characteristics (two red traces reproduces the yellow trace with higher rates) (Fig.5-6A).

Rate-dependent material properties can be produced by altering the silicone rubber chemically. Small amounts of “silicone slacker” added during the curing process produces a gel-like consistency. This tacky silicone material sticks to almost all indoor materials without leaving any residual on the substrate. We use this material for adhesion application for the robot (to be covered in the next section). By laminating this on a thin silicone sheet, the composite material becomes highly visco-elastic (Fig.5-6B).

In summary, the source of nonlinear mechanical behaviors has two levels. Macroscopically, different mechanical components can be put together or preloaded in different states. The emerging mechanical responses then exhibit nonlinearities even if each individual component is made of the linear materials. Microscopically, material elements or crystals can also have micro-structures or patterns that allow similar interactions to produce an emerging nonlinear behavior in the material. The mechanisms of nonlinear behaviors could be the same, but we call this later instance “nonlinear material”. In essence all materials are nonlinear under certain loading conditions and linear under small deformation. If we evaluate any loading curve over a small deformation scale, we can always fit a perfect straight line. Large deformation, in a sense, allows the structure to show its nonlinearity and that’s why soft structures/materials exhibit more pronounced nonlinearities.

5.4 Hole traversal and nonlinear actuator properties

Most soft-bodied animals are extremely good at burrowing and hole traversal. This is because they have great body flexibility and can squeeze body parts into different conformations. To explore the mechanics of negotiating through a narrow opening, we fabricated robots that can navigate through a 1cm hole. GoQBot-III is a radio-controlled robot that can perform more than two gaits and can be steered to go through a mouse hole or under a door (Fig.5-2C). This robot has two retractable adhesion pads at the head and the tail (the third mid-body adhesion pad is installed but not used) (*Section 5.4*). To maintain a

low profile while going through a hole, GoQBot-III uses two different gaits. As the head goes through the hole, the robot disengages the posterior adhesion pad and initiates a posterior flexion. This flexion displaces the posterior adhesion pad forward by about 1cm before the posterior pad is reattached to the substrate. An overall body relaxation is subsequently accompanied by detachment of the anterior adhesion pad. This posterior inching gait allows the body to slide forward into the hole (Fig.5-3B). When more than 2cm of body passes through the hole, GoQBot-III reduces the posterior flexion and flexes the anterior segment slightly to transfer this displacement forward. This loose crawling gait has the lowest body profile and resembles the caterpillar anterior-grade wave (Fig.5-3C). When more than half of the body slides through the hole, GoQBot-III smoothly reverts to the anterior inching gait which quickly pulls the body through and away from the hole (Fig.5-3A).

InchBot-IV, on the other hand, is capable of traversing a vertical hole. This robot flexes its head to penetrate down into a hole in the ground (Fig.5-2D). It has two retractable spines at the head which pull the body into the hole. Once the anterior segment is in the hole, the tail starts to flip. An anterior grade wave similar to the loose crawling gait drives the body further into the hole. We have not yet simulated caterpillar burrowing behavior inside a hole (Dominick, Truman 1984). InchBot-IV demonstrates the initial phase of burrowing using simple body undulations.

SMA actuation control is critical to both GoQBot-III and InchBot-IV since the mode of locomotion changes with body orientation. When the robot is controlled in real-time by a human operator the magnitude of actuation and the relative timing of movements must be continuously adjusted to maintain stable progression. To more completely characterize the performance of the SMA actuators several parameters were systematically altered while monitoring the evoked force-length relationships. SMA samples of different parameters were prepared (Fig.5-7A) and installed in series with a linearly elastic

cord for testing (Fig.5-7B). This setup allowed us to measure the force development in SMA coils as they contract against the elastic cords of different stiffnesses (Fig.5-7C).

Critical mechanical parameters for the SMA actuators included: the SMA coil size (2 levels), coil number (2 levels), pre-load (3 levels) and resisting load (3 levels). For actuator control, the energy input was kept constant but stimulation power was changed (3 levels) and each test was repeated 3 times. With all the different factors and test levels, 108 tests were performed. Please refer to Publication-5 for the experimental setup. From the loading curves, we extracted the peak force values and the initial loading rates. These multi-level conditions are illustrated in Table.5-1.

In this experiment, the SMA samples are driven by three different current controlled stimulation patterns (Fig.5-8A). These patterns are designed to deliver the same amount of energy at three different powers. In response to these stimuli, the SMA sample generally experiences a decrease of drive voltage as it undergoes phase transition (decrease of electrical resistance) (Fig.5-8B). Tetanus contractions are evoked as the result of these situations (Fig.5-8C). There are three major parameters that capture the actuation characteristics of each SMA configuration: peak force, initial loading rate, and maximum resistance change. From the 108 tests we extract the peak force value and the initial loading rate from each trial (Fig.5-8D). In addition, the maximum change of resistance in each trial can be calculated from the measured SMA drive voltage and the current control stimulation (Fig.5-8B).

In general, larger and longer SMA coils develop higher forces (Table.5-1). Within this trend, higher preloads also lead to higher peak forces as condition 3, 6, 9, 12 correspond to 200mN preload in Table.5-1. In addition, higher resisting stiffness always induces more SMA peak forces. These observations hold true for standard and high power conditions as well. Higher stimulation power also increases the peak force production. More specifically, there is a two-fold jump of peak force from the low power condition to the standard condition. The increase of peak force becomes less dramatic as the

power increases from standard condition to high power condition. The standard deviations of these peak forces, on the other hand, illustrate another trend (blue part of Table.5-1). Regardless of the stimulation power, the variation of peak forces is generally below 10mN. With low initial preload (condition 4, 7, 10), peak force tend to vary much more. For the largest and longest SMA coil, however, the peak force varies wildly with low power stimulation. This is because the stimulation power cannot keep up with the heat dissipation in larger SMA coils.

Initial loading rate was extracted from the second stimulation pulse of each SMA test (0.5~1s from the onset of stimulation) (Table.5-2). For the low power DC ramping tests, we define this parameter as the slope of the initial loading curve (2s from the onset of stimulation). In general, initial loading rates increase as the resisting loads increase, and decrease as the preload increases (green part of Table.5-2). At the initial phase of SMA activation, a higher preload stretches the SMA away from the optimal initial length for contraction and therefore prevents the SMA from acting too fast. Once the activation kicks in, the high resisting load demands tension quickly from the SMA actuator. Not surprisingly, variations in loading rate is largest at small preload conditions (installation condition 1, 4, 7, 10) (blue part of Table.5-2). In summary, preloading the SMA actuators reduces the initial loading rates slightly but makes the contraction speed much more consistent.

SMA electrical resistance drops as a result of phase transition. Fully activated samples typically experience 10~15% decrease of resistance (Table.5-3). Such change is independent of the loading conditions, but depends slightly on the stimulation power (green part of Table.5-3). In fact, under high power stimulation, SMA coils consistently experience much smaller resistance change. This early arrest of resistance drop is due to the enhanced thermal effect in high power actuations which increases the SMA resistance. Variations of resistance change are generally within 1% of the nominal resistance (blue

part of Table.5-3). There is, however, a slightly larger resistance change and variations for conditions with softer resisting load. Tension might discourage SMA phase transition after all.

5.5 Climbing and retractable adhesion pads

One attractive capability of caterpillars is their ability to climb. The most successful climbing robots are able to scale inclines or flat vertical surfaces (Menon, Sitti 2006, Spenko et al. 2008) but movement in complex three dimensional structures is beyond their abilities. Climbing requires attachments that are more than just traction on the substrate. An earlier idea for a wall climbing robot (InchBot-V) was a deployable surface that helped with lateral stabilization and surface adhesion (Fig.5-2E). This robot has two sets of silicone membrane extending from the body. These membranes adhere to most flat smooth indoor surfaces and are sufficient to hold the robot up on the wall. Spread by a foldable cross strut at the head, the main wing surface tapers down at the mid body. The tail wing is similarly supported. To move forward, InchBot-V peels the tail wing off the substrate first and flexes the body. It will then start to re-attach the tail wing by peeling the main wing off the substrate. Such reciprocal motion allows the robot to inch forward slowly. Unfortunately, InchBot-V never succeeded in climbing up a wall because the large main wing surface is too hard to control. With more active control of the fore-wing, climbing with deployable surfaces might be still feasible.

A more biomimetic approach is to use retractable adhesion pads originally developed in InchBot-VII and refined in GoQBot-III (Fig.5-9A). For inching and crawling gaits, only two adhesion pads are required. However, this setup is not ideal for secure climbing as the entire body could peel off the substrate after losing any one of the grips. To perform stable climbing, any soft robot will require additional attachments at the mid body. That is exactly why InchBot-VII has three adhesion pads. As it crawls, the posterior adhesion pad is released first and brought forward. Only when the posterior pad

reattaches does the mid body adhesion pad retract to transfer deformation to the anterior segment. The entire locomotion pattern ends with the reattachment of the mid body adhesion pad and the release of the anterior pad for body extension. This 3-point climbing gait captures the principle of caterpillar crawling very well (Fig.5-2F). In the mid crawling phase, it loads the robot in tension using the two end attachments and stretches out the posterior flexion with anterior body flexion. Using this biomimetic principle, InchBot-VII was able to climb up an incline over 45 degrees. With more mid body adhesion pads and better adhesion control, it should be able to do wall climbing.

There are two parts to the design of retractable adhesion pads: the adhesion material and the mechanism of pad retraction. The adhesion material is tacky silicone rubber made by adding “*Silicone Slacker*”(polyorganosiloxanes) to the platinum-cure silicones mixture. In general, the amount of slacker added determines how sticky the end product is (Tadesse et al. 2009). However, adding too much slacker could result in silicone gel that does not resist shear force very well. Through experimentation, the optimal ratio of silicon mixture to slacker is 1:1 for adhesion pad application. Casting about 2mm thick of such tacky silicone rubber directly on a silicone substrate makes a perfect adhesion pad.

Because adhesion needs to be controllable a mechanism was devised to deploy and retract the sticky pad. I constructed a laminated silicone rubber surface that was pre-stressed so that the construct naturally bulges out (Fig.5-9B). The adhesion pad was bonded to the exterior surface which was exposed by default. To retract the adhesion pad, a set of SMA actuators pulls on a membrane crest designed to fold inward (Fig.5-9B). Around this actuated membrane are structural reinforcements built from thicker silicone rubber. This ensures that only the membrane collapses inward. As the SMA actuator relaxes, the pre-stress in the membrane will buckle out and re-expose the adhesion pad.

The performance of this adhesion pad has been characterized by dragging a retractable pad unit (Fig.5-9C) across a smooth acrylic plate at a speed of 0.5mm/s (simulating static body sliding in my robots)

(Fig.5-9D). The adhesion pad unit weighs 3.0 ± 0.05 g (a typical weight an adhesion pad supports) and retraction of the adhesion pad is controlled by a set of SMA actuators (Fig.5-9E). The friction from the silicone surface without adhesion material is about 60mN (blue traces) (Fig.5-10A). Retraction of the silicone surface drops the friction to below 20mN (Fig.5-10A). With an adhesion pad, however, the static traction increases by almost 10 folds to right below 500mN (Fig.5-10B). Once moving, the sticky pad maintains a friction lever around 120mN (twice that of plain silicone rubber). Retraction of the adhesion pad removes the friction entirely. As the sticky pad is redeployed, the friction level recovers to over 150mN and maintain above 100mN consistently. Sticky pad can be actuated early to interrupt the static loading phase (olive green trace) without affecting any later operations.

5.6 Motor pattern pacing and gait transitions

Walking, crawling and inching gaits are all characterized by the maintenance of ground contact. In the absence of an airborne phase (such as hopping or running) the only way to increase locomotion velocity is to increase the step length or the pace frequency. Caterpillars can employ both strategies. They can perform a fast crawl by cycling the waves of muscle contraction very quickly or, in some cases, they transit from crawling to inching thereby taking the largest possible steps.

This behavioral adaptation can be replicated in GoQBot which starts with a loose-climbing gait moving its body at 2.56 ± 0.88 mm/s (9 steps), (Fig.5-2G) (Fig.5-11A,B). Increasing the actuator drive (electric current in SMA actuators) amplifies the body flexion and reduces the actuation overlap between posterior and anterior flexions (Fig.5-11A,C). Further compression of the gait pattern timing improves the body coordination and produces a fast inching with top average speed of 14.6 ± 1.85 mm/s (12 steps), about 5 times faster (Fig.5-3E). However, this locomotion speed comes with a cost on stability. Amplified flexion means raising the center of mass much further away from the ground adhesion pad

attachments. The probability of tipping over increases dramatically as the adhesion pads are also soft and cannot resist the lateral torques. In GoQBot, two tail struts made of flexible polypropylene (OD = $460 \pm 10 \mu\text{m}$) were added to the body. When fully extended, these two appendages originate 1cm anterior to the tail on two sides of the body and extends backward and outward for 2cm. Their tips spread apart by about 2cm and are slightly curved to facility ground contracts. These lateral skids are furthered described in Publication-5.

Interestingly, we found that increasing the actuator drive further sometimes tips the robot forward into a tumble. Such phenomenon prompted us to consider the possibility of creating a rolling motion to boost the locomotion speed. Looking into the literature, caterpillars indeed do perform such a rolling behavior but only under special conditions. A group of small caterpillars *Pleuroptya ruralis*, native to the United Kingdom, feed on low nettle vegetations and perform a backward ballistic roll when startled on a flat surface (Brackenbury 1997). We found several species in Costa Rica that perform comparable escape behaviors. These are a group of leaf rollers dwelling on the mountain range of volcano Cacao at altitude about 1000m above sea level.

Using this escape behavior as an inspiration and kinematic model we successfully reproduced ballistic rolling (Fig.5-3F) in several versions of GoQBots. The latest version GoQBot-V (Fig.5-2H) has been used to characterize the kinematics of ballistic behavior and to measure changes in the ground reaction forces at the head as the robot launches. On a flat level surface, this mode of locomotion boosts the speed of 14.6mm/s in fast inching to over 200mm/s (over ten-fold). For details of the rolling mechanics and control, please refer to the Publication-5.

Development of these soft robot gaits showed that gait transitions can arise from gradual changes in continuous processes for example by scaling the gait timing and actuator drives. From partial inching gaits to loose crawling, the robots can transfer body contraction forward with both ends locked down to

the substrate. This body wave then can be secured by an addition mid body attachment suitable for climbing. The 3-point climbing gait really resembles the moving principles of crawling caterpillars and illustrates the necessity of mid abdominal prolegs for larger crawling caterpillars. Fast inching can be directly derived from the loose crawling gait by pacing the CPG differently and increasing the actuator drives. Pushing this modification to the dynamic regime leads to a ballistic rolling behavior. Indeed, caterpillars performing ballistic rolling escape may only need to drive their typical reverse crawling pattern faster and more forcefully as suggested by the previous studies (Brackenburg 1999).

5.7 One step closer to a biomimetic controller

In my soft robot implementation, I started with open-loop gait development in InchBots series. The result suggests that the nonlinear loading of soft structure can contribute to the overall robot behaviors. I then demonstrated how to implement different nonlinear mechanical behaviors in isolation. Moving on to real-time human controlled systems, GoBot-III and InchBot-IV give us a feel (literally) of the type of feedback compensation necessary to keep the soft robot moving through obstacles. Taking these control intuitions, I eventually built in some necessary control responses into the robot body mechanics. The fast inching and ballistic rolling robots show a certain degree of morphological computation (Publication-5) and self control. At this point, the very next question is whether we are ready to implement real-time sensory feedback to the soft-robot? To find out, I developed a biomimetic SMA controller which generates a frequency modulated stimulation pattern analogous to commands from the motor neurons in a live animal. The width and amplitude of each individual pulse is fixed and predetermined for each actuator. Unlike the previous constant current controller, this system stimulates SMAs with an actuator specific fixed voltage level. The controller also provides tonic stimuli to keep the actuator warm by default. Increasing this tonic frequency will tense up the SMA coil. If a tetanic stimulus arrives at this moment, the SMA coil will react to the stimulus much faster. In effect, this “muscle tone” primes the

actuators to react to actual stimulations. Tuning the SMA coils then allows a roboticist to control the activation dynamics.

A simple miniature robotic limb was designed to test this SMA controller (Fig.5-12A). This system consists of a two-segment appendage connected to a base with attachment points for SMA coils to act across any of the two joints. An experimental version was produced with a low friction potentiometer that monitors the joint angle at the base and an isometric force transducer which measures the actuator tension acting across the joint (Fig.5-12B). The SMA controller was implemented in LabView 2009 (National Instruments, TX) and produced excitation signals via a simple high current amplifier circuit (Fig.5-12C). The tonic stimulation produces tetanic behaviors in the SMA actuator.

Increasing the stimulation frequencies accumulate more heat in the SMA coil and therefore more forceful tetanic contraction (Fig.5-13). In addition to the SMA force and robotic limb joint angle, the system also measures the electric current across the SMA actuator and computes the resistance. The result gives a fair assessment of the SMA state transition/activation as the SMA electrical resistance drops notably in response to each burst of pulse trains (Fig.5-13). This resistance drop correlates reasonably well to the force production, but does not reflect the gradual increase of joint angle amplitude. Compacting the pulses closer in the periodic bursts produces higher transient forces (Fig.5-14). This kind of high intensity short burst often fails to evoke a movement in the first sequence from tonic activities. However, once active, the short bursts produce more consistent movement with little hysteresis. This is because the SMA heating happens in such a short time that very little residual heat remains to affect the consequent movements. Curiously, there is a slight delay of SMA activation (resistance drop) in this mode of SMA actuation. In this dynamic actuation, force development no longer maps with either the joint angle or the SMA resistance. Precise control in this case requires a detailed characterization of this specific robotic limb.

Indeed, a more sustaining contraction can be achieved by lowering the initial joint angle and reducing the burst intensity (Fig.5-15). The SMA force steps up steadily over each actuation cycle and plateaus around 0.5N. The joint angle maps to the actuator force very well in this case. The tonic pulses between bursts are very critical to maintain the activation level. With appropriate periodicity, one can build up the temperature in the SMA coil and keep the joint angle at a certain level. Such an isometric control can be done in a much smoother manner using shorter pulse width and high frequency modulations (Fig.5-16). Unfortunately, due to various sources of nonlinearity, such isometric control requires highly adaptive modulation. Simple position feedback often drives the system out of control. It is also not clear how to find the appropriate parameters for a classical PID controller (if these parameters exist at all). Manual control is currently the only stable approach to isometric states (Fig.5-16). In this particular trial, the SMA force rises monotonically without any noticeable joint movement at the beginning. Stimulation intensity increases at around 6s time point and at ~8s time point again to push the actuator over the movement threshold. Once the joint angle achieves ~20 degrees of rotation, the stimulation frequency decreases again moderately to arrest the overheating effect observed in the SMA resistance change. As the joint angle stabilizes, small changes of stimulation frequency are still necessary to keep the SMA at reasonable activation.

I can actively tune the frequency in real-time based on the SMA resistance, force, system joint angle. However, this is based on my intuition after working with SMA actuators for so many projects. Misjudgments still occur, leading to super contraction of SMA coil or a complete lost of joint position. A proper nonlinear controller is necessary to handle this highly nonlinear actuator and load. The algorithm would probably need to incorporate information from all three categories: kinematics (joint angle), dynamics (SMA tension), and actuator states (SMA resistance). Studying the behaviors of a simple mechanical system such as this articulated robotic limb can aid any theoretical development of an

adaptive nonlinear controller. Alternatively, one can take an empirical biomimetic approach to find a working control algorithm. Humans learn various highly complex control tasks quickly. In the example of the SMA isometric control, I have developed “a feel” of fine tuning SMAs from many previous experiences. My brain, in a sense, has figured out a control strategy through these numerous physical trials. If we record many manual attempts of the exact same task (e.g. get the robotic limb up by 20 degrees in 2 seconds and hold for 5 seconds), it might be possible to extract control principles that I intuitively use to operate this nonlinear system.

References

- Ayers, J., Davis, J.L. & Rudolph, A. 2002, *Neurotechnology for biomimetic robots*, The MIT Press.
- Brackenbury, J. 1999, "Fast locomotion in caterpillars", *Journal of insect physiology*, vol. 45, no. 6, pp. 525-533.
- Brackenbury, J. 1997, "Caterpillar kinematics", *Nature*, vol. 390, no. 6659, pp. 453.
- Dominick, O.S. & Truman, J.W. 1984, "The physiology of wandering behaviour in *Manduca sexta*. I. Temporal organization and the influence of the internal and external environments", *Journal of Experimental Biology*, vol. 110, no. 1, pp. 35-51.
- Kim, S., Hawkes, E., Choy, K., Joldaz, M., Foley, J. & Wood, R. 2009, "Micro artificial muscle fiber using NiTi spring for soft robotics", *Intelligent Robots and Systems, 2009. IROS 2009. IEEE/RSJ International Conference on IEEE*, , pp. 2228.
- Menon, C. & Sitti, M. 2006, "Biologically inspired adhesion based surface climbing robots", *Robotics and Automation, 2005. ICRA 2005. Proceedings of the 2005 IEEE International Conference on IEEE*, , pp. 2715.
- Shaw, J.A. & Kyriakides, S. 1995, "Thermomechanical aspects of NiTi", *Journal of the Mechanics and Physics of Solids*, vol. 43, no. 8, pp. 1243-1281.
- Spenko, M., Haynes, G., Saunders, J., Cutkosky, M. & Rizzi, A.A. 2008, "Biologically inspired climbing with a hexapedal robot", *Journal of Field Robotics*, vol. 25, no. 4-5, pp. 223-242.
- Szücs, A., Varona, P., Volkovskii, A.R., Abarbanel, H.D.I., Rabinovich, M.I. & Selverston, A.I. 2000, "Interacting biological and electronic neurons generate realistic oscillatory rhythms", *Neuroreport*, vol. 11, no. 3, pp. 563.
- Tadesse, Y., Moore, D., Thayer, N. & Priya, S. 2009, "Silicone based artificial skin for humanoid facial expressions", *Proceedings of SPIE*, pp. 728709.
- Warshaw, D.M., Hayes, E., Gaffney, D., Lauzon, A.M., Wu, J., Kennedy, G., Trybus, K., Lowey, S. & Berger, C. 1998, "Myosin conformational states determined by single fluorophore polarization", *Proceedings of the National Academy of Sciences of the United States of America*, vol. 95, no. 14, pp. 8034.

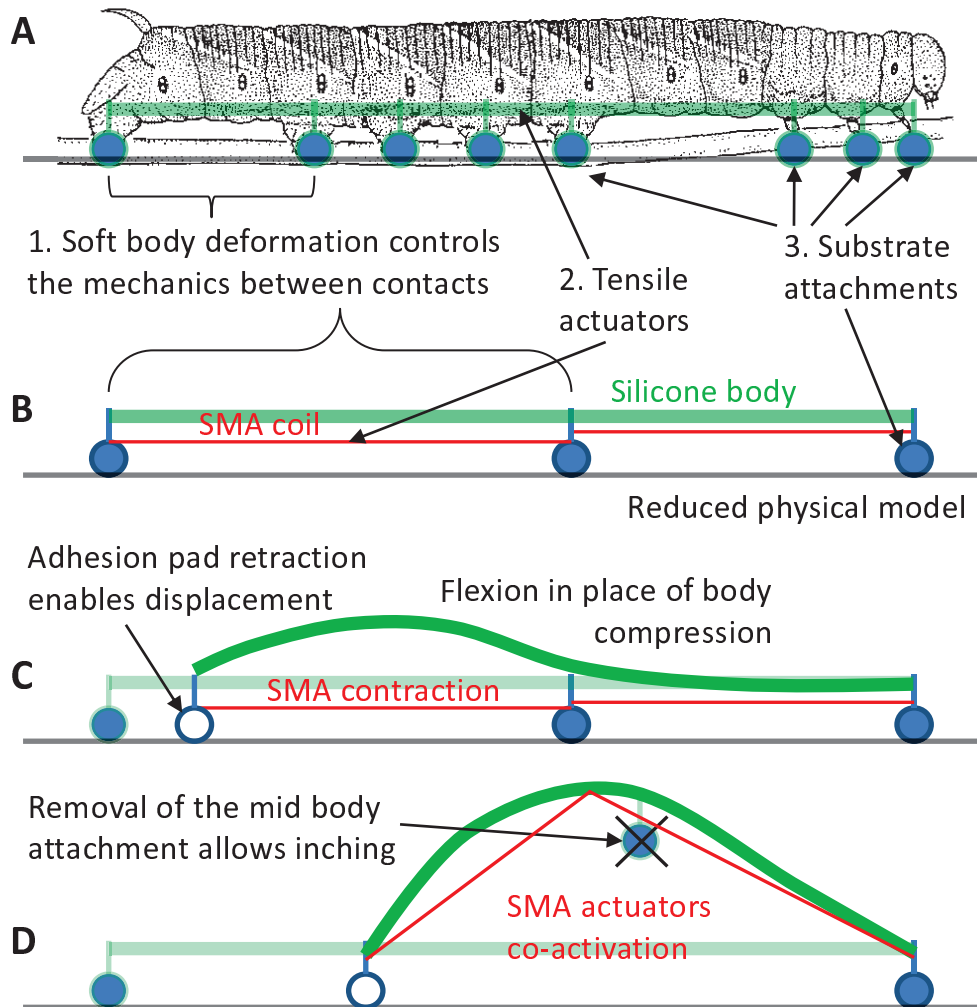


Fig. 5-1 Physical modeling of caterpillar locomotion. (A) According to the principles of locomotion, a crawling caterpillar can be reduced to three elements: soft body axial deformation, tensile actuators, and substrate attachments. (B) The reduced model is implemented using silicone rubber for the body and shape memory alloy (SMA) coils as the actuators. Controllable attachments are implemented as either retractable adhesion pads or unidirectional gripping flaps. (C) Flexion is the primary functional deformation in my soft robotic system. Embedded SMA contractions drive the flexions. (D) The removal of the mid body attachment enable the body to flex upward away from the substrate.

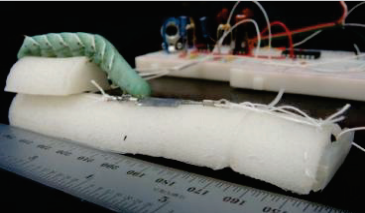
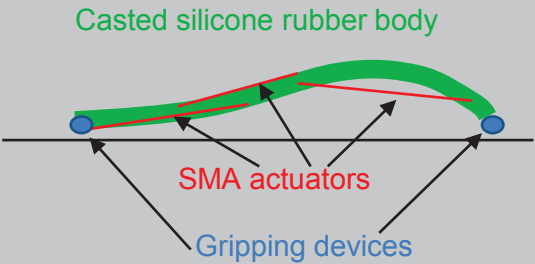
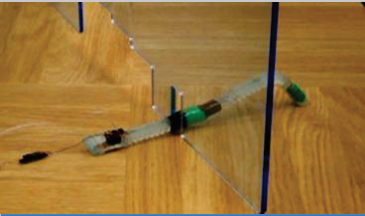
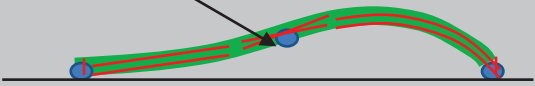
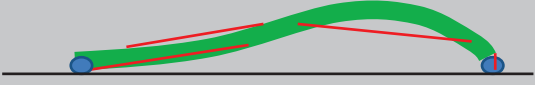
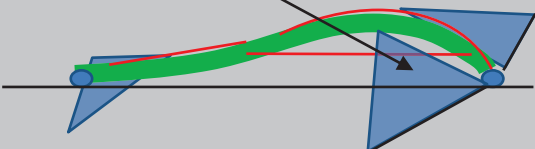
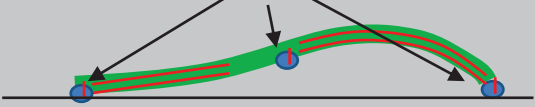
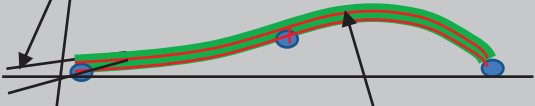
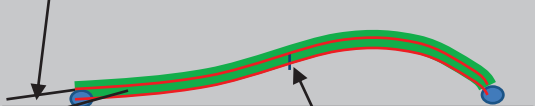
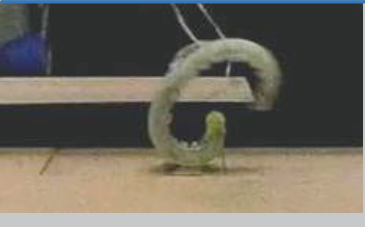
Robot names / dimensions / gaits / behaviors		Body plans & actuator configurations
<p>A</p> 	<p>InchBot-II 200*26*16mm (L*W*H) Tethered control Gait Fig. 5-3A 4 mm/s max Analogy CPG</p>	 <p>Casted silicone rubber body</p> <p>SMA actuators</p> <p>Gripping devices</p>
<p>B</p> 	<p>InchBot-III 150*26*16mm (L*W*H) On-board CPG open-loop Gait Fig. 5-3A 5 mm/s max Autonomous variable gait</p>	
<p>C</p> 	<p>GoQBot-III 120*8*6mm (L*W*H) 900MHz radio controlled Gait Fig. 5-3A,B,C 6 mm/s max Steering; hole traversal</p>	<p>Mid body attachment (not used currently)</p>  <p>Numerous actuators for steering and gait transition</p>
<p>D</p> 	<p>InchBot-IV 90*4.5*3mm (L*W*H) Tethered control Gait Fig.5-3A,B,C 4.12mm/s max Ground hole traversal</p>	
<p>E</p> 	<p>InchBot-V 80*7*5mm (L*W*H) Tethered control Gait Fig. 5-3A variations 3.6 mm/s max</p>	<p>Deployable wing structures</p> 
<p>F</p> 	<p>InchBot-VII 124*6*6mm (L*W*H) Tethered control with onboard batteries Gait Fig. 5-3D 3.2 mm/s max 45+ deg incline climbing</p>	<p>Three active retractable adhesion pads</p> 
<p>G</p> 	<p>GoQBot-I 105*8*6mm (L*W*H) Tethered control Gait Fig. 5-3A, B, C, E, F 14.6 mm/s (fast inching) ~150mm/s (ballistic rolling)</p>	<p>Flexible tail skids for lateral stabilization</p>  <p>Continuous dual SMA installation</p>  <p>Specializes in ballistic rolling (no mid body attachment)</p>
<p>H</p> 	<p>GoQBot-V 120*10*7mm (L*W*H) Tethered control Gait Fig. 5-3F >200 mm/s (ballistic rolling)</p>	

Fig. 5-2 Representative soft robots for the studies of caterpillar locomotion.

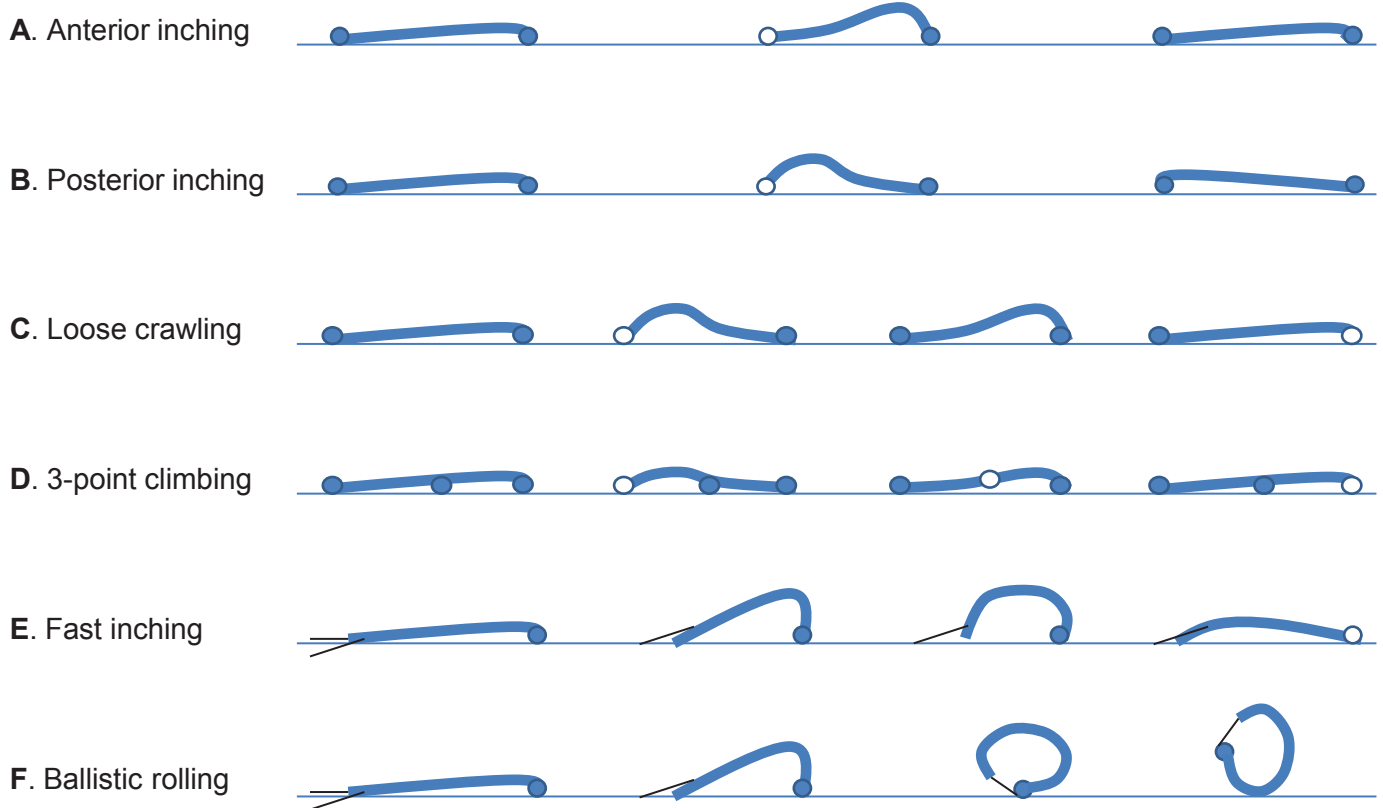


Fig.5-3 Gait map of the soft robots. From top to bottom, these are the 6 modes of locomotion that I achieved with my soft-bodied robots. From left to right, schematic diagrams illustrate the robot body configurations in a given gait pattern. Most soft robots have mechanisms for locking down the body (noted by solid circle). Open circles represents attachment devices in the retracted state to allow body displacement. Gait E and F involve a pair of tail skids for lateral stability.

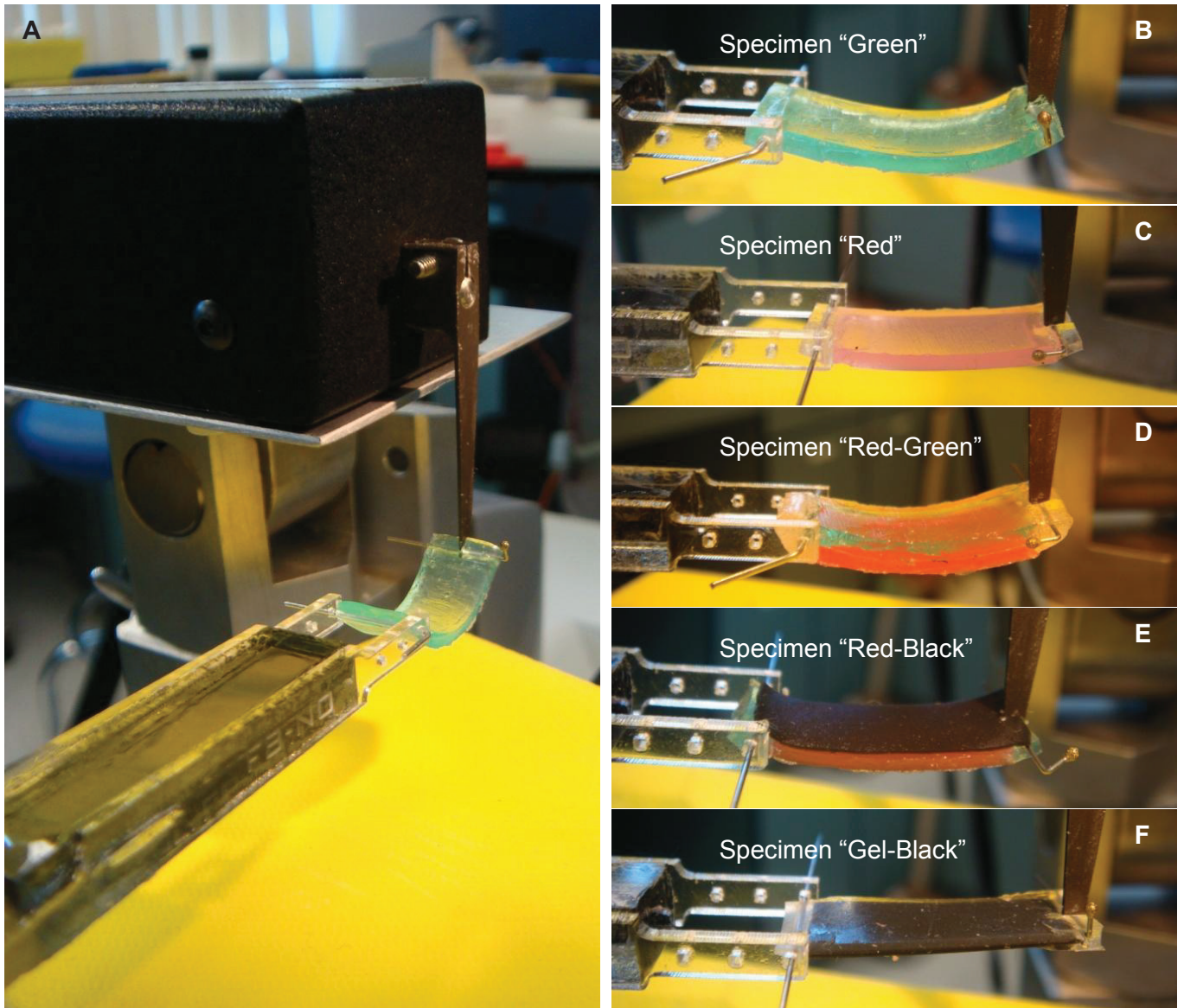


Fig.5-4 Nonlinear loading experiments. (A) The lever arm system controls the stretching-compression of the specimen while monitoring the load. (B) Specimen of VT800 rubber with green dye (thickness = 1.5mm). (C) Specimen of Dragonskin 20 rubber with red dye (thickness = 1.5mm). (D) Composite specimen from *Green* and *Red* (thickness = 3.0mm). (E) Composite specimen with residual stress in the black rubber sheet (thickness = 2.0mm). (F) Composite specimen with chemically slacken Dragonskin 20 rubber (thickness = 1.2mm). All specimens share the same areal dimensions (40*7mm) .

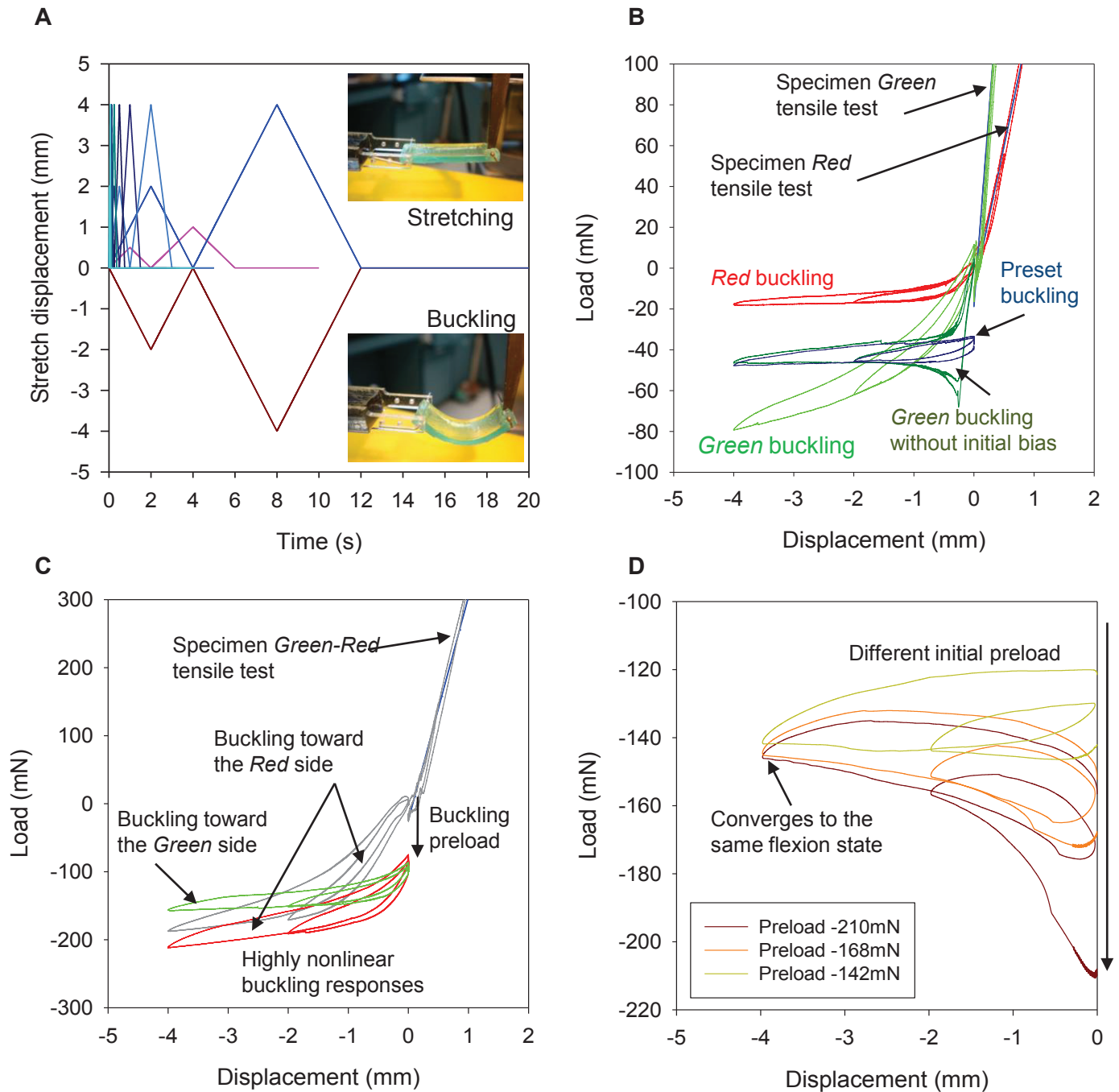


Fig.5-5 Nonlinear behaviors from linear materials. (A) Stretching and buckling protocols. (B) Stretching tests confirm the linearity of the material. Buckling is a nonlinear loading condition. (C) The composite specimen produces different responses depending on which side it buckles. Preloading has a significant effect on the loading curves. (D) In a certain preload range the specimen produces different loading curves all converging to the same flexion state.

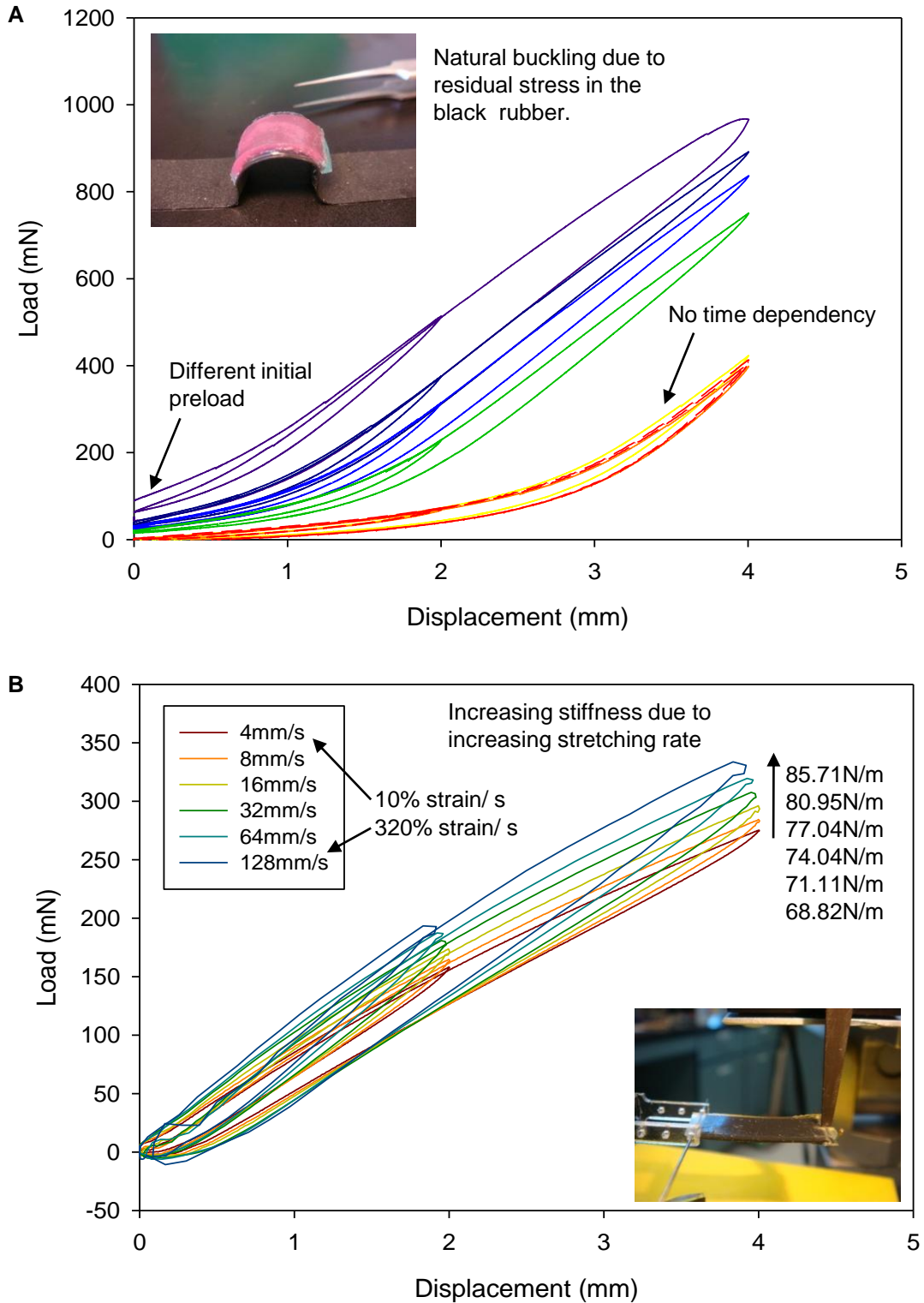


Fig. 5-6 Residual stress and chemical slacking. (A) Stretching a composite specimen with residual stress could produce preload dependent stress-stiffening effects. This effect is not strain rate dependent as dynamic loading curves (two red traces) overlap the quasi-static trace (yellow). (B) Mixing silicone slacker during the rubber curing process introduces visco-elasticity in the material.

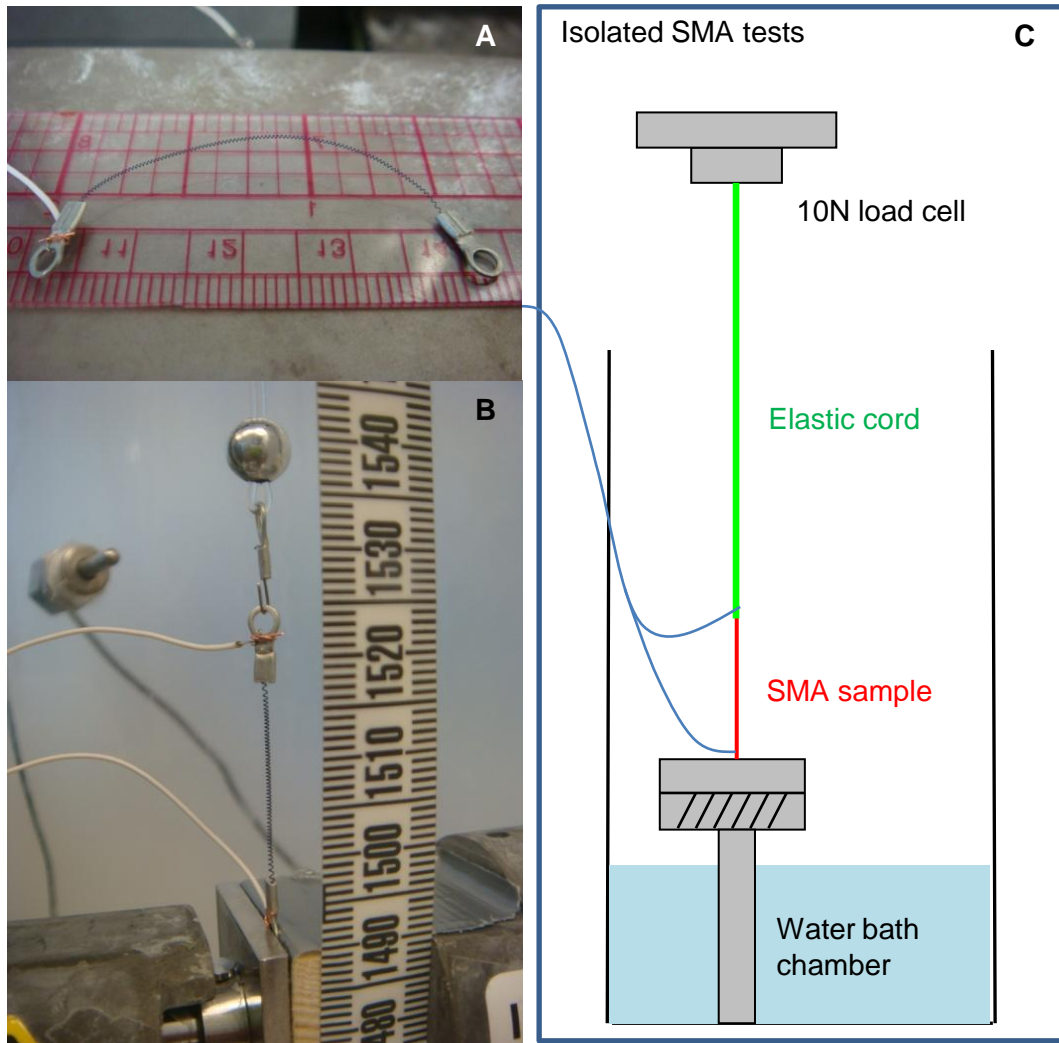


Fig.5-7 SMA test setup. (A) Different sizes of SMA coils with exact number of coils were prepared for testing. (B) The SMA sample is innervated by two light tether wires and loaded in series with an linearly elastic cord. (C) The SMA-elastic installment is in a semi-close chamber to minimize ambient temperature fluctuation. SMA actuation force is measured by the load cell.

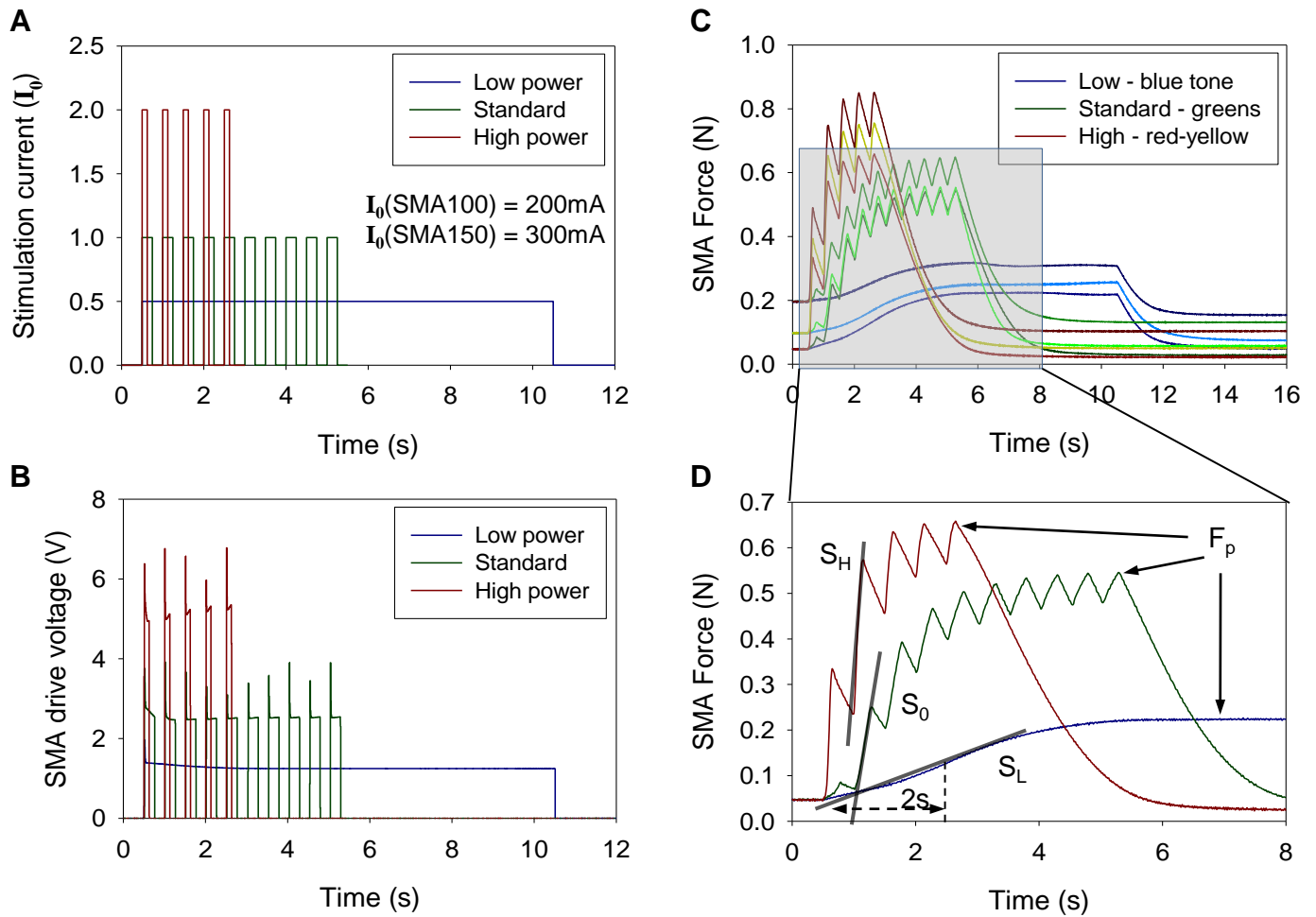


Fig.5-8 SMA test data analysis. (A) By controlling the current level and pulse duration, we can deliver the same amount of energy to the SMA at different rate. (B) SMA phase transition causes a drop of electrical resistance and therefore a change of drive voltage (in this current control system). In general, the drive voltage drops as the SMA sample activates. The maximum decrease of resistance can be computed using this voltage recording together with the stimulation current. (C) Force develop of the SMA samples were recorded under different preload and stimulation powers. This is repeated three times and also with different resisting loads. (D) The initial loading rates S_i and peak forces F_p are defined as shown.

<i>Stimulation:</i> Frequency = 2Hz $I_{\min} = 0.5I_0$; $I_{\max} = 2I_0$ Condition [I , t_h , t_p , n] $C_0 = [I_0, 250, 250, 10]$ $C_L = [I_{\min}, 500, 0, 20]$ $C_H = [I_{\max}, 125, 375, 5]$			Stiffness levels: $K_1 = 8.673\text{N/m}$, $K_2 = 34.90\text{N/m}$, $K_3 = 87.85\text{N/m}$											
			SMA parameters											
			100 μm ; $I_0 = 200\text{mA}$; $R = 0.13\sim 0.142\text{ohm/coil}$						150 μm ; $I_0 = 300\text{mA}$; $R = 0.095\sim 0.106\text{ohm/coil}$					
			50 coils (~1.5cm) 7.1ohm			100 coils (~3cm) 13ohm			50 coils (~2cm) 5.3ohm			100 coils (~4cm) 9.5ohm		
			50mN	100mN	200mN	50mN	100mN	200mN	50mN	100mN	200mN	50mN	100mN	200mN
Installation conditions			1	2	3	4	5	6	7	8	9	10	11	12
Peak force (mN)	C_L	K_1	115	150	212	148	164	228	154	187	300	213	257	384
		K_2	195	222	254	222	233	292	345	373	437	468	477	508
		K_3	209	234	276	234	258	323	473	499	540	530	558	543
	C_0	K_1	118	169	284	170	234	366	155	192	314	207	246	405
		K_2	301	343	443	422	479	560	354	436	556	608	657	780
		K_3	406	484	562	533	565	644	738	782	894	823	931	1070
	C_H	K_1	123	175	297	165	245	389	165	245	389	230	276	424
		K_2	316	369	488	490	537	659	395	464	599	600	678	827
		K_3	510	576	708	662	756	863	759	846	1004	1013	1106	1277
Variations (mN)	C_L	K_1	6	3	3	9	4	9	1	1	1	8	5	2
		K_2	3	1	2	8	8	5	5	3	5	27	27	65
		K_3	4	24	7	7	10	4	12	14	12	26	25	58
	C_0	K_1	4	0	2	21	5	1	2	1	1	5	11	1
		K_2	2	2	2	13	16	11	15	8	8	41	17	8
		K_3	6	25	7	13	10	4	15	6	2	15	11	6
	C_H	K_1	3	1	0	7	2	1	7	2	1	18	6	2
		K_2	2	0	1	7	5	2	16	6	3	13	6	3
		K_3	13	2	12	28	2	11	17	8	2	17	11	4

Table.5-1 SMA peak forces and standard deviations (mN). From left to right, the 12 columns represent 12 different SMA actuator installation conditions. From top to bottom, C_L , C_0 , and C_H denote the stimulation power from low to high. K_1 , K_2 , and K_3 represent three levels of resisting load stiffness. In general, larger and longer SMA coils deliver higher peak forces. Increasing the stimulation power and resisting load also induce higher peak forces in SMA coils.

<i>Stimulation:</i> Frequency = 2Hz $I_{\min} = 0.5I_0$; $I_{\max} = 2I_0$ Condition [I , t_h , t_p , n] $C_0 = [I_0, 250, 250, 10]$ $C_L = [I_{\min}, 500, 0, 20]$ $C_H = [I_{\max}, 125, 375, 5]$			Stiffness levels: $K_1 = 8.673\text{N/m}$, $K_2 = 34.90\text{N/m}$, $K_3 = 87.85\text{N/m}$											
			SMA parameters											
			100 μm ; $I_0 = 200\text{mA}$; $R = 0.13\sim 0.142\text{ohm/coil}$						150 μm ; $I_0 = 300\text{mA}$; $R = 0.095\sim 0.106\text{ohm/coil}$					
			50 coils (~1.5cm) 7.1ohm			100 coils (~3cm) 13ohm			50 coils (~2cm) 5.3ohm			100 coils (~4cm) 9.5ohm		
			50mN	100mN	200mN	50mN	100mN	200mN	50mN	100mN	200mN	50mN	100mN	200mN
Installation conditions			1	2	3	4	5	6	7	8	9	10	11	12
Initial rate (mN/s)	C_L	K_1	7	4	3	8	8	5	7	4	4	6	9	8
		K_2	20	15	11	35	32	28	9	11	24	79	66	41
		K_3	44	34	25	50	45	35	77	68	56	84	80	67
	C_0	K_1	173	146	97	270	226	180	203	168	132	71	53	58
		K_2	417	351	290	607	561	492	72	102	102	186	199	211
		K_3	613	575	524	758	710	692	259	253	257	206	233	297
	C_H	K_1	560	540	487	792	879	762	795	755	884	1439	1406	1733
		K_2	827	879	762	3361	3303	3324	2423	2543	2510	3607	3670	3484
		K_3	3385	3438	3529	4119	4441	4409	4289	4270	4074	5046	4988	4760
Variations (mN/s)	C_L	K_1	3	1	1	2	1	1	0	0	0	2	0	1
		K_2	1	1	0	4	2	1	2	0	3	7	5	14
		K_3	2	1	1	1	0	1	10	5	1	19	10	6
	C_0	K_1	22	8	14	25	17	23	18	3	5	13	46	50
		K_2	10	6	9	8	8	3	23	6	16	63	18	5
		K_3	30	13	11	7	10	4	37	21	9	29	11	2
	C_H	K_1	31	8	5	43	12	3	47	20	5	143	46	22
		K_2	68	12	3	58	38	12	154	61	9	134	76	38
		K_3	87	30	41	96	17	54	118	49	65	26	51	76

Table.5-2 SMA initial loading rates and standard deviations (mN/s). From left to right, the 12 columns represent 12 different SMA actuator installation conditions. From top to bottom, C_L , C_0 , and C_H denote the stimulation power from low to high. K_1 , K_2 , and K_3 represent three levels of resisting load stiffness. Small SMA coils tend to activate faster given the same stimulus. However, preload and resisting load can both significantly alter the initial loading rates.

<i>Stimulation:</i> Frequency = 2Hz $I_{\min} = 0.5I_0$; $I_{\max} = 2I_0$ Condition [I , t_h , t_p , n] $C_0 = [I_0, 250, 250, 10]$ $C_L = [I_{\min}, 500, 0, 20]$ $C_H = [I_{\max}, 125, 375, 5]$		Stiffness levels: $K_1 = 8.673\text{N/m}$, $K_2 = 34.90\text{N/m}$, $K_3 = 87.85\text{N/m}$												
		SMA parameters												
		100 μm ; $I_0 = 200\text{mA}$; $R = 0.13\sim 0.142\text{ohm/coil}$						150 μm ; $I_0 = 300\text{mA}$; $R = 0.095\sim 0.106\text{ohm/coil}$						
		50 coils (~1.5cm) 7.1ohm			100 coils (~3cm) 13ohm			50 coils (~2cm) 5.3ohm			100 coils (~4cm) 9.5ohm			
		50mN	100mN	200mN	50mN	100mN	200mN	50mN	100mN	200mN	50mN	100mN	200mN	
<i>Installation conditions</i>		1	2	3	4	5	6	7	8	9	10	11	12	
Resistance change (%)	C_L	K_1	11.2	11.1	8.1	12.8	12.0	9.4	11.6	11.3	11.3	13.5	12.5	12.4
		K_2	10.1	10.0	8.5	11.2	10.9	9.9	11.2	10.9	10.6	12.8	11.7	10.8
		K_3	10.3	9.9	9.0	10.3	10.2	9.4	10.9	10.4	10.1	11.0	10.9	10.4
	C_0	K_1	12.6	12.5	11.3	14.4	12.8	12.0	12.4	11.1	11.2	12.7	12.1	12.2
		K_2	10.3	10.1	9.5	10.3	9.9	9.3	12.0	11.3	11.1	12.5	11.5	11.1
		K_3	8.4	9.1	9.6	8.9	8.7	8.0	10.2	9.9	9.5	10.7	10.6	10.1
	C_H	K_1	3.1	2.9	3.1	3.2	3.4	3.3	6.5	7.6	7.5	6.9	6.4	6.5
		K_2	3.2	3.4	3.3	1.6	1.5	1.2	5.9	5.6	5.6	6.1	5.4	5.4
		K_3	1.9	1.6	1.2	1.0	0.8	1.0	4.1	4.1	3.8	4.6	4.3	4.3
Variations (%)	C_L	K_1	0.1	0.1	0.8	0.4	0.2	0.7	0.1	0.1	0.1	0.1	0.1	0.1
		K_2	0.2	0.1	0.1	0.3	0.1	0.0	0.2	0.0	0.1	0.9	0.4	0.5
		K_3	0.4	0.2	0.3	0.1	0.1	0.1	0.6	0.1	0.1	0.2	0.2	0.1
	C_0	K_1	1.5	1.0	1.0	0.6	0.4	0.2	1.0	0.2	0.1	0.6	0.1	0.1
		K_2	0.3	0.2	0.1	0.4	0.2	0.1	0.2	0.1	0.3	0.3	0.1	0.1
		K_3	0.4	0.2	1.1	0.4	0.3	0.3	0.6	0.2	0.1	0.2	0.2	0.1
	C_H	K_1	0.3	0.1	0.3	0.2	0.4	0.2	1.1	0.5	0.5	0.5	0.4	0.1
		K_2	0.2	0.4	0.2	0.2	0.1	0.2	0.1	0.1	0.7	0.4	0.2	0.3
		K_3	0.8	0.1	0.1	0.9	0.7	0.1	0.2	0.1	0.1	0.1	0.1	0.0

Table.5-3 SMA electrical resistance changes and standard deviations (% nominal resistance). From left to right, the 12 columns represent 12 different SMA actuator installation conditions. From top to bottom, C_L , C_0 , and C_H denote the stimulation power from low to high. K_1 , K_2 , and K_3 represent three levels of resisting load stiffness. The SMA activation typically leads to a 10~12% decrease of electrical resistance in the SMA coil. High power stimulation produces more heat in the SMA coils. The temperature effect increases the electric resistance in SMA coils, suppressing the resistance drop due to SMA phase transition.

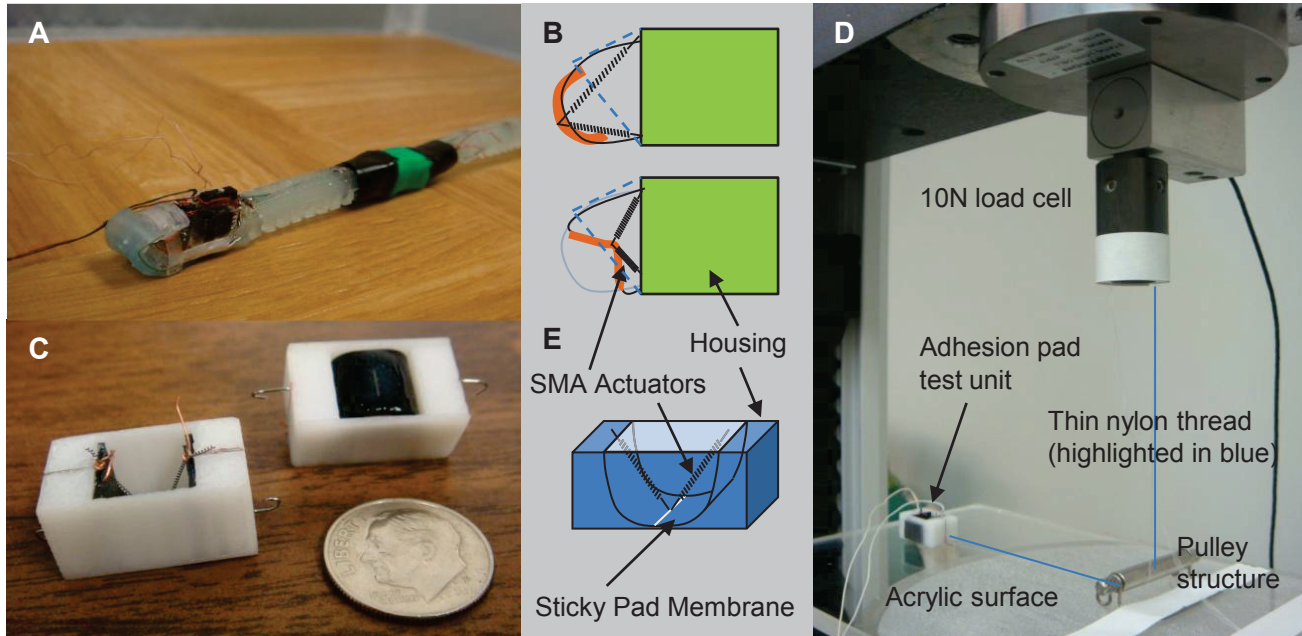


Fig.5-9 Controllable grip. (A) Retractable adhesion pad on GoQBot-III. (B) Schematics of adhesion pad retraction mechanism. (C) Adhesion pad units for testing traction performances. (D) The adhesion pad unit was dragged across an acrylic surface via a thin nylon thread over a pulley structure by the load cell.

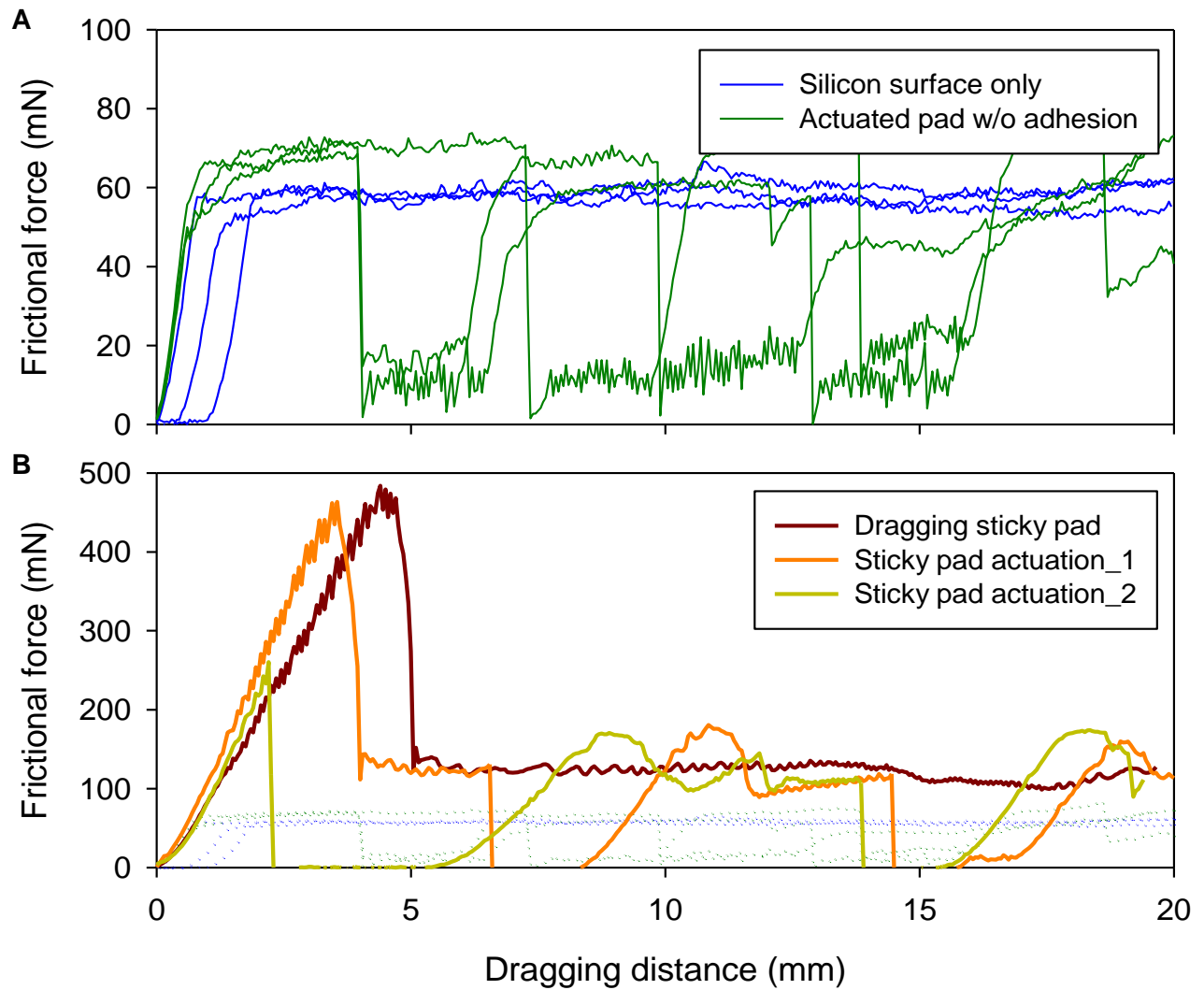


Fig. 5-10 Retractable adhesion pad test. (A) Without any adhesion material, silicone rubber provides frictional force around 60mN given an normal force of 1.5g. The retractable pad produces the similar traction and upon actuation, the friction can drop below 20mN. (B) The adhesion pad delivers static traction force close to 500mN before slipping. Once moving, the friction remains twice that pure silicone rubber provides. Actuation in this state removes the friction almost completely (orange trace). Redeployment of the pad reestablishes the friction. Similarly, adhesion pad can be retracted in the initial phase as well (olive green trace).

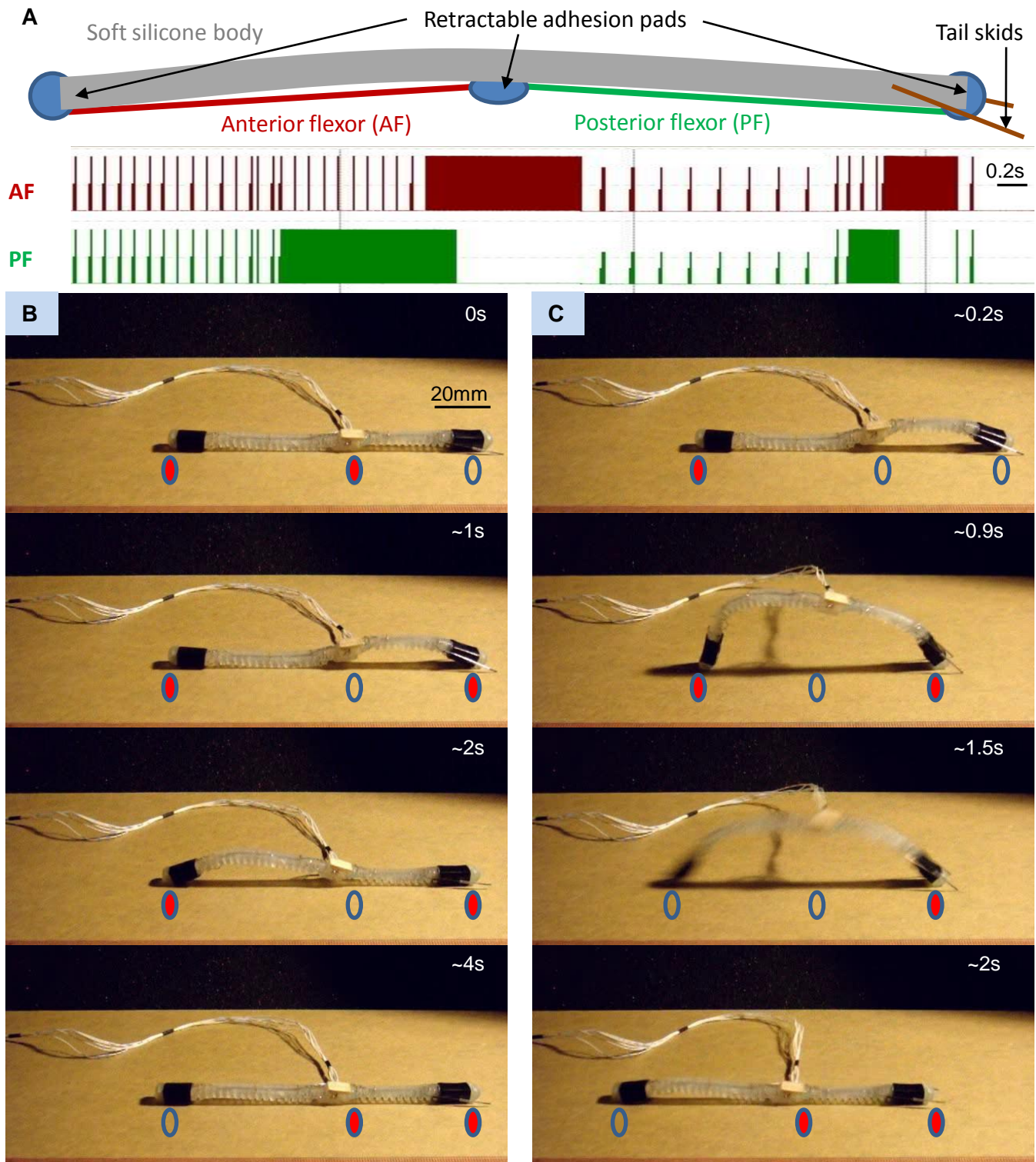


Fig. 5-11 Gait transition with motor pattern pacing. (A) GoQBot has two major actuation units: anterior flexor and posterior flexor. The motor pattern for crawling is quite simple with some overlap between the two flexors. The result is a graduated crawling gait as shown in (B). Pacing up the gait pattern and proportionally scale up the stimulation frequency (intensity) leads to a large amplitude inching gait as exemplified in (C). The adhesion pads control patterns are marked directly on the photo sequences for simplicity.

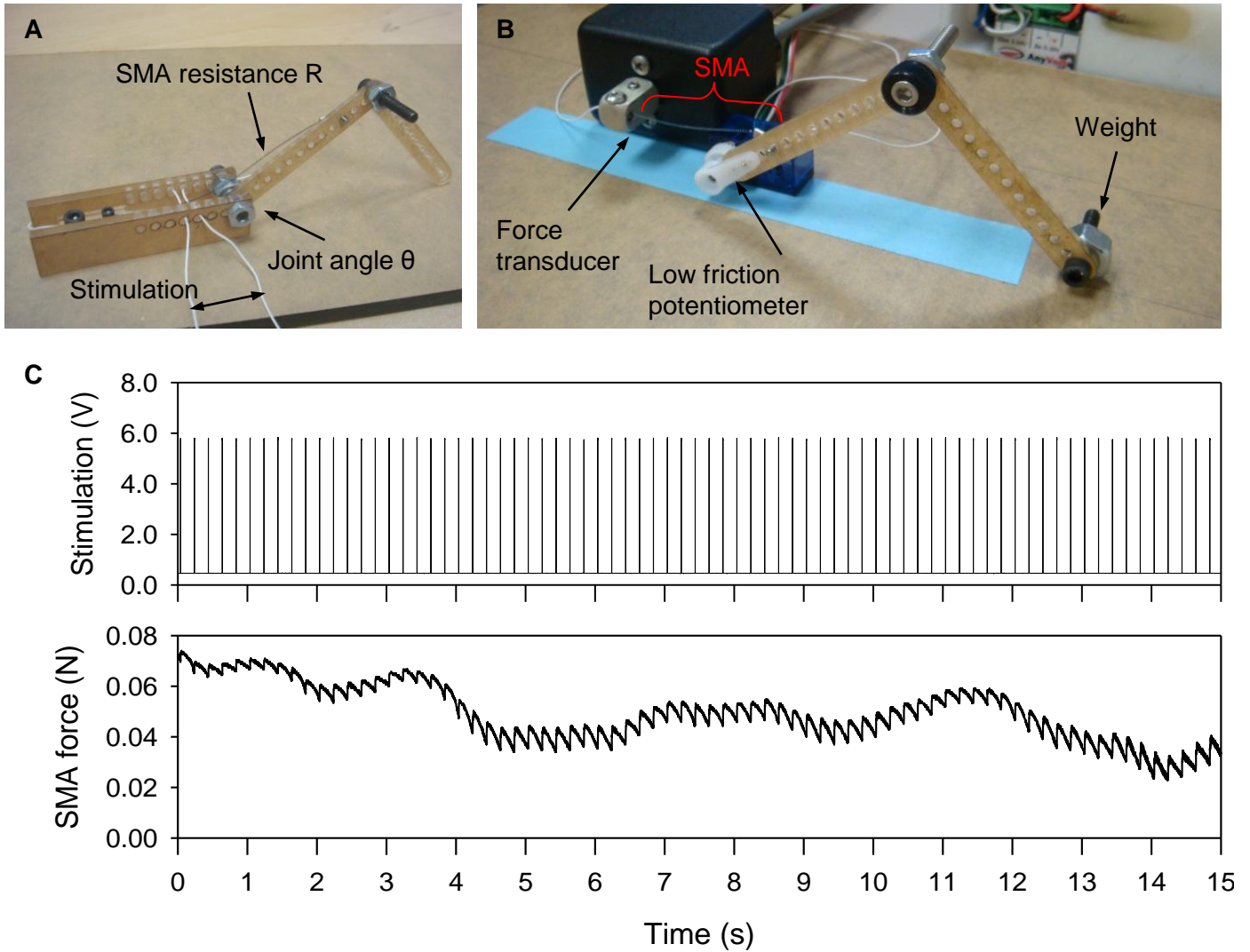


Fig. 5-12 A biomimetic SMA controller test device. (A) A miniature robotic limb was used for testing the SMA actuator mechanical output in response to different frequency modulated stimulation patterns. (B) The second version of the robotic limb includes SMA force and joint angle measurement. (C) Tonic activities produce a baseline SMA force with tetanic characteristics. Each pulse is 2ms long with a pulse train frequency 5Hz.

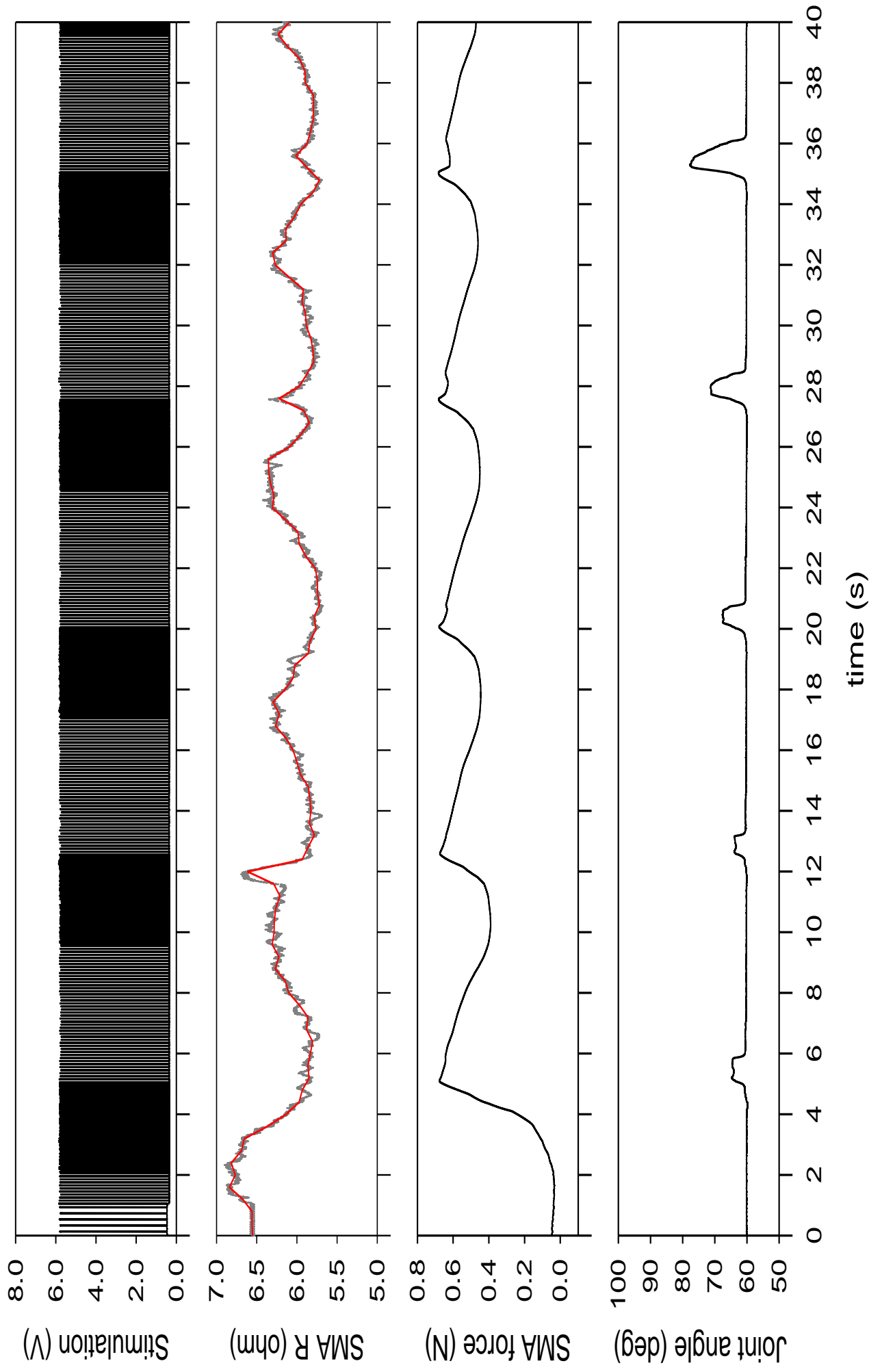


Fig. 5-13 Low power rhythmic activities with tonic modulation. Increase of stimulation frequency directly leads to temperature build-up and force development in the SMA actuator.

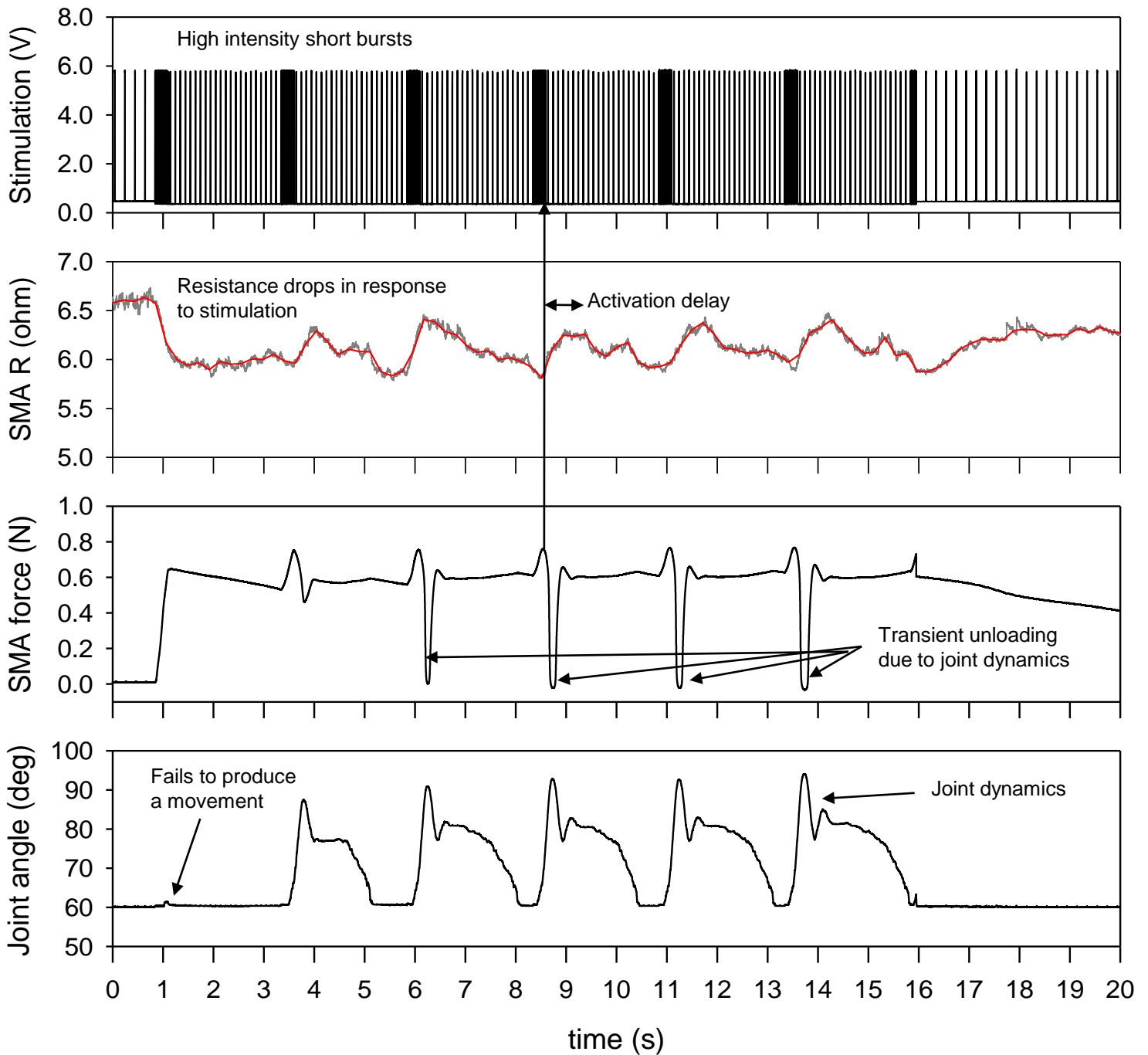


Fig. 5-14 High power rhythmic actuation with tonic modulation. High power stimulation bursts produce more distinct joint movements. The drop of SMA electrical resistance somewhat correlates to the force development with some delay.

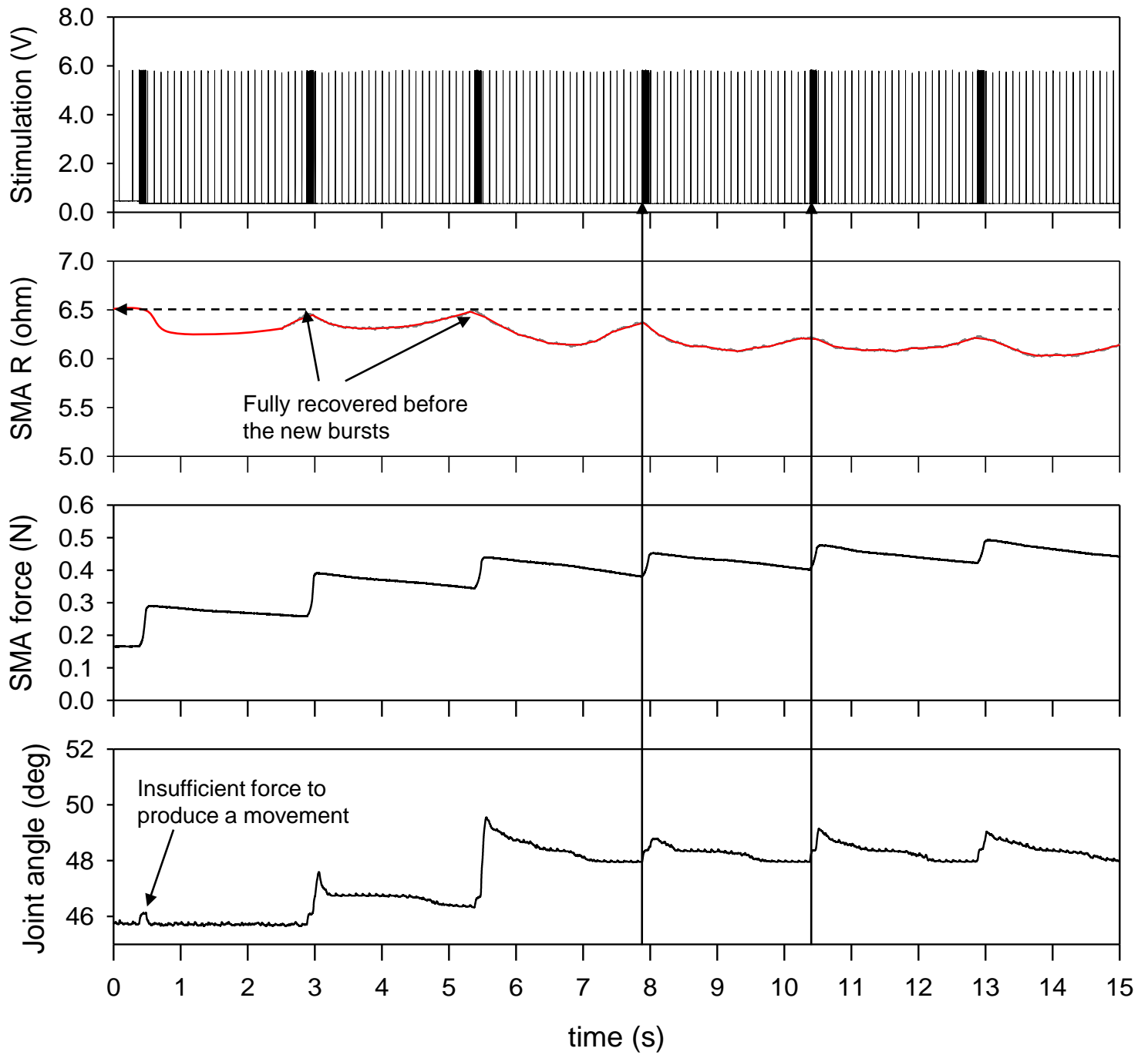


Fig. 5-15 Burst of activities with tonic modulation. Given certain range of tonic frequencies, high power burst trains can produce very smooth mechanical output.

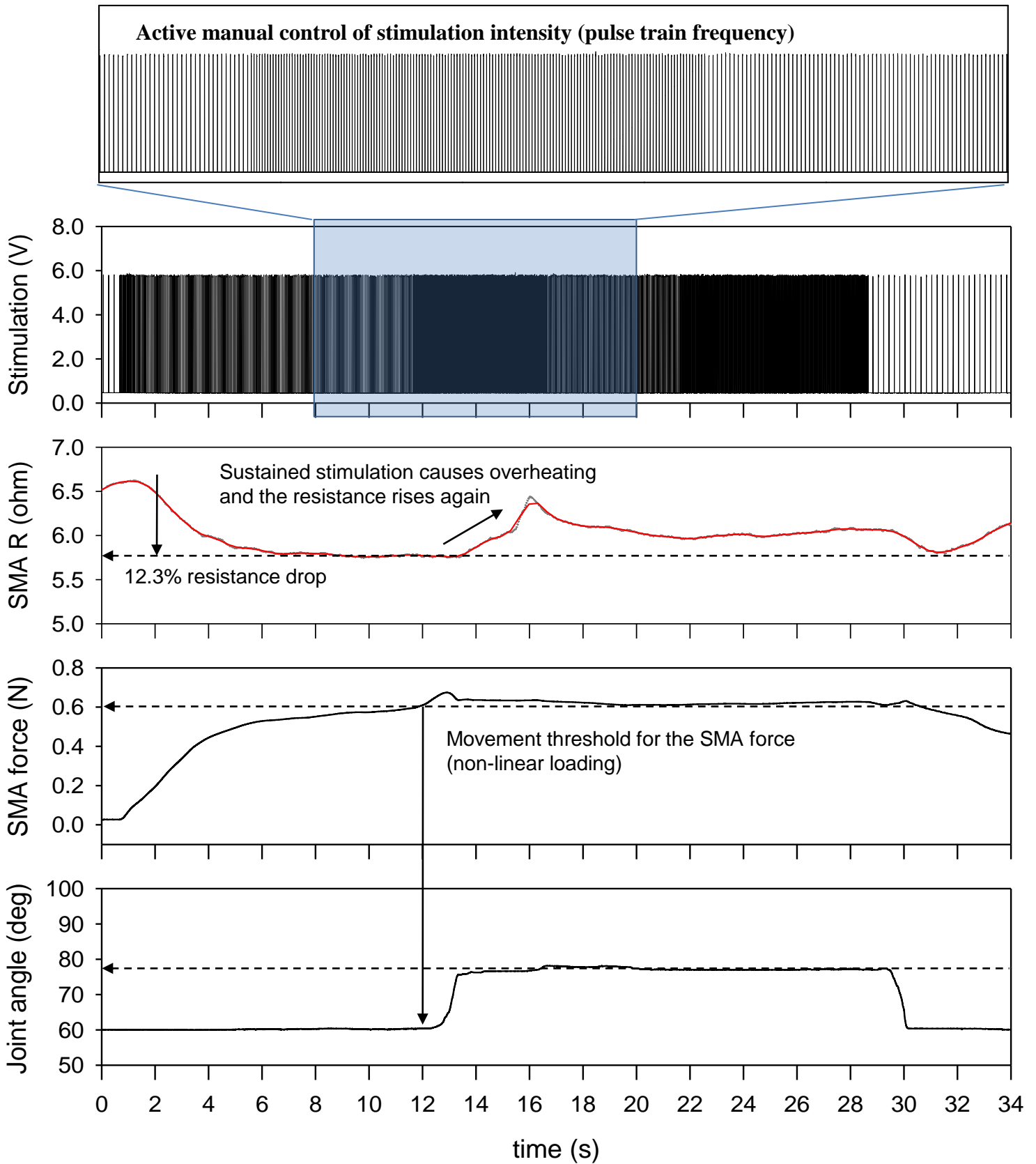


Fig. 5-16 Sustained isometric contraction with real-time feedback delivered manually. Controlling a nonlinear actuator against a nonlinear load is no easy task. There are many variables that contribute to the overall system behavior at any given instance. Currently only experienced operators such as myself can provide effective adaptive control to the robotic limb. Note the stimulation signal was manipulated in real-time extensively in order to maintain the isometric contraction.

Publication-5

Title: GoQBot: a caterpillar-inspired soft-bodied rolling robot

Authors: Huai-Ti Lin, Gary G. Leisk and Barry Trimmer

Keywords: Rolling locomotion; Biomimetic robots; Morphing; Soft-bodied robots, Caterpillar

Abstract

Rolling locomotion using an external force such as gravity has evolved many times. However, some caterpillars can curl into a wheel and generate their own rolling momentum as part of an escape repertoire. This change in body conformation occurs well within 100ms and generates a linear velocity over 0.2m/s, making it one of the fastest self-propelled wheeling behaviors in nature. Inspired by this behavior, we construct a soft-bodied robot to explore the dynamics and control issues of ballistic rolling. This robot, called GoQBot, closely mimics caterpillar rolling. Analyzing the whole body kinematics and 2D ground reaction forces at the robot ground anchor reveals about 1G of acceleration and more than 200rpm of angular velocity. As a novel rolling robot, GoQBot demonstrates how morphing can produce new modes of locomotion. Furthermore, mechanical coupling of the actuators improves body coordination without sensory feedback. Such coupling is intrinsic to soft-bodied animals because there are no joints to isolate muscle-generated movements. Finally, GoQBot provides an estimate of the mechanical power for caterpillar rolling that is comparable to that of a locust jump. How caterpillar musculature produces such power in such a short time is yet to be discovered.

1. Introduction

In the animal kingdom most locomotion is produced by oscillating or reciprocal motions generated by periodic activation of muscles working as tensile actuators. In terrestrial environments propulsion is typically accomplished with jointed legs which can negotiate uneven terrains. However, there are some wheelers in nature that exploit rotary mechanics for

continuous forward progression on smooth terrain. Unlike man-made rolling machines which generally rely on wheels for support and movement, animals can form wheels when they are needed (Armour, Vincent 2006). By reconfiguring their body structures (morphing) such animals can exploit the advantages of limbs (including non-locomotor purposes) and wheels in different situations.

1.1. Animals that wheel

Wheels work only as efficiently as the terrain allows (LaBarbera 1983). It is therefore not a surprise to find wheeling or tumbling only in certain environment. For example, on the flat intertidal zone a stomatopod *Nannosquilla decemspinosa* prefers to flip its body across the wet sand when there is no water to swim (Caldwell 1979). These shrimp-like creatures have legs specialized for swimming but not walking. When the tide recedes, this flipping locomotion offers an alternative to swimming. This motion can be performed up to one body length per second (~3.5cm/s for large individuals) (Full et al. 1993). More recently, a new kind of rotary locomotion was found in the Sahara desert performed by a nocturnal spider, *Araneus rota* (Puppe 2008, Winter 2009). After a running start, this spider somersaults like a gymnast across the desert at ~1m/s (personal communication, Dr. Ingo Rechenberg). There are many passive wheeling animals, but self-propulsion is rare and poorly understood.

1.2. Ballistic movements in caterpillars inspire a new class of rolling robots

Another group of animals that roll are the larvae of Lepidopterans (moths and butterflies). Caterpillars normally defend themselves with noxious chemicals or cryptic coloration but many species also make rapid striking movements to startle potential predators (Walters et al. 2001). Another strategy against more persistent predators is to quickly move away. There is a group of caterpillars that feed on nettles and normally hide in leaf rolls. When disturbed in the opening, they rapidly curl up into a wheel-like structure while keeping their anal prolegs anchored. This

process builds up momentum which can carry the animal into a rolling locomotion with top speeds over 20cm/s (~~supplemental video 1~~). This behavior can be found in multiple species of leaf-roller caterpillars in the family *Crambidae* (grass moths) (figure 1(a)). Specifically, the behavior has been documented in larvae of *Pleuroptya ruralis*, a small moth in the subfamily *Spilomelinae* common in the United Kingdom (Brackenbury 1997, Brackenbury 1999) (figure 1(b)). Despite the detailed qualitative descriptions of the ballistic rolling behavior, very little is known about its mechanics and control challenges. To complete body morphing in less than 100ms and launch itself into a stable trajectory, a caterpillar must exploit some mechanical control strategies to aid the neural motor commands. This study aims to analyze the mechanics of ballistic rolling in details by simulating the behavior in a soft-bodied robotic platform (figure 1(c)) (~~supplemental video 1~~). The robot implementation process informs the biological challenges and points us to the likely mechanical control mechanism.

The robot, named GoQBot, can crawl around in its default worm-like morphology and also ballistically curl into a wheel to increase locomotion speed over 20 fold. The rolling kinematics closely simulates the trajectory taken by caterpillars during the escape reflex (figure 1(c)). This robot received the name “Go-Q” for its body configurations as it pushes off into the free-wheeling state. For the scope of this study, we focus only on the ballistic rolling behavior recreated in this robot (~~supplemental video 2~~). The high speed kinematics tracking and ground reaction force measurement reveal a variety of key mechanical and control issues. These findings help us to understand the mechanical and neural challenges affecting the development of body control in caterpillars.

2. Soft Robots: Design and Methods

2.1. The overall soft robot architecture

To simulate caterpillar locomotion in soft robots, we reduce the caterpillar body into functional components. The result is a soft silicone body about 10cm long which flexes ventrally on demand to produce displacements between body contact points (figure 2(a)). Two major tensile actuators allow independent control of anterior and posterior flexion. A pair of tail skids provides lateral stability for any inching movement. The three discrete body anchors are modulated by three sets of retractable adhesion pads. In a typical crawling gait, the posterior portion of the body would flex to initiate a forward displacement (figure 2(b)). This displacement is then propagated forward via the activation of the anterior flexor and the relaxation of the posterior flexor. By pacing the same motor pattern faster, the two flexor activations overlap more and produce a large amplitude inching gait (figure 2(c)). All the robots in the GoQBot lineage maintain the same body architecture. For this specific study, we focus on the ballistic rolling behavior in the GoQBot repertoire. A new version of GoQBot was specifically designed for characterizing this behavior (details given in section 2.3).

2.2. Materials and fabrication techniques

The primary body materials for the robot are two kinds of castable silicone rubber (Dragonskin 20, Smooth-On, Easton, PA, USA and VTV800, MTT Tech Inc. Knoxville, TX). Both types of rubber are elastic over a large strain, resistant to tearing, and can be prepared with a wide range of cured stiffnesses. Simple uniaxial extension tests (extension rate 2.5%/s) were implemented to determine their material stiffness. These materials exhibit highly linear stress-strain relationships in tension up to at least 10% strain, thus linear regression was used to determine the tensile moduli from the entire loading curves (not shown). Dragonskin 20 gives 0.533MPa stiffness ($R^2 = 0.974$) and VTV800 gives 1.45MPa ($R^2 = 0.991$).

Robot parts were designed in a standard computer-aid-design (CAD) package (SolidWorks 2008 and 2010, SolidWorks, Concord, MA) (figure 3(a)) and fabricated from positive and/or

negative ABS plastic molds constructed with a 3D printer (Dimension 1200 SST, Stratasys Inc., Eden Prairie, MN). Well-mixed silicone rubber material was degassed using a vacuum casting machine (MCP5/01, MTT Tech Inc. Knoxville, TX), and poured or injected into the ABS molds. Materials were cured at $\sim 70^{\circ}\text{C}$ and any additional silicone rubber parts were attached using uncured silicone rubber as the glue. Other materials were attached to the body using cotton thread sutures or bare copper wires for electric contacts. Some small parts (*e.g.*, LEDs) were attached with cyanoacrylate adhesive (Loctite 4861, Henkel, Düsseldorf, Germany) (figure 3(b)).

2.3. *Body morphology*

In this version of GoQBot, we remove all the morphological features for behaviors other than straight-line ballistic rolling (*i.e.* retractable adhesion pads). However, the overall body form and dimensions are maintained. Like previous versions of GoQBot, the body deformation was biased to ventral flexion through two geometric features. First, the cross-sectional profile was domed. The solid dorsal material (VTV800) predisposes the body to bend in the ventral direction. Second, small wedge-shaped legs were fabricated along the ventral body (Dragonskin 20) to facilitate ventral flexion. These repetitive ventral features also provided many locations to attach SMA coils and signal wires (figure 3(a)). Three axial tunnels (figure 3(c)) were molded inside the solid body to accommodate SMA actuators and signal wires (figure 3(d)).

While the caterpillars roll backward to escape, we reproduce this behavior in GoQBot in the forward direction for convenience. Therefore, the hammer head and the tail skids of GoQBot function like the terminal prolegs (or anal prolegs) and thoracic legs of the animal respectively. Ballistic rolls require a firm pivoting anchor to generate thrust. GoQBot has a cylindrical hammer head (VTV800) with a thin layer of softer tacky silicone rubber (Dragonskin 20 with $\sim 20\%$ slacker) which improves friction. The laterally elongated head ensures sufficient ground contact and the cylindrical profile allows free ground pivoting (figure 3(b)). In caterpillars the

stiffer skeletal thoracic legs slide along the ground during the curling phase of a ballistic roll, acting as skids. GoQBot has a pair of lateral skids (polypropylene, $460\pm 10\mu\text{m}$ diameter) protruding from the tail (figure 3(a, b)). These struts provide low friction contact to the ground and help align the body in a ballistic curling motion. They also help stabilize the body trajectory especially during the low-speed initial stage of a ballistic curl.

2.4. Actuator installation

Shape memory alloy (SMA) such as nitinol has the ability to deform in response to heat. To mimic muscle, our robots use SMA wire in the form of coils (BioMetal Helix BMX100, coil diameter $500\mu\text{m}$ wire diameter $100\mu\text{m}$, Toki corporation, Tokyo, Japan). In SMA coils the relatively small temperature-induced changes in linear wire strain ($\sim 5\%$) are converted into large displacements similar to that of caterpillar muscles (Woods, Fusillo & Trimmer 2008) (20~50% depending on the resisting load). The coils are activated by resistive heating using pulses of current that simulate muscle tetanus. Like caterpillar muscles, SMAs do not have a definite resting length and can be set with pre-stress at any part of the robot.

A pair of parallel SMA coils were threaded through pre-cast $500\mu\text{m}$ tunnels (figure 3(c)) on the ventral side of GoQBot body and preloaded *in situ* to 100mN using a weight (50mN for each coil) (figure 3(e)). Speed is critical for GoQBot dynamic stability and these smaller actuators activate more quickly than a larger SMA coil. The ends of the preloaded SMA coils were tied down to the silicone rubber body using bare copper wire ligatures which also provided soldering points for insulated tether wires. All signal wires were gathered into another 1mm mid-line tunnel along the body axis of the robot where stretching was minimized (figure 3(d)). The tether exited on the right side of the body at the center of mass location (in the resting configuration). The pair of parallel SMA coils was divided functionally into two shorter actuators (anterior and posterior flexors) near the midpoint with a copper ring that formed the stimulation ground (figure

3(e)); current could then be passed through each flexor independently. To mimic the caterpillar's motor organization (generally a single motoneuron per muscle) the left and right SMA coils within each flexor were co-activated to operate as a single actuator.

In caterpillars, most major muscles are aligned longitudinally, connecting at the inter-segmental folds. Muscle coupling is unavoidable as the soft integument cannot isolate movements as in an articulated skeletal system. In good robotic practice, however, independent actuators should not have any mechanical cross-talk. This is to facilitate precise control of each movement. To compare the two control strategies in the context of ballistic rolling, GoQBot actuators were arranged in two configurations (figure 3(f)). In the *coupled* configuration the combined length of the actuators is free to slide through the ventral tunnel so tension in the SMA coils is distributed along the entire body in the low flexion states (similar to the anatomical situation in caterpillars). The tension developed in either motor unit is shared by the two ventral flexors until it is ultimately affected by tunnel friction (once the robot is sufficiently curled). In the *decoupled* configuration the midpoint copper ring is sutured to the body and the anterior and posterior flexors work independently (isolation according to traditional robotic practice). Ballistic rolls can be achieved in both configurations so we compared the mechanics of repeated ballistic rolls in the two configurations with the same stimulus.

2.5. Actuator characterization

The thermomechanical properties of nitinol are quite complex with hysteresis due to strain history as well as temperature history (Shaw, Kyriakides 1995, Shaw 2000). A detailed analysis of nitinol is outside the scope of this study. For our application, we empirically determined the actuation characteristics of the Biometal Helix coils using a material testing device (Model 3366, Instron, Norwood, MA) with a 10N load-cell capable of measuring down to 10mN. Two SMA lengths were tested (50 and 100 coils) with three repetitions. Each SMA coil was mounted in

series with an elastic cord and then stretched to a set preload (figure 4(a)). By applying different stimuli to the SMA actuator, we could determine how the SMA works against a defined load profile (the elastic cord). The stimuli consisted of DC pulses delivering at three input power levels using a constant current power supply (Agilent E3634A, Agilent Technologies Inc., Santa Clara CA) controlled by a USB relay module (NI USB-9481, National Instruments, Austin, TX) (figure 4(b)). For the BMX100 SMA coil, the low, medium and high power stimuli were 100mA (one 10s DC pulse), 200mA (ten 0.5s DC pulse at 2Hz) and 400mA (five 0.125s DC pulses at 2Hz) respectively (not shown in the figures). It was difficult to control the energy consumption without real-time feedback as the SMA electrical resistance changed upon heating. However, the above stimulation arrangement kept the input energy roughly constant.

Due to the nitinol phase transition and heating, SMA coil resistance drops during each activation. This effect was monitored by measuring the voltage across each SMA in real time using a USB data acquisition module (NI USB-9201, National Instruments, Austin, TX). This relationship between electrical resistance and phase transition has been exploited and modeled in different applications from strain measurements to position control (Ma, Song & Lee 2004, Li, Mao & Ou 2005, Cui, Song & Li 2010). For the purpose of our robotic implementation, we use the increase of current draw as an index of actuator activation. The SMA actuation, resistance measurement and Instron control were synchronized by a computer (LabView 2009, National Instruments, Austin, TX) using an external trigger from the Instron machine. The SMA contraction was calculated from the spring constants of the elastic cords at different preloads and with different stimuli designed to encompass those used in GoQBot. For the focus of this paper, only the properties pertaining to the performance of GoQBot are presented from the SMA actuation tests. We have also performed similar tests on SMA coils of large size. The full analysis of the 108 SMA tests will be covered by future publications.

To assess the in-situ tension experienced by the actuators, we tethered the actuators out from the hammer head to the same Instron 10N load cell (figure 4(c)). As shown in the figure, the constrained head could pivot but not translate on the substrate. By stimulating the robot to perform a constrained ballistic roll, we can directly measure the tension in the anterior flexor. Ballistic movements often demand high power output from the actuators especially in absence of elastic energy storage. The rapid development of force by SMA coils depends on the preload, the resisting load and residual heat from prior stimulation (figure 5(a)). With the same resisting load an increase in stimulation power results in sustained contractions (analogous to tetanus in muscle) that are faster and of larger amplitude. As expected for muscles, the resisting load also affects the performance of SMA actuators. Under small loads the actuator is free to contract but does not reach its full loading potential. Conversely high loads limit displacement and therefore the work output. Medium loads (34.9 N/m) allow the SMA to develop optimal work, trading off force and displacement (figure 5(b)).

The initial slopes of the loading curves from each SMA test can be used to quantify the loading rates. Under low resisting loads, shape changes in the SMA coils dominate the overall dynamics and the SMA acts like a displacement actuator (*i.e.*, a servo). In general, increasing load stiffness leads to faster initial force development and higher peak forces. At sub-maximal load, preloading the SMA increases the maximum force output but decreases the initial contraction speed (figure 5(c)). Hence, for loading applications at this preload (as in GoQBot), the only way to maximize speed and peak force simultaneously is to use multiple SMA coils in parallel. Sharing the preload between the two coils, each SMA unit can operate at a lower preload while working against a moderate resisting load. GoQBot has two bilaterally symmetric coils running along the entire body. Each coil experiences about 50mN preload (highest initial contraction) while the robot body is still properly loaded with 100mN.

In a given crystal state nitinol increases its resistivity with increased temperatures. However, as nitinol transforms from martensite to an austenite state the electrical resistance drops significantly (9~15%) (Vidal et al. 2008). This can be seen in electrically heated SMA coils which decrease resistance exponentially because of non-uniform temperature changes (figure 5(d)): some regions pass through the transition temperature (~70 degrees Celsius) before others. When most of the coil is above the transition point the resistance increases slowly with temperature. This effect is easily detectable by measuring the current draw from the SMA at constant voltage, and can be used as an index of SMA activation state.

2.6. Control system

Although radio controlled untethered versions of GoQBot have been developed, the low instantaneous power output of existing batteries limits robot rolling performance. Therefore the new GoQBot for this particular study is powered from an external supply through thin wire tethers. The anterior and posterior flexors were controlled by independent relay channels to produce different motor activation patterns. Unlike in the isolated SMA tests, all functional robots received fixed voltage control signals (instead of fixed current) which simplified the multi-actuator control implementation. For crawling and inching movements (figure 2(b, c)) the actuators were controlled by frequency modulated stimuli (not shown). For rolling movements the actuators were powered by sustained DC pulses for maximum power and the current draw of each flexor was monitored from the voltage drop across a 0.2 ± 0.005 ohm resistor in series with each SMA pair. A working pattern was empirically determined by shifting the relative timing between the two actuations (the activation sequence is reflected in figure 8(a)). With such high power stimulation (>15W), a timing phase delay of 10ms was enough to produce the desirable sequential firing of the actuators. During this 10ms, the anterior flexor was not fully activated.

Instead, it was preheated sufficiently so it became activated significantly faster when the co-activation stimulus arrived.

2.7. Simultaneous Kinematics and dynamics recording

GoQBot was staged on a custom platform for simultaneous kinematics and dynamics recording (figure 6(a)). The platform houses a custom force plate which measures the push-off reaction forces at the GoQBot hammer head in two directions: forward thrust and body weight support. The detailed body trajectories of ballistic rolling were evaluated with a 3D motion capture system (VICON, Los Angeles, CA, USA). Five infrared optical cameras provided stereo 3D mapping in a calibrated volume (20x30x20 cm) at 200fps (figure 6(b)). A high speed camera was used occasionally to collect video from any specific angle (not critical for data acquisition). Five surface mount infrared (850nm) LEDs SFH4050 (Opto Semiconductors, Regensburg, Germany) were installed on the robot as kinematic markers. These high intensity IR emitters have small profile dimensions of 1.7mm×0.8mm×0.65mm (L×W×H) and a 160 degrees viewing angle (figure 6(b)). They appear like distant stars in the VICON optical cameras and offer very discrete position marking (figure 6(c)). The calibration accuracy was found within 1mm according to the known marker distances on a resting GoQBot randomly place in the calibrated volume. A typical ballistic roll occurs within half a second. Reaction forces from the head anchor in the normal and fore-aft directions were recorded simultaneously. The complete GoQBot weighs 5.0±0.01g without the tether (~6.2g with tether).

All capture trials were triggered automatically by the GoQBot stimulus and recorded for one full second. We focused our analysis on the first 400ms where all the interesting dynamics occurred. The marker coordinates were reconstructed automatically by the VICON Nexus 1.6.1 (VICON, Los Angeles, CA, USA) using a simple free-joint model (figure 6(d)). Occasional trajectory gaps due to undetected markers were filled using a 3D spline or a reference trajectory

from the adjacent marker. Trials with gaps of more than 3 frames (15ms) or gaps with two consecutive markers undetected were discarded as unsuccessful recordings.

2.8. Data processing and geometric extrapolation

All analog signals were captured at 1kHz. Each trial produced 19 channels of synchronized data: XYZ coordinates for the five LED markers on the robot, ground reaction force in two directions, and SMA current supplied to both flexor units. The kinematics and dynamics data were processed in four stages. In the first stage, a MATLAB (Mathworks, Natick, MA) script was used to determine the GoQBot heading and to project the marker coordinates on the sagittal plane. The heading was determined by a simple linear regression of the rolling trajectory in the X-Y plane. Since the force plate only measures forces in two axes, trials with heading deviating from the intended track by more than 10 degrees were considered unsuccessful. Once this angle is determined, the actual robot sagittal plane was rotated to align with the X-Z plane. The program then exported the projected X-Z coordinates of the markers to a spreadsheet.

In the second stage a Solidworks 3-D model of GoQBot was constructed (figure (6(e)) assuming pure body bending between markers (axial compression was negligible in GoQBot). This model was used to up-sample the GoQBot kinematics data from 5 markers to 24 equally spaced reference points along the body using non-linear geometric extrapolation (outlined below). The kinematics marker coordinates were imported using the design table to create a series of model configurations corresponding to each kinematic time point. A circular arc of the assumed length was fitted between each adjacent marker pair to estimate the body curvature. A polynomial spline was then fitted on top of the four arcs at the midpoints to force continuity in SolidWorks (figure 6(e)). The end conditions of the spline were adjusted to fit the arcs as closely as possible. Twenty-four repeated features were created and equally distributed (~4.7mm intervals) along this spline, producing 24 coordinates which can be read out from the SolidWorks design table. The extrapolation process relies on the assumption that GoQBot body flexes

without significant change of length. Visual inspection of some high speed videos convinces us that the extrapolation is accurate within 5%. In the new coordinate system X coordinate is designated in the forward direction of the GoQBot while Y coordinate is in the direction opposite to the gravity.

In the third stage, the GoQBot kinematics data were up-sampled temporally using a trajectory smoothing protocol in MATLAB. A piece-wise 3rd order polynomial curve-fit was applied to all the marker trajectories and the sampling rate was increased 5 times from 200Hz to 1kHz (matching the analog signals from the force-plate). The 4 extrapolated points between any pair of original data were assumed to have a constant speed during each 5ms interval and the X and Y velocity components on the sagittal plane were calculated for each of the 24 reference points by differentiating the smoothed trajectories. The temporal extrapolation relies on the assumption that speed is constant for each piece-wise 5ms interval. Since GoQBot has a near constant cross-section and homogeneous density distribution along the body axis (the densities of the two rubbers are essentially the same), we assign 1/24 of the total body mass (differentiated body mass) to the 24 equally spaced reference points. This allows the computation of center of mass (CoM) dynamics as well as the angular momentum.

In the final stage, the voltage data across the in-series 0.2 ohm resistors were filtered at 100Hz (low-pass) and divided by the resistance to obtain current through each actuator. The force plate signals were filtered at 30Hz (low-pass) and converted to ground reaction forces using the calibration curves for the force beam. The kinematics and analog data were combined to calculate the following parameters:

1. Body trajectories and center of mass (CoM) trajectory
2. Differentiated body mass velocities and CoM velocities
3. Angular momentum about the head contact and about the CoM
4. Total body kinetic energy and the CoM kinetic energy

5. Head contact ground reaction forces in vertical and forward direction
6. Work done against the ground over the curling phase
7. The actuator activations (monitored via resistance change)

3. Results

3.1. Kinematics and Actuation

Body curling is an extremely unstable movement. Neither the robot nor the caterpillar can maintain static stability in the curled postures. Instead, the ballistic rolling behavior is dynamically stabilized by accelerating the body masses into a stable trajectory. The kinematics data from GoQBot reveal such a trajectory. The GoQBot completes its body curl and the head detaches from the ground about 250ms after the onset of stimulation. During this process, the body follows a parabolic trajectory which peaks around the anterior anchor (figure 7(a)). As the center of mass (CoM) rises (up to ~2cm), the robot experiences an increasing moment of tipping sideways. The body acceleration is expected to be comparable to gravitational acceleration G in order to achieve stable rolling. Indeed, GoQBot CoM reaches a forward velocity over 0.5 m/s within the first 200ms (figure 7(b)). More specifically, most acceleration happens within 50ms (from 150~200ms in figure 7(b)), reflecting about 1- G of acceleration. In the meantime, the CoM vertical velocity starts to plummet to zero as GoQBot rapidly reduces its radius to less than 2cm (figure 7(c)). Note that the tracking system did not detect any appreciable movement until about 50ms into the stimulation. This initial 50ms seems to account for time lags in SMA actuator heating and tension development. So from the onset of motion to the time of push-off is only ~200ms.

While the stimulation voltage is fixed, the increasing actuator current draw directly reflects the decreasing electrical resistance due to phase transition. The empirically determined stimulation pattern involves a 10ms pre-stimulation of the anterior flexor (figure 8(a)). During

this period, the actuator is slightly activated and develops tension along the body. When the co-activation stimulus arrives, the anterior flexor responds much faster than the posterior flexor, reaching the mid-activation region around 80ms into the stimulation. The posterior flexor does not attain this stage until 160ms into the stimulation. Clearly, the SMA activation time-lag is comparable to the stimulus sequence timing. Variations on this time-lag can potentially compromise the body coordination if uncompensated.

The dynamic body curling generates forward angular momentum around the head anchor (figure 8(b)), the initial angular momentum with respect to the CoM is slightly negative (red). This is associated with the CoM lifting and posterior flexion (figure 7(a)). After the head peels off the ground (~250ms), the angular momentum about the CoM peaks over 60 $\mu\text{N}\cdot\text{m}\cdot\text{s}$ (figure 8(b)). After 200 ms GoQBot begins to free-wheel with a moment of inertia of $\sim 1.5 \times 10^{-6} \text{ kg}\cdot\text{m}^2$ and a rotation rate more than 300rpm.

3.2. Reaction forces and energy transfer

During its resting state, GoQBot's head supports 20~30% of the body weight (BW) (figure 8(c)). When the actuator is activated anterior flexion pulls the body forward and lifts the abdomen to shift body mass onto the head anchor. Although the head is the last point to leave the ground the vertical GRF under the head never reaches body weight, peaking around 70% of the body weight 175ms after the start of stimulation. This time coincides with the peak vertical velocity of the CoM (figure 7(c)) thereby unloading the ground force sensor. The tail skids must share a significant portion of upward external forces.

Forward propulsion is generated by the body curling and creating backwards forces under the head anchor. In the initial 50ms no-motion window, the body clearly develops some internal tension as the SMA actuators starts to build up heat. Since the entire body is lying flat on the ground, the fGRF at the hammer head has to overcome the static friction before body flexion

starts (fGRF \sim 20% body weight). Once the body begins to move, the fGRF exceeds one body-weight (BW) at about 75ms into the stimulation and is sustained above this level until push-off (figure 8(c)). The GoQBot therefore experiences more than 1-G of forward acceleration for at least 100ms. This short impulse causes the CoM to accelerate quickly, reaching a velocity over 0.5m/s. Of course, some of this force has to resist the friction of the tail skids as well as the ventral side of the body in the initial phase. Such acceleration corresponds to a ground power in the forward direction peaking at \sim 40mW (figure 8(d)). The ground power in the vertical direction is always under 10mW. However, it is occasionally sufficient to get GoQBot airborne momentarily.

The energy transfer in the ballistic push-off is surprisingly efficient. Mechanically, GoQBot performs net work of \sim 3.26mJ during the ground push-off. During the curling process, most of this energy goes into kinetic energy ($>80\%$) (figure 8(d)). Given the moment of inertia for a hollow thin cylinder, a non-slip wheel should have rotational energy more than half and less than the total translational kinetic energy. At the tipping point (\sim 200ms), the CoM kinetic energy is less than half of the total kinetic energy, suggesting that rotational energy is dominant and that the CoM is still accelerating via rotary movements. Some slipping occurs during this phase as the robot loses its ground contact. By about 240ms the CoM kinematic energy equilibrates to more than half of the total kinetic energy and the GoQBot reaches a non-slip free-wheeling state.

3.3. Actuator mechanical coupling as a means of motor coordination

In caterpillars, muscles pull on one another through common attachment points on the soft body wall. To explore the effects of such actuator coupling, ballistic rolls were repeatedly induced in the GoQBot with the anterior/posterior flexor junction attached to the body wall (decoupled) or free to slide as a unit (coupled). In the coupled configuration, the tension in the anterior flexor is directly transmitted to the posterior flexor. This effect is minimized in the decoupled

configuration where the flexor junction is sutured to the body (isolated anterior and posterior flexions). To compare mechanical performance the push-off time is defined as the time at which the total kinetic energy reaches maximum (slightly after the GoQBot transforms into a wheel shape). This time is used to calculate the push-off angular momentum, the work done to the ground, and the nominal rolling radius (figure 9(a)).

During the initial 50ms no-motion window, there is no obvious difference between the coupled and decoupled configurations. We define the initiation of motion as the time GoQBot obtains at least 1mJ of overall kinetic energy. Although the mechanical coupling tend to result in slight delay in body movement, there is no significant difference in motion initiation between the two robot configurations (two-tail t-test, $p = 0.0521$, $df = 18$). Mechanical coupling also increases movement variability, but it has no significant effect on the average push-off time or the push-off angular momentum (statistics are included in figure 9(a)). It does, however, significantly increase the maximum total kinetic energy by 54.6%. Given that the total time of ground contact is similar, the increased kinetic energy can only be attributed to higher ground forces at the head anchor. This explanation is confirmed by the significant more work done to the ground by 87.4% in the coupled configuration. Decoupling the flexor units decreased the nominal rolling radius by 27.1% which may be advantageous for dynamic stability on a flat surface (lower CoM). However, smaller wheels are also disadvantageous for negotiating small obstacles in the path.

3.4. Cost of transport in different modes of locomotion

In order to achieve 1G acceleration, GoQBots typically draws 0.6~1A current through each pair of SMA coils (figure 8(a)). The total instantaneous electric power can range from 20W to 30W but the brief activation profile keeps the total electric energy cost around 8.26J (figure 8(b)) over the entire ballistic rolling event. The transformation of this applied electric energy to SMA work

done inside the robot is not very efficient. In-situ SMA loading measurements of anterior flexor reveals a simple monotonic loading profile, peaking at $320\pm 20\text{mN}$ (curves not shown). The actuator displacement necessary to produce the observed curvature is estimated (by replacing the SMA with a stiff tether) to be $\sim 1.5\text{cm}$. Therefore, assuming a linear loading profile the maximum in-situ SMA work is 2.4mJ . The large energy loss from electrical to mechanical work is consistent with the low efficiency of resistive heating (only a few percent) (Thrasher et al. 1994).

To compare the cost of transport from different gaits we need to define a criterion for assessing the performance of the ballistic roll. Unlike crawling and inching gaits, ballistic rolls can land erratically and are very dependent on the surface condition. In the worst scenario when the ballistic curling fails to produce continuous free-wheeling, GoQBot covers only one body length of $\sim 10\text{cm}$. If it successfully curls into a freewheeling state, GoQBot typically achieves at least 2~3 rotations before becoming unstable (due to imperfection in the body wheel curvature and the interference from the tails skids). Assuming the average nominal rolling radius of $20.3\pm 0.8\text{ mm}$ and two rotations, we can safely estimate the typical range to be $25.5\pm 1\text{ cm}$ (or a little over two body lengths). From the behavioral measurements of the previous version of GoQBot (same body weight and dimensions), inching and crawling take similar amounts of energy per step with the similar gait period. The inching gait, however, covers around 30% body length while crawling gait can only achieve less than 10% body length in the optimal condition (figure 9(b)). Compared to the inching gait, the ballistic roll consumes more than double the energy per step. However, the distance covered well exceeds 8 times of that from inching. Such performance put ballistic roll into the best energy efficient mode of locomotion on flat ground for GoQBot.

4. Discussions

4.1. Stability and body coordination

GoQBot completes the curling phase of its motion very quickly within 200ms from the onset of movements (or 250ms after stimulation). Caterpillars can do so in less than half the time. Given such a rapid movement it is difficult for an animal to collect mechanosensory information and to control movements by muscle activation. In similar fast behaviors, such as insect jumping, the coordination of movements is accomplished by mechanical interactions (Burrows 2009, Burrows, Bräunig 2010). In GoQBot, it was found that mechanical coupling between the two flexor units enhances the body coordination significantly. During the 10ms pre-stimulation, the GoQBot anterior flexor activates slightly and produces a tension without moving the body. In the coupled configuration, this anterior tension is passed to the posterior flexor, thereby changing the initial loading conditions for the ballistic curling movement. According to the SMA actuation data, the increased preload in the posterior flexor should enhance the force output at the cost of initial loading speed. In the case of fast acting anterior flexor, the posterior flexor will be primed to take up higher load as the curling movement starts. The accompanying slower initial loading speed is compensated by the free sliding actuator junction as the posterior flexor does not pull on the robot body directly in the initial state.

Bad coordination often occurs when the posterior flexion cannot provide the loading demand set up by the anterior flexion. The actuator coupling allows communications between the two actuators and also dampens out the abrupt initial activation of either actuator. Essentially, GoQBot takes the same motor stimulus and modifies the actuation characteristics in real-time according to the current state of the actuators. This may be an example of “morphological computation” as suggested in the robotics community (Hara, Pfeifer 2000, Pfeifer, Iida & Bongard 2005). In this specific example, a soft body is required to allow such long-range internal load redistribution. While rigid joints decouple the angular motions across two segments (the

joint angles from two joints can be independent), soft bodies allow mechanical information to be transmitted throughout the body via internal deformation. Caterpillars might use the same strategy to improve body coordination since all the longitudinal muscles are coupled mechanically through the body wall.

4.2. Initial acceleration of a ballistic roll

Any rolling locomotion has to overcome low speed instability to roll effectively thus the initial acceleration is very important. The kinematics of GoQBot suggests that the angular momentum is produced mostly from dynamic body flexion. However, without any initial linear velocity, forward motion would have to rely on transforming rotational energy into translation via the wheeling mechanism. Caterpillars are able to generate translational and angular velocity in one single motion, thanks to the deformable prolegs. These appendages allow rotation around the contact points and subsequent controlled detachment.

From the study of GoQBot locomotion, it seems like rolling outperforms the crawling and inching gaits in speed and cost of transport. Why don't caterpillars roll more often? There are three major factors that probably affect this choice. First, we compared GoQBot locomotion on smooth level surfaces. Wheeling performance varies dramatically with the terrain conditions. For locomotion on uneven terrains, rolling may even produce negative results. Secondly, mechanical power may come at a great cost in biological systems. In GoQBot, rolling demands over one order of magnitude more power from the actuators. While metallic phase transition is rate invariant in SMA, rapid heating tends to produce better efficiency by minimizing heat dissipation. Muscle efficiency varies with contraction speed and resisting load in a more complicated manner (Josephson 1993, Josephson, Malamud & Stokes 2001). Finally, such a fast mode of locomotion might not serve the caterpillar any foraging purposes except in case of predator attack. All

ballistic rolling events end with an unpredictable tumble. The caterpillar can easily lose its substrate (food plant) after performing such a behavior.

Since the ballistic escape roll is an episodic reflex, the caterpillars are not likely to exploit any power amplification mechanism. The high power output probably comes straight from muscle forces. For each ballistic roll, the GoQBot has peak mechanical power of $\sim 30\text{mW}$, comparable to the peak power in a locust jump (Bennet-Clark 1975). However, its mass specific power ($\sim 6\text{W/kg}$) is still two orders of magnitude lower than the sustained aerodynamic power in insect flight (Ellington 1985). The caterpillars that perform ballistic rolls typically weigh less than 0.1g (Lin *et al*, unpublished data). This is less than 2% of the GoQBot weight, so we expect these caterpillars to gather at least 0.6mW mechanical power per escape episode. Since the caterpillar also accelerates four times faster than GoQBot, the estimated mechanical power can be scaled up to 2.4mW . Caterpillar muscles can produce 0.18W per kg muscle mass during strain cycling that simulates crawling (Woods, Fusillo & Trimmer 2008). Taking the body weight into account (mass specific power) suggests that typical power from a single muscle is a few mW per gram animal mass. It is not clear what kind of maximum power these muscles can achieve, and would be an interesting topic to pursue in the future. Despite the soft bodies, many caterpillars perform ballistic behaviors from self-defense to escape jumps. Instantaneous muscle recruitment seems very important for these behaviors.

4.3. Three characteristics of soft-bodied robots

A major challenge to controlling soft structures is that it is difficult to define a mechanical state. In practice, the posture of a soft body is quite variable due to passive deformations. In fact, it would be difficult to classify a robot as “soft-bodied” if its state was conventionally defined and it was forced to adopt specific postures. By definition, deformation is deviation from a reference

geometry. In traditional robotics, this is the target posture. These differences prompt the following three observations about soft-bodied robots.

1. *Soft robots undergo relatively large deformation under typical loading conditions*
2. *Soft robots exploit passive body deformation to accommodate the environment*
3. *Soft robots are under-actuated systems that benefit from adaptive control*

The GoQBot locomotion, for example, can be simulated with a multi-linkage linear robot given that enough segments are present and each joint is compliant in a specific way. Joint rotation can certainly create large deformations and interact with the environment in a useful way. However, in this approach it quickly becomes computationally expensive to monitor each joint angle and to accurately control the robot's posture. Additional passive joint properties can be used to reduce the number of required actuators or the complexity of control input to the actuators. By continuing this reduction process, the multi-linkage device will probably become very compliant. A soft robot is an extreme form of under-actuated system that accommodates the environment with numerous degrees of freedom. Since the passive compliance in soft robots allows various body configurations unintended by the robot, the control strategies must change to account for the current body posture. Adaptive control would be very useful for soft robots in real applications. Our experiments show that some adaptive control may be embedded in the mechanics as in the case of actuator coupling.

To implement further adaptive control, soft robots still need to sense the environments and assess the situation of its own body in order to operate with full autonomy. However, due to the natural variation of soft mechanics, roboticists must be very conservative in implementing sensory modalities in soft robots. Many parameters are very difficult to measure and may be irrelevant to the functioning of a soft robot. For instance it is very difficult to monitor the length of SMA coils in GoQBot since it depends on temperature as well as the loading conditions. Even if we can measure the SMA coil length, it still does not tell us the soft body conformation since

the body itself can deform greatly. SMA resistance, on the other hand, is a good index of actuator activation and can be used to tune the overall gait timing. In addition, by monitoring the resistance of the SMA wires in real-time, it is possible to adjust the electric drive to compensate for the environmental temperature fluctuations. GoQBot operating in a colder environment simply requires higher actuator drive power.

4.4. Revolution of rolling robots --- Morphing as a solution to locomotion

A major reason why robots are modeled after organisms that are shaped like snakes, worms, or caterpillars is their talents for accessing difficult spaces by crawling, climbing and burrowing. However, these limbless bodies often place severe mechanical limits on locomotion speed. While some forms of serpentine locomotion and fast peristalsis can improve level ground speed dramatically, none of them can match the speed and efficiency of rolling locomotion. Many rolling robots, on the other hands, are versatile and capable of traveling in space using various mechanisms (Michaud, Caron 2002, Bhattacharya, Agrawal 2002, Winter 2009, Sugiyama, Hirai 2006). However, due to their circular or spherical body configuration, accessing narrow spaces would be quite challenging. Despite the low actuator efficiency, the GoQBot achieves ~ 78 J/kg-cm cost of transport. This is one order of magnitude higher than a crawling caterpillar (Casey 1991), but quite impressive among soft robots. Indeed, a linear limbless body can easily morph into a spoke-less wheel to roll. The new body configuration not only allows rolling motion but also increases the effective dimension of the robot so it could “run-over” some obstacles. Currently, the GoQBot does not have a righting reflex to recover from each ballistic roll. However, by changing the body design to one with a dorsal-ventral symmetry the need to recover to the initial state could be easily eliminated. Such a device could perform a ballistic roll from either side (ventral or dorsal). With additional modification, the device could also perform the ballistic roll in either direction (forward and backward). We would like to propose ballistic

roll as a solution to fast locomotion in robotic devices with linear bodies (snake-like or worm-like). This motion has been inspired by escape behaviors in caterpillars and we have demonstrated how to replicate it in a soft robot and provided detailed dynamics analysis of the motion.

Acknowledgment

This research was supported by the DARPA ChemBot project. We would like to thank Tim Lo for his initial contribution on robot implementation and Ethan Golden for his suggestions on silicone casting protocols.

References

- Armour, R.H. & Vincent, J.F.V. 2006, "Rolling in nature and robotics: A review", Journal of Bionic Engineering, vol. 3, no. 4, pp. 195-208.*
- Bennet-Clark, H.C. 1975, "The energetics of the jump of the locust *Schistocerca gregaria*", The Journal of experimental biology, vol. 63, no. 1, pp. 53-83.*
- Bhattacharya, S. & Agrawal, S.K. 2002, "Spherical rolling robot: A design and motion planning studies", Robotics and Automation, IEEE Transactions on, vol. 16, no. 6, pp. 835-839.*
- Brackenbury, J. 1999, "Fast locomotion in caterpillars", Journal of insect physiology, vol. 45, no. 6, pp. 525-533.*
- Brackenbury, J. 1997, "Caterpillar kinematics", Nature, vol. 390, no. 6659, pp. 453.*
- Burrows, M. & Bräunig, P. 2010, "Actions of motor neurons and leg muscles in jumping by planthopper insects (hemiptera, issidae)", The Journal of comparative neurology, vol. 518, no. 8, pp. 1349-1369.*
- Burrows, M. 2009, "Jumping strategies and performance in shore bugs (Hemiptera, Heteroptera, Saldidae)", The Journal of experimental biology, vol. 212, no. Pt 1, pp. 106-115.*
- Caldwell, R.L. 1979, "A unique form of locomotion in a stomatopod—backward somersaulting", .*
- Casey, T.M. 1991, "Energetics of caterpillar locomotion: biomechanical constraints of a hydraulic skeleton", Science, vol. 252, no. 5002, pp. 112-114.*
- Cui, D., Song, G. & Li, H. 2010, "Modeling of the electrical resistance of shape memory alloy wires", Smart Materials and Structures, vol. 19, pp. 055019.*

- Ellington, C.P. 1985, "Power and efficiency of insect flight muscle", *The Journal of experimental biology*, vol. 115, pp. 293-304.
- Full, R., Earls, K., Wong, M. & Caldwell, R. 1993, "Locomotion like a wheel?", *Nature*, vol. 365, pp. 494.
- Hara, F. & Pfeifer, R. 2000, "On the relation among morphology, material and control in morpho-functional machines", *From animals to animats 6: proceedings of the Sixth International Conference on Simulation of Adaptive Behavior* The MIT Press, , pp. 33.
- Josephson, R.K. 1993, "Contraction dynamics and power output of skeletal muscle", *Annual Review of Physiology*, vol. 55, no. 1, pp. 527-546.
- Josephson, R.K., Malamud, J.G. & Stokes, D.R. 2001, "The efficiency of an asynchronous flight muscle from a beetle", *Journal of Experimental Biology*, vol. 204, no. 23, pp. 4125-4139.
- LaBarbera, M. 1983, "Why the wheels won't go", *The American Naturalist*, vol. 121, no. 3, pp. 395-408.
- Li, H., Mao, C.X. & Ou, J.P. 2005, "Strain self-sensing property and strain rate dependent constitutive model of austenitic shape memory alloy: experiment and theory", *Journal of Materials in Civil Engineering*, vol. 17, pp. 676.
- Ma, N., Song, G. & Lee, H.J. 2004, "Position control of shape memory alloy actuators with internal electrical resistance feedback using neural networks", *Smart Materials and Structures*, vol. 13, pp. 777.
- Michaud, F. & Caron, S. 2002, "Roball, the rolling robot", *Autonomous Robots*, vol. 12, no. 2, pp. 211-222.
- Pfeifer, R., Iida, F. & Bongard, J. 2005, "New robotics: Design principles for intelligent systems", *Artificial Life*, vol. 11, no. 1-2, pp. 99-120.
- Puppe, A. 2008, "Radschlag in der Wüste", *Technical University of Berlin Intern*, December, viewed 2nd December, 2010, (in German) http://www.pressestelle.tu-berlin.de/newsportal/forschung/2008/radschlag_in_der_wueste/
- Shaw, J.A. 2000, "Simulations of localized thermo-mechanical behavior in a NiTi shape memory alloy", *International Journal of Plasticity*, vol. 16, no. 5, pp. 541-562.
- Shaw, J.A. & Kyriakides, S. 1995, "Thermomechanical aspects of NiTi", *Journal of the Mechanics and Physics of Solids*, vol. 43, no. 8, pp. 1243-1281.
- Sugiyama, Y. & Hirai, S. 2006, "Crawling and jumping by a deformable robot", *The International Journal of Robotics Research*, vol. 25, no. 5-6, pp. 603-620.
- Thrasher, M.A., Shahin, A.R., Meckl, P.H. & Jones, J.D. 1994, "Efficiency analysis of shape memory alloy actuators", *Smart Materials and Structures*, vol. 3, pp. 226-234.

- Vidal, N., Asua, E., Feuchtwanger, J., García-Arribas, A., Gutierrez, J. & Barandiaran, J.M. 2008, "FEM simulation of the Nitinol wire", *The European Physical Journal-Special Topics*, vol. 158, no. 1, pp. 39-44.
- Walters, E.T., Illich, P.A., Weeks, J.C. & Lewin, M.R. 2001, "Defensive responses of larval *Manduca sexta* and their sensitization by noxious stimuli in the laboratory and field", *Journal of Experimental Biology*, vol. 204, no. 3, pp. 457-469.
- Winter, C. 2009, "Hand-Springing Spider Excites Bionics Experts", *Spiegel Online International*, 22 Januaray, viewed 2nd December, 2010,
<http://www.spiegel.de/international/germany/0,1518,602160,00.html>
- Woods, W.A., Jr, Fusillo, S.J. & Trimmer, B.A. 2008, "Dynamic properties of a locomotory muscle of the tobacco hornworm *Manduca sexta* during strain cycling and simulated natural crawling", *The Journal of experimental biology*, vol. 211, no. Pt 6, pp. 873-882.

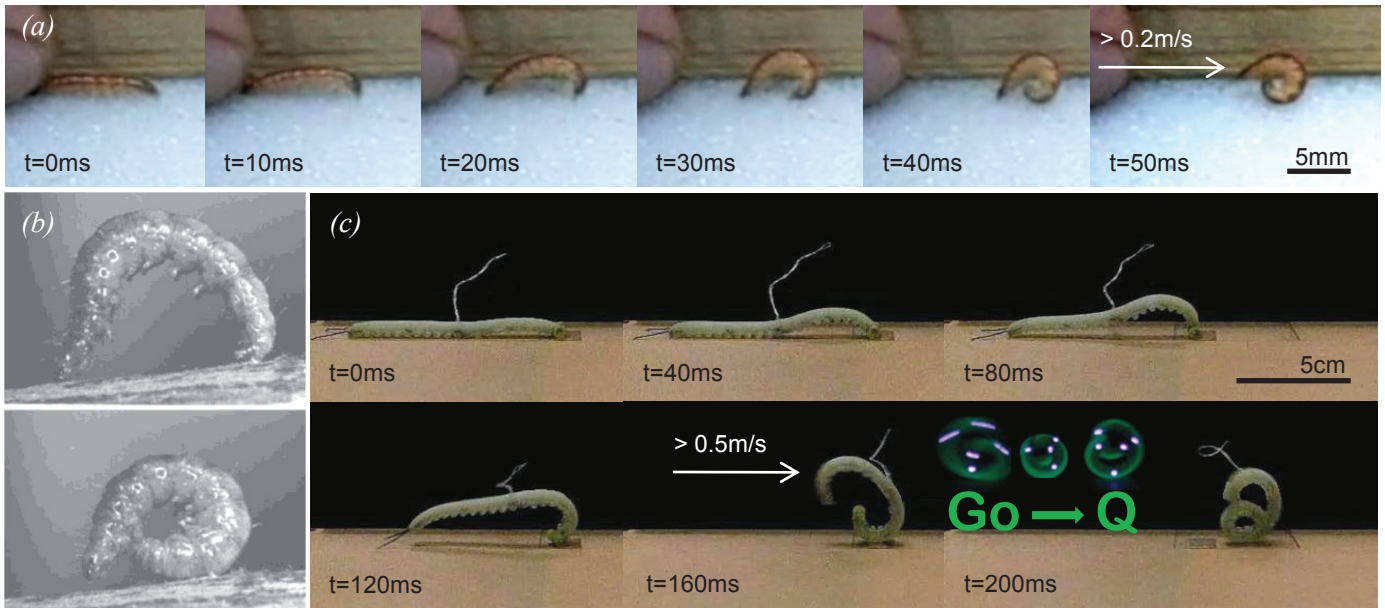


Fig. 1 Ballistic rolling escape in caterpillars and the robotic simulation. (a) After receiving a head blow on the ground, many leaf-roller caterpillars curl rapidly backward into a wheel to escape. The snapshots of the high speed video show a typical movement sequence from a caterpillar in the family *Crambidae*. (b) This behavior has been reported previously in *Pleuroptya ruralis* (photos adapted from Brackenbury 1997). The photo sequence shows how a caterpillar uses the terminal prolegs as the ground anchor and the thorax-head as the skid. (c) **GoQBot** is a soft-bodied robot that simulates this ballistic rolling behavior in details. It received the name **Go-Q** for its body conformations at the push-off phase. The robot is roughly 5 times larger than the animal in dimensions. It takes about 4 times longer to accelerate the robot (80~100 times heavier) into the rolling trajectory. Note that the caterpillars roll backward to escape. **GoQBot** copies the motion in the forward direction for implementation convenience.

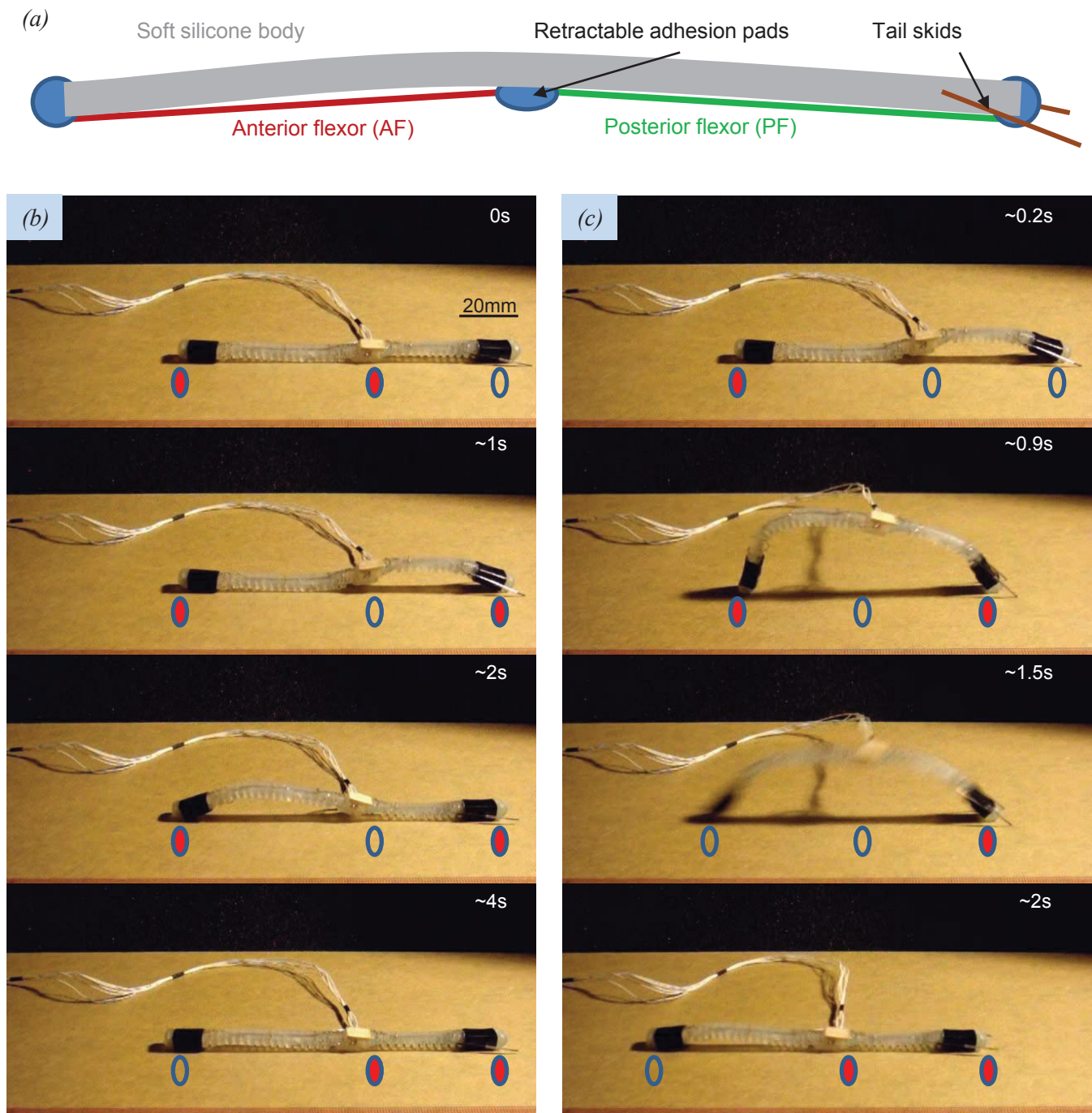


Fig. 2 Overall soft robot architecture. (a) GoQBot has two major actuation units: anterior flexor and posterior flexor. The motor pattern for crawling is quite simple with some overlap between the two flexors. Three retractable adhesion pads are controlled in sequence (marked) to produce appropriated ground anchors. The result is a crawling gait as shown in (b). During crawl-inch operation, the tail skids are retracted slightly to facilitate the functioning of posterior adhesion pad. Pacing up the gait pattern and proportionally scaling up the stimulation intensity leads to a large amplitude inching gait as exemplified in (c). The details of the adhesion pads and gait control is beyond the scope of this paper. This figure only introduces the basic architecture of GoQBot. Different versions of GoQBot may have morphological variations specific to our experimental goals.

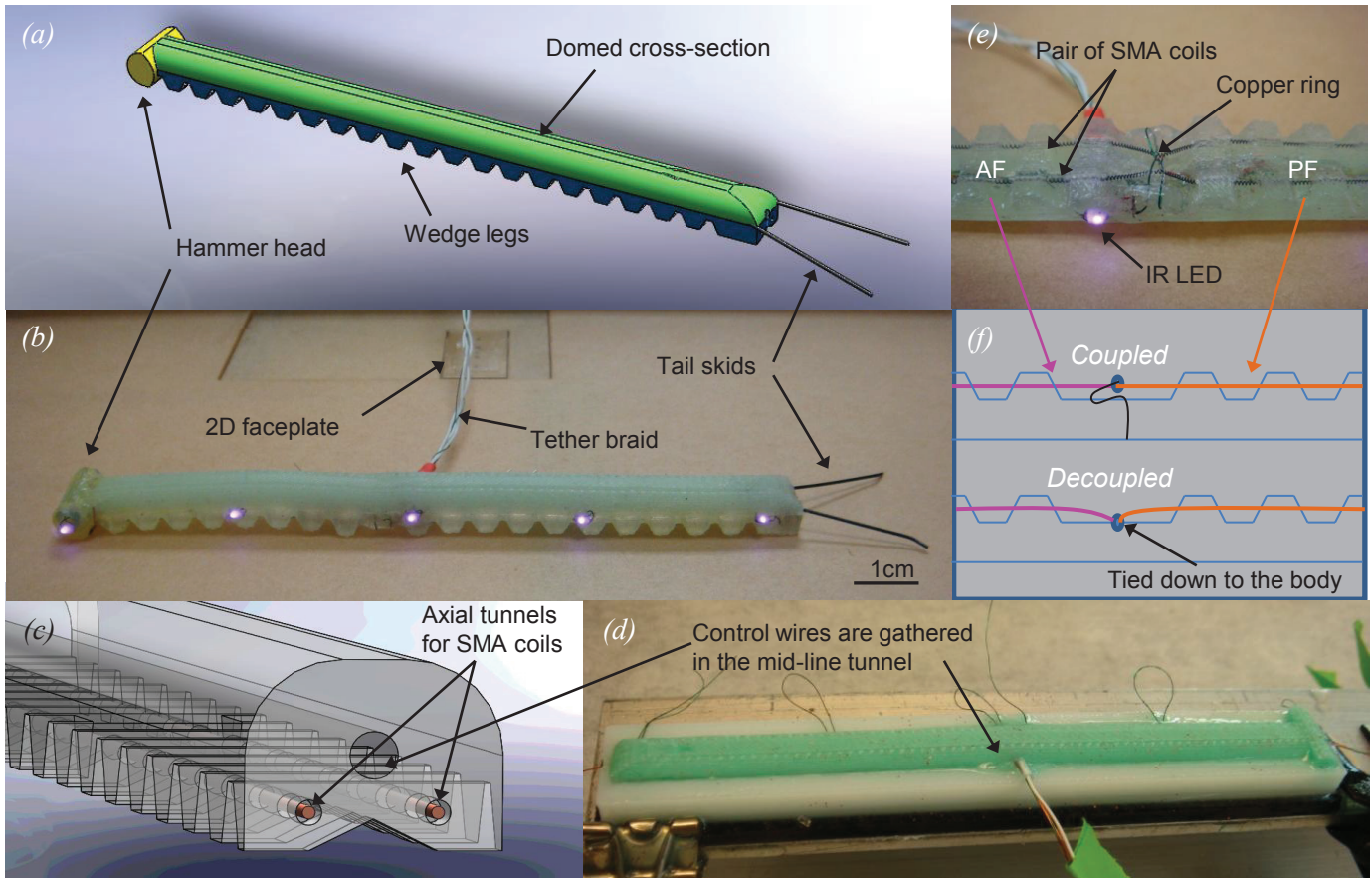


Fig. 3 Soft-bodied GoQBot morphologies. A new version of GoQBot was created specifically for characterizing the ballistic rolling behavior. (a) GoQBot has a composite body consisting of several mixtures of silicone rubbers (shown as different colors in this CAD drawing). The wide hammer head takes on a cylindrical shape to allow free pivoting. Tail skids were made of flexible polypropylene. (b) Five infrared LEDs are bonded on the left side of the body for kinematics tracking. All the signal wires are gathered into a 50cm tether braid coming out from the right side of the robot around the center of mass. (c) GoQBot has two ventral axial tunnels to accommodate the two SMA coils. Another mid-line tunnel houses all the control wires. (d) Body tether and control wires are pre-installed in the casting process. (e) Two shape memory alloy (SMA) coils are threaded through the entire length of the robot side by side with preload 50mN each. A copper ring is used to divide both coils into two functional units assuming bilateral symmetry: anterior flexor (magenta) and posterior flexor (orange). (f) The two flexors can be mechanically coupled through a loose tether or decoupled by a suture. In the coupled configuration, anterior flexor contraction directly stretches the posterior flexor within a displacement limit.

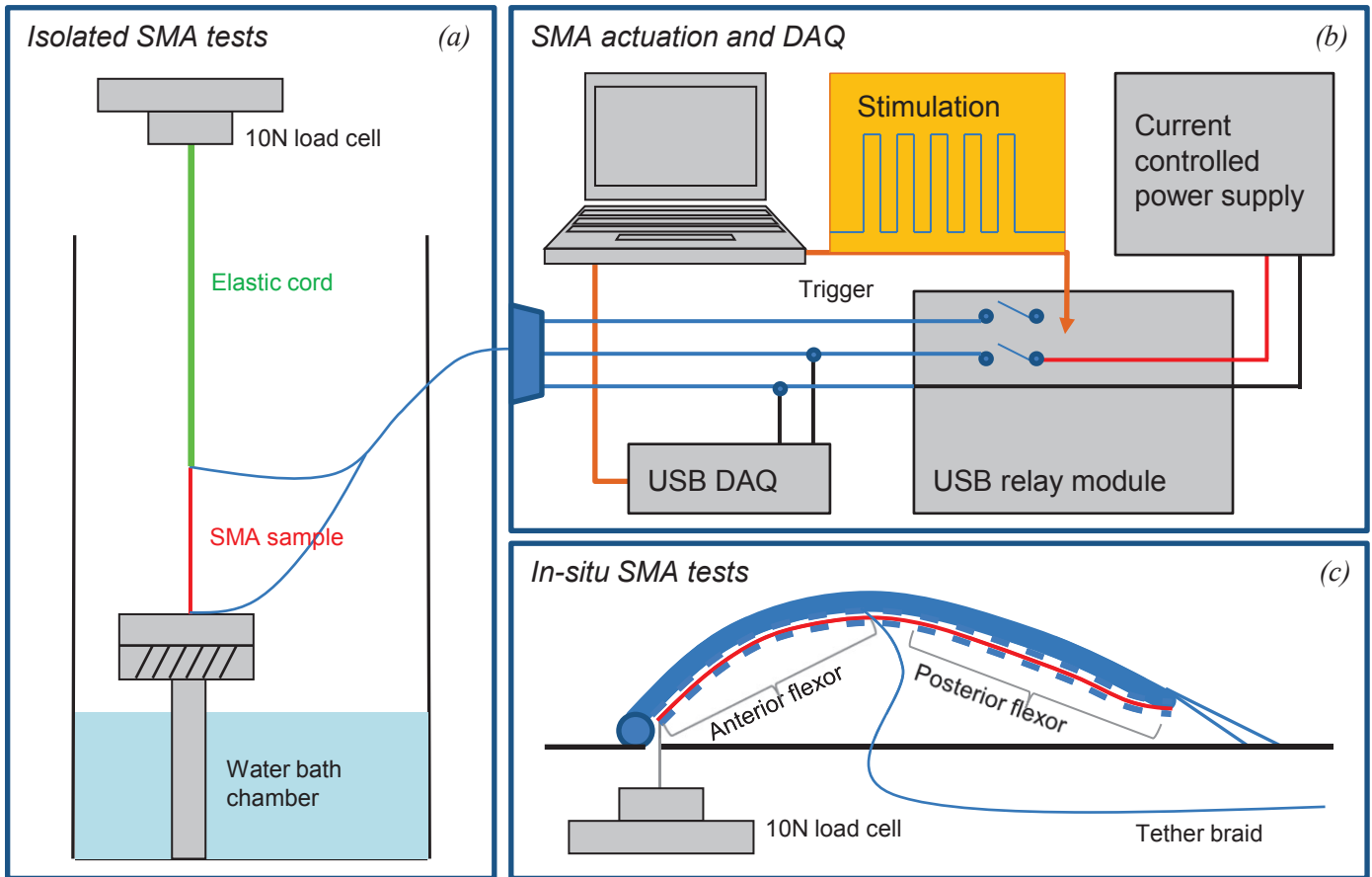


Fig. 4 The shape memory alloy coil tests. (a) SMA coils actuations were characterized in series with an elastic cord. Three different cords were utilized (stiffness 8.67, 34.9 and 87.9m/s) to resist the contracting SMA coil. The softest cord simulated free SMA contraction up to ~40%, and the stiffest cord provided near-isometric conditions (<10%). (b) In order to resolve the SMA activation dynamics, three levels of activation power were delivered to the SMA coil via current controlled DC pulses. The voltage across the SMA was monitored in all trials to determine the change of electrical resistance in the SMA coil. (c) In-situ SMA tests were implemented to examine the loading conditions inside the robot. During the test, the GoQBot was stimulated to perform a ballistic roll while the head was restrained on the substrate. The anterior flexor tension was transmitted directly through a tether to the load cell.

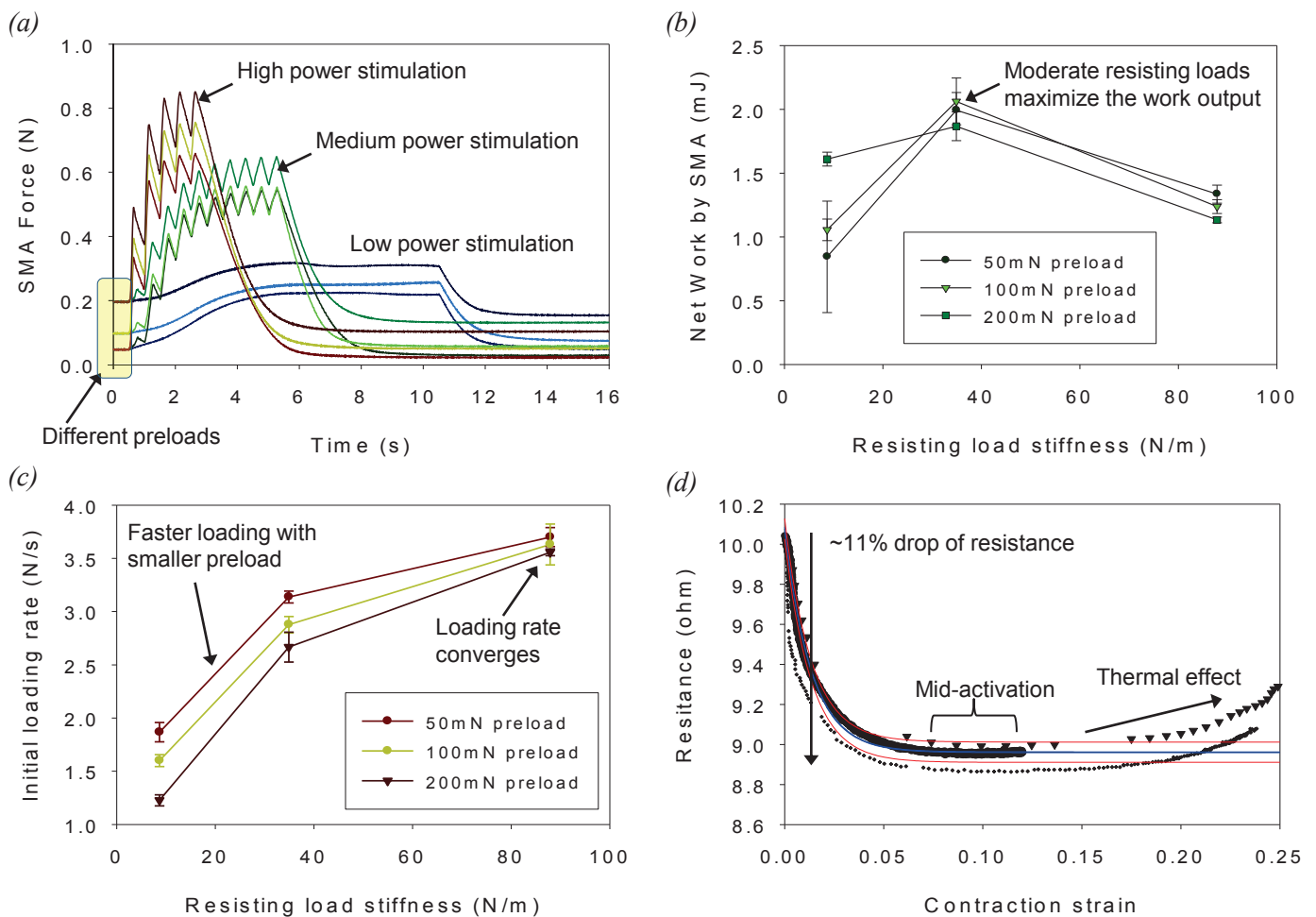


Fig. 5 SMA actuation characteristics. To illustrate actuation behaviors in GoQBot, all the SMA data shown are from 100 coils length specimens of BMX100 (BioMetal Helix nitinol). (a) SMA coils develop forces at different scales in response to pulses of current delivered at different powers. Low power stimulation creates smooth force curves with plateaus determined by the initial preload (ocean-tone curves). SMA coils stimulated at medium power start to exhibit tetanus-type force profile similar to that of muscles (forest-tone colors). High power stimulation produces the highest peak forces approaching 1N (earth-tone colors). (b) With little resisting load, SMA coils produces largest displacement accompanied by hysteresis-associated variations. As the resisting load increases, the displacement starts to decline but the tension per unit displacement increases. This leads to an increase of work production. Further increase of resisting load starts to limit the displacement and compromising the work output. (c) As expected, the initial rate of force development increases with stiffer load. The example shows the results from stimulation power 1.6W. Smaller preloads tend to give rise to faster initial loading. (d) The electric resistance drops exponentially (as indicated by the curve fit) when the SMA transits from martensite to austenite phase. The resistance curves flatten at around halfway to the full contraction strain. We call this stage “mid-activation”. Continuous heating causes the resistance to rise again as most parts of the SMA are in austenite phase. This overall trend can be used to monitor the actuator activities.

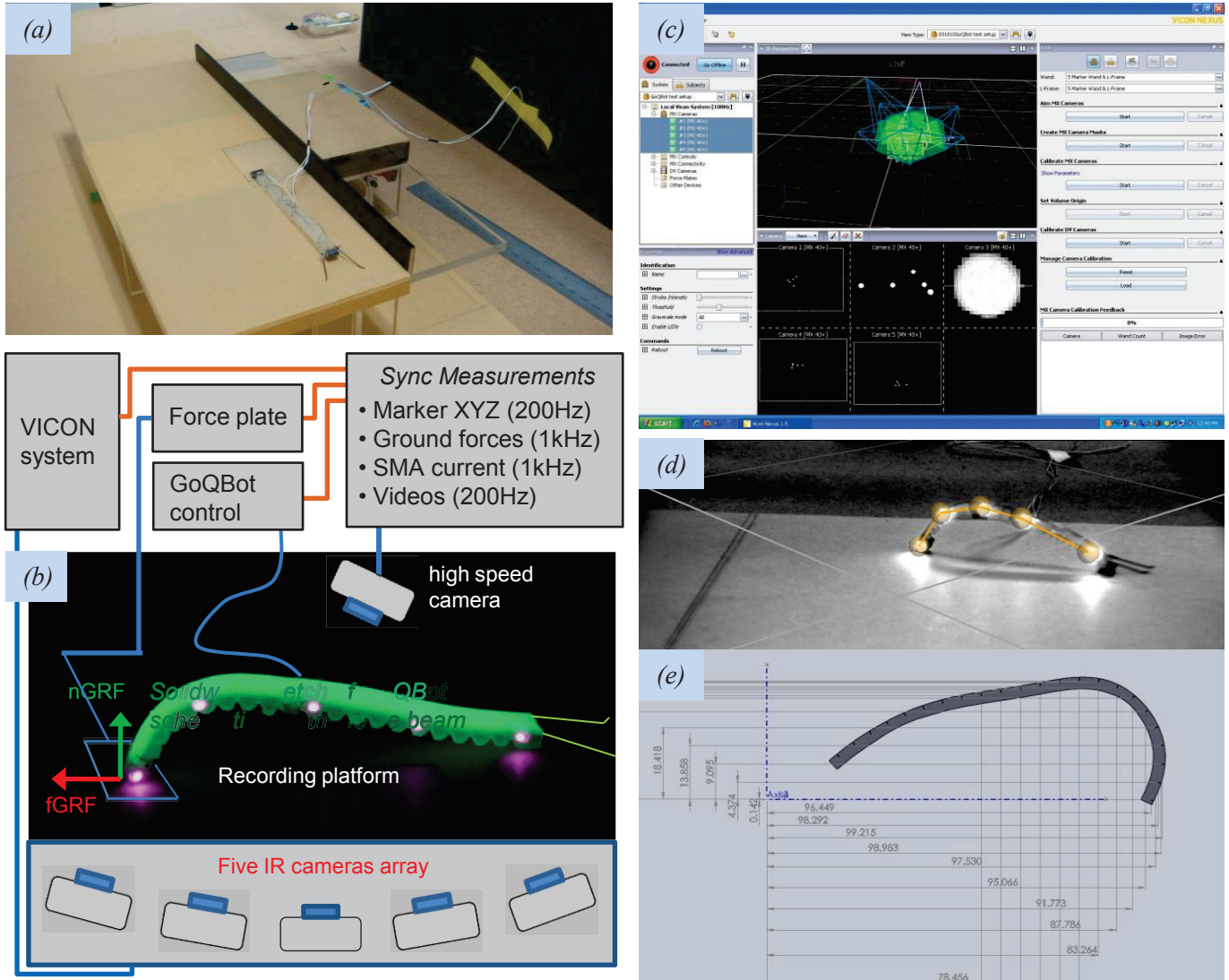


Fig. 6 Kinematics and dynamics measurements of ballistic rolling. (a) GoQBot was staged in a calibrated volume ($\sim 30\text{cm} \times 10\text{cm} \times 10\text{cm}$) on a flat linear track for motion analysis. The elevated track houses a custom force plate which measures the push-off ground reaction forces of the hammer head in two directions. (b) Some phosphorescence materials were added to highlight the robot for visualization purposes. Three dimensional kinematics data was captured by a five IR cameras array in the VICON system at 200Hz. Simultaneous force plate recording measured the ground reaction force at the hammer head of GoQBot (1kHz). The GoQBot control system provided voltage control stimulation to the SMA actuators while measuring the current draw to each actuator (1kHz). (c) The calibration frame was also custom made with high intensity IR emitters. These miniature LEDs have decent marker characteristics in the VICON tracking system. (d) A simple free joint model was constructed in VICON Nexus to automate the marker tracking. (e) A geometric model in SolidWorks was used to extrapolate body postures from the five IR marker coordinates. Since GoQBot has homogeneous body morphology, the body flexion can be captured by simple geometric constraints accurately.

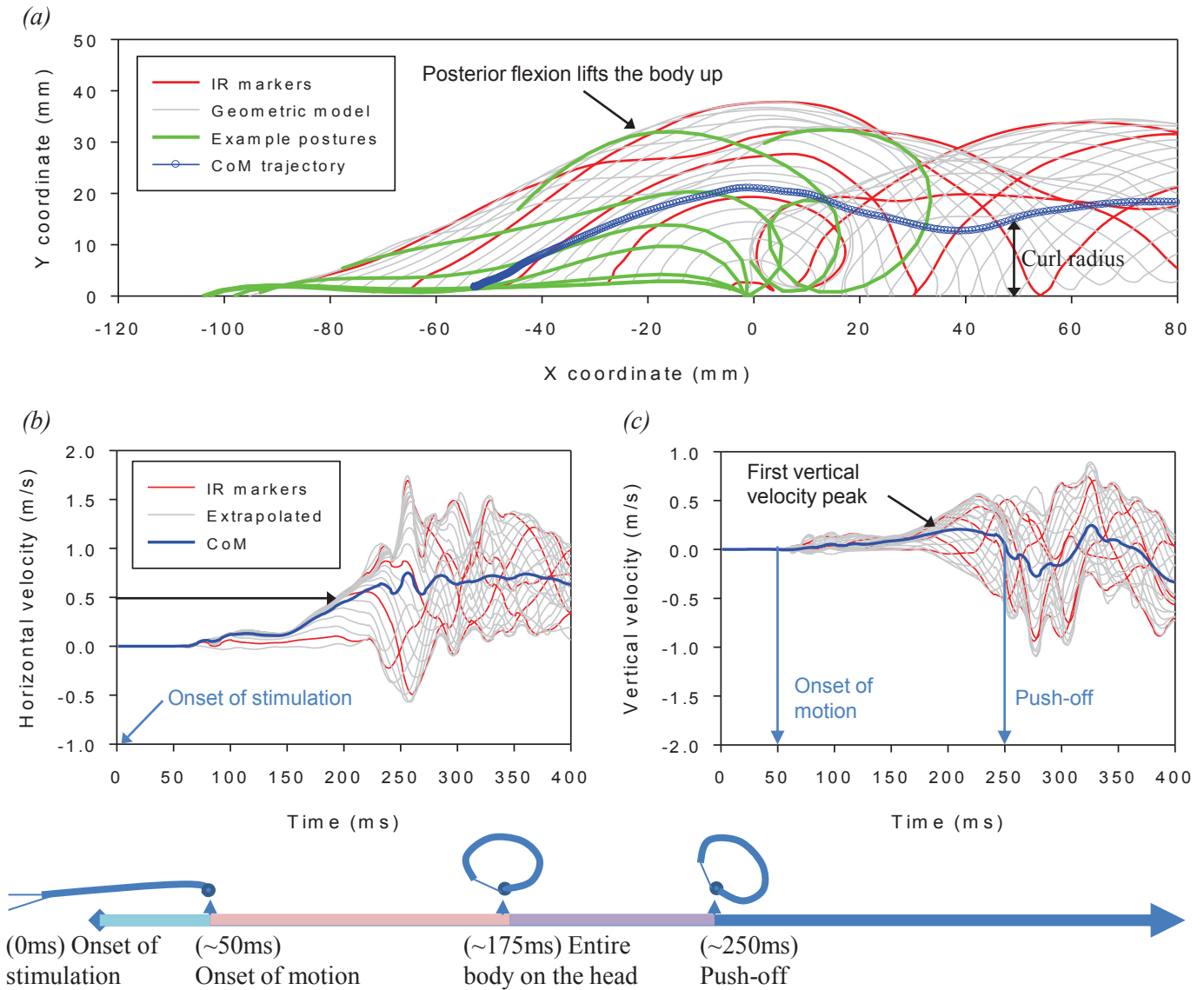


Fig. 7 Kinematics of a ballistic roll event. (a) GoQBot body differential masses follow a parabolic trajectory during the dynamic curling process as shown in the example. The center of mass is projected forward and maintained at slightly below 2cm from the ground after the body is curled into a wheel. (b) GoQBot accelerates forward to over 0.5m/s within 200ms from the onset of stimulation. This linear velocity sustains for at least another few hundreds of milliseconds, making the rolling range up to 25cm possible. (c) The tracking system does not detect any appreciable motion until around 50ms into the stimulation. Counting from the point of push-off around 250ms, the whole body curling motion was completed within 200ms (about twice the time a caterpillar would take).

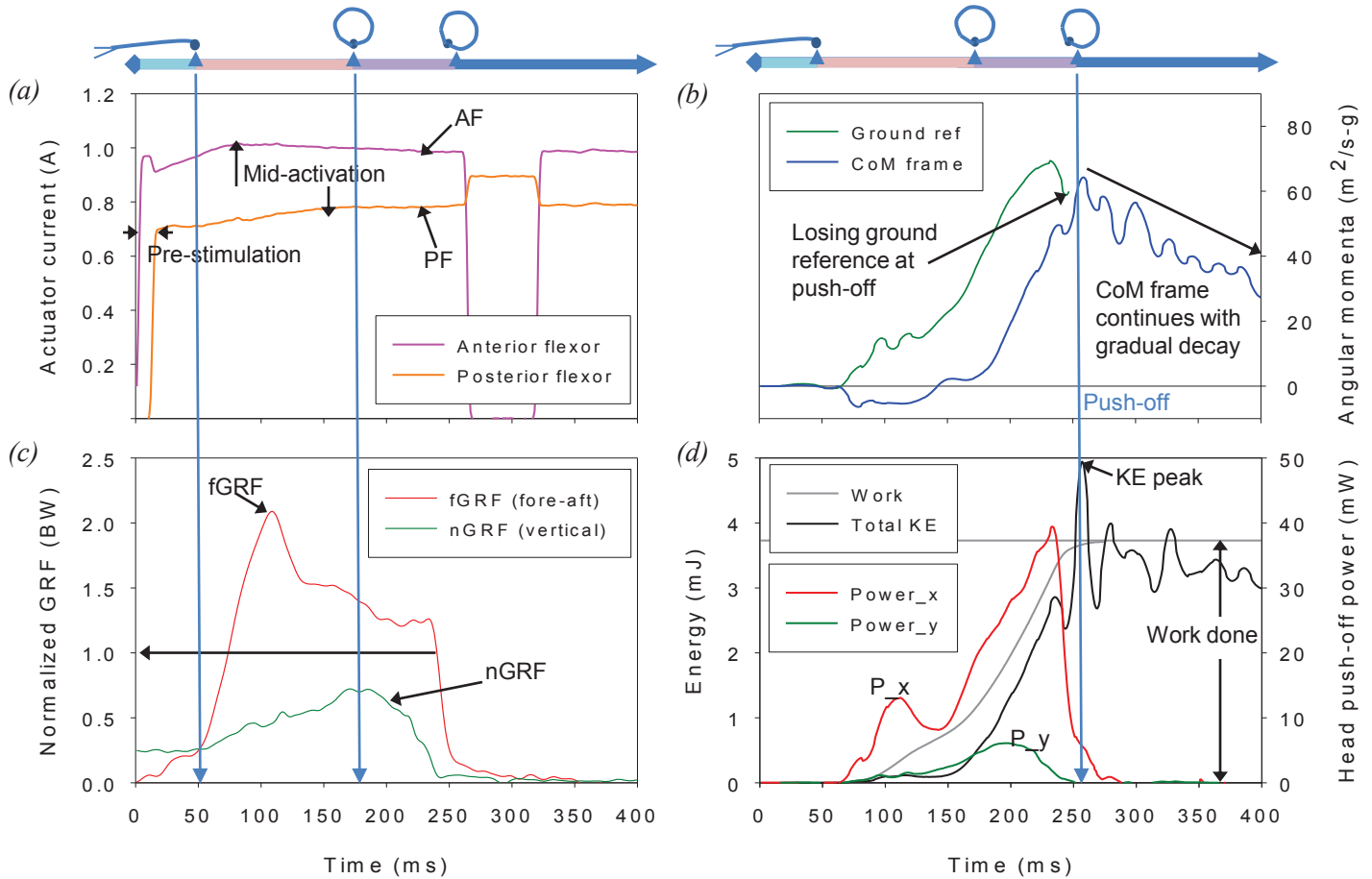


Fig. 8 Timing, angular momenta, ground reaction forces and energies of a ballistic roll event. (a) GoQBot rolling was achieved by a working actuation pattern determined empirically. The current draw of the actuators not only reflects the control signals but also shows the activation states. Higher current draw signifies the decrease of electrical resistance and therefore SMA activation. (b) GoQBot's angular momentum has a negative initial phase due to ventral flexion (blue trace). Once the tail skids start to tip the robot forward, the angular momentum builds up quickly. To characterize how the robot pivots about the hammer head, we can also calculate the angular momentum around the ground reference (the head contact point) (green trace). As soon as GoQBot pushes off, there is no ground reference anymore. (c) The ground reaction forces (GRF) at the hammer head of GoQBot show the push-off dynamics. In the vertical direction, the hammer head supports about 25% of the body weight (normal ground reaction forces nGRF in green). Forward thrust develops from the onset of actuator stimulation (fore-aft ground reaction forces fGRF in red). However, GoQBot does not have any observable motion only until after 50ms. This initial no-motion window accounts for the SMA activation and internal loading of the robot body. (d) Mechanical ground work from the hammer head (grey) is efficiently converted into Kinetic energy (black) in the form of both rotational momentum and linear momentum. The first peak of kinetic energy was used to define the push-off timing. It exceeds the total work done by the head (grey) because the tail skids also provides significant support in developing the vertical velocity. The ground power in the forward direction reaches almost 4mW close to the push-off moment.

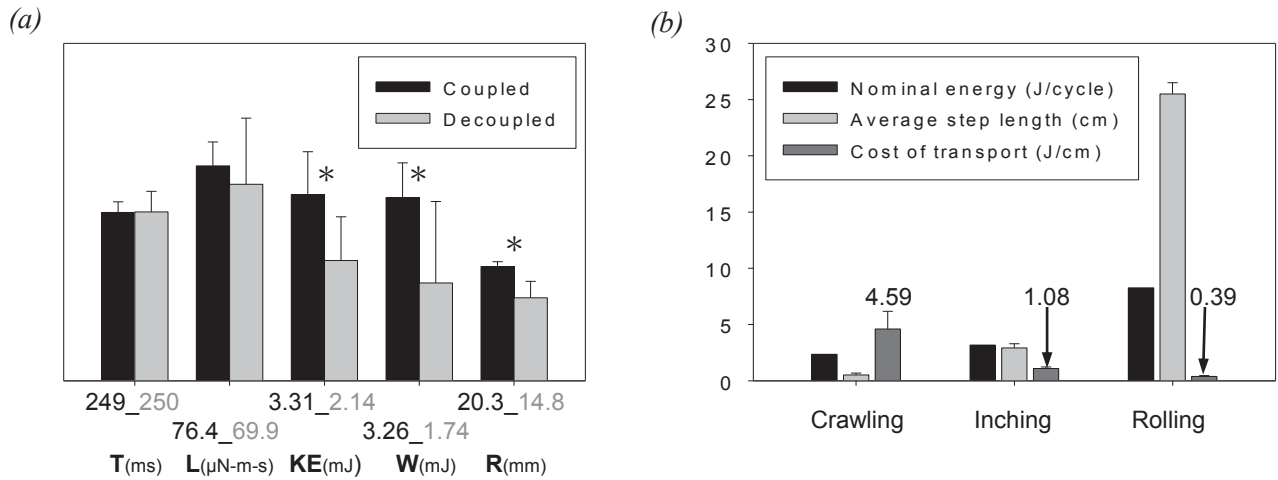


Fig. 9 GoQBot coordination and costs of transport. (a) The performance parameters were measured from repeated ballistic rolls with and without actuator coupling ($n=10$ each). The standard deviations in the decoupled configuration show greater variability. There were no significant difference in push-off time (T) and angular momentum (L) (two-tail t-test, $p > 0.05$, $df = 18$). Mechanical coupling leads to significant increase of maximum kinetic energy (KE) by allowing the head anchor to do more work (W) (two-tail t-test, $p < 0.02$, $df = 18$). Decoupled configuration, however, produce tighter nominal curl radius (R), since no tension is lost in stretching the other actuators (two-tail t-test, $p = 0.021$, $df = 18$). (b) Comparison between the three GoQBot gaits performed on flat surfaces (i.g. crawling, inching, rolling) shows great energetic advantage in rolling. The crawling and inching data were obtained from the previous version of GoQBot with similar body weight. The nominal energy was derived from the stimulation pattern and static SMA resistance therefore has no deviations. Step lengths from crawling and inching gaits were measured by marking the distance travel from 12 steps. While the energy cost per ballistic roll is more than twice the cycle energy in inching, the distance traveled is 6 times larger. This performance places the cost of transport for ballistic roll to half of that for inching.

Chapter 6: The principles of (loco)motion in soft-bodied animals

6.1 Hydrostatic skeleton vs. Environmental skeleton

Animal locomotion is constrained by one-dimensional tensile actuators. Regardless of the mode of locomotion, every movement has to come from muscles which only provide tension. To generate any useful three dimensional movements from these one dimensional contractions, animals need structural components to distribute and transmit muscle forces. A skeleton guides these one dimensional tensile deformations to produce three dimensional movements.

Soft-bodied animals, by definition, lack an articulated skeleton either internally (as bones in vertebrates) or externally (as exoskeletons in crustacean). Muscle contractions have to be constrained by other forms of structural support. Hydrostatic skeletons are a common solution in which the soft tissues provide stiffness through pressurization. This can be provided by muscles acting on a constrained incompressible fluid or on the muscle tissues themselves. Through my detailed analysis of force transmission in caterpillar crawling, I describe an alternative structural support that takes the place of the hydrostatic skeleton. A soft-bodied animal can use its environment as an external skeleton to translate muscle contractions and guide body deformation. This “environmental skeleton” strategy is not unique to caterpillars or soft-bodied animals. There are abundant examples in articulated systems as well. Soft-bodied animals simply express this strategy most evidently due to their lack of stiff skeletons. For caterpillars, this strategy greatly simplifies body coordination by removing the necessity of mapping the environment during locomotion. When a soft-bodied animal conforms to the substrate, it does not need to know the substrate geometry because it becomes part of the substrate geometry. The “environmental skeleton” strategy essentially collapses a three dimensional control problem to one dimension. A caterpillar crawling on a substrate can only go along the substrate.

While the environmental skeleton and hydrostatic skeleton might be mutually exclusive in principle, soft-bodied animals can switch between them back and forth to cope with environmental variations. Caterpillars can be extremely soft and flexible when they are attached to a substrate, but they can also cantilever almost their entire body to search for new substrates. This switching is a very subtle process and seems to depend on the scaling of the hydrostatic skeleton and the numbers of deployable body anchors. The modeling results of the caterpillar hydrostatic skeleton suggest that stiffer and more effective hydrostatic skeletons are more likely to exist in smaller bodies. An extensive caterpillar locomotion gaits analysis also confirms that mid-body attachments are necessary for constraining body deformation via the substrate. In short, we can draw two conclusions from these analyses. First, smaller bodies make better hydrostatic skeletons. Second, body attachments provide the constraints necessary for employing an environmental skeleton.

6.2 The evolution of caterpillar locomotor diversity

The two important conclusions highlighted above produce a plausible explanation for the evolution of caterpillar locomotion and even justify the existence of a soft-bodied larval stage in *Lepidoptera*. In order to process large amounts of energy-poor foliage, caterpillars require a disproportionately large abdomen which houses and maintains the digestive system. Sclerotizing the entire body surface is costly for the animal and incompatible with the rapidly molting and growing lifestyle. However, a soft bag of protein is difficult to control without any structural support. Abdominal prolegs evolved to provide local anchors and lock down the soft body to the substrate. These appendages immediately serve as useful constraints and reduce the degrees of freedom necessary to control. The crawling gait emerges as a simple method to stretch out the body progressively and gain net displacement using the environmental skeleton strategy.

Inching gaits were most likely progressively derived from the crawling gait by removing the mid body anchors and strengthening the hydrostatic skeleton. In a brief field survey, I have witnessed many forms of proleg reduction in caterpillars and corresponding variation in their locomotion. The absence of anterior abdominal prolegs encourages the mid body to buckle away from the substrate during locomotion. Many caterpillars with this body plan still retain the proper crawling kinematics in the posterior end of the abdomen while the anterior segments start to inch. Vestigial prolegs can be found in some species which also go through the proleg retraction motion signature of crawling gait even during an inching phase. Proleg reduction from the posterior end also leads to motor adaptation. The non load-bearing terminal prolegs appear to twitch during each inching cycle as if they are being stimulated in sequence with the rest of the motor program. The crawling motor pattern seems to be well conserved in these inch-crawl caterpillars.

In looking for caterpillars that have an inching repertoire, a magnifying glass is necessary as the animals become notably smaller. Inching is a much more dynamic gait in which the animals cycle their bodies several times faster than in most crawling gaits. High speed video analysis reveals many unstable postures during an inching step. With such a long body and no mid-body support, inchworms preferably locomote on top of the substrate and drag their abdomens along the substrate as much as possible. Lateral tipping is common and hysteric unstable vibrations are characteristics of inching. Crawling gaits can be recovered in inching caterpillars by mechanically restraining the mid body looping, resulting in a stereotypical crawl at high frequency. Inching is fundamentally a faster crawling pattern without mid body anchors. By limiting the body size, an inchworm gains stability and control from its hydrostatic skeleton but even here the caterpillar seems to exploit the support of the substrate to guide the dynamic abdomen contraction whenever possible.

6.3 What does a caterpillar know and need to know during locomotion?

These observations, together with the results of kinematic, dynamic and motor pattern measurements, establish the basic principles of caterpillar locomotion. However, my thesis cannot end without exploring what kind of information is necessary for controlling soft bodies. Based on my arguments on force transmission and the results of substrate manipulations, body stretching is an important factor for locomotion. Indeed, caterpillars have muscle-associated stretch receptors that respond to body stretch (Weevers 1965, Weevers 1966b, Weevers 1966a). In *Manduca* caterpillars, the tonic activities of the stretch receptors encode the segment length while the phasic activities represent the stretch velocities (Simon, Trimmer 2009). Interestingly, the tonic responses from such sensors adapt to the new segment length in a stretch-and-hold scenario quite readily within a minute. The amount of segmental stretch is, in a way, “forgotten” quickly while the sensors continue to detect new changes of segmental length. Mechanosensory feedback in soft-bodied animals has to account for various body contortions. For this reason, any proprioception must be fast adapting and recalibrated constantly. There is no evidence to show that caterpillars require real-time feedback from the stretch receptors to perform normal crawling behaviors. However, as body stretching can elicit locomotion, it is possible that body stretch is measured for higher decision making other than local body coordination.

Other mechanical sensing modalities in caterpillars tend to be very localized and specific. There is a plexus of multidendritic sensory neurons in the epidermis of *Manduca sexta* that respond to various types of tactile stimuli on the body wall (Grueber, Graubard & Truman 2001). The information coding in the three classes of these sensory neurons help the animal to identify noxious stimuli (predator attack) and perform a repertoire of defensive moves (Walters et al. 2001). In response to sharp poking or pinching, *Manduca* caterpillars can accurately and rapidly strike the source of the stimulus. Presumably mechanosensory hairs covering the entire body of the animal work with the multidendritic sensory

neurons to coordinate body coordination. Predatory caterpillars detect prey using only sensory hairs. A fly might be simply walking along a substrate and happen to trigger these hairs. The caterpillar can strike back precisely to the location of the fly and grab the victim on the escape take-off. Such mechanosensing is truly extraordinary and yet excessive for the execution of locomotion. Perhaps the body proprioceptive mapping in caterpillars deserves a little more attention in future research.

There are also plantar hairs lining the lateral edge of the prolegs which trigger a proleg withdrawal reflex via monosynaptic connections (Weeks, Jacobs 1987). Due to the location of these hairs, the interpretation of the afferent signal is fairly straightforward and corresponds to the proleg encountering an obstacle. However, other sensory information can modulate this reflex. Animals hanging upside down consistently reattach the prolegs faster after a withdrawal event and are more reluctant to perform proleg withdrawal behaviors (Belanger, Bender & Trimmer 2000). Caterpillars apparently can detect the direction of gravity very well. This is exemplified in inchworms' preference to move on top of the substrate. Detailed kinematic tracking experiments also demonstrated that caterpillars can anticipate obstacles in the path via local tactile sensing (van Griethuijsen, Trimmer 2010). Sensory information is clearly being processed and shared across body segments.

Olfaction and vision are relatively less important for terrestrial soft-bodied animal locomotion. Airborne chemical information fluctuates quickly with air currents. Odor tracking behaviors often require that the animal explore the spatial gradient of the odor plumes and with a certain navigation algorithm. This has been shown in robotic simulation as well as in aquatic animals (Ishida et al. 2001, Gardiner, Atema 2010). It is very difficult for slow moving caterpillars to make use of odor information. Similarly, visual information is relevant only when body trajectory can be monitored by visual cues (i.e. hand-eye coordination). With such mechanically forgiving bodies, caterpillars don't really need visual information to coordinate the body. It is possible for the six pairs of "eyes" (ocelli) on the caterpillar head capsule to

jointly detect large objects in close range (Ichikawa, Tateda 1982); (Dethier 1943). Some behaviors studies show that caterpillars can distinguish colors and patterns. However, these abilities are mostly examined in the context of navigation and threat detection (Götz 1936, Hundertmark 1936, Hundertmark 1937). No evidence suggests that caterpillars require visual information to coordinate the body movements.

6.4 Morphological computation and the future of soft robotics

In addition to sensory information, any complex mechanical system contains mechanical information in its structure and materials. For instance, the caterpillar prolegs retraction can be performed reliably by only two major muscles. This is possible through the well-organized tissue structures at the plantar membrane. Appropriate cuticular folds and reinforcements guide the trajectories of the ~25 crochets (micro hooks) to disengage them from the substrate in any situation. Presumably, the buckling stiffness of different cuticular folds help to encode the timing and dynamics of the proleg retraction behavior.

On a lower level, the mechanical responses of different tissues can also modulate the behaviors and even physiological conditions of an animal. In *Manduca* caterpillars, the soft cuticle has a nonlinear self-adapting property which accommodates volume fluctuation due to food intake or water loss. Rather than being perfectly elastic, the integument unloads some internal stress when loaded for an extended period of time and reestablishes stress when experiencing decreasing body pressure. This material behavior buffers the animal's body pressure and sustains the integrity of the hydrostatic skeleton.

Similar scenarios can be found in soft-bodied robots. In my crawling-inching robots, there is an inherent variability independent of the control pattern. Whenever I seek a working motor pattern, there is always a range of parameters that work equally well. Sending control patterns with values anywhere in the range makes no noticeable difference. The emerging behaviors and performance of the robots, in other

words, have a large mechanical component that is not associated with the control input. The robots crawl partly because their bodies want to crawl under the guidance of their body mechanics. Of course, these systems typically lack dynamics and therefore are inherently less sensitive to the initial conditions or sudden perturbations.

In a dynamic system, morphological computation plays a different role. Instead of acting to buffer body trajectories, morphological computation can be implemented to prepare a set of initial conditions for dynamic behavior. In the GoQBot ballistic rolling behavior, the nonlinear actuators coordinate with each other in mechanical terms (forces). The activation of one actuator can “inform” the other to get ready for the upcoming stimulation.

My thesis is not only about caterpillars or soft robots, both of which are tools for my scientific inquiry. I am broadly interested in how soft structures are controlled and respond to different control strategies in Nature. The quest for a universal soft body control theory and implementation of soft robots should not end with my thesis. So far we have identified the main principles of locomotion in caterpillars and simulated various mechanics and control strategies in soft robots. However, it is still not clear how to develop a system to generate stable controllers for highly nonlinear system involving soft body mechanics. The biomimetic SMA controller was my humble attempt to promote a new approach for developing soft body control theories. As it is too difficult to reproduce realistic and accurate soft body mechanics in virtual models, the next best thing is to perform physical simulations using robotic devices.

For future soft robot implementations, two shortcuts are available to speed up the development of working prototypes. First is to learn from the soft-bodied animals. This allows us to steal the physical simulation results from Mother Nature. Evolution has essentially run physical simulations for millions of years to figure out what works. The second shortcut is to exploit human intelligence by giving complex control tasks to human subjects and characterized the emerging control strategies empirically. We are

amazingly good at learning complex coordination and develop good intuitions. A similar approach has been deployed in a human-guided optimization method in which human guesswork on protein folding speeds up the search for the correct protein folding solution (Klau et al. 2002). Soft mechanical systems demand a highly compliant (and plastic) controller, and human adaptive intelligence is a great source of bio-inspirations. Our physical experiences of the world essentially serve to optimize our nonlinear motor controllers over time. After all, isn't human brain the most adaptable and flexible control system we know?

References

- Belanger, J.H., Bender, K.J. & Trimmer, B.A. 2000, "Context dependency of a limb withdrawal reflex in the caterpillar *Manduca sexta*", *Journal of Comparative Physiology A: Neuroethology, Sensory, Neural, and Behavioral Physiology*, vol. 186, no. 11, pp. 1041-1048.
- Dethier, V.G. 1943, "The dioptric apparatus of lateral ocelli. II. Visual capacities of the ocellus", *Journal of Cellular and Comparative Physiology*, vol. 22, no. 2, pp. 115-126.
- Gardiner, J.M. & Atema, J. 2010, "The Function of Bilateral Odor Arrival Time Differences in Olfactory Orientation of Sharks", *Current Biology*, .
- Götz, B. 1936, "Beiträge zur Analyse des Verhaltens von Schmetterlingsraupen beim Aufsuchen des Futters und des Verpuppungsplatzes", *Journal of Comparative Physiology A: Neuroethology, Sensory, Neural, and Behavioral Physiology*, vol. 23, no. 3, pp. 429-503.
- Grueber, W.B., Graubard, K. & Truman, J.W. 2001, "Tiling of the body wall by multidendritic sensory neurons in *Manduca sexta*", *The Journal of comparative neurology*, vol. 440, no. 3, pp. 271-283.
- Hundertmark, A. 1937, "Das Formenunterscheidungsvermögen der Eiraupen der Nonne (*Lymantria monacha* L.)", *Journal of Comparative Physiology A: Neuroethology, Sensory, Neural, and Behavioral Physiology*, vol. 24, no. 4, pp. 563-582.
- Hundertmark, A. 1936, "Helligkeits- und Farbenunterscheidungsvermögen der Eiraupen der Nonne (*Lymantria monacha* L.)", *Journal of Comparative Physiology A: Neuroethology, Sensory, Neural*, vol. 24, no. 1, pp. 42-57.
- Ichikawa, T. & Tateda, H. 1982, "Receptive field of the stemmata in the swallowtail butterfly *Papilio*", *Journal of Comparative Physiology A: Neuroethology, Sensory, Neural, and Behavioral Physiology*, vol. 146, no. 2, pp. 191-199.
- Ishida, H., Nakamoto, T., Moriizumi, T., Kikas, T. & Janata, J. 2001, "Plume-tracking robots: A new application of chemical sensors", *The Biological bulletin*, vol. 200, no. 2, pp. 222.
- Klau, G.W., Lesh, N., Marks, J. & Mitzenmacher, M. 2002, "Human-guided tabu search", *PROCEEDINGS OF THE NATIONAL CONFERENCE ON ARTIFICIAL INTELLIGENCE* Menlo Park, CA; Cambridge, MA; London; AAAI Press; MIT Press; 1999, , pp. 41.

- Simon, M.A. & Trimmer, B.A. 2009, "Movement encoding by a stretch receptor in the soft-bodied caterpillar, *Manduca sexta*", *Journal of Experimental Biology*, vol. 212, no. 7, pp. 1021.
- van Griethuijsen, L.I. & Trimmer, B.A. 2010, "Caterpillar crawling over irregular terrain: anticipation and local sensing", *Journal of Comparative Physiology A: Neuroethology, Sensory, Neural, and Behavioral Physiology*, vol. 196, no. 6, pp. 397-406.
- Walters, E.T., Illich, P.A., Weeks, J.C. & Lewin, M.R. 2001, "Defensive responses of larval *Manduca sexta* and their sensitization by noxious stimuli in the laboratory and field", *Journal of Experimental Biology*, vol. 204, no. 3, pp. 457-469.
- Weeks, J.C. & Jacobs, G.A. 1987, "A reflex behavior mediated by monosynaptic connections between hair afferents and motoneurons in the larval tobacco hornworm, *Manduca sexta*", *Journal of Comparative Physiology A: Neuroethology, Sensory, Neural, and Behavioral Physiology*, vol. 160, no. 3, pp. 315-329.
- Weevers, R.D. 1966a, "The physiology of a lepidopteran muscle receptor. II. The function of the receptor muscle", *The Journal of experimental biology*, vol. 44, no. 1, pp. 195-208.
- Weevers, R.D. 1966b, "The physiology of lepidopteran muscle receptor. I. The sensory response to stretching", *The Journal of experimental biology*, vol. 44, no. 1, pp. 177-194.
- Weevers, R.G. 1965, "Proprioceptive Reflexes and the Co-ordination of Locomotion in the Caterpillar of *Antheraea pernyi* (Lepidoptera)", *The physiology of the insect central nervous system: papers from the 12th International Congress of Entomology held in London, 1964* Academic Press, , pp. 113.